UNIVERSIDAD POLITÉCNICA DE MADRID
ESCUELA TÉCNICA SUPERIOR DE INGENIEROS DE TELECOMUNICACIÓN

Development and optimization of new cancer treatments based on the hyperthermia technique mediated by magnetic nanoparticles

DOCTORAL THESIS

Submitted for the degree of doctor by:

LILIA SOUIADE

Master in Pharmaceutical Biotechnology
Engineer in Biotechnology

Madrid, 2025

UNIVERSIDAD POLITÉCNICA DE MADRID
ESCUELA TÉCNICA SUPERIOR DE INGENIEROS
DE TELECOMUNICACIÓN

Doctoral Degree in Biomedical Engineering

Development and optimization of new cancer treatments based on the hyperthermia technique mediated by magnetic nanoparticles

DOCTORAL THESIS

Submitted for the degree of doctor by:

LILIA SOUIADE
Master in Pharmaceutical Biotechnology
Engineer in Biotechnology

Under the supervision of:

Dr. JOSE JAVIER SERRANO OLMEDO
Dr. MILAGROS RAMOS GOMEZ

Madrid, 2025

Title: Development and optimization of new cancer treatments based on the hyperthermia technique mediated by magnetic nanoparticles

Author: Lilia Souiade

Doctoral Program: Biomedical Engineering

Thesis Supervision:

Director : Pr. Jose Javier Serrano Olmedo, professor at the University of Polytechnique of Madrid and principal investigator at the center for biomedical technology

Co-supervisor: Dr. Milagros Ramos Gómez, professor at the University of Polytechnique of Madrid and principal investigator at the center for biomedical technology

External Reviewers:

Thesis Defense Committee:

Thesis Defense Date: "This thesis has been partially supported by the Spanish Agency of Research projects PGC2018-097531-B-I00, PDC2022-133028-I00 y PID2022-138881OB-I00"

ACKNOWLEDGEMENT

I would like to express my sincere gratitude to all the people who helped me during my PhD journey. In particular, my parents ***Ouarda*** *and* ***Salah*** *who gave me valuable advice and provided me with support that carried me through all the stages of my PhD. Your prayers for me were what sustained me this far, thanks to you. I thank my brother* ***Aboubaker****, my brother* ***Mohamed Hamdi*** *and his wife* ***Myra Ramirez*** *for their support, help and advice all the time.*

I am also extremely thankful to my supervisor, ***Pr. Jose Javier Serrano Olmedo****, for his guidance, feedback and support throughout my research project, thank you for making this work possible. I also extend my heartfelt thanks to my co-supervisor* ***Dr. Milagros Ramos Gómez****, for her continuous support, guidance and invaluable suggestions. Their vast expertise has enriched this project substantially.*

I would also like to give special thanks to the research group of the laboratory of Bioinstrumentation and Nanomedicine, and in particular to my research group of "Magnetic Hyperthermia for cancer treatment" from the Center or Biomedical Technologies, ***Javier Domingo Diez****,* ***Cesar Alcaide*** *and* ***Miguel Rodriguez Ramon*** *for collaborating in this work. Thanks to* ***Niloufar Kazemi*** *and* ***Shiyang Li*** *for their support and friendship. Also, I would like to thank* ***Mahdi Yonesi*** *from the Center of Biomedical Technologies for his support, help and friendship, and to* ***Soledad Martinez*** *for her help.*

In addition, I thank my mobility supervisor ***Dr. Theodoros Samaras*** *from the Aristotle University of Thessaloniki for his teaching and guidance in computational simulations of magnetic hyperthermia and the experimental study in dosimetry. I also thank all the members of the physics department and those of the MagnaCharta laboratory, for having accompanied me throughout the mobility and for sharing their experience with me. My appreciation also goes to* ***Pr. Dario B. Rodrigues*** *from the University of Maryland for his help and suggestions in this study.*

I am profoundly grateful to the ***Algerian Ministry of Higher Education and Scientific Research****, for the fully financed PhD scholarship. Finally, I would like to Thank* ***GOD****, for his guidance, support and for giving me this opportunity and opening for me the doors for success, science, acknowledgement and self-development.*

Abstract

Magnetic hyperthermia (MHT) is an antitumor therapy that employs magnetic nanoparticles (MNPs) to generate localized heat using a low-frequency alternating magnetic field (AMF). Recently, trapezoidal pulsed alternating magnetic fields (TPAMF) have been shown to improve heating efficiency compared to sinusoidal fields, enhancing therapeutic effects. Since thermal therapies are often combined with treatments such as chemotherapy to improve clinical outcomes, this study sought to increase the effectiveness of MHT by using non-sinusoidal AMF waveforms and combining them with chemotherapy.

The tumor cell lines B16F10 and CT2A, along with C57BL/6 mice, were used to evaluate the effects of different waveforms: trapezoidal (TP), quasi-square (TS), triangular (TR), and sinusoidal (SN). In in vitro testing, MNPs were incubated at non-cytotoxic concentrations (1 and 4 mg/mL). Exposure to SN and PAMF alone did not cause significant cell mortality, but non-sinusoidal waves, especially TS and TP, showed greater efficacy in inducing cell death.

Furthermore, the synergistic effect of combining MHT generated with TPAMF and the chemotherapeutic agent 5-fluorouracil (5-FU) was evaluated. CT2A cells treated with MNP and exposed to two cycles of MHT using a TS waveform (200 kHz, 2 mT, 30 min per cycle with a 45-min interval), showed a 58.9% increase in cell death when combined with 5-FU, compared to 31.4% observed with MHT alone. Cell death was primarily due to necrosis, and improved immunogenicity was observed, with a 17% increase in calreticulin-positive (CRT) cells compared to 10% generated by MHT alone. Preliminary in vivo studies showed a slight reduction in tumor size with TPAMF compared to sinusoidal AMF. In silico simulations revealed a stable thermal distribution (~37°C) at intensities below 5 mT, without significant thermal side effects, confirming the safety of TPAMF. At higher frequencies and amplitudes, eddy current effects with exponential temperature increases were detected, highlighting the need for careful parameter control.

In conclusion, non-sinusoidal TP, TS, and TR waveforms were more effective than traditional sinusoidal waveforms at inducing cell death in MHT treatments. The combination of MHT with TPAMF and chemotherapy not only increased cytotoxic efficacy but also induced enhanced immunogenic cell death (ICD), which suggests that it is potentially capable of promoting the immune system activation. This combined approach could represent a promising strategy for improving cancer treatments.

Resumen

La hipertermia magnética (HTM) es una terapia oncológica que emplea nanopartículas magnéticas (MNP) para generar calor localizado mediante un campo magnético alterno (AMF) de baja frecuencia. Recientemente, se ha demostrado que los campos magnéticos alternos pulsados trapezoidales (TPAMF) mejoran la eficiencia del calentamiento respecto a los campos sinusoidales, potenciando los efectos terapéuticos. Dado que las terapias térmicas suelen combinarse con tratamientos como la quimioterapia para mejorar los resultados clínicos, en este estudio se buscó incrementar la efectividad de la HTM mediante el uso de formas de onda AMF no sinusoidales y su combinación con quimioterapia.

Se utilizaron las líneas celulares tumorales B16F10 y CT2A, junto con ratones C57BL/6, para evaluar los efectos de diferentes formas de onda: trapezoidal (TP), casi cuadrada (TS), triangular (TR) y sinusoidal (SN). En las pruebas in vitro, las MNP se incubaron a concentraciones no citotóxicas (1 y 4 mg/mL). La exposición a SN y PAMF por sí solos no causó una mortalidad celular significativa, pero las ondas no sinusoidales, en especial TS y TP, mostraron una mayor eficacia en la inducción de muerte celular.

Además, se evaluó el efecto sinérgico de combinar la HTM generada con TPAMF y el agente quimioterapéutico 5-fluorouracilo (5-FU). Las células CT2A, tratadas con MNP y expuestas a dos ciclos de HTM usando una onda TS (200 kHz, 2 mT, 30 min por ciclo con 45 min de intervalo), mostraron un aumento en la muerte celular del 58,9% al combinarse con 5-FU, en comparación con el 31,4% observado con HTM sola. La muerte celular fue principalmente por necrosis, y se observó una mejora en la inmunogenicidad del tratamiento, con un aumento del 17% en células positivas a calreticulina (CRT) frente al 10% generado por HTM sola.

Los estudios preliminares in vivo mostraron una leve reducción del tamaño tumoral con TPAMF frente a ondas sinusoidales. Por su parte, las simulaciones in silico revelaron una distribución térmica estable (~37 °C) con intensidades menores a 5 mT, sin efectos térmicos secundarios significativos, lo que confirma la seguridad del uso de TPAMF. A mayores frecuencias y amplitudes, se detectaron efectos de corrientes parásitas con aumento exponencial de temperatura, destacando la necesidad de un control cuidadoso de los parámetros.

En conclusión, las formas de onda no sinusoidales TP, TS y TR resultaron más eficaces que las sinusoidales tradicionales para inducir muerte celular en tratamientos con HTM. La combinación de HTM con TPAMF y quimioterapia no solo incrementó la eficacia citotóxica, sino que también indujo una muerte celular inmunogénica mejorada (ICD), potencialmente capaz de estimular el sistema inmunológico mediante la activación de células presentadoras de

antígenos (APC). Este enfoque combinado podría representar una estrategia prometedora para mejorar los tratamientos contra el cáncer.

Table of contents

List of Figures

List of Tables

Abbreviations

AC	Alternating Current
APCs	Antigen presenting cells
APS	3-aminopropyl-trietoxysilane
ATP	Adenosine triphosphate
CAD	Computer-aided design
CRT	Calreticulin
DAMPs	Damage associated molecular patterns
DLS	Dynamic light scattering
DMEM	Dulbecco's modified eagle's medium
DSO	Digital storage oscilloscope
EMFs	Electromagnetic Fields
ER	Endoplasmic reticulum
FBS	Fetal bovine serum
FDTD	Finite Difference Time Domain
FEM	Finite Element Method
FIT	Finite Integration Technique
FR-WBH	Fever-range whole-body hyperthermia
FU	Fluorouracil
GBM	Glioblastoma multiform
HMGB1	High mobility group box-1
HSP	Heat shock protein
HT	Hyperthermia
ICD	Immunogenic cell death
IR	Infrared

LF	Low frequency
MHT	Magnetic hyperthermia
MMPs	Magnetic microparticles
MNPs	Magnetic nanoparticles
MoM	Method of Moments
MQS	Magneto-quasi-static
PBHTE	Pennes bio-heat transfer equation
PBS	Phosphate buffered saline
PCL	Poly-Capro-Lactone
PEG	Poly-Ethylene Glycol
PFA	Paraformaldehyde
PI	Propidium Iodide
PLA	Poly-Lactic Acid
PLGA	Poly -Lactic-Co-Glycolic Acid
TP-PAMFs	Trapezoidal Pulsed alternating magnetic fields
RES	Reticuloendothelial system
ROS	Reactive oxygen species
SAR	Specific absorption rate
SEM	Standard error of the mean
SLP	Specific loss power
SN	Sinusoidal
SPM	Superparamagnetic
TP	Trapezoidal
TR	Triangular
TS	Trapezoidal-Square
TT	Trapezoidal-Triangular

I Chapter 1: Generale Introduction

1. Motivation

Nanoscience and nanotechnology are areas of science, engineering, and technology that involve manipulation of materials at the nanoscale ranges between 1 and 100 nanometers and can be used in a wide range of scientific disciplines, including medicine, biology, chemistry, physics, electronics, materials science and engineering(Bayda et al., 2020). Nanotechnology is gaining significant attention worldwide for disease treatment and has expanded its applications in several areas of biomedical science including drug delivery and drug carriers, disease detection and diagnosis, targeted and gene therapy, molecular imaging, biomarker mapping, and drug carriers (Tekade et al., 2017). The study of nanomaterials has been around since the industrial revolution, with Richard Zsigmondy proposing the concept of manipulating matter at the atomic level in 1959. The 21st-century saw increased interest in nanoscience and nanotechnology, with President Bill Clinton advocating for funding in this emerging technology during a speech at Caltech in 2000. Japanese scientist Norio Taniguchi was the first to use the term "nanotechnology" to describe semiconductor processes occurring at the nanometer scale. The golden era of nanotechnology began in the 1980s with the discovery of fullerenes. Eric Drexler, a Massachusetts Institute of Technology (MIT) professor, used ideas from Feynman and Taniguchi to develop molecular nanotechnology, which later advanced with the development of carbon nanotubes (Hulla et al., 2015). The application of nanotechnology in medicine is known as nanomedicine, where nano-oncology is a branch of nanomedicine that uses nanotechnology in diagnosis and cancer therapy (Tekade et al., 2017). Nanotechnology research for cancer therapy is fueled by recent achievements in the conception of various nano-vehicles for efficient drug delivery including liposomes, micelles, dendrimers, quantum dots and nanocarriers (Chaturvedi et al., 2018). Furthermore, physiochemical properties that characterize the bionanomaterial such as being ultrasmall, large surface, controllable size, high reactivity and functionalizable surface, led to the development of magnetic nanoparticles with unique properties suitable for biomedical application including cancer diagnosis and therapy(Tekade et al., 2017).The cancer therapy has faced numerous challenges throughout history. Traditional treatments consist of chemotherapy, radiotherapy, alongside with surgery for solid tumors, but they have not been very successful due to their side effects. Hyperthermia is one of the modern cancer treatments and has been previously investigated(Kok & Crezee, 2020). Most hyperthermia techniques have limitations either due to the damage to surrounding healthy

tissues and considerable side effects during regional or whole-body hyperthermia (S. Kim et al., 2024), or the inability to deliver heat effectively, achieving or maintaining the optimal temperature necessary for treatment in the tumoral targeted area without damaging healthy tissues when non-invasive methods are used in particular to treat the deep seated tumors (Treatments, 2021). Hence the adequate hyperthermia system will need to target and localize the heat in the tumor tissues without causing hot spots due to eddy currents, which can cause significant damage to the surrounding healthy tissues, reducing the treatment efficacy. Beside, its need to have the ability to combine with other treatment modalities. The intersection of nanotechnology advancements targeted therapeutic techniques, and hyperthermia clinical practicality has led to the emergence of hyperthermia-mediated magnetic nanoparticles as a promising cancer treatment approach, due to their ability to target tumoral tissues and treat the cancer by local heating (Rubia-Rodríguez et al., 2021).

2. Problematic

Magnetic hyperthermia (MHT) is a localized form of hyperthermia which adopts magnetic nano-mediators to absorb the electromagnetic energy and convert it into heat under an alternating current (AC) magnetic field (Jordan et al., 1999) (Suto et al., 2009). The advantages of this hyperthermic treatment form include localized magnetic nanoparticles (MNPs) accumulation, targeted heat delivery to the tumor affected region, minimized damage to the healthy tissues, reduced side effects, the ability to combine with the traditional cancer treatments (Peiravi et al., 2022) (H. C. Kim et al., 2015) (Shirvalilou et al., 2021). The amount of heat during the treatment increases with nanoparticles concentration, but this parameter must be carefully monitored to minimize potential toxicity. Massive amounts of nanoparticles can cause inflammation, oxidative stress, and cell damage. Hence, optimizing the dose of MNPs while minimizing toxicity is a critical parameter for an optimum therapeutic efficacy (Frtús et al., 2020) (Chang et al., 2018).MNPs are characterized by hysteretic properties when exposed to an alternating magnetic field (AMFs) which give rise to magnetically induce heating. An efficient hyperthermic treatment is achieved by delivering an optimal thermal dose inside the targeted tumor area without causing any damage to the surrounding healthy tissues. For that fact, MNPs surface must be functionalized to reduce agglomeration, improve biocompatibility, prevent protein absorption, reduce toxicity, and extend the NP time in blood circulation. In the absence of coating, MNPs that have a hydrophobic surface and a high surface- to-volume ratio agglomerate to form large clusters (Kritika, N., & Roy, I. (2022). In parallel, it is important to

accumulate the MNPs inside the cancer zone to be treated, therefore researchers are exploring different strategies for delivering MNPs to tumor cells, such as using targeted drug delivery systems or surface modification techniques. Cancer cells overexpress certain surface receptors in contrast to normal cells, allowing for active targeting adequately functionalization with targeting molecules such as an antibodies, peptides, or ligand proteins. This contrasts with the passive targeting obtained by the EPR effect (Pirollo & Chang, 2008).

Various strategies have been employed by different research groups to overcome the associated limitations for further progression in clinical practice and to improve the efficacy of MHT for cancer treatment. The main purpose in MHT is to increase the heating efficiency of MNPs to achieve an optimum therapeutic thermal dose, hence maximum effects against tumoral cells. The optimum thermal dose is achieved by MNPs depending on various intrinsic and extrinsic parameters. This can be achieved either by adjusting intrinsic parameters of MNPs, such as the size, shape, composition and coating (Crăciunescu et al., 2021; De La Presa et al., 2012; Khandhar et al., 2012; Narayanaswamy et al., 2021a; Portilla, Fernández-Afonso, et al., 2022). For instance, in (Salas et al., 2013), iron oxide nanoflowers of 38 nm exhibit superior heating efficiency compared to nanocubes under identical conditions. This enhanced performance is attributed to the unique morphology of nanoflowers, which promotes better magnetic interactions and heat dissipation, resulting in a high SAR. However, nanocubes of 19 nm are supposed to be more efficient than any other nanocubes. Or by adjusting extrinsic parameters that influence the electromagnetic fields (EMFs), such as the frequency, the amplitude, the coil geometry since the amount of heat dissipated is proportional to these parameters (Obaidat et al., 2019) (Vicentini et al., 2024). The AC magnetic field applied to induce heat by MNPs should meet safety restrictions and respect a limited threshold of use for the frequency and/or amplitude to prevent any generation of hot spots due to eddy currents occurrence in the biological material, which could damage healthy cells. Recently, in (Zeinoun, Serrano, et al., 2021) a new approach for MHT cancer treatment was investigated which consist in the application of non-sinusoidal waveforms instead of the conventional sinusoidal waveform. A MHT system newly designed by the MHT team of the laboratory of Bioinstrumentation and Nanomedicine of the Center for Biomedical Technology affiliated to the University of Polytechnic of Madrid, aims to enhance the heating efficiency through the application of non-sinusoidal waveforms. These waveforms are capable of increasing the heat produced by nanoparticles compared to the sinusoidal ones under the same conditions. This study is devoted for optimizing MHT cancer treatment using non-sinusoidal alternating magnetic fields against two types of cancer considered among the

most dangerous forms of tumors, the melanoma and glioblastoma multiform (GBM), seeking to enhance the therapeutic effects inside cancer cells and increase damage impacts while preventing any damage to healthy cells.

3. Hypothesis

Non-sinusoidal waveforms can induce more efficient heating in MNPs compared to traditional sinusoidal signals. Previous work on Zeinoun's system indicates that non-sinusoidal waveforms can enhance the heating efficiency of MNPs as seen in Figure 1. For instance, trapezoidal and almost-square signals have been shown to allow MNPs to reach higher efficiency in heat generation. This increased efficiency is attributed to the steeper slopes and abrupt transitions inherent in non-sinusoidal waveforms, which may enhance the magnetic relaxation processes responsible for heat generation.

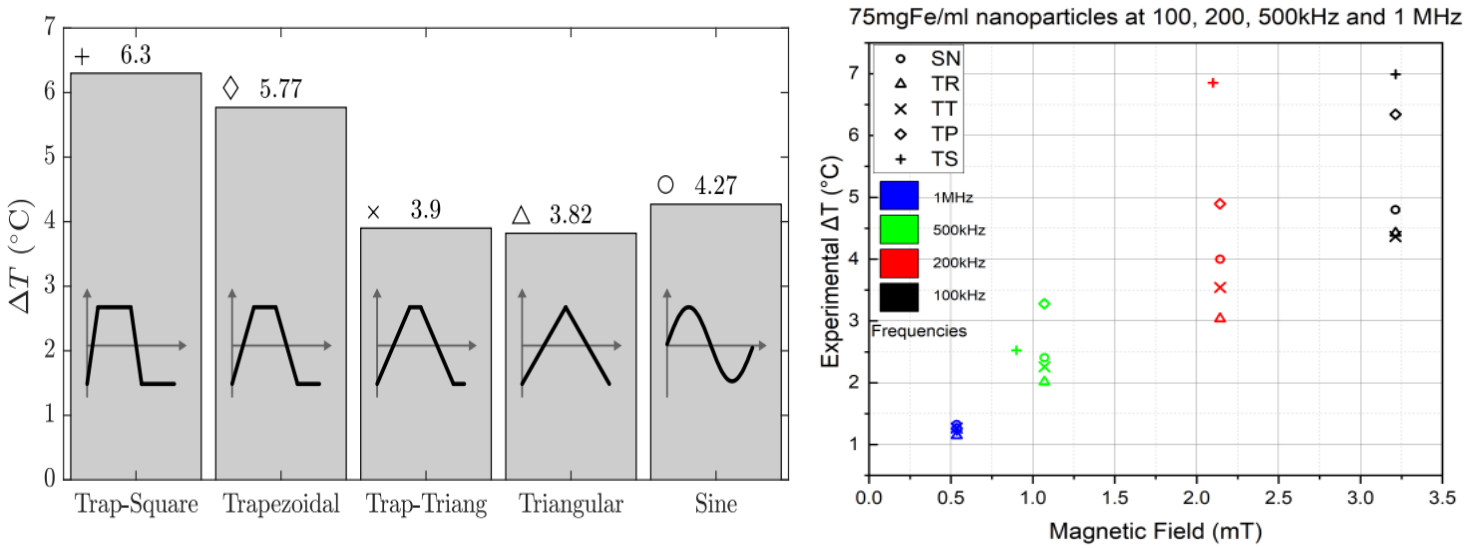

Figure 1: Heat efficiency experimental outcomes relative to the signal slope at 100 kHz and 3.21 mT for an assembly of 10 nm MNPs at 75 mg/ml. Experimental temperature measurement for different non-sinusoidal waveforms, different frequencies (100 kHz-200 kHz-500 kHz-1000 kHz) and different amplitudes going from 0.5 to 3.2 mT, using a sample of iron oxide nanoparticles at 75 mg/ml (Zeinoun, Serrano, et al., 2021) (Zeinoun, Domingo-Diez, et al., 2021).

The experimental results on a magnetic ferrofluid carried out on Zeinoun's system have shown a superior heat generation by almost square and trapezoidal over 71% and 45%, respectively, of the thermal power generation efficiency compared to SN. Therefore, the use non-sinusoidal

signals beside the enhancement of the NP features could allow it to overcome the issues posed in both preclinical and clinical studies and permit NPs to reach their optimal alignment to optimize the killing effect on tumor cells and the MNP internalization process.

Numerical research by another group found that using non-harmonic field waveforms may significantly improve the SAR of iron oxide nanoparticle Neel relaxations (Figure 2). Therefore, trapezoidal and almost square waveforms are particularly promising.

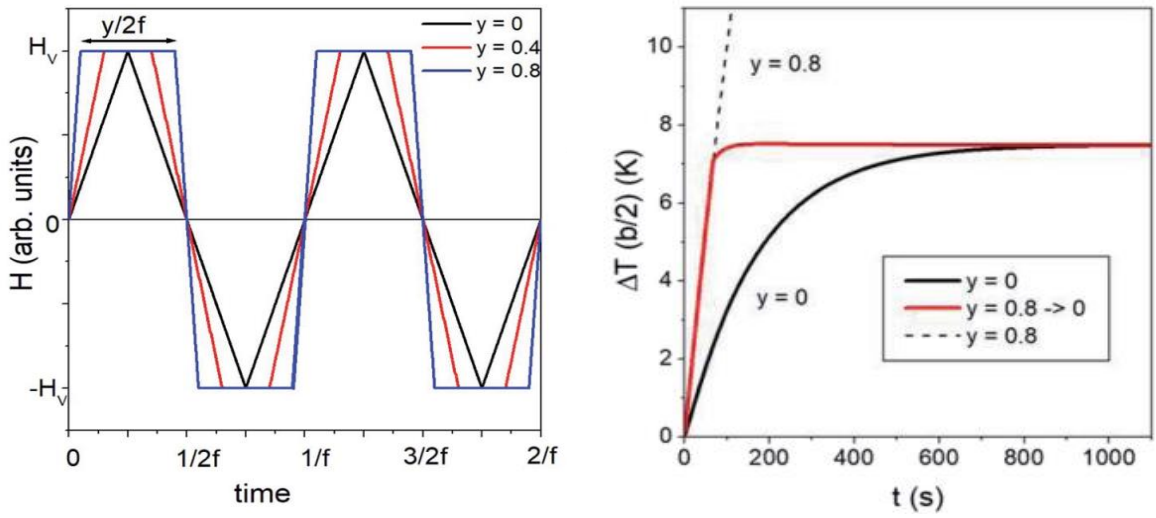

Figure 2: Left panel: parameters defining the Trapezoidal waveform. Right panel: temperature curves in function of time depicting the increase in temperature rate with non-harmonic driving fields with respect to the harmonic one (Barrera et al., 2020).

In this study, we assume that the increase in SAR by the non-sinusoidal waveforms compared to the sinusoidal waveform, as demonstrated by Zeinoun's work and predicted by Barrera's theory, will improve the cell damage. SAR increase due to the the slope of the signal waveform might be due to the rapid transitions inside magnetic nanoparticles and this can potentially accelerate the relaxations processes. In other words, we assume that the non-sinusoidal signals (TS and TP) may increase considerably the rates of absorption and conversion of the external magnetic field energy to heat by MNPs due to a faster reorientation and alignment of the nanoparticles magnetic moments with the direction of the AMF, in comparison to the sinusoidal signal for same AMF conditions, which leads to larger heat production and enhance the heating efficiency of the MNPs, hence a significant increase of cancer cell death. Another possible suggestion, is that the magnetic moments of MNPs exposed to non-sinusoidal signals achieve a maximum alignment compared to the sinusoidal signals which increase the SAR and the killing effects against cancer cells.

Moreover, we hypothesize that magnetic hyperthermia treatment using non-sinusoidal signals in combination with chemotherapy, may induce immune system activation by promoting immunogenic cell death (ICD), thereby enhancing the therapeutic effects of MHT. Chemotherapeutic drugs such as doxorubicin, paclitaxel, mitoxantrone and oxaliplatin, as well as gamma irradiation, were considered as inducers of ICD due to their ability to eliminate tumor cells by provoking endoplasmic reticulum (ER) stress. The ICD pathway plays a crucial role in stimulating an immune response. It is characterized by the release of damage-associated molecular patterns (DAMPs) from dying cancer cells, such as the calreticulin (CRT) and heat shock proteins. These DAMPs collectively stimulate dendritic cells to process and present tumor antigens, leading to the activation of tumor-specific T cells that target and remove the remaining cancer cells. The exposure of CRT on the membrane of dying cells serves as a signal that binds to APC, prompting the activation of an immune response against tumor through the recruitment of CD4+ and CD8+ cells (Figure 3) (Zhu et al., 2021) (Troitskaya et al., 2022) (Z. Li et al., 2022).

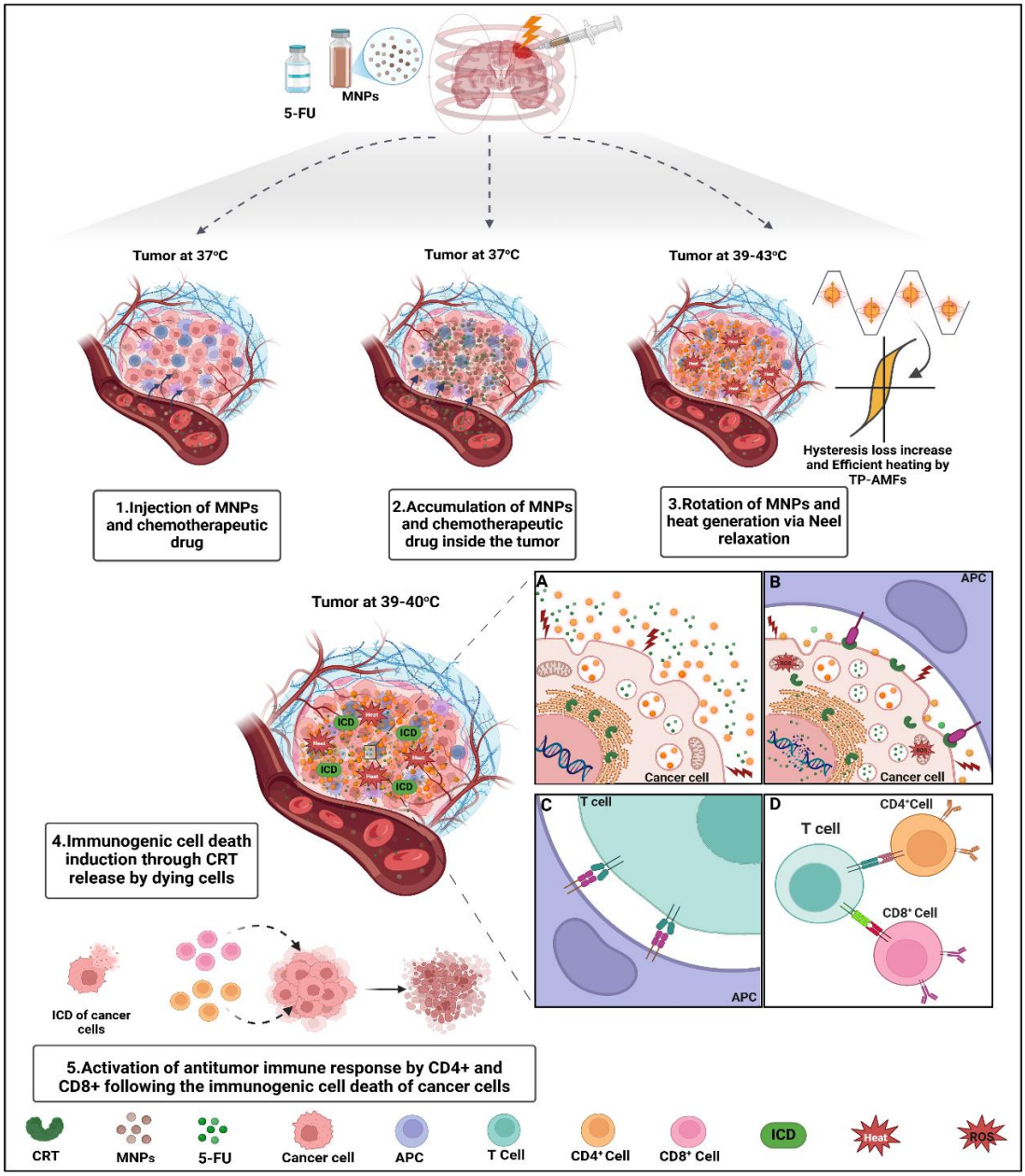

Figure 3: Synergistic effects between MHT and chemotherapy in activation of an antitumor immune response. MNPs are efficiently internalized by cancer cells and their exposure to TP-AMFs allows an efficient heat release causing permeabilization of biological membranes and enhancing the uptake of chemotherapeutic drugs (A). The combined treatment with chemotherapy (5-FU) and MHT provoke important consequences in cancer cells, including the production of reactive oxygen species (ROS), DNA fragmentation, ER stress and leading to CRT exposure (B). The expression of CRT by dying cells serves as a signal that binds to APC (C) which in turn prompting the activation of an immune response against tumor via recruitment of CD4+ and CD8+ cells (D).

4. Objectives

This thesis was carried out in the Center for Biomedical Technology (CTB) in Madrid, in the framework of the PID2022-138881OB-I00 "KNOWLEDGE GENERATION PROJECTS" and PDC2022-133028-I00 "Proof of concept projects". The scholarship was fully funded by the Algerian Ministry of Higher Education and Scientific Research.

The main objective of this Thesis is the optimization of magnetic hyperthermia treatment using pulsed alternating magnetic fields instead of the conventional sinusoidal fields to improve the thermal killing effects against cancer cells. The study focuses on preclinical tests (in vitro and in vivo) against glioblastoma multiform (GBM) and melanoma by magnetic hyperthermia mediated-non sinusoidal signals. In particular it focuses on the following objectives:

- Study the internalization of magnetic nanoparticles by cancer cells (GBM and Melanoma)
- Screening of the optimum parameters of the electromagnetic field, frequency (100 kHz-1000 kHz) and amplitude(0.5mT-3mT), and MNPs concentration and incubation time in order to achieve an optimal therapeutic effect.
- In vitro tests to explore the enhancement of magnetic hyperthermia via non-sinusoidal signals compared to magnetic hyperthermia via sinusoidal ones.
- In vitro tests to increase the therapeutic outcomes and explore the synergistic effects of the combined treatment with magnetic hyperthermia mediated by non-sinusoidal signals and chemotherapy (5-Fluorouracil)
- In vivo tests to evaluate the safety of the non-sinusoidal signals and to treat the tumor in a C57BL/6 mouse model.
- In silico study using sim4life software to simulate the eddy currents effects of the non-sinusoidal signals compared to the sinusoidal one inside biological model to mimic in vitro and in vivo experiments, and to simulate MNPs heating based on Rosensweig's model.

5. Thesis Outline

In the following, I present the contents of the chapters in more detail:

In Chapter 1: First chapter includes a general introduction to the thesis project, including as first point, the motivation with which the study raised, than the problematic posed and the hypothesis of enhancing the therapeutic efficacy of MHT by using non-sinusoidal AMFs instead of the sinusoidal one. At the end, the principal objectives of the project have been described.

In Chapter 2: This chapter consists in the state of the art of our thesis project, it includes a detailed definition and clarification of the magnetic hyperthermia anticancer treatment, and how this treatment approach raised from several concepts and research areas. It also includes many research studies which investigated the same approach.

In Chapter 3: In this chapter, materials and methods used in this study to achieve the meaningful objectives were defined. First of all, a detailed description of the MHT device used was provided and all the tools utilized alongside the device. Second, we introduced all the biological materials and equipments used for the preclinical tests. Third, we identified all the methodologies and protocols used before, during and after the treatment process for preclinical tests, in which MHT treatment have been performed alone using sinusoidal and non-sinusoidal signals, and /or in combination with chemotherapy (5-Fluorouracil). Schematic illustrations have been delivered alongside the methodologies for further clarification. We provided also the mathematical model and software used for analyzing and presenting the data which consisted in the software package GraphPad Prism Version 8.0.1 for Windows.

In Chapter 4: The in vitro MHT produced by non-sinusoidal AMFs post-treatment results have been illustrated compared to SN-AMF and for different treatment strategies: MHT alone or in combination with chemotherapy. Later, the in vivo preliminary post-treatment results using MHT produced by TS-AMF were presented compared to SN-AMF. Then, all the data obtained were discussed and compared to research studies from other scientific groups.

In Chapter 5: This chapter is devoted to the doctoral training of three moths made in the Aristotle University of Thessaloniki, Greece. The training was based on in -silico study using the computational platform Sim4life to simulate the MNPs heating and to evaluate the eddy currents effects using non-sinusoidal AMFs aiming to define the safety limit for the application of these new efficient waveforms.

In chapter 6: The scientific publications and contributions obtained by this project are represented.

In chapter 7: A final conclusion on the whole study was delivered.

II Chapter 2: State of the art

1. Hyperthermia

1.1. Hyperthermia in cancer treatment

Progress in cancer treatment remains a high priority, considering that cancer is still the leading cause of death all over the world. In 2020, there were nearly 19.3 million new cancer cases and 10.0 million deaths per year. In 2040, it is expected to be 28.4 million cases (Sung et al., 2021). In cancer treatment, there are different modalities to cure cancer patients. The traditional modalities consist of surgery, radiotherapy and chemotherapy, while the modern modalities include hormone therapy, immunotherapy, gene therapy and hyperthermia (Figure 4). Traditional treatments often come with significant and various side effects and can cause damage to healthy tissues (Abbas & Rehman, 2018) (Danewalia & Singh, 2021) (Czarnywojtek et al., 2023).

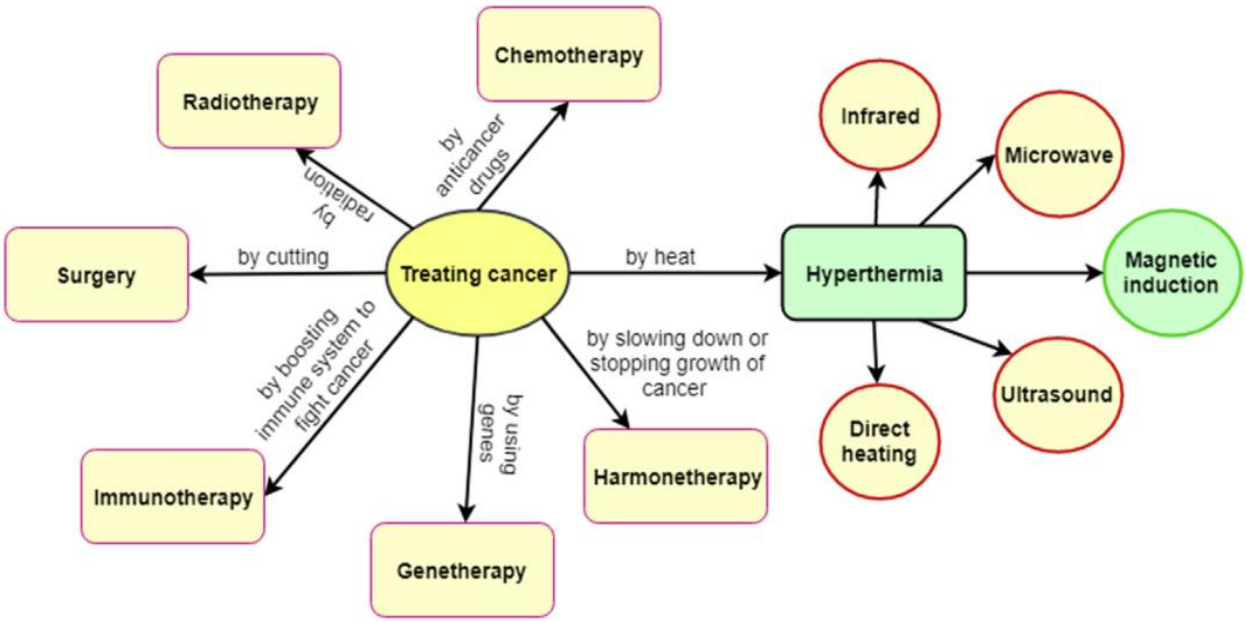

Figure 4: Cancer treatment modalities (Danewalia & Singh, 2021)

An interest in utilizing hyperthermia emerged as an alternative or adjuvant treatment modality for cancer. Hyperthermia involves a controlled heat raising of the tumor site between 39-43°C for 60 minutes leading to tumor shrinking. It employs electromagnetic wave energy as heat of source over other conventional heating methods owing to their penetration capability and conversion into volumetric heat energy in the targeted tissues (Treatments, 2021).

In ancient times, hyperthermia was employed by various cultures for therapeutic purposes. For example, ancient Egyptians used hot sand baths to induce hyperthermia and treat various diseases. In ancient Greece, Hippocrates recognized the potential benefits of hyperthermia in treating various diseases and described the use of heat as a therapeutic modality. During the Middle Ages, European physicians continued to explore hyperthermia as a treatment. They used methods such as hot water baths and cautery to raise body temperature in hopes of promoting healing. However, it was not until the 19th century that hyperthermia gained significant scientific and medical attention. The development of more precise temperature control techniques and understanding the effects of hyperthermia on the body led to its use in the treatment of various conditions such as cancer. During the 20th century, hyperthermia as a cancer treatment gained more recognition and was studied extensively. These studies led to advancements in hyperthermia technology and the development of more targeted and controlled methods of applying heat to tumors. Carl D. W. Busch (1826 - 1881), a German surgeon, wrote the first scientific study on hyperthermia in 1866, describing the regression of sarcoma in a patient who had been suffering from protracted high fevers caused by an infectious condition. Inspired by the basic discovery that increased temperatures may selectively destroy malignant cells while preserving healthy tissue, the young American surgeon William B. Coley (1862 - 1936) attempted a similar experiment. In 1891, he created Coley's toxin, a bacterial pyrogen that causes fever in patients on purpose. Because of this accomplishment, he was dubbed the "Father of Modern Hyperthermia Against Cancer." This therapy for inoperable cancer can increase five-year survival rates up to 64%. In 1898, Swedish doctor Frans J. E. Westermark (1853 - 1941) sought to cure incurable uterine cervix tumors using high temperature water (42 - 44°C) flowing in a metal coil. However, it had one major drawback, each patient reacts differently to the treatment. As a result, this approach gradually fell out of use (Gas, 2011).

1.2. Hyperthermia mechanism

Hyperthermia is an aid to conventional therapies (chemotherapy, radiotherapy, surgery) used against cancer. It is almost always used in combination with these other techniques in order to increase their effectiveness (Ressel et al., 2002) (Datta et al., 2015). The hyperthermia mechanism consists in heating the lesion site based on the response of the tumor tissue and healthy tissue to heat (Figure 5). In normal tissues, blood vessels dilate when subjected to a heat source. Unlike healthy cells, a tumor is a group of compressed, tightly packed abnormal cells and as a result, blood circulation in the tumor is restricted and slow. The tumor's vascular

abnormality creates a hypoxic environment, and mild temperatures 39°C to 42°C improve oxygenation and reduce pain-sensing nerve excitability. However, temperatures above 42°C damage tumor vasculature, leading to increased permeability, fluid accumulation, and increased interstitial fluid pressure. This heat process inhibits tumor growth and proliferation by disrupting proteins and cellular structures, and increasing the membrane fluidity, which directly damages the cancer cells movement and intracellular signal transduction, leading to their death and inhibiting metastasis. The reason for raising tumor tissue temperature is due to cell-killing effects and synergistic interactions between heat, radiation, and chemotherapeutic agents (Behrouzkia et al., 2016) (Gao et al., 2016) (Cheng et al., 2019). The combination of hyperthermia with radiation therapy reduces the repair of DNA damage and increase the oxygenation of tumor site making cancer cells more easily and more effectively destroyed by radiation (Jordan et al., 1999)(Brusentsov et al., 2001). Indeed, when the temperature of tumors is raised to a high level, the tumors become much more absorbent to chemotherapeutic agents since increased blood flow due to heat improves the delivery of these drugs. In this configuration, hyperthermia is used as an activator to accelerate the chemical reactions of chemotherapeutics. Hyperthermia may also play an immunological role in cancer therapy, inducing the synthesis of cytokines, chemokines, and heat shock proteins, potentially increasing specific immune responses to cancer cells (Gao et al., 2016).

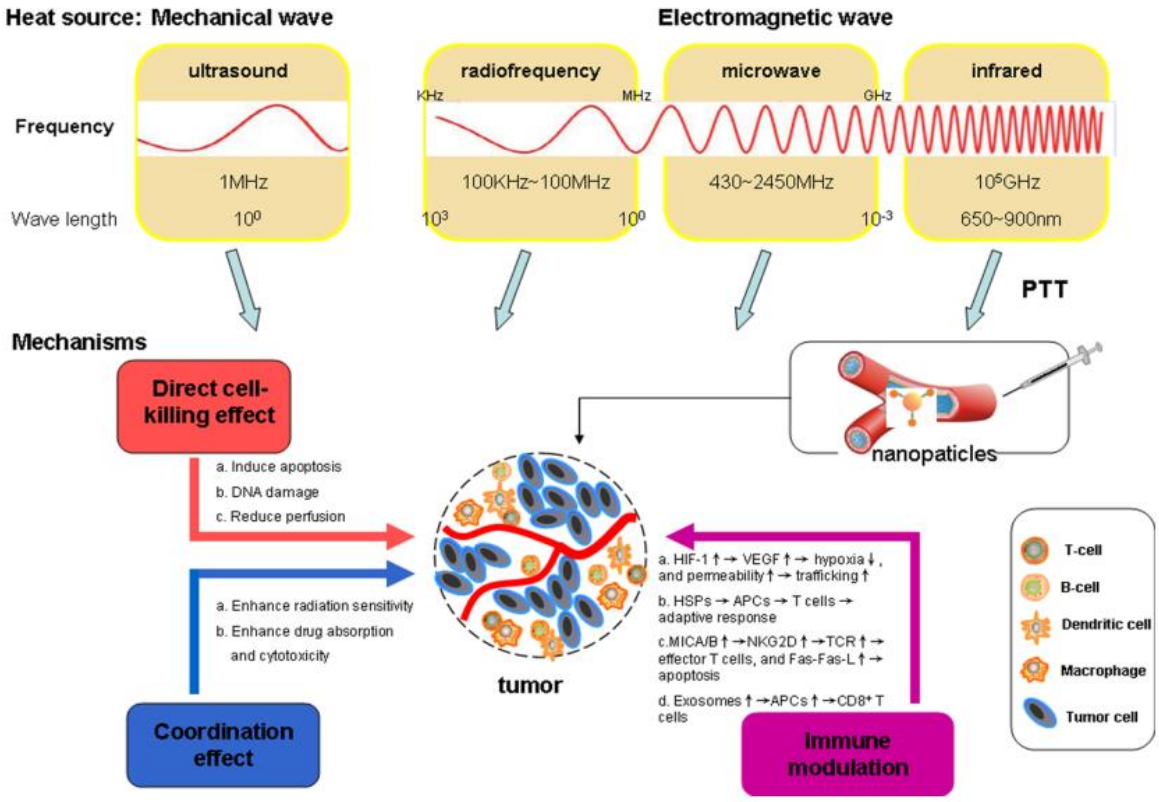

Figure 5: Hyperthermia heat sources and the mechanisms induced (Gao et al., 2016).

1.3. Hyperthermia techniques

Heating methods are of two types: external or internal. External techniques use ultrasonic or electromagnetic waves as their main energy sources like microwave or radiofrequency waves to heat the tumors from the outside. Internal techniques deliver the heat directly to deep-seated tumors through the insertion of probes, needles, or catheters where the device transfers the heat from energy sources like ultrasound, radiofrequency or microwave. Several frequency bands are allocated to the use of electromagnetic waves in clinical settings, ranging from ultrasounds to radio frequencies and microwaves, as shown in Figure 5. The choice of frequency is imposed by the location and extent of the area to be treated and its extent. We can differentiate between local hyperthermia, focused directly on the tumor, regional hyperthermia, around the tumor and whole-body hyperthermia. The choice between these different types of hyperthermia is dictated by the tumor's location and nature (Glazer & Curley, 2011) (Behrouzkia et al., 2016) (Kok et al., 2021)

1.3.1. Whole-body hyperthermia

Generalized hyperthermia follows a different principle from regional or local hyperthermia. Here, the main goal is to heat the tumor tissues and the entire body of the patient. The term Whole Body Hyperthermia or WBH is often used in literature to designate generalized hyperthermia. Generalized hyperthermia is primarily used to treat metastatic cancers (that have spread throughout the body). It can be carried out using hot water blankets, hot wax, inductive coils (like that of electric blankets), thermal chambers (like large brooders: incubators) or infrared rays. Fever-range whole-body hyperthermia (FR-WBH) is an experimental technique used as a supportive oncological therapy in combination with radiotherapy and chemotherapy. Studies have shown beneficial immunological effects, including increased survival in experimental sepsis, induction of immunostimulatory heat shock proteins (HSPs), monocyte stimulation, and improved immunocompetence during radiotherapy/chemotherapySulyok et al., 2012). Generalized hyperthermia allows a rise in temperature throughout the human body and therefore it is the only form of hyperthermia that can treat metastasized tumors. It is also used for tumors that cannot be locally heated, which is the case for lung tumors or stomach tumors. In generalized hyperthermia, infrared systems (Aquatherm) are also used to heat the blood. With this system, blood is withdrawn from the patient, then heated and then reinjected with the aim of producing a rise in temperature throughout the body (Lassche et al., 2019; Zheng et al., 2021).

1.3.2. Regional hyperthermia

Regional hyperthermia (RHT) applies heat to large areas of the body, for treating advanced tumors like sarcoma, melanoma, head and neck tumors, recurrent breast cancer, cervical cancer, and bladder cancer. Its clinical effectiveness has been proven in randomized clinical trials with various advanced tumors. It includes deep tissue techniques, regional perfusion, and continuous hyperthermic peritoneal perfusion. Deep tissue techniques treat cancers like cervical or bladder by placing heat-delivering devices around the affected area. Regional perfusion techniques treat cancers in the arms and legs, such as melanoma, and organs like the liver or lung. Blood is removed, heated, and pumped back into the limb or organ, often with chemotherapy. Continuous hyperthermic peritoneal perfusion treats cancer within the peritoneal cavity during surgery, where heated chemotherapy drugs flow through the area (van der Zee & van Rhoon, 2006)(Chicheł et al., 2007) (Hager, 2008) (Aklan et al., 2019)

1.3.3. Local hyperthermia

For local hyperthermia, heating is devoted to treat small tumors around 3 cm up to 6 cm. Temperatures in the rest of the body remain stable around the physiological temperature (37°C) (Behrouzkia et al., 2016). Local hyperthermia is used for the treatment of superficially located tumors ≤ 3 cm from the surface (superficial local hyperthermia). It is also used for deep tumors, located approximately 10 cm deep (deep local hyperthermia). These two types of hyperthermia require different technological approaches. Clinicians strive to cause the temperature of the cancerous tumor to rise to 40-43°C or higher. The duration of the treatment is approximately one hour, whether using with external or internal applicators (insertion of applicators or probes as in microwave antennas or radiofrequency electrodes). The size of the treatment surface and the depth of penetration depend on the size of the applicator and the technique used. Local hyperthermia is more expensive than generalized hyperthermia and requires quality control (Datta et al., 2015) (Johannes, 2021).

Local hyperthermia can be categorized into external hyperthermia, interstitial hyperthermia, and endocavitary hyperthermia. External methods are used to treat cancers located on or just above the skin. For this form of hyperthermia, doctors allocate heat-generating equipment around or near the treatment area. Interstitial hyperthermia is involved in treating tumors deep within the body, such as those in the brain, where the tumor temperature is raised to higher levels than with external methods. It consists in injecting heat directly into tumor sites using high-frequency needle electrodes, microwave antennas, ultrasound transducers, laser fiber optic conductors, or ferromagnetic seeds. Endocavitary hyperthermia, also known as intraluminal or endocavitary hyperthermia, is a treatment method used to treat tumors within or near body cavities, where probes create heat and are inserted into the tumor to generate heat (Johannes, 2021) (Hager, 2008) (Chicheł et al., 2007). The selection of an appropriate method for heat delivery to the tumor area is a critical and challenging issue in hyperthermia. Different energy sources are highlighted and are currently under use to locally heat the tumor, which include microwave, radiofrequency, laser and ultrasound sources. The use of electromagnetic fields in hyperthermia consists of two techniques. If we want to directly heat the tumor, electric fields are used, where the interaction of the electric field and the tissues is at the origin of an increase in temperature at the level of the tissues struck by the wave. On the other hand, with the use of magnetic fields, it is not the tissues which are heated but a metal material that absorbs the magnetic energy and converts it into heat within the tumor (Chicheł et al., 2007) (Hergt et al., 1998).

2. Magnetic hyperthermia

2.1. History

The history of Magnetic hyperthermia (MHT) can be traced back to the 1950s with initial studies conducted on small particles exposed to AC magnetic fields. In 1957, Gilchrist et al. proposed for the first time the concept of MHT after demonstrating that small magnetic particles (20 nm to 100 nm) could be selectively delivered to the tumor affected-region and activated under an AMF to induce heat in the lymph nodes of dogs (Gilchrist et al., 1957). This approach gained renewed attention with the discovery of the high specific absorption rate of superparamagnetic iron oxide nanoparticles (SPIONs) (Jordan et al., 1999).

In 2005-2006, the Charité Hospital in Berlin carried out a phase 1 trial on 14 patients with glioblastoma multiforme (GBM), demonstrating the feasibility and tolerance of hyperthermia mediated MNPs (Maier-Hauff et al., 2006). Clinical investigations have shown improved survival rates for patients with glioblastoma recurrence and prostate cancer (Maier-Hauff et al., 2006). (Johannsen et al., 2005) (Johannsen et al., 2006). Since then, significant progress has been made in the field, including the development of new perspectives and advances in the preparation of MNPs, physical modeling of magnetic heating, and the influence of biological matrices on heating efficiency(Périgo et al., 2015).

Currently, the ferrofluid NanoTherm® is the only commercially available SPION clinically authorized for magnetic hyperthermia in Europe. MagForce (MagForce® Nanotechnologies AG, Berlin) manufactures this ferrofluid, which contains NPs with an average size of 15 nm dispersed in water-based solution.

2.2. Definition

MHT technique has attracted considerable attention in the past two decades as a potential alternative or adjuvant therapy for cancer. It is one of the current modalities of hyperthermia and has excellent potential among thermal therapies. This hyperthermic oncological treatment consists of internal heating of tumors via the insertion of nano-heat mediators (MNPs). Unlike other inserted heating sources, e.g. radiofrequency and microwave antennas, MNPs convert electromagnetic energy into heat when exposed to an external AMF. The AMF induces movement of the magnetic moment of MNPs inside the tumor. As the MNPs magnetic moment moves they produce heat as a result of different processes including hysteresis, Neel and

Brownian relaxation The development of MHT as a therapeutic modality is an exciting advancement in the field of hyperthermia and holds great promise for improving cancer treatment outcomes. Overall, the history of hyperthermia spans thousands of years and has evolved from ancient practices to modern medical applications (Suto et al., 2009) (Obaidat et al., 2019) (Peiravi et al., 2022). MHT offers several advantages, such as being noninvasive and not damaging to healthy tissues, since the applied AC magnetic fields pass harmlessly across tissues. This technique takes also advantage of the unique features of nanoparticles, which are small enough to cross the blood brain barriers and to locally raise temperature level within tumoral tissues and destroy them while preserving the healthy surrounding tissues. Another advantage that makes MHT a suitable technique for tumor treatment is the surface modification of MNPs, which can be coated using different molecules to optimize the binding with cancer cells leading to a selective and local heat dissipation (Kumar & Mohammad, 2011). Despite a research lapse, the scientific community has made substantial efforts to advance MHT, with a focus on nanoparticle synthesis, bio-compatibilization, and in vivo testing(Rubia-Rodríguez et al., 2021). These advancements in MHT can revolutionize cancer treatment and provide a less invasive alternative to surgical procedures, since the use of MNPs allows for controlled drug delivery and the potential for inducing antitumoral immunity (Tang et al., 2021). Combinations of MHT with chemotherapy and radiation therapy have shown promising results in preclinical studies. These synergistic approaches can improve the overall therapeutic outcome by targeting different aspects of tumor biology and overcoming treatment resistance (Shirvalilou et al., 2021).

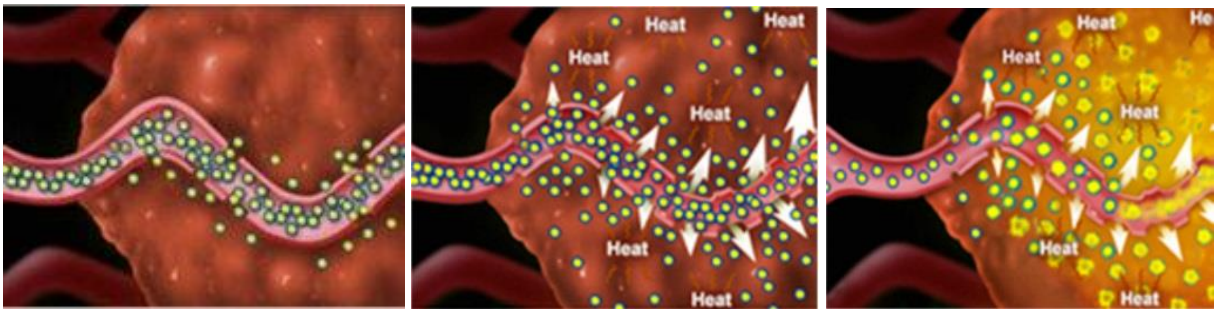

Figure 6: Illustration of hyperthermia mediated-magnetic nanoparticles treatment approach, from the injection of MNPs into the tumor to heat generation under external AMF irradiation (Langlands, 1990).

3. Nanomaterials

Nanomaterials have gained considerable attention in biomedical engineering and are distinguished by their nanoscale size less than 100 nm and possess unique physical and chemical properties. Many different forms of nanomaterials have already been characterized, and many studies are published in a variety of fields, including medicine, cancer therapy and diagnostics, biosensing, and material research because of their biocompatibility, chemical stability, high saturation magnetization, large surface area, and ease of functionalization (Chaturvedi et al., 2018; Tekade et al., 2017; Villanueva et al., 2009). Different nanomaterials are used in medicine for cancer treatment and/or diagnosis, such as MNPs and gold NPs for thermal therapies (Sharma et al., 2019), MNPs for magneto-mechanical destruction of cancer cells. Liposomes, micelles and polymeric NPs are employed for targeted drug delivery, moreover, quantum dots are used to improve biosensor for selective diagnostics and to enhance the imaging techniques such as computed tomography (CT) and magnetic resonance imaging (MRI). These multifunctional NPs can be engineered to carry imaging agents, allowing for simultaneous monitoring of the treatment progress and accurate targeting of tumor cells, which holds great promise for personalized cancer treatment (Farzin et al., 2020) (Rashidi et al., 2024). Nanomaterials used for hyperthermia-based therapy are the ones interested in this case, since the objectives of this study are based on MHT for cancer treatment. Figure 7 shows a general classification of the nanomaterials employed for hyperthermia.

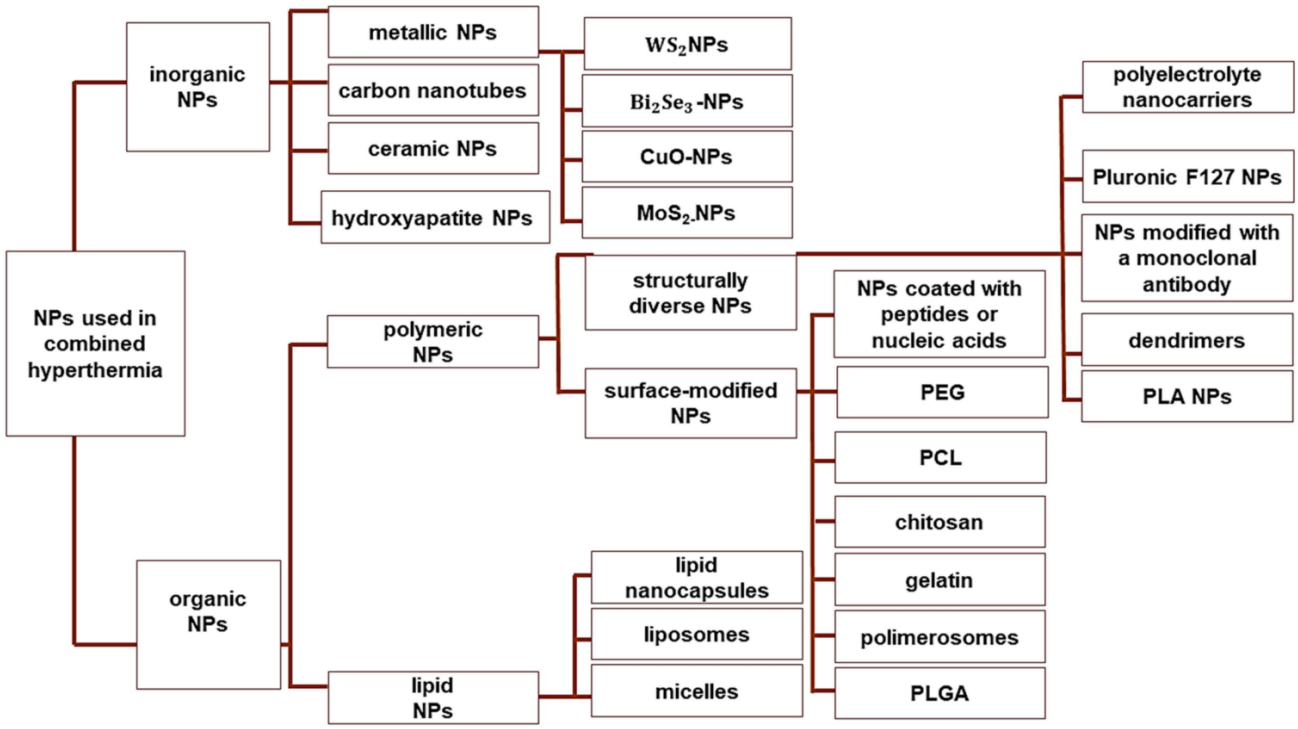

Figure 7: Classification of different nanomaterials used for hyperthermia. Abbreviations: tungsten disulfide quantum dots (WS2NPs), bismuth selenide nanoparticles (Bi2Se3-NPs), cupric oxide nanoparticles (CuO-NPs), molybdenum disulfide nanoparticles (MoS2-NPs), polyethylene glycol (PEG), poly (caprolactone) (PCL), poly (lactic-co-glycolic acid) (PLGA), Poly (D, L-lactic acid) (PLA) (Szwed & Marczak, 2024).

3.1. Magnetic nanoparticles

MNPs consist of magnetic elements such as iron (Fe), cobalt (Co), nickel (Ni) and their alloys, and therefore, are ferromagnetic and superparamagnetic. Among the different types of magnetic nanomaterials, IONPs mainly magnetite (Fe_3O_4) and maghemite (γ-Fe_2O_3), are the most widely used for decades in biomedical applications due to their high surface-to-volume ratio, high magnetic saturation, and high stability for the fact that iron oxide is less sensitive to oxidation than pure metals (Manh et al., 2014) (Martins et al., 2021). A variety of methods are employed for the synthesis of MNPs including co-precipitation, thermal decomposition hydrothermal, hydrothermal, polyol, sol-gel and micro-emulsion methods which are considered as safe, effective and economical synthesis techniques, with an easy control of size, shape, composition and surface properties (Peiravi et al., 2022) (Alrushaid et al., 2023).

3.1.1. Magnetic properties

From the magnetic behavior point of view, magnetic materials are classified into diamagnetic, paramagnetic, antiferromagnetic, ferrimagnetic or ferromagnetic, and superparamagnetic, this classification is made by investigating the response of the material to an external magnetic field. The magnetic behavior of a material exposed to a magnetic field (H) is the net response of the magnetic moment of the atoms that compose it. The overall magnetic response (magnetization behavior) is described in terms of the magnetization vector (M) in function of H and can be calculated using the equation (1) where χ is the susceptibility, which gives rise to the sigmoidal shape of the M-H curve (different between materials and depends on material composition, physical and geometrical properties).

$$M = \chi H \quad (1)$$

Diamagnetism concern materials containing atoms without a net magnetic dipole moment because all their electrons are paired, hence the magnetic susceptibility χ is below zero (negative). Once a magnetic field H is applied, these materials induce a magnetic field opposite to this field, thus they are repelled. Most diamagnetic materials consist of organic substances (e.g. biological tissues), graphite, bismuth).When materials present unpaired orbital electrons, thus the atoms composing the material have a magnetic dipole moment this is paramagnetism and materials are paramagnetic. The absence of magnetic interactions prevents the occurrence of a net magnetization, in the absence of a magnetic field. When applied to a magnetic field the microscopic magnetic moment aligns in the field direction giving rise to a net macroscopic magnetization and a positive magnetic susceptibility. Antiferromagnetic materials have atoms where magnetic moments aligned in an antiparallel manner canceling the overall magnetization “antiferromagnetism”. Ferromagnetic materials display parallel alignments of magnetic and the magnetic interactions are very strong larger than the Earth’s magnetic field, thus large magnetization even in the absence of an external magnetic field. Similar to ferromagnetic materials, ferrimagnetic materials have large magnetic susceptibility and the atoms have antiparallel magnetic moments not cancelling each other. This type of material includes ions like Fe^{+2} and Fe^{3+}, thus magnetite exhibits ferrimagnetic behavior. As the size of the particles decreases below a certain value known as "Ds," domains begin to behave like superparamagnetic (SPM) characterized by a single domain magnetic moment that can be aligned with the applied magnetic field, and do not exhibit coercivity in the M(H) loops. Figure

8 represents the M-H curve of the corresponding magnetic behavior for ferromagnetic and superparamagnetic. Ferromagnetism and superparamagnetic are the two main types of magnetic behavior exhibited by MNPs and are mainly governed by the size. Small MNPs (10-20 nm) exhibit superparamagnetic behavior which is of interest in biomedical applications as it prevents remanent magnetization when the applied magnetic field is turned off, ensuring colloidal stability and avoiding undesired clustering. Particles smaller than 100 nm are assumed to be single domain, while particles between 100 nm to few microns are multi-domain. Ferromagnetic are permanent magnets that show high remanent magnetization and coercivity after the withdrawal of the external magnetic field. When large multidomain MNPs are reduced in size further (single domain), their coercivity increases and achieves a maximum, then falls sharply to zero. At this level, material becomes a temporary magnet, and the magnetic behavior is superparamagnetic, where the magnetic moments revert to *the non-aligned* state once the external magnetic field is turned off, therefore, have negligible remanent magnetization and coercivity (Slimani et al., 2019) (Ribeiro et al., 2022)(Kritika & Roy, 2022).

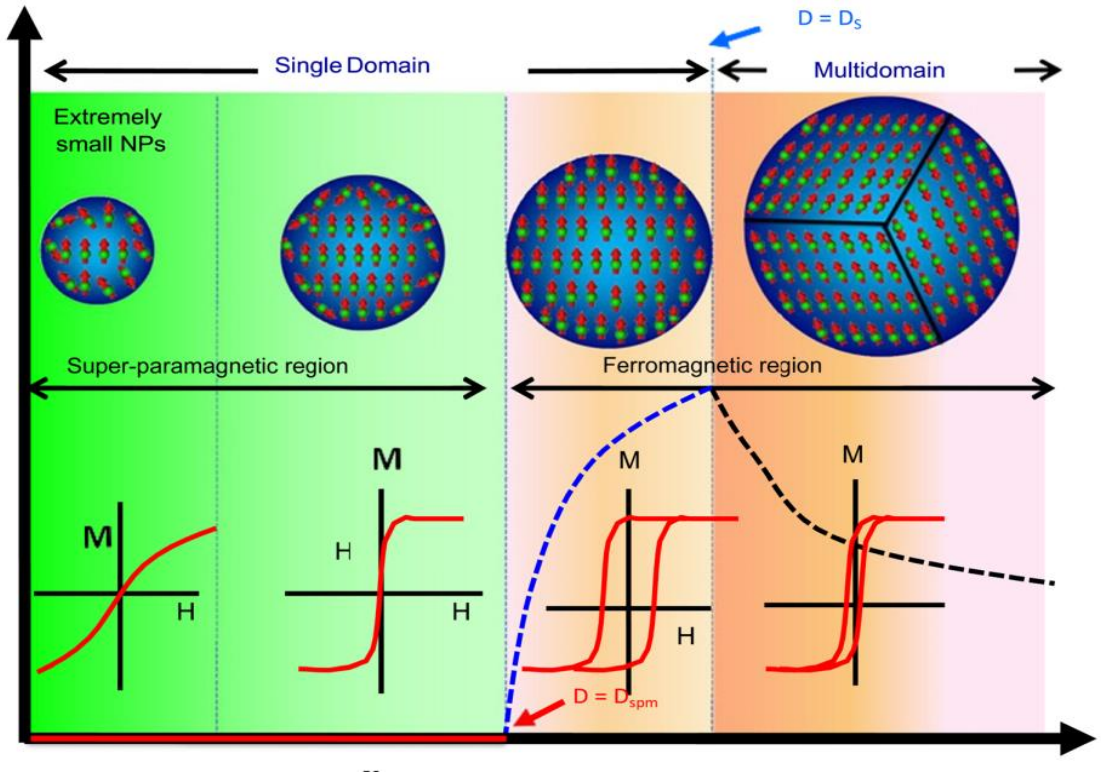

Figure 8: Size-dependent magnetic behavior and M-H curves in MNPs (Kritika & Roy, 2022).

3.1.2. Curie Temperature

The Curie temperature (T_n) is the temperature at which a magnetic material changes from ferromagnetic to paramagnetic, losing its permanent magnetism. The Curie temperature in magnetic nanoparticles is affected by particle size and shape. According to studies, as the size of nanoparticles decreases, the Curie temperature might rise or fall, depending on the material and its surface features. This size-dependent behavior is critical in applications such as magnetic hyperthermia for cancer treatment, which employs nanoparticles with specified Curie temperatures to assure precise heating. Materials with Curie temperatures ranging from 41 to 46°C, are desired to prevent normal cells from overheating, as they lose magnetic above this temperature, restricting further heating. Magnetic materials produce higher heating in the ferromagnetic state (below Curie temperature) and lower heating in the paramagnetic state (above TC). Hence, curie temperature works as a temperature control switch, maintaining a consistent target temperature in the tumor zone. (Penny et al., 2019).

3.2. Magnetic heating mechanisms

The main objective of our study is to kill cancer cells using the heat delivered by MNPs. MNPs can be remotely activated by an AMF due to their intrinsic ability to convert magnetic energy into heat. The heating efficiency of nanoparticles to generate heat due to AMF is quantified in terms of the specific absorption rate (SAR) or specific loss power (SLP). Various mechanisms define the MNPs' heating behavior: hysteresis, Néel relaxation, Brownian relaxation and eddy current. The hysteresis loss corresponds to the energy dissipated in the form of heat. The dissipated energy is proportional to the surface area of the hysteresis loop (Kumar & Mohammad, 2011).

3.2.1. Hysteresis losses

Hysteresis loss is related to the phenomenon of hysteresis, and it concerns ferromagnetic materials that possess hysteretic properties under a time varying magnetic field. As was mentioned previously, ferromagnetic substances are characterized by the presence of domains thus two processes lead to hysteresis losses in heat form, the displacement of domain walls or the rotation of magnetic moments inside domains. The amount of heat dissipated P by ferromagnetic nanoparticles exposed to an AMF of frequency f and amplitude H during one

cycle of magnetic field equals to the area of hysteresis loop A multiplied by frequency f (expressed by W/m^3), given by:

$$P = \mu_0 \int H\, dM \times f \rightarrow P = \mathrm{A} \times f \tag{2}$$

μ_0 is the magnetic permeability in free space.

$\int HdM$ is the hysteresis loop area (A)

The heating potential of MNPs is measured by SLP that relies on the power given by nanoparticles per unit mass of magnetic material. It is calculated by dividing Equation (2) by the density of magnetic nanoparticles (ρ_{MNPs}), expressed by W/g:

$$SLP = \frac{\mu_0}{\rho_{MNPs}} \int H\, dM \times f \tag{3}$$

In the illustration of Figure 9, the ferromagnetic material is exposed to an external magnetic field, that will gradually orient the magnetic moments of the material in its direction. This corresponds to the magnetization curve (red arrow). When all the magnetic domains are orientated in the direction of the external magnetic field, it becomes magnetically saturated and achieves its maximum magnetization value (Ms), known as saturation magnetization.

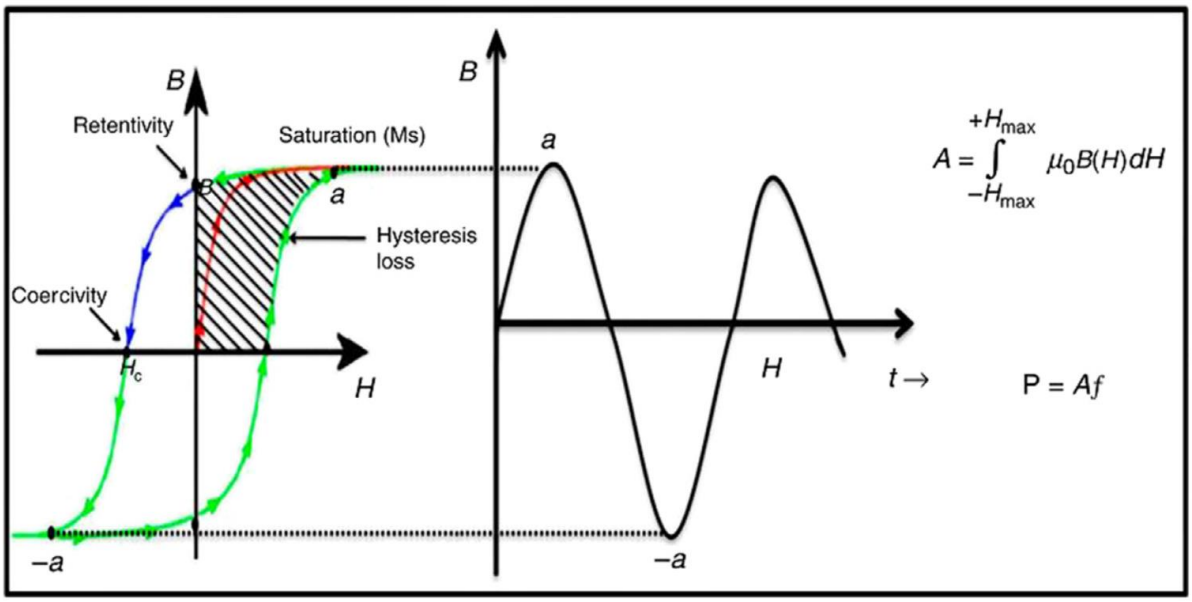

Figure 9: Hysteresis loss process during magnetic hyperthermia (B is the induction field) (S. Ahmed et al., 2020).

The saturation magnetic field (Hs) is the value of the magnetic field that allows saturation magnetization to occur. When reducing H, the M value does not return to zero value, the ferromagnetic material retains its non-zero magnetization in the direction of the previously applied magnetic field. And is identified as remanent magnetization (Mr) or retentivity. To restore this magnetization to zero, a magnetic field of sufficient amplitude (-Hc) and opposite direction to the remanent magnetization, known as the coercive field (blue arrow), must be applied. If the opposing magnetic field grows, the Weiss domains will orient themselves in its sense and direction until saturation at -Hs (S. Ahmed et al., 2020).

Due to the unique properties of superparamagnetic iron oxide nanoparticles (SPIONs), they exhibit minimal hysteresis loss when subjected to an external magnetic field. Once the magnetic field is removed, these particles lose their magnetization because their magnetic moments immediately realign to the initial state. As a result, SPIONs lose small amounts of energy as heat due to hysteresis (which is characteristic of larger magnetic particles). However, under some conditions, tiny hysteresis loss can still occur due to dipolar interactions between particles (Gudoshnikov et al., 2012).

3.2.2. Relaxation losses

Heat is produced through a delay in the relaxation mechanisms in the form of Neel and Brownian processes. Magnetic materials exhibit anisotropy due to electron's spin-orbital interactions. Magnetic anisotropy is the reason for maintaining magnetic moments oriented in a specific direction. Atomic orbitals tend to align in a given crystallographic direction known as the easy direction (easy axis). In magnetic materials with high magnetic anisotropy, the atomic spin and orbital angular moments are strongly connected, allowing the magnetization to align in the easy direction.

Anisotropy energy is required to rotate the magnetization away from the easy direction and is given (per particle) by:

$$E = K V \sin^2\theta \tag{4}$$

For uniaxial system, where:

E: Anisotropy energy

K: Anisotropy constant (J/m^3)

V: Volume of the magnetic particle

θ: Angle between the magnetization and the easy axis of the material

Equation (4) shows that the anisotropy energy is directly related to particle size (V) and the anisotropy constant (K). When the anisotropy is given at a fixed value, hence the anisotropy energy (E) decreases with the particle size reduction. When the size becomes smaller and possesses a single magnetic domain, E may become smaller than the thermal energy $E_{th} = k_B T$, where k_B is the Boltzmann constant. The particle magnetic moment flips randomly in all directions, resulting in zero net magnetization (at H = 0).

Once a magnetic field is applied, the energy is transferred to the particles, causing their magnetic moments to align along the field direction away from the easy axis. When the field is turned off, the magnetic moments relax and align along the easy axis. As a result, the energy absorbed from the applied magnetic field will be dissipated as heat. In the case of an AMF, this alignment and relaxing of moments processes will continue, generating heat as long as the AMF is applied (Laurent et al., 2011) (Obaidat et al., 2019).

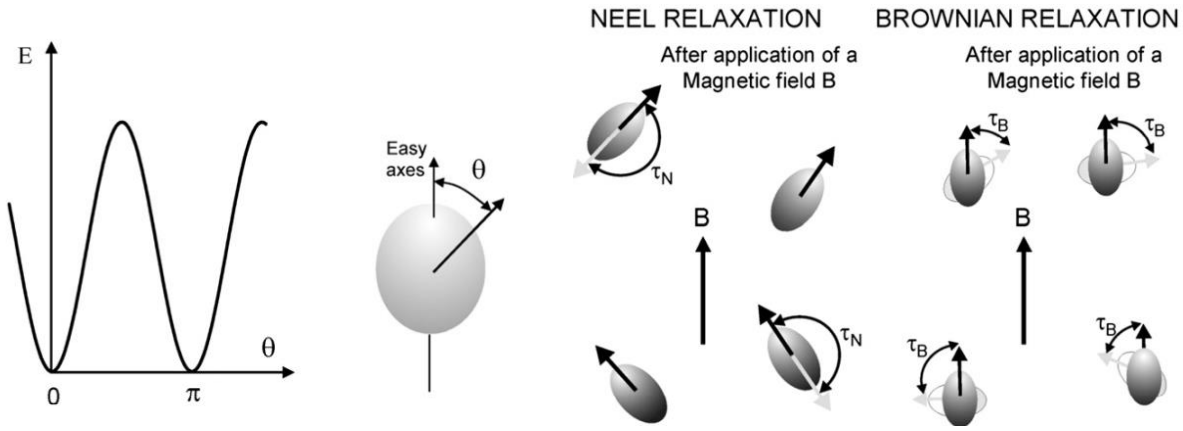

Figure 10: Schematic illustration representing relaxation losses mechanisms of a magnetic fluid under a magnetic field (Laurent et al., 2011).

3.2.2.1. Neel relaxation

For single domain MNPs, the magnetic moments orient in the direction of the applied AMF without a physical rotation (internal dynamics) then returns to the equilibrium orientation, this is called Néel relaxation, and the relaxation time of the particle moment is called Néel relaxation time τ_N expressed as:

$$\tau_N = \tau_0 \, e^{\left(\frac{K V}{k_B T}\right)} \quad (5)$$

τ_0: the attempt time and equal to 10^{-9}.
During experiments for magnetization measurement of MNP, if $\tau_m < \tau_N$ (τ_m refer to the measuring time in a magnetic measurement) the MNP's magnetic moment will randomly change direction multiple times, resulting in zero average magnetization which is the superparamagnetic state in this case. If Néel relaxation time becomes longer than the experimental time $\tau_m > \tau_N$, the MNP's magnetic moment will be blocked at the initial non-zero value at the start of the measurement because it won't have sufficient time to change direction during the measurement which is referred to the blocked state. A change from the superparamagnetic state to the blocked state takes place when $\tau_m = \tau_N$. In this situation, the temperature at which this transition occurs is known as the blocking temperature T_b and is dependent on particle size, magnetic anisotropy and particle to particle interaction (Sharma et al., 2019)(Obaidat et al., 2019)

3.2.2.2. Brownian relaxation

Brownian relaxation refers to a physical motion of particles (external dynamics) under an applied magnetic field. The particles magnetic moments will align along with the magnetic field direction causing them to physically rotate in the medium (thus influenced by the viscosity), this leads to collisions between particles and the medium generating thermal losses in the surrounding medium. In the absence of the field, particles will reorient their again and the magnetic moments relax, the time of relaxation is noted as τ_B at temperature (T):

$$\tau_B = \frac{3\, V_H\, \eta}{k_B\, T} \tag{6}$$

where η is the viscosity of the medium and V_H is the hydrodynamic which is calculated using the magnetic volume V_M ($4\pi R^3/3$) plus the coating layer thickness δ.

$$V_H = \left(1+\frac{\delta}{R}\right)^3 V_M \tag{7}$$

From equation (6), Brownian relaxation is size and viscosity dependent, the more the size increases the more the Brownian relaxation time increases proportionally.

Depending on whether $\tau_N > \tau_B$ or $\tau_N < \tau_B$ the dominant relaxation process is determined by the shorter relaxation time. For small particles and viscous medium, Néel relaxation is faster hence the dominant process which makes it the preferred mechanism for vivo MHT application for the fact the in vivo viscosity is significant. Brown relaxation takes place at larger size particles and in a low viscous medium thus it is canceled for in vivo studies. When $\tau_N = \tau_B$, both mechanisms are involved (Rosensweig, 2002) (Etemadi & Plieger, 2020). Therefore, new parameter called the effective magnetic relaxation time τ is defined when both mechanisms are produced:

$$\frac{1}{\tau} = \frac{1}{\tau_B} + \frac{1}{\tau_N} \tag{8}$$

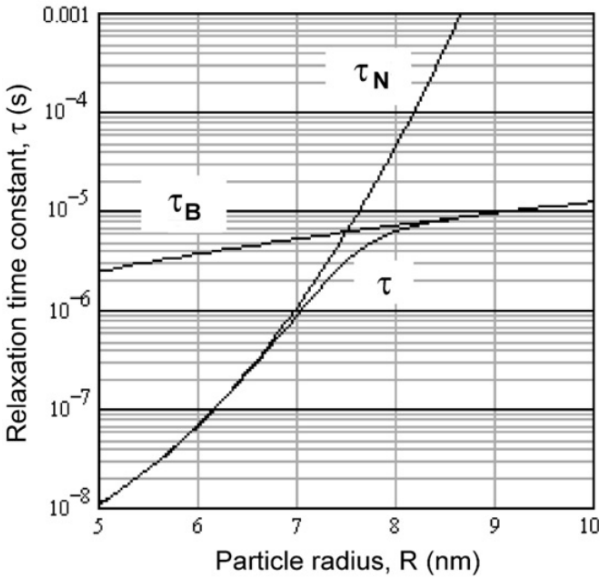

Figure 11: Relaxation time constants in function of the size of MNPs of a fluid (Rosensweig, 2002).

Linear response theory (LRT) is a model that describes the heating activated process considering both independent relaxation processes of Néel and Brownian that take place simultaneously to generate heat in the fluid containing superparamagnetic NPs. The LRT theory assumes that magnetization M has linear response to the magnetic field H (equation (1) given by M= χH), thus χ is constant:

$$\chi = \chi' + i\chi'' \tag{8}$$

Where χ' is the real part and χ"is the imaginary part of the magnetic susceptibility χ of the MNPs studied expressed as:

$$\chi' = \frac{\chi_0}{1+(\omega\,\tau)^2} \tag{9}$$

And:

$$\chi'' = \frac{\chi_0\,\omega\,\tau}{1+(\omega\,\tau)^2} \tag{10}$$

Regarding the LRT model, loss power density P released by superparamagnetic NPs (not applicable for ferromagnetic regime) subjected to an AMF with magnetic intensity H and frequency f ($\omega = 2\pi f$) has been proposed to rely on magnetic moment relaxations and is given by:

$$P\,(f.H) = \mu_0 \pi\, \chi'' H^2 f \tag{11}$$

A demonstration of power loss density of equations (11) is given by (Rosensweig, 2002) as follows:

In accordance with the first law of thermodynamics also known as law of energy conservation, mathematically expressed by:

$$dU = \delta Q + \delta W \tag{12}$$

Giving:

U is the internal energy of the system

Q is the heat added

W is the magnetic work done by the system.

For an adiabatic process (isolated system) $\delta Q=0$, the magnetic work generated by the system given by $\delta W = H.dB$, hence the result is:

$$dU = H.dB \tag{13}$$

The collinearity of the fields allows for the relation to be expressed in magnitude terms as $dU = H.dB$ with $B=\mu_0 (H+M)$, $\mu_0 = 4\pi\times10^{-7}$ is the permeability of free space.

The substitution followed by integration in equation (12) as:

$$\int dU = \int H.d[\mu_0 (H+M)] \tag{14}$$

$$\int dU = H.\ \mu_0 (H+M) - \int \mu_0 (H+M).dH \tag{15}$$

Give a final result of:

$$\Delta U = -\ \mu_0 \oint M\ dH \tag{16}$$

As was previously mentioned in equation (1) the magnetization M of the magnetic fluid is expressed in terms of susceptibility and the susceptibility is expressed by a real and imaginary parts equation (8), then with an applied magnetic field of:

$$H(t) = H_0 \cos \omega t = Re[H_0 e^{i\omega t}] \tag{17}$$

The end result magnetization is:

$$M(t) = Re[\chi H_0 e^{i\omega t}] = H_0 (\chi' \cos \omega t + \chi'' \sin \omega t) \tag{18}$$

The replacement of H(t) and M(t) from equations (17) and (18) in equation (16) leads to the following equation:

$$\Delta U = 2\ \mu_0\ H_0^2\ \chi''\ \int_0^{2\pi/\omega} \sin^2 \omega t\ dt \tag{19}$$

χ'' is the remaining magnetic susceptibility part and called the loss component, it is related to the ferrofluid material parameters. Multiplying the equation (19) by the frequency f = ω/2π we acquire the volumetric power dissipation of MNPs:

$$P = \Delta U f = \mu_0 \pi\ \chi'' H^2 f \tag{20}$$

Replacing χ'' from equation (10) in equation (20), the heat dissipation for a monodispersion is given by:

$$P = \pi \mu_0 \chi_0 H_0^2 f \frac{2\pi f\tau}{1+(2\pi f\tau)^2} \quad (21)$$

With χ_0: $$\chi_0 = \chi_i \frac{3}{\xi}(coth\ \xi - \frac{1}{\xi}) \quad (22)$$

The heating efficiency or SAR is measured in watts per gram as:

$$SAR\ (f,H) = \frac{P}{\rho_{MNPs}} = \frac{\mu_0 \pi\ \chi"H2f}{\rho_{MNPs}} \quad (23)$$

Experimentally, the determination of SAR of a mass of MNPs can be carried out by measuring temperature increase ΔT in time of the ferrofluid heated up when an AMF is applied, given by:

$$\text{SAR} = \frac{\Delta T\ C}{\Delta t\ m_{Fe}} \quad (24)$$

C is the volumetric specific heat capacity of ferrofluid, m_{Fe} is the mass concentration of MNPs (X. Liu et al., 2020).

3.2.3. Eddy current losses

Eddy current losses refer to undesired heat generated inside materials or tissues when exposed to AMFs due to the generation of electrical current loops known as eddy currents as a result of induced voltage. These currents lose magnetic energy in the form of heat. The electrical conductivity in nanomaterials is very weak for producing significant induction heating and nanomaterials are unable to produce considerable electrical voltage. The intensity of eddy currents depends on the frequency and amplitude of the magnetic field and the electrical conductivity of the surrounding medium. Eddy currents might produce a non-specific and undesirable temperature rise in normal tissues, limiting treatment effectiveness (Salmanian et al., 2021). Therefore, to prevent potential difficulties caused by induced eddy currents for patients after injection of a ferrofluid and exposure to an AMF, a biophysical constraint of the effects of AC magnetic field parameters was proposed in 1984, as the Atkinson-Brezovitch safety limit $H.f < 4.85\times10^8$ A(m/S) (Atkinson et al., 1984), and of $H.f < 5\times10^9$ A(m/S) by Hergt

and Dutz (Hergt & Dutz, 2007). Measures exceeding this limit are not suitable for clinical trials. This guideline aims to balance therapeutic efficacy and patient safety in therapies. According to Faraday's Law the eddy current power loss in the case of nanoparticles is expressed as:

$$P_{eddy} = \frac{H_0^2 f^2 \pi^2 d^2}{6c\rho D} \quad (25)$$

Where d is the diameter of NP, c is constant, ρ is the resistivity of NP and D is the density of NP.
In the case of a tissue, it is expressed as:

$$P_{eddy} = \sigma\,(\pi\mu_0)^2 H_0^2\, f^2 r^2 \quad (26)$$

corresponds to the conductivity of tissue or cell, and r is the tissue radius under AMF (Hossain & Hossain, 2022).

4. Magnetic hyperthermia: in vitro and in vivo aspects

Clinical applications require first the optimization of MHT components (MNPs and AMFs parameters) via in vitro and in vivo tests to have an initial understanding of their antitumoral potential, the toxicity, efficacy and tolerability. A variety of reports has described the important effects of MHT on cells, both in vitro and in vivo. Hyperthermia has a number of consequences at both cellular and molecular level, which can limit cancer cell growth, division, function, and viability by promoting apoptosis and/or necrosis. Most preclinical assays are carried out on rodents, in particular mice and rats (Brusentsov et al., 2001),although larger animals, such as dogs (GILCHRIST et al., 1957), and rabbits (J. Liu et al., 2013), have also been used.

In vitro tests are based on the use of representative cancer cells from humans or animals. Human cells need to be tumorigenic to produce a tumor inside animal body (in vivo tests). It is important to take into consideration that the sensitivity to heat may differ between cancer cell lines which lead to different treatment outcomes for similar therapeutic temperature profile for the fact that heat shock proteins (HSP) are considered to be a significant factor responsible for this divergence of susceptibility to heat between cancer cell lines due to an altered expression of HSP between them. Moreover, in vitro and in vivo systems differ significantly in complexity

and composition, leading to variations in viscosity, which is an important factor to take into consideration during MHT treatment. In MHT, and in contrast to the Néel heating mechanism, the Brownian mechanism is assumed to be dominant for less viscous fluids and bigger particle sizes. As a consequence, the heat dissipation by Brownian relaxation is insignificant in vivo due to the high viscosity of the extracellular matrix and since the best MNPs for preclinical application are the ones with small size for an effective intracellular uptake and accumulation in tumors, thus the Néel relaxation is the main mechanism for heat dissipation inside tumoral tissue during MHT treatment (X. Liu et al., 2021) (Somu et al., 2024).

MNPs injected into live animals have to traverse multiple biological milieus, including those at the injection site (e.g. gastrointestinal transit for oral delivery). After they pass the first local barrier and reach the bloodstream, complicated interactions will take place between nanoparticles and biological fluids, as they comprise various circulating cells and biomolecules. Once in disease tissues nanoparticles will face the extracellular proteins, supportive cells, cell membranes, and finally reach the cells in order to exert the therapeutic effects. The control of nanoparticle transport from the injection site to the site of action is a difficult task. It is challenging to ensure a homogeneous distribution of MNPs within the tumor at a concentration adequate for maximal thermal response. The distribution of MNPs within the tumor influences the efficacy of MHT treatments therefore MNPs are typically injected directly intratumorally to ensure a higher concentration in the region that is affected. In contrast, intravenous administration is used primarily to reach areas that are inaccessible with local administration. It must be highlighted that static in vitro cell culture conditions are not mimicking ideally the real MNPs-cellular interactions and the full complexity of the extracellular matrix as in vivo conditions (Cai et al., 2017). Anyway, MNPs are internalized by cells via different endocytosis mechanisms (Figure 12) consisting of:

- Phagocytosis: a cellular process that concerns phagocytic cells of neutrophils, monocytes and macrophage. This process is mainly responsible for nanoparticles phagocytosis in vivo and their clearance.
- Pinocytosis: is a size-dependent pathway for non-specific uptake of nanoparticles. It includes macropinocytosis where nanoparticles are internalized in endosomes avoiding fusion with lysosomes where they can escape to reside in the cytoplasm and reach the DNA, clathrin/caveolae-independent endocytosis (receptor independent

pathways) and clathrin/caveolae-dependent endocytosis which are receptor-dependent pathways and nanoparticles contained in endosomes fuse with lysosomes.

The coating of MNPs is a major contributor for their stability protecting them from oxidation, humidity or acidity, as well as preventing their agglomeration by creating a hydrophilic environment. The coating drives their intracellular trafficking depending on the type of cell to be used and its affects also the protein corona (PC) formation on the MNPs of different size and composition when they interact with biological medium prior to their internalization thus influencing the endocytosis pathways. (Cai et al., 2017) (Osaci & Cacciola, 2020) (Portilla, Mulens-Arias, et al., 2022).

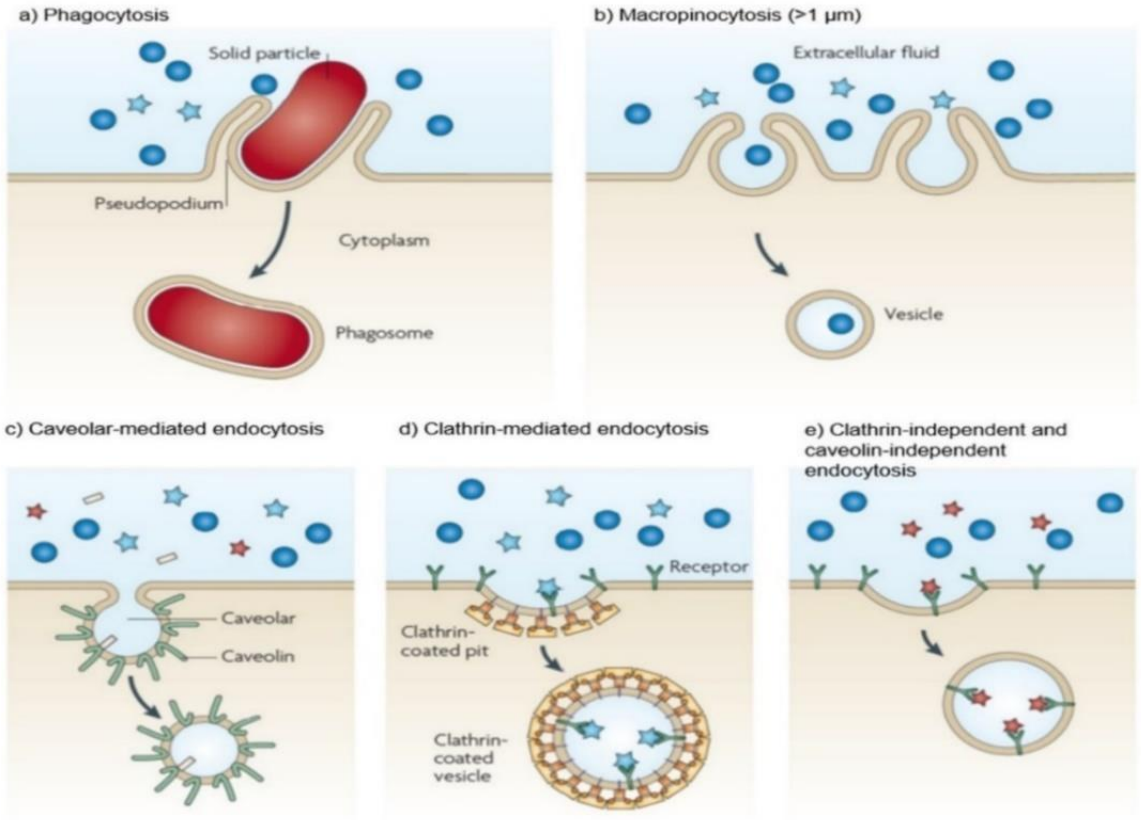

Figure 12: Illustration of the different mechanisms for nanomaterials internalization by cells (Cai et al., 2017).

The size and the coating of NPs are two important properties that strongly affect their performance and heat generation. SAR typically increases with particle size up to a threshold, after which it may drop or plateau. This behaviour is related to the transition from superparamagnetic to ferromagnetic regimes as particle size increases. For example, a study on

MNPs found that SAR values for particles larger than 10.2 nm were greater across a wide range of field amplitudes and frequencies (Narayanaswamy et al., 2021b). This indicates that increasing particle size within a certain range can improve SAR, while increasing the concentration may decrease the SAR values. The interaction of nanomaterials in biological fluids lead to their aggregation which directly impacts the SAR (as measure of heating efficiency) and induce a reduction of 50% in heating (Etheridge et al., 2014). A study by(Sanz et al., 2016), has demonstrated the specific power absorption SPA (W/g Fe_3O_4) by MNPs dependence on magnetic fields in three different colloids, water, cell culture medium (DMEM) and inside cells. Where the SPA data demonstrated a slight decrease in DMEM and compared to the water since they have quite similar viscosity (η_{DMEM}=0.98 mPa.s and η_{water}=1.00 mPa). Inside the cells the SPA decreases more due to higher viscosity.

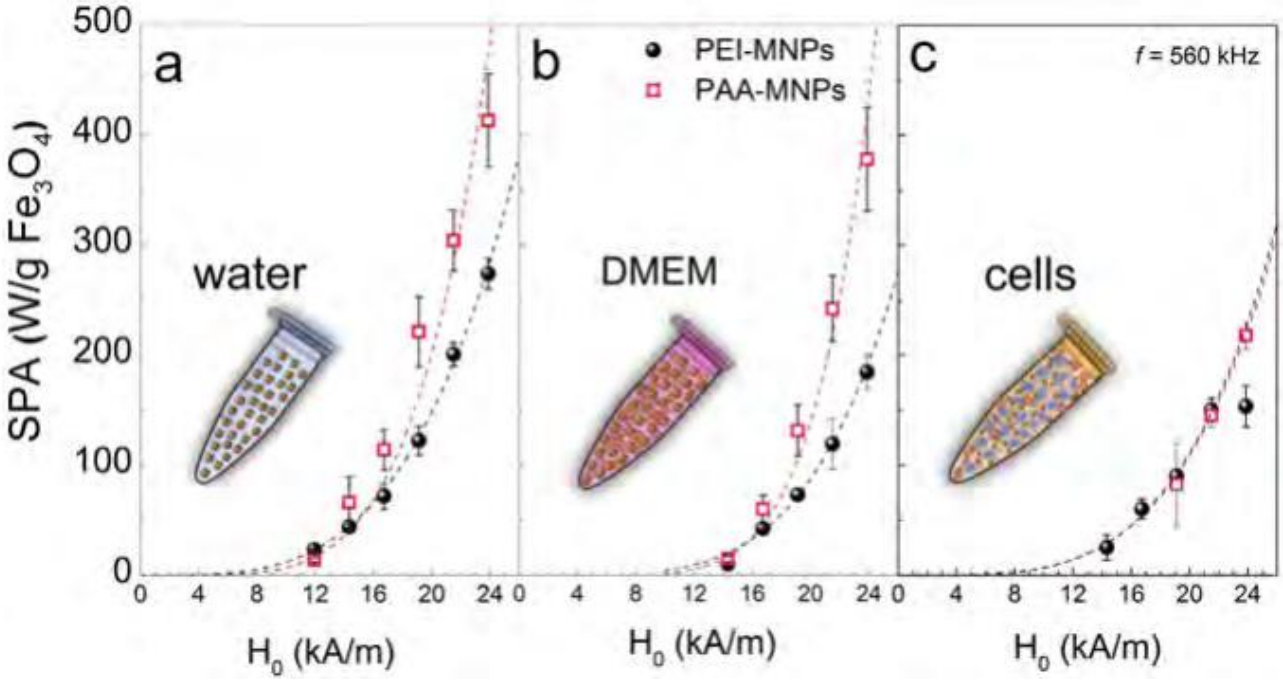

Figure 13: Specific power absorption dependence of MNPs (two different types) on magnetic field H_0 in water, DMEM and inside cells (Sanz et al., 2016).

Moreover, the protein corona could lead to significant modifications of nanoparticles by increasing their size, reducing their stability, impacting their biodistribution throughout the body and modifying the surface area for interaction with the AMF. As a consequence, this may reduce SAR, especially during the in vivo tests where the biological system is more complex and dynamic) (Cai et al., 2017) (Portilla, Fernández-Afonso, et al., 2022). The adsorption of

human serum albumin, a widely used molecule for nanoparticles coating, has been shown to extend blood circulation time (Chubarov, 2022). Nanomaterials administered intravenously or orally can be distributed to different organs and tissues. Nanoparticles with diameters less than <10 nm are predominantly removed by renal clearance. This process involves glomerular filtration in the kidneys, which allows these tiny particles to flow into urine and be eliminated from the body, decreasing the toxicity associated with accumulation in organs such as the liver and spleen. In contrast, larger MNPs (>200 nm) are retained in spleen via mechanical filtration, preventing them from moving around freely in the circulation. Size-dependent filtration is a natural defense system that removes foreign molecules from the body. MNPs between 10-200nm, present a variety of biodistribution patterns. These particles have a prolonged blood time circulation and frequently collect in organs of the reticuloendothelial system (RES), such as the liver and spleen, as a result of opsonization and subsequent uptake by phagocytes. Understanding the relationship between nanoparticle size and in vivo behavior is critical when developing nanomaterials for specific medicinal purposes. Nanoparticle size and surface optimization characteristics are critical for achieving optimal biodistribution and clearance profiles while maintaining safety and efficacy in clinical settings, and it can improve MHT cancer treatment and diagnostic efficiency while minimizing side effects. (Michelle L.,2012) (Ferretti et al., 2021)(Nowak-Jary & Machnicka, 2023) (Lu et al., 2023).

4.1. Magnetic hyperthermia aspect at the cellular and molecular level

Magnetic hyperthermia mediated by nanoparticles has many effects at the cellular and molecular level resulting in the loss of cell homeostasis and directly influencing the cancer cell growth and function inducing cell death by apoptosis and/or necrosis. The route of cell death caused by MHT relies on various factors including the temperature range achieved during the treatment. Lower hyperthermic temperatures ~40-45 °C promote apoptosis and/or necrosis. The exposure duration is another important factor, prolonged exposure to high temperatures raises the risk of necrosis owing to chronic cellular stress. Cell phenotypes also play a role in mechanism of apoptosis or necrosis due to the divergence in heat sensitivity among different cell types (different HSP levels) (Zaidi et al., 2004) (Bettaieb & Averill-Bates, 2015) (Szwed & Marczak, 2024).

4.1.1. Apoptosis and necrosis

MHT can cause apoptosis and/or necrosis by raising temperatures to levels that disturb cellular functioning without causing rapid membrane rupture. Hyperthermia can activate apoptosis through intrinsic mechanisms, resulting in regulated cell death. This is a controlled cell death pathway that causes cell shrinkage, DNA fragmentation, and membrane blebbing. The apoptosis consists of two major pathways, the intrinsic apoptosis and the extrinsic apoptosis, and both are regulated by caspase and Bcl-2 protein families (major apoptosis regulators).

Caspases are a group of cysteine proteases that are important for starting and carrying out apoptosis. They are classified as initiator caspases (e.g., caspase-2, -8 and -9) and executioner caspases (e.g., caspase-3, -6 and -7) (Figure 14). Initiator caspases react to apoptotic signals by activating executioner caspases, which then cleave particular substrates, causing cellular disintegration and death.

The Bcl-2 family includes pro- and anti-apoptotic proteins that control mitochondrial outer membrane permeabilization (MOMP), an important phase in apoptosis. Anti-apoptotic members (Bcl-2 and Bcl-xL) protect mitochondrial integrity by blocking pro-apoptotic members (Bax and Bak) (Figure 14). In the intrinsic apoptosis, the pro-apoptotic protein Bid promotes the translocation of the pro-apoptotic protein Bax to the mitochondrial membrane leading to MOMP, and the release of cytochrome c and Apaf1 (apoptotic protease activating factor 1) resulting in the formation of apoptosomes and caspase-9 activation. Cancer cells frequently overexpress anti-apoptotic Bcl-2 proteins, which contribute to tumor survival and apoptosis resistance.

Necrosis is the unregulated death of cells caused by stress, which results in cell enlargement and membrane rupture. Higher temperatures obtained during MHT can result in necrosis by denaturing proteins and disrupting cell membrane integrity. This mechanism distributes intracellular substances into the tumor milieu, perhaps triggering an immunological response (Olsson & Zhivotovsky, 2011) (Szwed & Marczak, 2024).

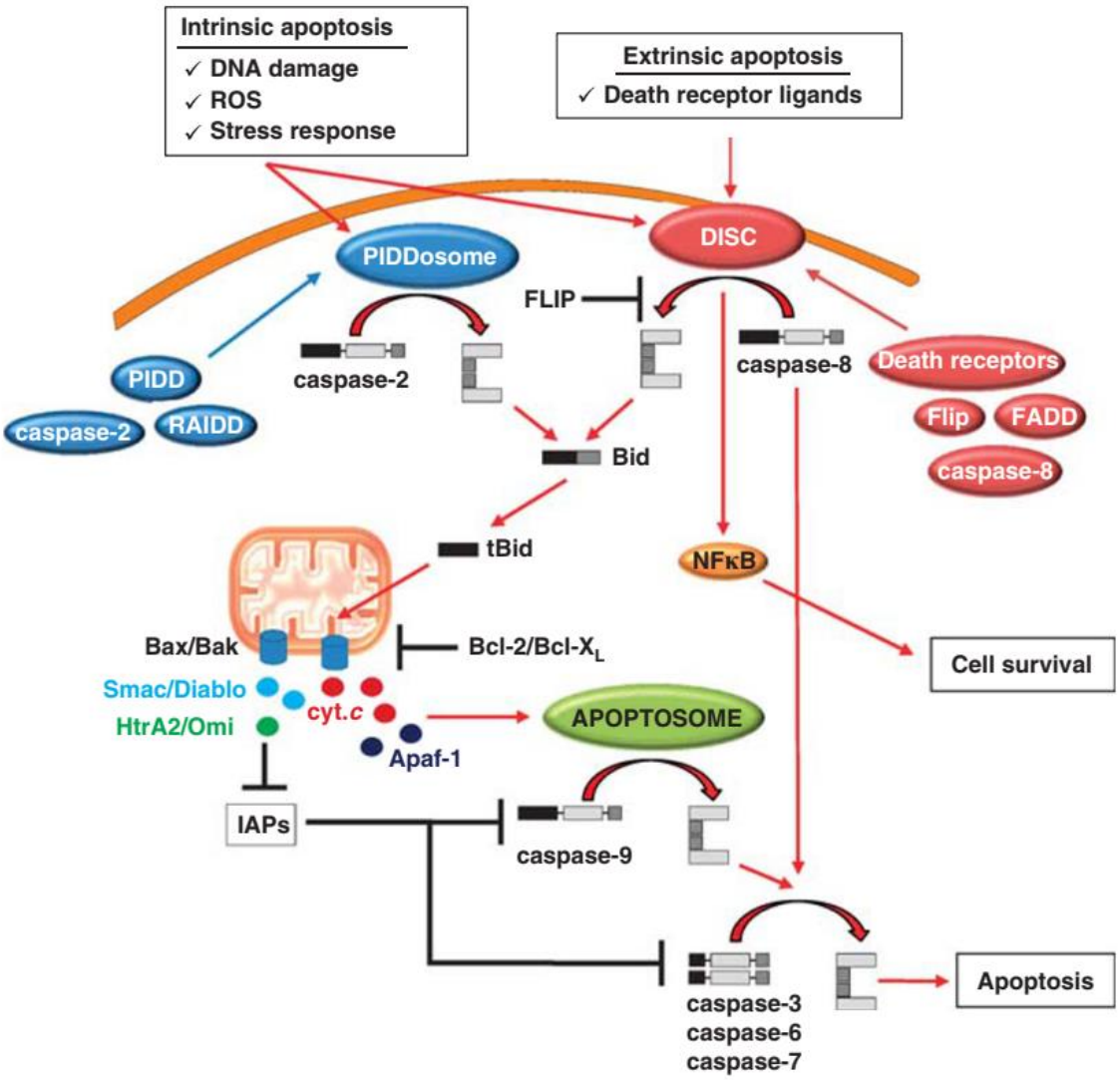

Figure 14: A general overview of the apoptosis initiators and inhibitors after hyperthermia (Olsson & Zhivotovsky, 2011).

4.1.2. Reactive oxygen species and lysosomal membrane permeabilization

An increase in reactive oxygen species (ROS), a group of oxygen derived radicals and derivatives, can promote cancer cell death. ROS are formed in mitochondria via Fenton reaction, among other pathways. The excessive production of ROS causes oxidative stress and damage macromolecules, proteins, lipids, and DNA. Antioxidant systems serve to neutralize ROS generation, but a severe imbalance between antioxidants and high ROS concentrations during hyperthermic exposure might render the cell defenseless to the consequences of oxidative stress.

Hyperthermia has shown to increase ROS levels in the form of hydrogen peroxide, superoxide anion, and hydroxyl radicals. Hyperthermia can lower antioxidant levels, including superoxide dismutase (Wydra et al., 2015). Localized heating by MNPs may increase ROS generation, resulting in lysosomal membrane permeabilization, which causes the release of enzymes that boost ROS generation, resulting in a feedback loop that intensifies cellular damage and cancer cell death. ROS may also regulate cell death and trigger the classical apoptotic pathway resulting in cytochrome release, caspase activation, and cell death (Domenech et al., 2013) (Egea-Benavente et al., 2021).

4.1.3. Membrane and nuclear damage

Hyperthermia increases the fluidity of cell membranes, influencing the function of proteins attached to the membrane and receptors. In (de Andrade Mello et al., 2017) hyperthermia has shown to induce membrane fluidity, which can facilitate the activation of the P2X7 receptor and the formation of membrane pores, ultimately leading to cell death. Moreover, the disruption of membrane proteins can cause an influx of calcium ions, which, if excessive, can activate degradative enzymes and induce cell death (Roti, 2008).

Elevated temperatures can damage DNA directly by breaking both single and double-stranded DNA, phosphorylation of H2AX to γ-H2AX for genomic stabilization, inhibiting the function of important DNA repair proteins such as the DNA polymerase β, an essential enzyme in the base excision repair pathway, preventing the reconstruction of single-strand breaks. Hyperthermia also has an effect on the non-homologous end joining (NHEJ) pathway, causing the Ku protein to aggregate and become inactive. Heat stress also disrupts the homologous recombination (HR) pathway by causing the MRN complex (Mre11/Rad50/Nbs1) to translocate from the nucleus to the cytoplasm, preventing the recruitment of recombinase Rad51 and protein BRCA (Fu et al., 2018) (Huang & Zhou, 2020). Indirectly, hyperthermia may stimulate ROS production, thereby halting the cell cycle and inhibits DNA replication, leading to cell death. Furthermore, HT induces irreversible DNA damage, which enhance the effects of chemotherapy and radiotherapy (Yang et al., 2018).

4.1.4. Thermotolerance

Thermotolerance is a cellular adaptation process for survival under heat stress conditions that would otherwise be lethal. The direct impact of hyperthermia on cells depends on the temperature level and exposure duration. Cellular thermotolerance is produced by low heat

doses (~40°C), is strongly related to the expression of heat shock proteins, an assembly of molecular chaperones produced in cells in response to an increase in temperature levels. HSPs play a crucial role in preventing apoptosis and regulating heat stress responses, they help with protein folding, inhibit misfolded proteins aggregation and aid in the repair or degradation of damaged proteins. HSP27, HSP70 and HSP90 are the main expressed proteins during heat shock response for protecting cells from the harmful effects of hyperthermia (Singh & Hasday, 2013) (Bettaieb & Averill-Bates, 2015) (Gao et al., 2016).

4.1.5. Immune system activation

Hyperthermia induces both tumor cell cytotoxicity and immune response stimulation through several mechanisms, including the induction of immunogenic cell death, the activation of HSP and the modulation of immune cell activity**.** Immunogenic reactions activate the innate and adaptive immune systems, such as macrophages, natural killer cells, dendritic cells, and T cells.

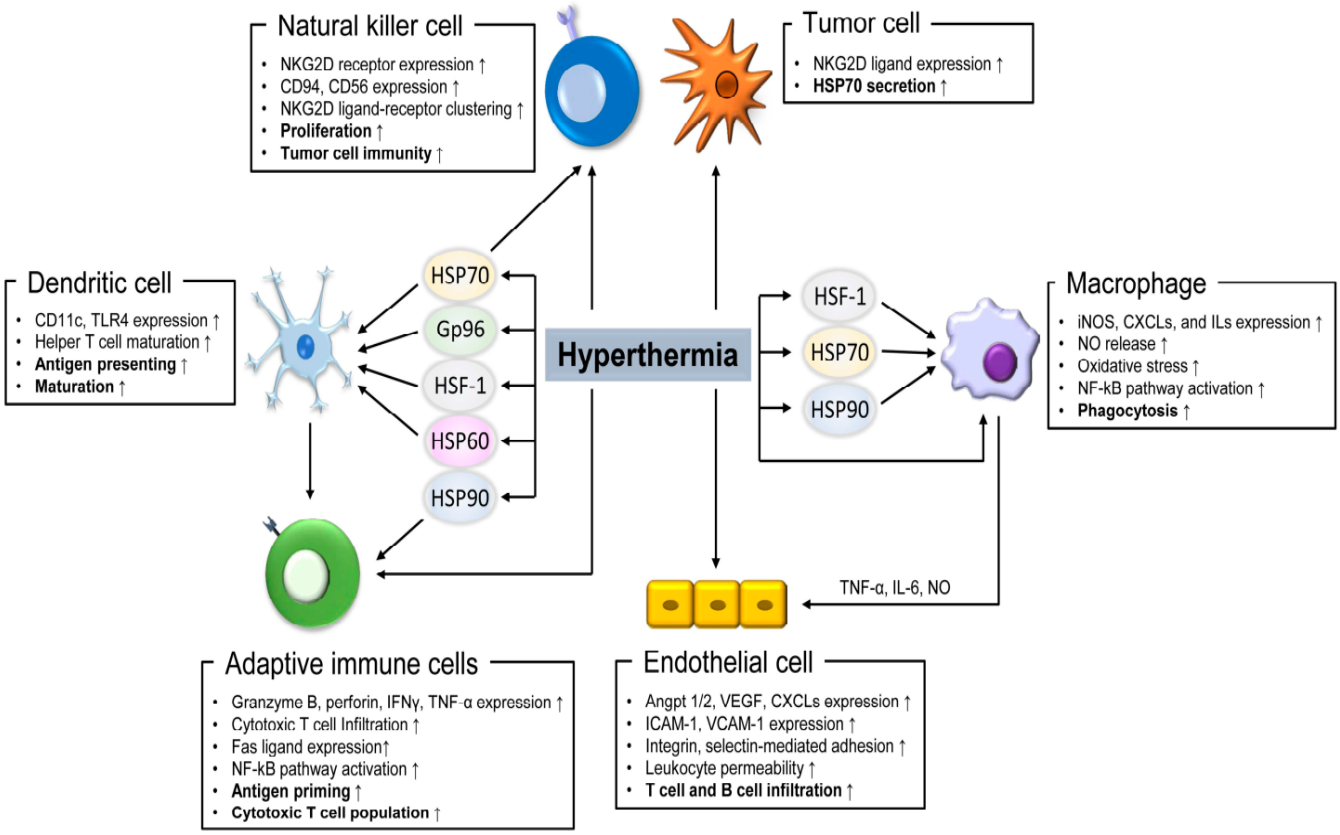

Figure 15: Immune response stimulation after hyperthermia treatment through HSP activation, immunogenic cell induction and modulation of immune cell activity (Lee et al., 2018).

Heat stress during hyperthermia can cause tumor cells to produce exosomes containing tumor-associated antigens (TAAs) and HSPs, which are then processed, by antigen-presenting cells (APCs). HSP expression results in improved antigen presentation. These HSPs can bind to tumor antigens and aid in their uptake by APCs, such as dendritic cells, increasing the activation of tumor-specific T cells. This strategy efficiently connects innate and adaptive immunity, improving the body's ability to identify and fight tumor cells. In parallel, immunogenic cell death (ICD) is a process that includes the exposure or damage-associated molecular patterns (DAMPs) from dying tumor cells, such as calreticulin (CRT), ATP and HMGB1, which act as, eat me signals to the immune system. The presence of DAMPs leads to the recruitment and activation of immune cells near the tumor site, establishing an environment favorable for anti-tumor immunity (Zhang et al., 2023).

5. Nanorobotic antitumoral treatment (magneto-mechanical destruction):

Nanorobotics is an alternative non-heating cancer treatment modality that is based also on the coaction of magnetic particles and the external magnetic field. In this study we aim to evaluate the outcomes compared to MHT treatment. Nanorobotics refers to the magnetomechanical destruction of cells due to the alignment and linear movements of an assembly of MNPs or magnetic microparticles (MMPs) under an external low frequency magnetic field which are considered to be safe fields for healthy tissues. The mechanical forces play a key role in influencing cell behaviour,adhesion, migration, differenciation and cytoskeletal disruption resulting in cancer cell damage and death. For instance, if the metochondria are targeted this will induce morphological changes in cancer cells leading to apoptosis (Master et al., 2016) (M. Chen et al., 2020).The linear movement of the particles internaliezed inside cancer cells via lysosomes will cause mechanical disruption of cell organelle, leading to apoptosis caused by extravasation of lysosomal contents into the cytoplasm and a decrease of intracellular pH. One interesting approach is the combination of this antitumoral therapy with chemotherapy. When the particles enter the lysosomes, the drug loaded on the particles will be released due to the low pH inside these organelles. Then, magnetic field is applied to cause the rupture of the lysosomes, dumping all the content into the cytosol (E. Zhang et al., 2014).

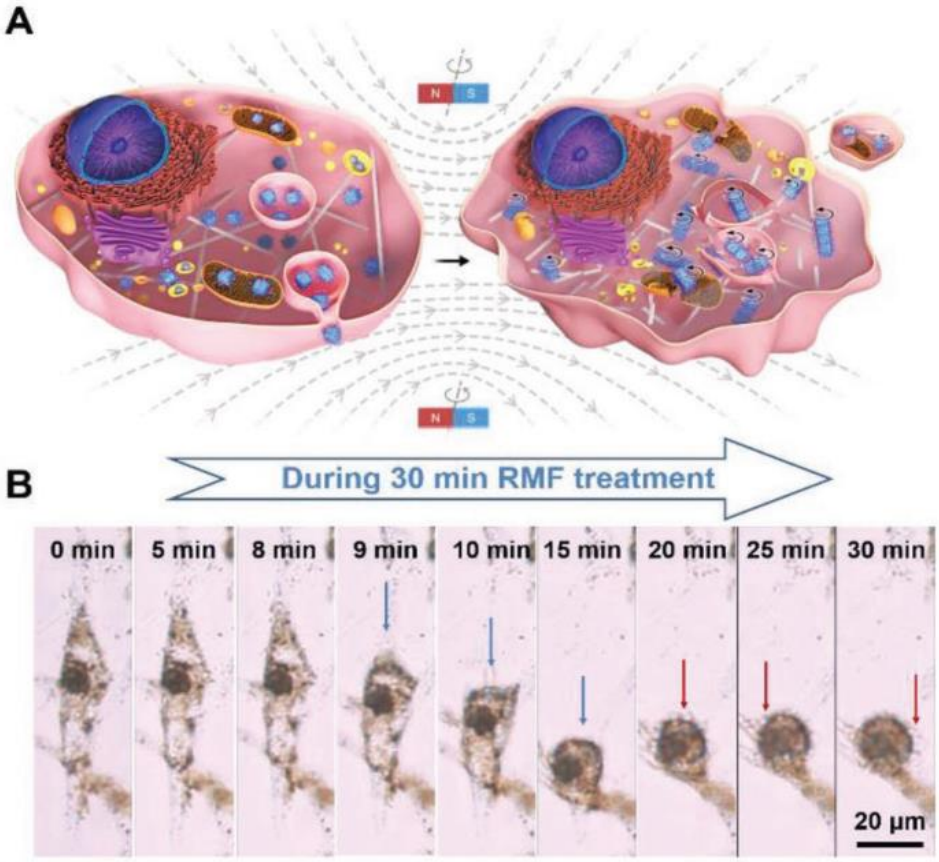

Figure 16: Illustration of mitochondrial-targeted MNPs (20 nm) triggered magnetomechanical destruction of cancer cells (U87) under rotating magnetic field for 30 min (A and B) (M. Chen et al., 2020).

Moreover, a previous research carried out in our laboratory (Amaya-Jaramillo et al., 2017) have determined the interaction of MMPs and fibroblastic cells (3T3) under different conditions of incubation time with MMPs, particle size, AMF exposure duration, different current waveforms at different frequencies to produce a magnetic field gradient. They demonstrated a high cell death rate at 1Hz with square waveform within 1 h of irradiation.

III Chapter 3: Materials and Methods

This chapter is devoted to the experimental investigation, both in vitro and in vivo, of the safety of applying an AMF based on new non-sinusoidal signals in coaction with spherical iron oxide nanoparticles, evaluating their efficacy as an antitumor treatment. The goal is to increase the cancer cell damages and induce immunogenic cell death through the exposure of DAMPs in a combination treatment with chemotherapy, which may subsequently can stimulate the activation of the immune system.

The in vitro experiments were conducted on two cancer cell lines, the glioblastoma multiforme (CT2A) and the melanoma (B16F10), which are considered among the most deadly cancer types. The in vitro assays consist in culturing the cells in suitable dishes that fit the sample holder in the MHT device, followed by their incubation with MNPs and finally their exposure to the AMF under specific conditions.

The in vivo experiments were carried out on a C57BL/6 mouse model, where different groups have been exposed to different AMF conditions to check the safety of the non-harmonic fields on the mice and ensure the absence of eddy currents inside the body that may be lethal if it is induced in certain organs. The hyperthermic treatment mediated by MNPs was initiated after confirming the safety of the device. A GBM tumor model was established on the mouse leg to facilitate the injection of nanoparticles and the exposure of different mice groups to the treatment under AMF, compared to the untreated group (control group).

In parallel, a simulation study was initiated during my internship as part of the doctoral training to assess the eddy currents effects that could be produced by a pulsed alternating magnetic field inside biological medium (DMEM/Mouse model) using Sim4Life Multiphysics platform. The in-silico tests aim to simulate electromagnetic radiation, power density deposition, and the temperature distribution in 3D cell culture media contained in a polystyrene petri dish, with and without nanoparticles, as well as a mouse model upload from the IT'S foundation platform. The main objective is to be able to make simulations with non-harmonic signals and compare them to the conventional sinusoidal signals, using a wide range of frequencies and amplitudes.

1. Magnetic hyperthermia experimental device

The most common energy sources used for generating heat using nanoparticles are light and alternating magnetic field. A range of devices have been developed for MHT, a cancer treatment that uses magnetic fields to heat and destroy tumor cells. Mier (2002) and Yang (2012) both developed systems for inducing hyperthermia, with Mier focusing on a magnetic induction heating system and Yang on a magnetic fluid hyperthermia system. Both systems were successful in achieving the desired temperature range for hyperthermia (Mier et al., 2002) (W. Yang et al., 2012). Abu-Bakr further enhanced the understanding of this technique by demonstrating that the interaction between ferromagnetic particles in a rotating magnetic field can significantly increase heat production (Zubarev et al., 2015). Garaio engineered device to generate controllable and homogeneous AC magnetic fields for magnetic hyperthermia experiments, where the applicator distinguishes itself by integrating an AC magnetometer for accurate measurements (Garaio et al., 2014). These studies collectively contribute to the development and understanding of MHT as potential treatment modality. In (Mohseni & Rajaei, 2018), a design optimization of an AMF generator for hyperthermia research application has been described, to maximize the power dissipation by MNPs, regarding coil geometry and power electronic characteristics (magnitude and frequency of voltage).

The ability to precisely control the heating effect through the modulation of the alternating magnetic field makes this technique a promising avenue for the future of cancer therapy. Recent numerical research on MHT investigated the non-harmonic derived fields to enhance the heating efficiency (Allia et al., 2019) . The use of non-sinusoidal signals emerged as a promising approach to achieve a more effective heating process. The magnetic hyperthermia device used in our study for performing in vitro and in vivo experiments has been newly developed at the CTB. In the following text we will describe in detail the system used.

1.1. The AMF circuit design

The device consists of a full bridge inverter (DC-AC inverter), transforming a DC input to an AC output, made up by four MOSFETS or semi-conductors (Figure 17) which work diagonally, meaning, Q1 with Q4 and Q2 with Q3. The operation of these MOSFETS is given by the core (PCB) which is responsible for directing their opening and closing in order to generate a specific signal waveform. The model used is STM32F446RE (core). This generates 3.3 V, but as the MOSFETS need 12 V, a gate driver is used to amplify it. On the other hand, this core has four

channels: channel CH1 sends a signal to Q1, CH1N to Q2, CH2 to Q3 and CH2N to Q4. The semi-conductors (Q1, Q2, Q3, Q4) act as two different diagonal branches, with the load (coil) placed in the middle of the inverter. A graphical representation of the inverter design, the load and the power supply can be seen in Figure 17.

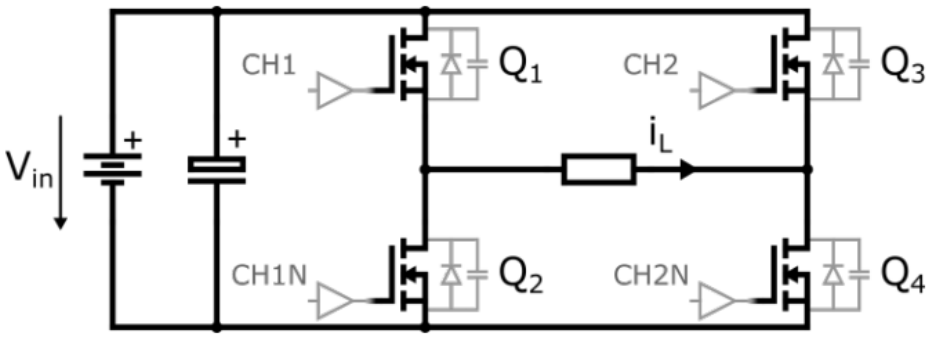

Figure 17: Magnetic hyperthermia device's full bridge iverter for sinusoidal and non-sinusoidal AMF signal generation.

The circuit transforms the DC input current to an AC output current. The MOSFET work in pair, Q1 works with Q4 and Q2 with Q3, in such a way that when the current passes through Q1 and Q4 generating the positive current of the magnetic field, hence, called the positive switching (in red arrow). When the current passes through Q2 and Q3, the current changes direction, thus generating the negative one of the magnetic fields and called the negative switching (in blue arrow). When the semi-conductors of the same branch are closed (Q1 and Q2), the current flows in one direction. When the second branch is closed (Q2 and Q4), the current flows in the opposite direction, changing the orientation of the magnetic field over time. In this way, an AMF is created as seen in Figure 18.

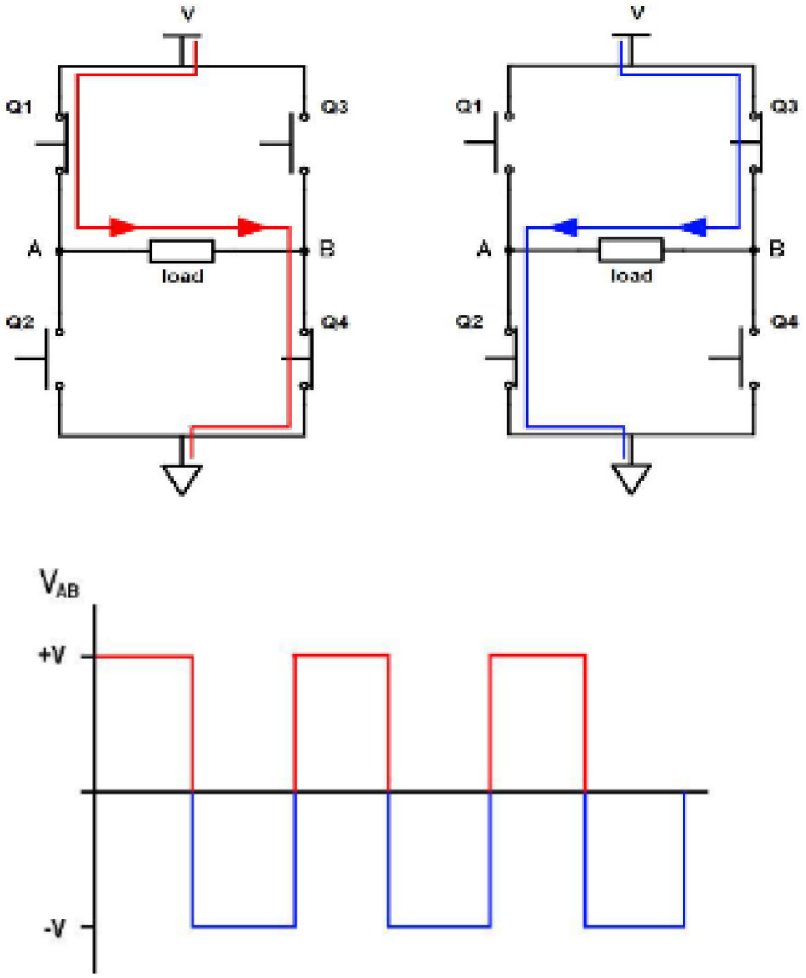

Figure 18: MOSFET's bridge inverter circuit functionning fundamental (up) and the AC output generated wheree V_{AB} is the voltage across the load(down).

The MHT system is able to generate 5 different signals at 6 different frequencies, ranging from 100 kHz to 500 kHz and 1 MHz, the signals waveforms are:

-Triangular (TR)

-Trapezoidal-Triangular (TT)

-Trapezoidal (TP)

-Trapezoidal-Square (TS)

-Sinusoidal that is derived from the triangular signal by placing in a series a resonator filter between the system and the coil.

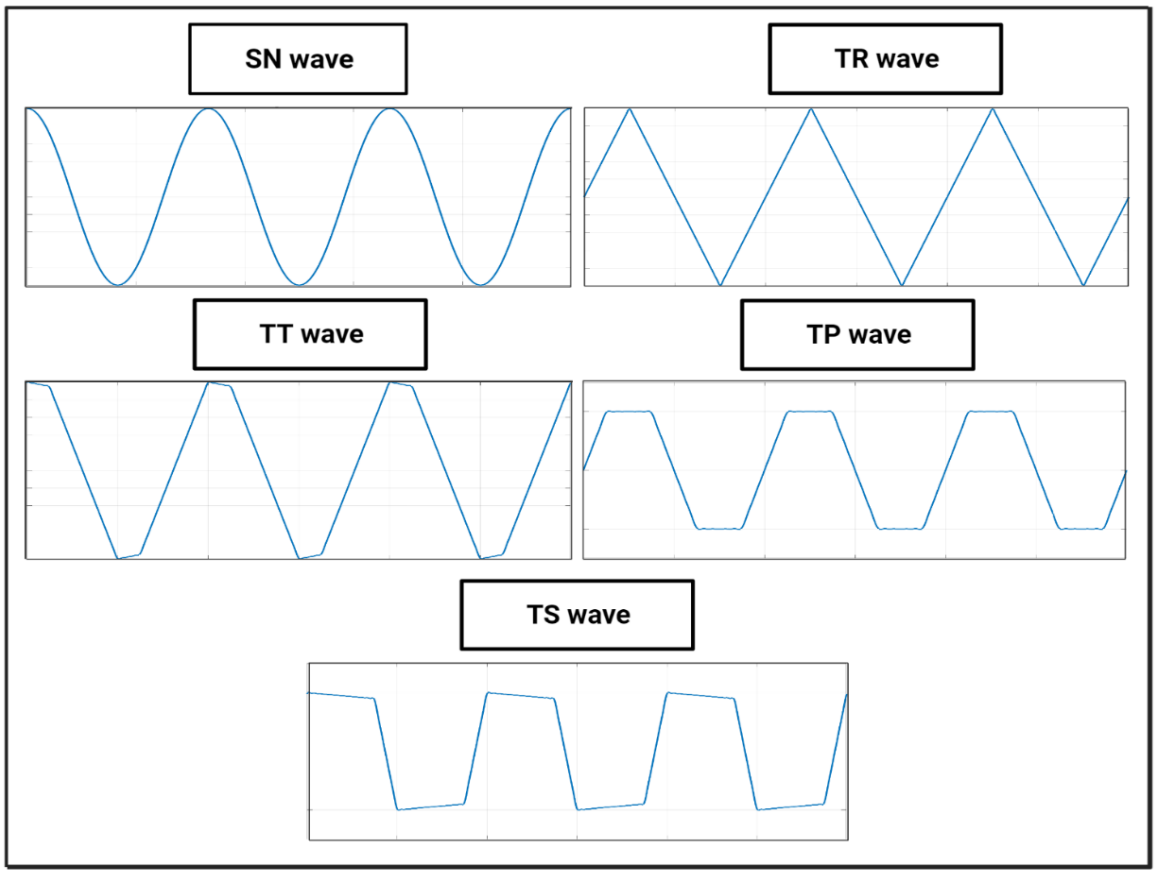

Figure 19: The waveforms of the AMF generated through the full bridge inverter of MHT device.

1.2. The fundamentals of non-harmonic waveforms generation

The AMF signal generation through the circuit is based on two fundamental terms, the duty cycle (measured in percentage) which is the ratio of time the signal is ON within an interval of time or period, and the phase-shift (measured in degree or radian) that corresponds to the angular displacement between two alternating currents of similar frequency. Conventional phase-shift control is the key behind the various waveforms obtained. Each switching leg has a constant 50% duty cycle and switches at the same frequency as the required output form. Changing the phase-shift (φ) from Q1 to Q3 from 0° to 180° changes the shape of the current waveform, as depicted in the following Figure 20:

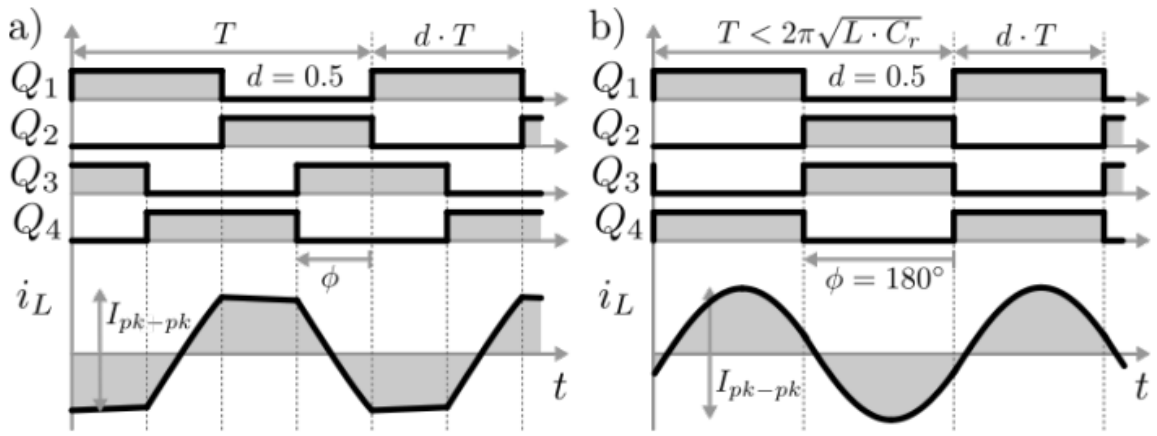

Figure 20: Output signal generated by the Inductive load. a) A 90◦ phase-shift for trapezoidal generation b) Sinusoidal signals generation by adding Cr.

The phase-shift "ϕ" takes the values 45°,90°,135° and 180° giving the trapezoidal-square, trapezoidal, triangular-trapezoidal and triangular, respectively.

The device is limited in the voltage dissipation capability of the power supply source used, more the slope increases the needed voltage increase, and due to extreme coil heating the threshold set to never surpass the 300 V in the power supply. Given that the relation between the input voltage Vin and the peak-to-peak current in the inductor Ipk-pk as follows:

$$I_{pk-pk} = \frac{T*\phi*V_{in}}{L*2*180^{\circ}} \quad (27)$$

It can be seen that TS waveform is the more limiting one as it has the smallest phase-shift (45°), hence it requires higher Vin to compensate for this low value on the phase and achieve the same peak-to-peak current. For instance, the required voltage to reach 300 kHz for TR is less than the required voltage to reach the same frequency for TS. In this case, higher voltage is needed for similar frequency and or amplitude. The system tends to show interferences when using higher voltage >300 V with TS and TP in order to achieve high amplitude and/or frequencies for higher heating performance. Also, the MOSFETS are heated up for a long interval of time and end-up by being damaged. Thus, we decided for preclinical tests, to choose the optimal conditions for each signal and to compare them to the sinusoidal under similar AMF conditions, and not to make comparison between the different waveforms in vitro performance.

The amplitude of the signal is controlled by the DC power supply that is linked to the bridge inverter, presented in Figure 21 (Left image). In contrast, a software controls the signal's waveform and frequency via a user interface that is connected to the control card (Right image).

Figure 21: DC power supply model connected to the bridge inverter (Keysight technologies N8928A 10'000W 500V/60A) (Left). Device electronic circuit composed by the bridge inverter, the control board, gate driver and DC capacitor bank (Right).

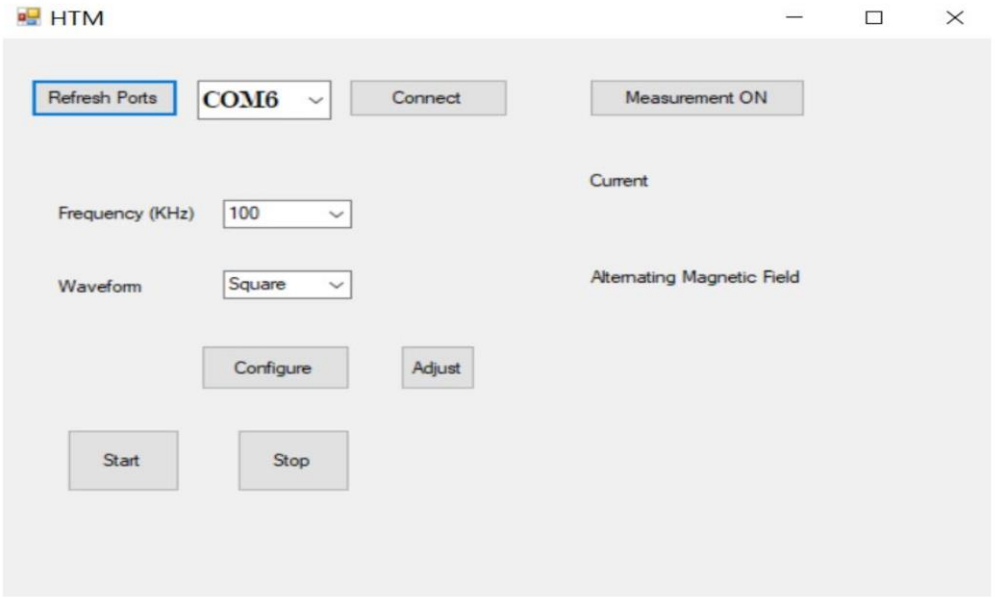

Figure 22: The user interface for controlling the frequency and waveform of the AMF.

1.3. The coil and sample holder

The coil for AMF generation consists in a solenoid of 14 turns. Each turn is made from a single-strand wire composed of 30 wires of 0.55 mm radius (Figure 23). The coil is 5.5 cm height. An inner diameter of 6 cm and an outer diameter of 7 cm. Regarding that coil's height we can place in three petri dishes of 35 mm or P35 for in vitro experiments. The coil was placed in a Faraday cage to contain the electromagnetic waves generated by the circuit (Figure 25).

Figure 23: The coil geometry of the AMF device.

During MHT treatment, the cell samples must be thermally isolated, especially from the solenoid coil that shows harsh heating during the EMF exposure. Thus, a PLA sample holder connected to the water pump was designed to keep the temperature of the cell cultures stable at 37°C during AMF exposure. The petri dishes are introduced into a sample holder first with the aid of support than placed directly inside the coil as shown in Figure 24. The software used for building the holder and the support was Blender, and the 3D printer was the IIIP Delta Pro, (Monoprice, California, United States) and the material was PLA (Polylactic acid). Several challenges were faced while developing and testing the new holder. The thin layer of glue was added around the holder to avoid any possible leakage of water during the experiments. The Pasteur pipette support is used to place the optic fiber sensor inside a Pasteur pipette; hence the sensor will be directly immersed inside the cell culture medium in order to measure the temperature during experiments, without and with the MNPs.

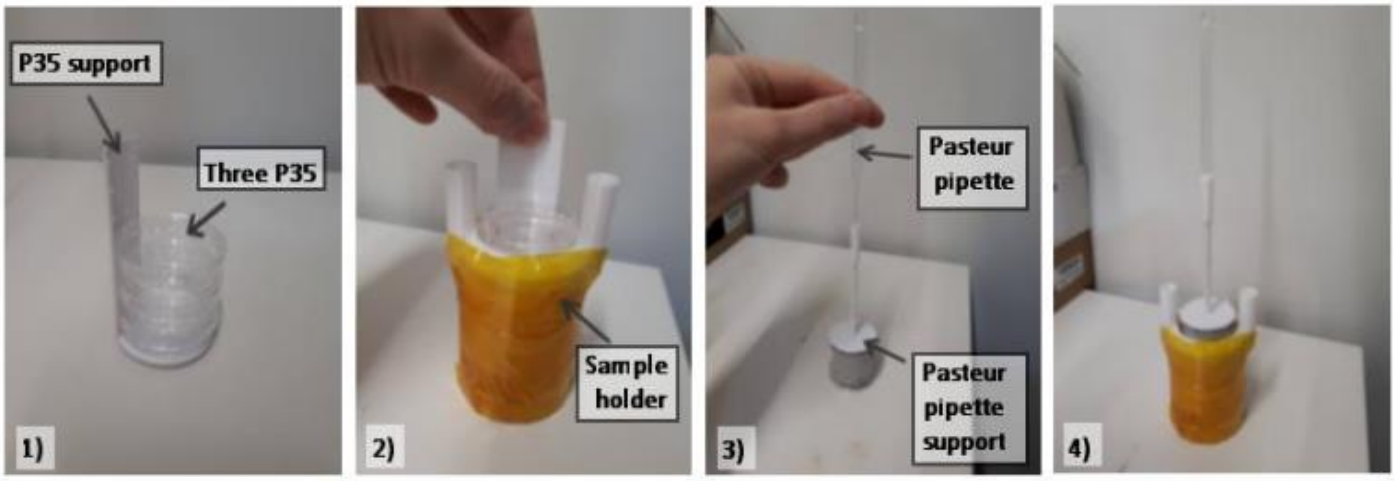

Figure 24: Cell petri dishes placement inside the PLA holder.

1.4. Water bath

The water bath is an immersion thermostat with manual selector and digital temperature reading. Manufactured by JP Selecta, it offers a temperature range from 0 °C to 100 °C with a stability of ±0.05 °C. The device utilizes a microprocessor-based system, allowing users to set and monitor parameters such as maximum and minimum temperature limits. It includes a low liquid level sensor to prevent operation under unsafe conditions. Equipped with stainless steel INCOLOY heating element, the unit is resistant to high temperatures and corrosive environments, ensuring durability and longevity. An adjustable flow rate pump facilitates external temperature control, and 12 liters per minute are pumped. The main objective to use this water bath is to maintain the in vitro or in vivo samples at their physiological temperature of 37°C. Therefore, the Digit-cool water bath is connected to the sample holder with thick tubes for water flow (Figure 25).

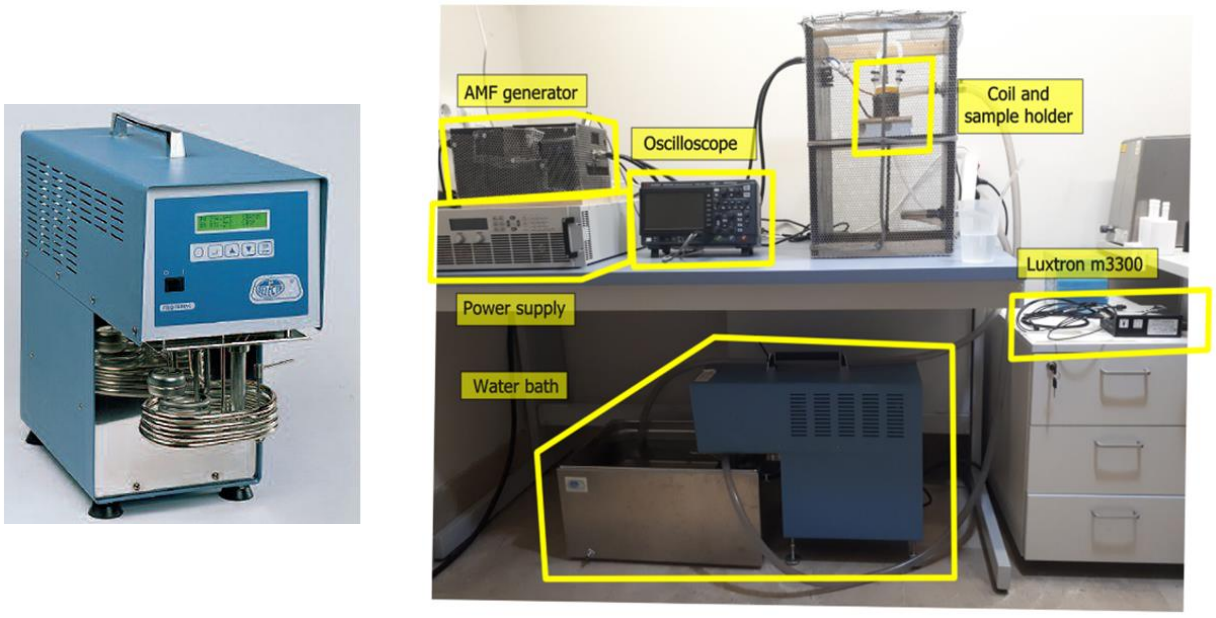

Figure 25: Digit-cool water pump (left) and the water bath placement within the MHT system (right).

1.5. Temperature monitoring tools

1.5.1. Thermal camera

A RS PRO RS730 thermal camera was used during our study to monitor the temperature of the coil, the electronic components of the circuit and the cell samples in presence or absence of nano-heaters. The thermal camera is a handheld thermal imaging camera that uses infrared (IR) technology. It is characterized by a temperature range from 0 to 150°C and a detector resolution of 160 x 120 pixels, a display resolution of 320 x 240 pixels, a measurement accuracy of ±2 ensuring reliable temperature readings and a minimum focus distance of 0.1m.

1.5.2. Fiber optic sensor

Luxtron's m3300 Biomedical Lab Kit is a fiber optic thermometry system designed for precise temperature measurements for medical applications. The system includes a "fluoroptic" thermometry equipment, a steel box for protection, sensors, and 2 m fiber optic cable extensions. The measuring range is 0 to 120 ºC, with an error of ±0.2ºC or ±20ºC around the calibration point. The instrument possesses four measurement connections (channels with 1 to 4Hz each one) and is connected to the user computer via a RS-232 serial port. The Luxtron Fluoroptic

Probe and extension (LumaSense Technologies) is a 200 µm hard clad silica fiber with a Tefzel protective cover and a length of 1 meter. The probe has a diameter of 0.5 mm, and the diameter of its tip, which contains the sensor, is approximately equal to 0.5 mm. This technology utilizes a temperature-sensitive phosphorescent sensor located at the fiber's optical termination. The photon pulses sent by the fiber optic excites the sensor, resulting in light emissions. The response time equals 0.25 seconds in stirred liquid. The instrument captures light pulses and estimates the delay between them. This delay changes according to the temperature of the sensor.

Figure 26: RS PRO RS730 thermal imaging camera.

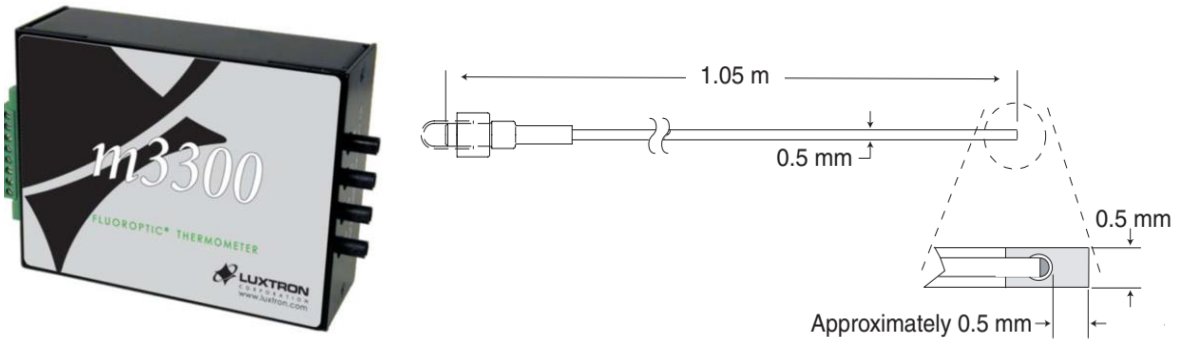

Figure 27: Luxtron m3300 thermometry instrument (left) and the Luxtron Fluoroscopic probe design (right).

1.6. Oscilloscope and Amplifier

A keysight DSOX1204 oscilloscope was utilized in all the experiments. It is a versatile 4-channel digital storage oscilloscope (DSO) that forms part of Keysight's InfiniiVision 1000 X-Series. It comes with a standard bandwidth of 70 MHz, which is upgradeable to 100 MHz. The screenshots and data can be quickly and easily saved with built-in USB port and USB storage device and it have a memory depth up to 2 Mpts. A current probe Keysight N2782B is used with the oscilloscope for an accurate AC and DC currents measurment. It offers a bandwidth of 50 MHz and can measure currents up to 30 Arms, with a maximum peak current of 50 A.

Figure 28 : Keysight DSOX1204 oscilloscope with the current probe N2782B.

A Keysight N2779A amplifier is a power supply used for the N2780-83A/B current probe that provides clean DC power to the probe. This power supply is designed specifically for use with the N2780-83A/B AC/DC current probe to ensure safe operation.

Figure 29: Keysight N2779A amplifier.

2. Magnetic nanoparticles

2.1. Description and synthesis method

Iron oxide nanoparticles in the form of spheres with two different size of 10.6 nm and 8 m (standard deviation =0.2) and biofunctionalized by a positive coating of 3-aminopropyl-trietoxysilane (APS) were used in our project. The APS coating was used for biofunctionalization and is considered to enhance the uptake of MNPs since the cells have a negative global charge from the outside while the APS is positively charged which reinforces the attraction forces and increases the internalization of the nanospheres.

The nanoparticles are characterized by a hydrodynamic size (H_D) of 65 nm measured by dynamic light scattering (DLS) and a polydispersity index (PDI) of 0.23. A zeta potential (ζ) measured at pH 7 equal to +25mV. At this small size, the nanoparticles will achieve better performance for MHT application at low field amplitude (<5 mT) and also exhibit excellent colloidal stability in liquid medium (Ajinkya et al., 2020).

The synthesis method of APS-MNPs follows Massart's coprecipitation protocol (Massart, 1981)for synthesizing maghemite nanoparticles. In brief, the preparation of 10 nm nanoparticles requires the addition of a mixture of 445 mL containing FeCl3·6H2O (0.09 moles) and FeCl2·4H2O (0.054 moles) to 75 mL of alkaline medium (NH4OH 25%) under vigorous stirring and at room temperature. Next, using magnetic decantation, the precipitate was washed three times with distilled water. After that, a protocol of oxidation and activation of the surface of the particles was followed by an acidic treatment using 300 mL of HNO3 (2 M) with stirring (15 min), then the supernatant was removed using magnetic separation and pouring in 75 mL of Fe (NO3)3 (1 M) and 130 mL of water, heating to boiling temperature (30 min) and cooling to room temperature and removing the supernatant again. Finally, 300 mL of HNO3 (2 M) was added, and the mixture was washed several times with water. To modify the surface of the particles and obtain the APS coating (positively charged), 1.22 mL of APS was slowly added (10 µL/s) to a 20 mL mixture of particles (28 g Fe2O3/L) in methanol under vigorous stirring for 12 h. Methanol was removed with a rotary evaporator (Luengo et al., 2013). The hydrodynamic size and the evolution of the zeta potential versus the pH were evaluated in a ZETASIZER NANO-ZS device (Malvern Panalytical, Cambridge, UK). The hydrodynamic size was measured at pH 7 and at room temperature from a dilute suspension of the sample in a standard cuvette.

For explanation, the donated MNPs used in the magnetic hyperthermia study using non-sinusoidal signals as single treatment had a size of 10.6 nm. While the donated MNPs utilized during the combination treatment between MHT and chemotherapy, had a size of 8.3 nm.

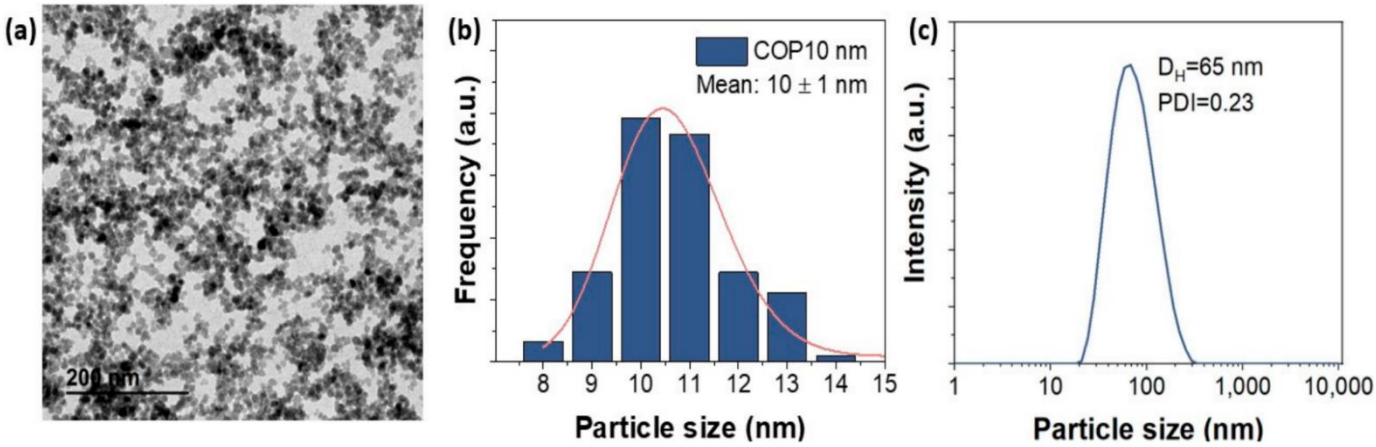

Figure 30: (a) Transmission electron microscopy (TEM) micrographs of APS-SPIONs. (b) Size distribution of APS-SPIONs in water with TEM and (c) Hydrodynamic size at pH 7 measured using dynamic light scattering (DLS).

3. Device safety

The in vitro temperature measurement using a flexible fiber-optic thermometer (m3300 Biomedical Lab Kit, LumaSense Technologies, Santa Clara, CA, USA) were performed in the absence and the presence of MNPs.

First of all, we had to analyze if the non-sinusoidal waveforms induce any temperature increase in the medium without nanoparticles, to verify the occurrence of any possible eddy currents and temperature changes. Also, any external heating from the coil may lead to temperature variation inside the cell sample that may cause cellular damage which is not good for our preclinical experiments in which we aim to treat cancer cells by the unique effects of magnetic hyperthermia (coaction between MNPs and AMF). Therefore, the main objective of this experiment is to demonstrate that our cell samples are isolated from any external temperature. Thus, cells were cultured in petri dishes of 35 mm and placed inside the holder. The temperature of the culture dishes was measured during AMF exposure using two fiber optic fiber sensors, which did not include any metallic components and temperature measurements are made by infrared light, hence accurate measurements are maintained.

The temperature measurement in the presence of MNPs was carried out to demonstrate the heat generation by the coaction of nanoparticles under external electromagnetic field and to select the optimum AMF parameters capable of giving the maximum heat increment. The concentrations were chosen relative to the results of the cytotoxicity tests. The optic fiber sensors are placed within the samples as follows:

- The first one was placed on a glass of distilled water to measure the room temperature.
- The second one was placed inside the petri dish within the cell culture medium through a Pasteur pipette as demonstrated in Figure 31, to measure the temperature variation of the cell sample.

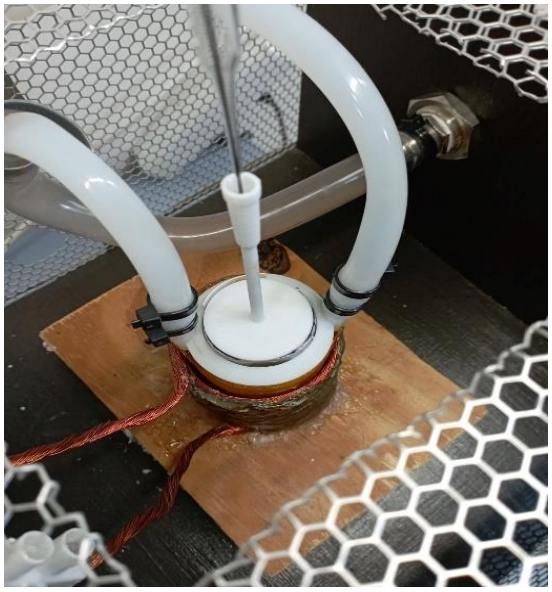

Figure 31: Cell sample holder placed inside the coil and connected to water bath. An optic fiber sensor is immersed within the cell culture sample by a Pasteur pipette.

All temperature measurements are plotted in real time on the user's computer with an interface programmed in python and all measurements are saved in a .csv file which will include the time at which every measurement is taken (the date, hour, minute, second) and the measurements from both optic fibers.

The AMF parameters selection was based on our first results of the study done by M. Zeinoun (2021) on a ferrofluid sample. The results showed a temperature increase of 3°C with TS relative to the SN at 200 kHz and 2.14 mT under AMF for a duration of 15 minutes, while TP had a temperature increase by 1°C relative to SN. At 500 kHz and 1.07 mT the temperature almost the same between TS and SN, but the TP increased by almost 0.5°C relative to SN. The TT and

TR had no increase in temperature above the SN waveform (Zeinoun, Serrano, et al., 2021) (Zeinoun et al., 2021). If the frequency and or the amplitude increase the final temperature achieved for a fixed interval of time will be higher. Due to certain limitations in the electronic circuit, we worked at low levels of amplitudes (≤ 3 mT) within a range of frequency from 100 kHz to 500 kHz and 1MHz. When the frequency is increased, then the amplitude must be kept at low levels and when the amplitude is increased then the frequency must be kept at low levels. For instance, at 3.21 mT all the non-sinusoidal waveforms were possible to obtain at 100 kHz but at 200 kHz only TP, TT and TR were possible to obtain. Where TP gave the highest increase among them. Therefore, for our study we decided to select the optimum frequency and amplitude we can obtain for each waveform relative to our first data published in (Zeinoun et al., 2021) and also based on the values of the final temperature achieved in cell culture samples in the presence of MNPs. Thus, The TS was selected at 200 kHz and 2.14 mT, the TP at 300 kHz and 2.78 and TR at 300 kHz and 3.42 mT. Generating pure TP and TS signals at magnetic field parameters of 300 kHz and 3.42 mT was not possible with our AMF applicator, due to coil overheating and substantial interferences. For this reason, the amplitude for was selected to be 2.78 mT while keeping the same frequency of 300 kHz. Both frequency and intensity of TS needed to be reduced to 200 kHz and 2.14 mT.

The following Table summarize the AMF's conditions selected:

Waveform	***Slope factor***	***Frequency (kHz)***	***Amplitude (mT)***
TS	1/8	200	2.14
SN	1/2π	200	2.14
TP	1/4	300	2.78
SN	1/2π	300	2.78
TR	1/2	300	3.42
SN	1/2π	300	3.42

Table 1: The AMF's parameters selected for the in vitro MHT treatment.

4. Cancer cell lines

Glioblastoma multiform (CT-2A) and melanoma (B16F10) are the cancer cell lines used to study the optimization of MHT antitumoral treatment using non-sinusoidal waveforms. The cell lines were obtained from Cajal Institute (CSIC).

The CT2A cell line is a mouse glioma (astrocytoma) cell line derived from a malignant astrocytoma in a C57/BL6 mouse. The tumor was induced by the implantation of a highly carcinogenic hydrocarbon (methylcholanthrene) inside the cerebrum of C57BL/6 mice (Zimmerman, 1961). In vitro, the cells grow adherent to the substrate as a monolayer, an essential key for their proliferation. These cells are characterized by an elongated shape compared to B16F10 and tend to die at high confluence

The B16F10 cell line is a murine melanoma cell line derived from a spontaneous skin tumor in a C57BL/6J mouse. B16F10 is an extremely aggressive tumor, and known for its high metastatic potential, especially to the lungs and lymph nodes. It has been shown that in cell culture, the B16F10 cell line has rapid proliferation rates and presents a heterogeneous population, with cell size varying depending on the stage of maturation. In addition, the melanoma cells can be present in three different sizes: 9, 12, and 15 µm. The more abundant are the more mature cells, with a bigger size (J. L. Duval et al., 1999) (Nakamura et al., 2002). B16F10 cells are transformed cells (unlimited cell divisions) that produce melanin. When the cells reach 100% confluence, melanine production turns the cell culture medium to a black color, which facilitates the visualization of tumors during in vivo experiments.

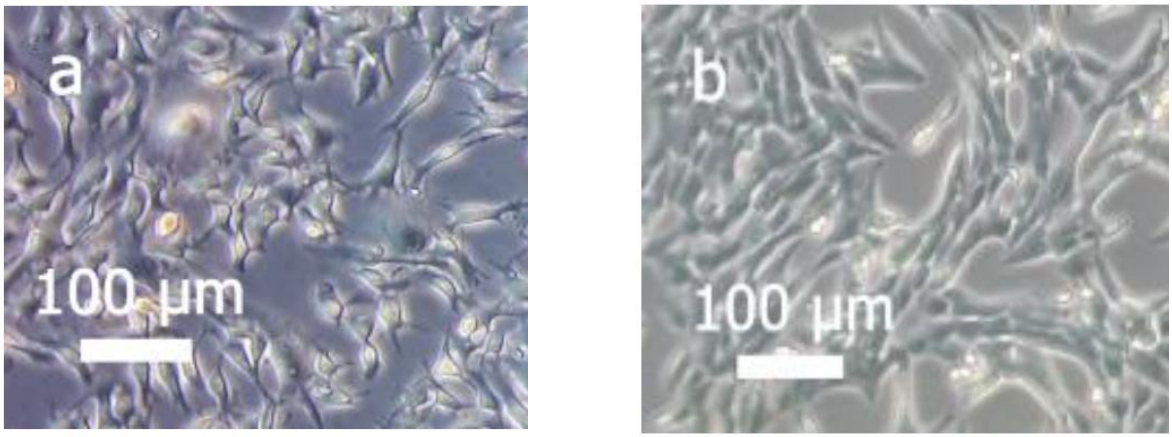

Figure 32: Light microscopy images of B16f10 (a) and CT2A(b) cells grown in DMEM under specific conditions and captured using a Leica DMI 3000 B inverted microscope.

5. Protocols for in vitro assays

The experiments performed for magnetic hyperthermia treatment using pulsed electromagnetic fields alone, were carried out on both CT2A and B16f10 cell lines. In the other hand, the experiments for treating cancer using the combination treatment between magnetic hyperthermia and chemotherapy were done, particularly, on CT2A cells.

5.1. Cell culturing

The B16F10 and the CT2A cancer cell lines were cultured in P100 plates with DMEM (Gibco, Billings, MT, USA) supplemented with 10% heat-inactivated fetal bovine serum (FBS), 2 mM of Glutamine (Gibco, USA), 100 units/mL antibiotics of penicillin and 100 µg/mL of streptomycin, and nonessential amino acids. The cells were then incubated in a humidified atmosphere with 5% CO_2 at 37°C until they reached 85 to 95% of confluence. The cultured cells were observed under a light microscope (Leica DMI 3000 B inverted microscope) to verify their growth, attachment and the achieved confluence. Cells were detached from culture palates using Trypsin-EDTA (Gibco) at the desired confluence, washed with phosphate buffered saline (PBS) (pH=7.4), centrifuged in 15 ml tube at 1500 (rpm) for 5 minutes, and subcultured according to specified dilutions for eventual usage. The cell lines were subcultured and stored at -80ºC after resuspending the cells pellet in DMEM supplemented with 10% FBS. Before storing cells at -80° they should be added to a solution of FBS and DMSO (9/1) then transferred to a freezer container for 24h in order to decrease the temperature gradually avoiding any cell damage.

5.2. Cancer cell treatment by magnetic hyperthermia using pulsed alternating magnetic fields

To assess the MHT therapeutic effects, both cell lines were seeded in P35 cell culture dishes in order to place them inside the coil and excite nanoparticles under AMF. The protocol, as illustrated in Figure 33, involves seeding of 1.6×10^4 cells/cm^2 for B16F10 and 3×10^4 cells/cm^2 for CT2A cells. The cell culture dishes were divided into four groups: cells without any treatment (−AMF−MNP), cells exposed to AMF without nanoparticles (+AMF−MNP), cells. Therefore, the cells were incubated at incubated with nanoparticles (−AMF+MNP), and cells incubated with nanoparticles and exposed to AMF (+AMF+MNP). Once the cells reached approximately 85% confluence, nanoparticles (APS- SPIONs) were added to the culture dishes (−AMF+MNP) and (+AMF+MNP) at different concentrations: 1 mg/mL and 4 mg/mL for 24

h and 2 h of incubation, respectively. Subsequently, the culture dishes (+AMF−MNP) and (+AMF+MNP) were placed within the solenoid coil under the AC external magnetic field set at TS/SN for 2.14 mT/200 kHz, TP/SN for 2.78 mT/300 kHz, and TR/SN for 3.42 mT/300 kHz during an exposure period of 30 min. The treatment time in our study was applied for 30 min to prevent extreme coil overheating and damage to the system. All experiments were initiated at 37°C, which is the body's physiological temperature. The frequency and amplitude of the nonharmonic signals (TR, TP, TS) were chosen based on the values that resulted in the highest increase in temperature inside the cell culture medium (1–1.5°C) in the presence of APS-SPION and, therefore, the same frequency and amplitude parameters were set for their corresponding harmonic signals (SN).

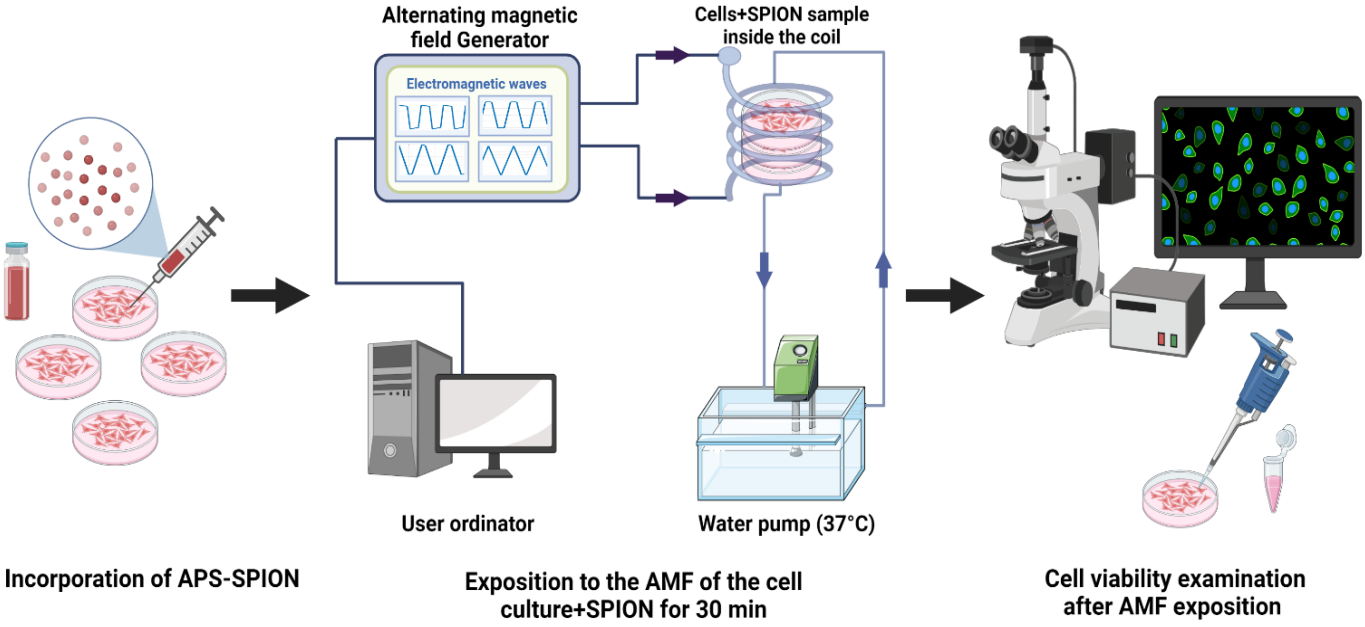

Figure 33: Experimental protocol to apply MHT in vitro.

5.3. Combination of chemotherapy and magnetic hyperthermia treatment using pulsed alternating magnetic fields

To evaluate the increase of the therapeutic effect by combining chemotherapy with MHT against glioblastoma cells, in vitro experiments were performed under an AMF at 200 kHz and 2 mT, with 30 min of exposure for each hyperthermic cycle and 45 min of rest between the two exposures. CT2A cancer cells were seeded in P35 dishes at 3×10^4 cells/cm^2 and cultured for 24 h. The cell culture dishes were divided into different experimental groups: the control group

without any treatment, the group treated with magnetic field and chemotherapy (AMF+5-FU), the group treated with nanoparticles only (APS-MNP), the group treated with chemotherapy only (5-FU), the group treated with MHT alone (2 cycles MHT), and the group treated with MHT plus chemotherapy (2 cycles MHT+5-FU). Once cells reached 85% of confluence in culture dishes, APS-MNP were added at 1 mg/ml to the group treated with only MNP and the group treated with chemo-magnetic hyperthermia, while 5-FU at 0.1 µg/ml was incubated with the group treated by only 5-FU, the group treated with AMF+5-FU and the group treated with chemo-magnetic hyperthermia. The in vitro treatment under AMF was initiated at 37°C.

5.4. MNPs cellular localization

To determine the localization of APS-SPION, an antibody targeted against lysosomes, anti-CD63 antibody (Abcam, Carlsbad, CA, USA), was used. B16F10 and CT2A cells were grown on coverslips at a density of 1.6×10^4 cells/cm^2 and 3×10^4 cells/cm^2, respectively, and incubated with 10.6 nm nanoparticles at 1 mg/mL for 24 h. Then, the cells were rinsed 3 times with PBS to remove the excess nanoparticles and fixed using 4% paraformaldehyde (Sigma-Aldrich, St. Louis, MO, USA) in 0.1 M phosphate buffer at pH 7.4 for 30 min at room temperature. The fixed cells were washed 3 times in PBS and blocked for 1 h with a PBS solution containing 10% horse serum (Gibco, Carlsbad, CA, USA) and 0.25% Triton X-100 (Sigma Aldrich, USA). Later, the cells were incubated overnight at 4°C with an anti-CD63 antibody diluted to 1:500 in PBS solution with 0.25% Triton and 1% horse serum. After removing the solution with the primary antibody and rinsing, samples were incubated with antirabbit Alexa Fluor™ 488 secondary antibodies (Abcam, USA) diluted to 1:500 in PBS solution with 0.25% Triton and 1% horse serum for 30 min at room temperature. Finally, after staining, the coverslips were washed with distilled H_2O, allowed to dry, and mounted with ProLong (Invitrogen, Eugene, OR, USA).

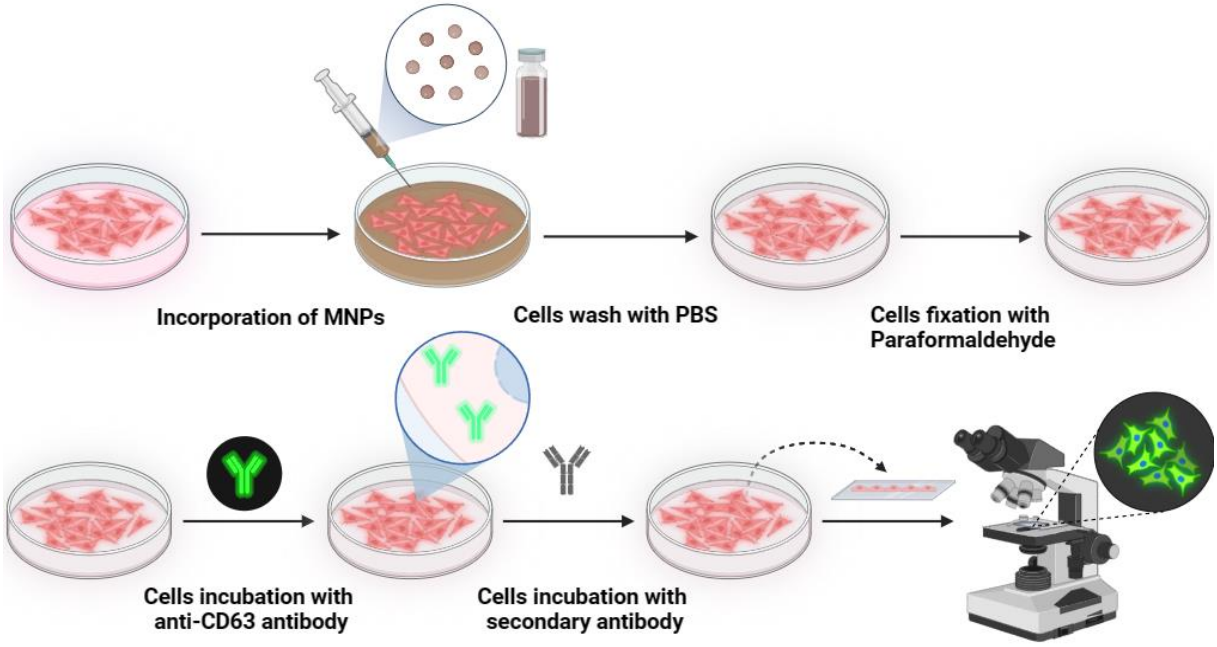

Figure 34: Protocol for MNPs cellular localization.

5.5. Cell viability analysis

5.5.1. MNPs cytotoxicity quantification

The potential cytotoxicity of the APS-SPION on B16F10 and CT2A cell lines was investigated using the XTT (2,3-bis-(2-methoxy-4-nitro-5-sulfophenyl)-2H-tetrazolium-5-carboxanilide) (AppliChem GmbH, Darmstadt, Germany) colorimetric assay to select the adequate APS-SPION concentrations to use during MHT in vitro tests. The XTT assay is a colorimetric method used to assess cell viability, proliferation, and cytotoxicity by measuring cellular metabolic activity. It utilizes the tetrazolium salt XTT (2,3-bis-(2-methoxy-4-nitro-5-sulfophenyl)-2H-tetrazolium-5-carboxanilide), which is reduced by mitochondrial enzymes in metabolically active cells to form an orange-colored, water-soluble formazan product. The intensity of the color, measured spectrophotometrically, is directly proportional to the number of viable cells (Berridge et al., 2005).

For the XTT assay, B16F10 and CT2A cells were seeded in 24-well plates at a density of 3×10^4 cells/cm^2 and 1.6×10^4 cells/cm^2, respectively, and incubated at 37°C for 24 h. Next, the cell culture medium was removed, and fresh medium containing 1 and 5 mg Fe/mL of APS-SPION was added for 6 h, 24 h, and 48 h. Untreated cells were used as controls. Later, the

medium was discarded, and the wells were washed twice with DMEM and incubated with 350 µL of XTT master mix for an additional 1 h at 37 ◦C. After that, the absorbance of each well was determined at 470 nm using an ELX808 microplate reader (BioTeK, Winooski, VT, USA) to estimate the cell viability. The absorbance value of the control was equated to 100%, and all the rest of the values were calculated relative to the control. The assay was repeated in triplicate.

5.5.2. 5-FU and DMSO cytotoxicity quantification

The 5-FU cytotoxicity in CT2A cells was also determined using the XTT (2,3-bis-(2-methoxy-4-nitro-5-sulfophenyl)-2H-tetrazolium-5-carboxanilide) colorimetric assay. CT2A cells were seeded in 24-well plates at a density of 3×10^4 cells/cm^2 and grown for 24 h. Cells were then treated with 0.1, 0.125 and 0.2 µg/ml of 5-FU and dimethyl sulfoxide (DMSO) for 48 h and the untreated cells were used as control. The assay was repeated in triplicate. Later, the wells were washed twice and incubated with 350 µl of XTT master mix for an additional 1 h at 37°C. The assay was repeated three times (n=3).

5.5.3. Fluorescent microscopy for cell death analysis

Fluorescence microscopy is a widely used optical technology that was invented in the early 20th century. To determine cell viability by fluorescence microscopy, a fluorescent dye is injected in the cell sample for evaluating the physio-pathological status and cell response to external stimuli, as well as therapeutic strategies. The phenomenon of fluorescence takes place when a substance called a fluorochrome absorbs light of a specific wavelength, causing the excitation of electrons from the fundamental energy level to an excited level. Then the electron returns to its fundamental energy level, emitting an energy-transferred wave whose length varies from 2 nm to more than 1 mm. This stimulated fluorescence emission can be visualized by fluorescence microscopy, whose resolutions are related to the properties of both the light and the fluorochrome used. Applied to cell viability assays, cells are labeled with fluorochromes and can be biochemically monitored for cell viability using fluorescence microscopy for the analysis of fluorescence emission characteristics, while the intracellular localization could also be identified. Fluorescent microscopy provides us information on cell numbers, proliferation, morphology, cell membrane integrity and allows for the tracking of single protein molecules in living cells, the determination of organelle morphology in tissue sections, the mapping of particular antigens and proteins in cells and tissue assemblies.

In a fluorescence microscope, the illumination is provided by a powerful light source, such as a mercury-vapor or a xenon arc lamp, or in some cases, by a laser that emits monochromatic light. In addition, it contains an excitation filter and an emission filter. The excitation filter transmits only light that is able to excite the specimen with its particular dye. The light emitted by the specimen has to pass through the emission filter before it reaches the detector. The emission filter is only translucent for light with a distinct wavelength, like the light emitted by the specimen (M.J. Sanderson, 2014)

Figure 35: DMI 3000B Fluorescence Microscope.

5.5.3.1. Calcein/PI assay

In the next section, we present the procedure employed for cell viability examination after the hyperthermic treatment on our cell lines (B16F10 and CT2A) exposed to TP, TS, and TR and compared to SN waveform using the same frequency and amplitude parameters for 30 min.
Calcein-AM and Propidium Iodide (PI) staining were used to qualitatively measure the cell viability after various hyperthermic treatments applied to the B16F10 and CT2A cell lines. Cell viability was measured by determining the percentage of alive/dead cells relative to the total number of cells in the P35 dish. The cells were incubated for 15–20 min, with the two

fluorescent markers Calcein-AM for labeling viable cells and PI for staining the nucleus of dead cells. Observations and image acquisitions were carried out using the DMI 3000B Fluorescence Microscope (Leica, Nussloch, Germany). Calcein-AM is a hydrophobic fluorogenic compound that passively crosses the plasma membrane of cells. Once in the cytoplasm, intracellular esters hydrolyze Calcein-AM to a fluorescent green derivative in viable cells (Johnson et al., 2013). Propidium iodide is a red fluorescent nuclear marker impermeable to the cellular membrane. Therefore, the nuclei of cells with damaged membranes (necrotic cells) will be stained with this dye (Arndt-Jovin & Jovin, 1989). The cells were hence stained with a combined solution of 0.5 µM Calcein acetoxymethyl (Invitrogen, Eugene, OR, USA) and 0.75 µM Propidium Iodide (Sigma-Aldrich, St. Louis, MO, USA) prepared in DMEM for approximately 10-15 min at 37°C. Cells were imaged after incubation with the imaging system of the Fluorescence Microscope. The excitation light wavelength for Calcein-AM and PI was 495 nm and 535 nm, and the emission light wavelength was 515 nm and 617 nm, respectively. To illustrate the results obtained, the GraphPad Prism and ImageJ programs were implemented. We selected this technique to evaluate cell viability rather than others like XTT because it allows us to observe modifications in cell morphology. Cell viability of the −AMF−MNP group was measured for the sake of comparison with the other predefined groups (+AMF−MNP, −AMF+MNP, +AMF+MNP), while the cell viability of the +AMF+MNP group, using sinusoidal signal (SN), was evaluated for comparison with the +AMF+MNP group using the non-sinusoidal signals (TP, TS, TR).

5.5.3.2. Annexin V/PI assay for apoptosis and necrosis analysis

CT2A cell death apoptosis or necrosis was determined using Annexin V (ABCAM, Cambridge, UK) and Propidium Iodide (Sigma-Aldrich) for staining apoptotic and necrotic cells, respectively. Twenty-four hours after treatment, the cells were washed twice with PBS and once with 1×binding buffer. Then, the cells from each group were stained with Annexin V and PI for 15-20 min in the dark at room temperature, followed by Hoechst staining to visualize the nuclei. Annexin V is a green fluorescent protein that binds to the amino-phospholipid phosphatidylserine on the plasma membrane's inner layer, which is externalized to the membrane's outer layer during apoptosis, allowing the detection of apoptotic cells before they lose membrane integrity. The analysis of stained cells and image acquisitions was carried out using the fluorescence microscope (Leica DMI 3000B). The excitation light wavelength for Annexin V, Hoechst and PI was 649 nm, 350 nm and 535 nm, respectively, while the emission

light wavelengths were 670 nm, 461 nm and 617 nm, respectively. ImageJ and GraphPad Prism programs were used to illustrate the results.

5.6. Calreticulin Immunocytofluorescence analysis

Immunocytofluorescence analysis was used to assess the CRT protein expression in CT2A cancer cells. Cell samples of the experimental groups (control, AMF,5-FU, MNP, 2 cycles MHT, 2 cycles MHT+5-FU) were washed and fixed using 4% paraformaldehyde (PFA, Merck) in 0.1 M phosphate buffer at pH 7.4 for 20 min at room temperature. Cells were than washed 3 times in PBS and blocked using 10% horse serum (Gibco/Life Technologies) for 30 min. Later, the cells were incubated overnight at 4°C in the dark with an anti-CRT antibody diluted to 1:400. Finally, the samples were rinsed and incubated with anti-FITC secondary antibody diluted to 1:400 in PBS for 1 hour at room temperature.

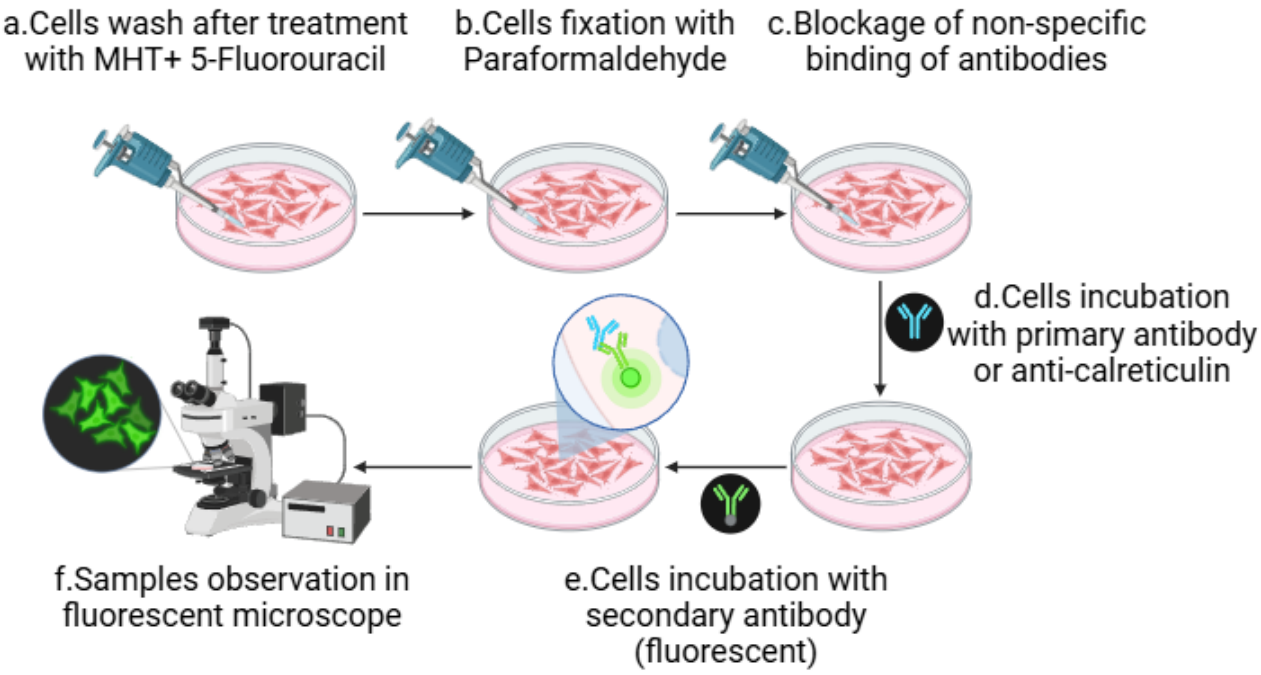

Figure 36: Protocol of CRT immunostaining in CT2A cancer cells after treatment.

6. Protocol for in vivo MHT treatment

6.1. Mouse model

C57BL/6 mice were maintained under controlled conditions of temperature, humidity, food and water in the animal facilities of the CTB (ES280790002070). Three-month-old mice weighing approximately 30 g and their lengt between 12 to 15 cm (with the tail) were used in all in vivo experiements. All the procedures were conducted in compliance with local and national ethical and legal regulations and authorized by the Ethical Committee of the Universidad Politécnica de Madrid, by the regional government of Madrid (authorization number PROEX 149.3/22), and according to the Animal Research: Reporting In Vivo Experiments (ARRIVE) guidelines. The inbred strain of C57BL mice was created by Clarence Cook Little (1881-1971) at the Bussey Institute for Research in Applied Biology. It is widely used in research and is the second mammalian species, after humans, to have its whole DNA sequenced (2002). As a result, its genetics are well characterized, making this mouse strain a great candidate for human disease research studies. C57BL/6 mice have almost brown or black coats. They are more sensitive to sounds and odors, and they bite more frequently than more docile laboratory strains like BALB/c.

6.2. MHT device safety

In order to evaluate the safety of the equipment for in vivo applications and ensure that the new non-sinusoidal waveforms do not induce any lethal damage inside the mouse body, we exposed mice to AMF using the most effective signals with the highest slopes (TS and TP). Two groups of two mice each one, were used for this assay, the first group were exposed to the SN waveform and the second group to the TS waveform, at 200 kHz and 2.14 mT for 30 min of exposure. Thus, each C57BL/6 female mouse was placed on a PLA bed and positioned inside the coil after being anesthetized with 20 µl of cocktail of ketamine (100 mg/kg) and xylazine (10 mg/kg) via intraperitoneal injection. The mice were maintained at their physiological temperature of 37°C during all experiments by the PLA holder connected to the water bath as described in the previous section for in vitro tests. This test was repeated as follows:

- First test, two exposures of 30 min separated by one week.
- Second test, three exposures of 30 min separated by 24h.

Figure 37: Anesthetized C57BL/6 mouse positioned inside the coil for AMF exposure.

6.3. Hyperthermia treatments

In vivo MHT tests using non-sinusoidal signals for MNPs excitation were carried out for the purpose of increasing the therapeutic effect in reducing the tumor size and eliminating the tumor growth compared to the sinusoidal signal. Therefore, an in vivo melanoma model was generated by injecting B16F10 cells subcutaneously into the right leg of the mice (Balivada et al., 2010). For the experiments, 5×10^5 viable tumor cells dispersed in DMEM supplemented with 10% FBS were inoculated subcutaneously into the leg of anesthetized C57BL/6 mice. Tumors became measurable by a digital caliper within 7 days. At that time, the mice were divided into six groups (two mice per group) as follow:

i) Untreated group or control.

ii) MNPs group: mice received MNPs via intratumoral injection

iii) Treated group with AMF: two mice were exposed to SN signal at 200 kHz and 2 mT.

iv) Treated group with AMF: two mice were exposed to TS signal at 200 kHz and 2 mT.

v) Treated group with MHT : mice received MNPs via intratumoral injection and exposed to TS signal for 30 min at 200 kHz and 2 mT.

vi) Treated group with MHT : mice received MNPs via intratumoral injection and exposed to SN signal for 30 min at similar conditions of TS, for comparision, 200 kHz and 2 mT.

To start the treatment, the MHT device was regulated to maintain mice temperature at 37°C. On the first day of treatment (Day 0), mice were anesthetized with 20 µl of a mixture of ketamine (100 mg/kg) and xylazine (10 mg/kg) via intraperitoneal injection. Subsequently, the mice in groups (ii) (v) (vi) received MNPs by injecting 10 µl of APS-SPION of 8.3±2 nm and 25.5 [Fe] mg/ml, intratumorly into the mice leg using sterile syringe of 1 ml. Later, the mice of groups (v) (vi) were sequentially exposed to AMF for 30 min, immidiately after MNPs injection. Groups (iii) and (iv) were only anesthetized and exposed to AMF, for further evaluating device safety, while the control group were only anesthetized and did not received any posterior treatment. The tumor size was monitered each session before treatment, using a digital caliper in the 3 dimensions to measure, the height, width and legth of the tumor in centimeter (cm). The treatment process was repeated six times, day (0), day (2), day (4), day (6), day (12) and day (14), as seen in Figure 38. One week later, the mice were euthanized, and the tumors were dissected, measured in three dimensions, and weighed. Histological analysis on tumoral tissues sections has not been performed due to the dark appearance of the tissues caused by the brown color of the MNPs.

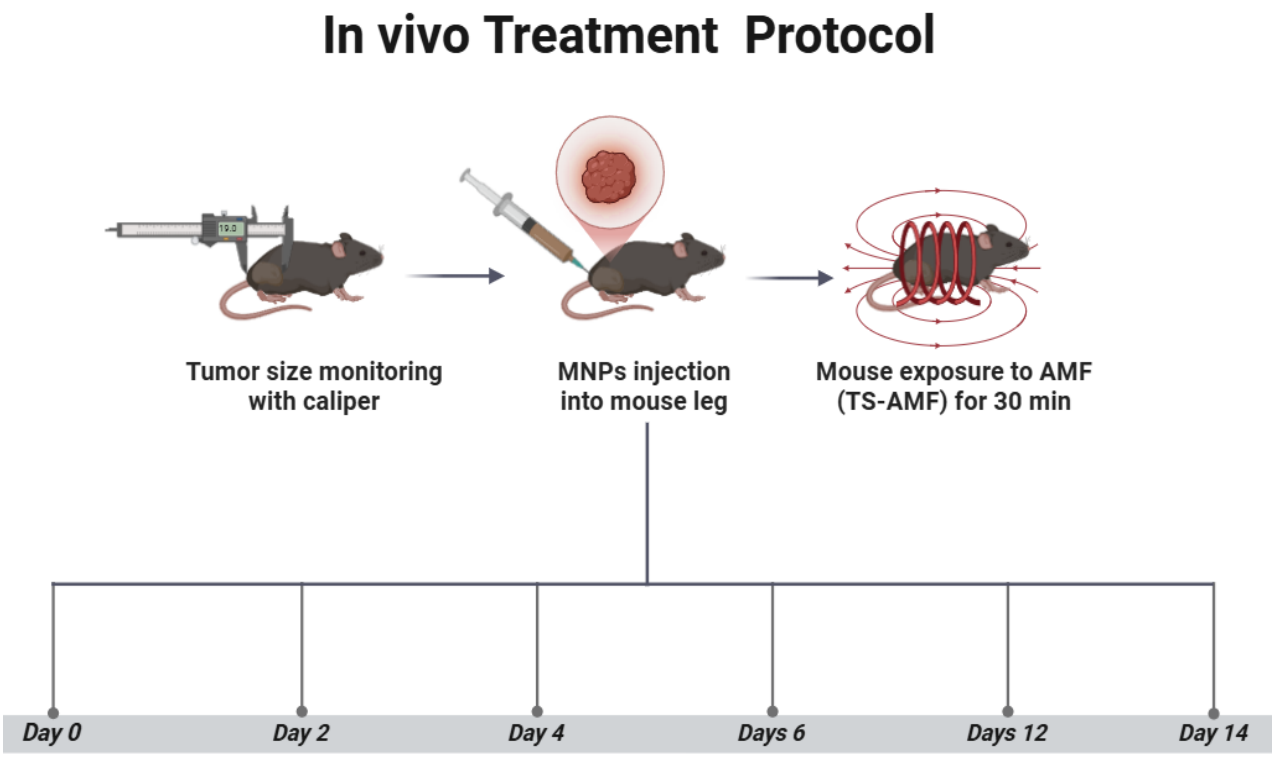

Figure 38: Schematic representation of the protocol applied in in vivo hyperthermia treatments in a C57BL/6 melanoma mouse model.

7. Nanorobotics anti-tumoral treatment (magneto-mechanical destruction):

7.1. Magnetic particles used

For Nanorobotics the microparticles used for experiments were purchased from Chemicell GmbH, Berlin, Germany, These particles are: SiMAG-MP-DNA and SiMAG-K-DNA .

- SiMAG-MP-DNA

This type of particles presents a core of magnetite [Fe3O4] , a size of 2-10 µm and a coating of porous silica. The particles are biofunctionalized with functional groups of Silanol (-Si-OH).

- SiMAG-K-DNA

The composition of this microparticles is quite similar to SiMAG-MP-DNA. They present a core of magnetite [Fe3O4] and a coating of porous silica with silanol as their functional group. They are superparamagnetic and their size is 1 µm.

7.2. Nanorobotic device

This part of study aim to employ the coaction between magnetic particles and AMF in an alternative way to treat cancer cells, without producing any temperature increase, and then to evaluate the treatment effects in comparision to MHT treatment.

7.2.1. First set-up model

The nanorobotics system used for this study was built and designed in the laboratory of Bioinstrumentation and Nanomedicine of the CTB. The equipment used is intended to generate linear movement of MMPs once they are exposed a to magnetic field gradient. In order to generate the force into the particles, the equipment uses two permanent coils that produce a constant magnetic field and a gradient coil made by two Maxwell coils to generate the homogeneous gradient magnetic field as shown in Figure 39. The system is able to generate six signals which are, sinusoidal, square, sawtooth positive, sawtooth negative, trapezoidal and triangular plus frequencies from 1Hz to 50 Hz. The generation of the six AMF signals was based on sine pulse width modulation (SPWM) method that allows the variation of the duty cycle at each pulse generation changing the output signal. Moreover, during the experiments,

cells are placed on a hollow container that will contain running water at a constant temperature of 37ºC (Thermomix BU, B. Braun, Melsungen, Germany). In addition to that, an AMF generator is coupled to the Maxwell coils so that it is possible to vary the frequency or waveform of the magnetic field. The constant magnetic field of 100 mT will magnetize the MMPs, allowing them to be moved by the gradient magnetic field. The gradient magnetic field is generated by two Maxwell coils in such a way that each coil has the same amplitude of current flow as the other coil, but in the opposite direction. The heat produced by the coils or by the particles can induce cellular death via hyperthermia, which is not the goal of this experiments. Thus, sample heating must be avoided. The equipment has already been tested in order to observe if heat was generated. The magnetic field was applied at 7 A and 1 Hz for 2 hours to two control samples; water alone and water containing MMPs at a concentration of 0.05 mg/ml. No difference between samples was observed, meaning that the MMPs don't induce heat at such a low frequency of the AMF. Thus, a reduction in cell viability cannot be caused by hyperthermia.

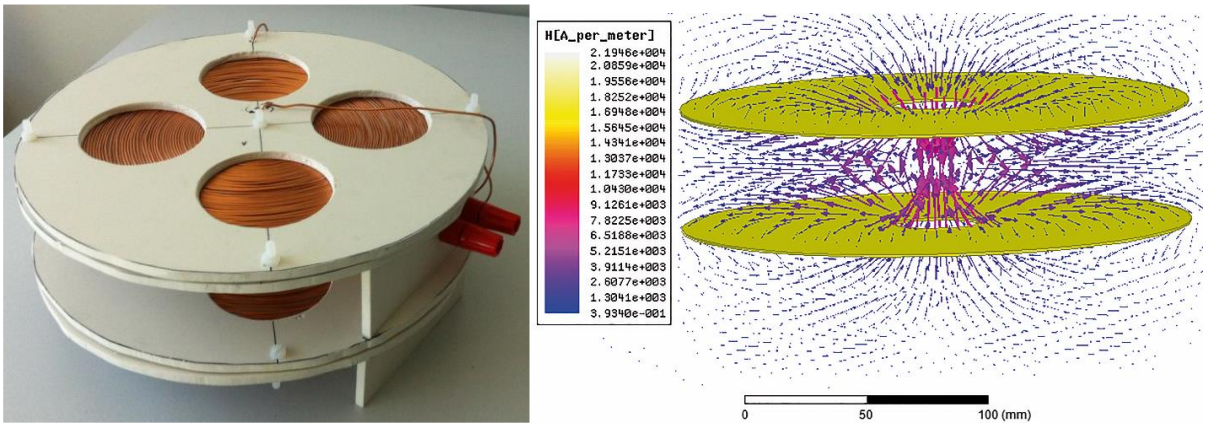

Figure 39: Maxwell coils used (left). Gradient magnetic field flow generated by the Maxwell coils (right).

Regarding the electronics of the equipment, a full-bridge inverter is used to generate the different waveforms. It is composed of four IGBTs semiconductors distributed in diagonal pairs that form two branches. When one branch is activated (closed) and the other one opens, current will flow in one direction. To make the current flow in the opposite direction, alternate the switching on and off of the branches. That switching on and off is controlled by a STM32F446RE board (referred as nucleo). A gate driver (SI8233BB) is required to amplify the output voltage from the nucleo (3.3 V) to the 12 V required from the semiconductors. Different

waveforms are generated when inducing a phase delay on the switching on and off of semiconductors from the same branch. The Maxwell coils are placed in series on the middle of the two branches of the full-bridge inverter. A power supply provides the circuit with the current required to generate the magnetic field (EA-PS 2042- 10B Bench Power Supply, EA Elektro-Automatik, Viersen, Germany).

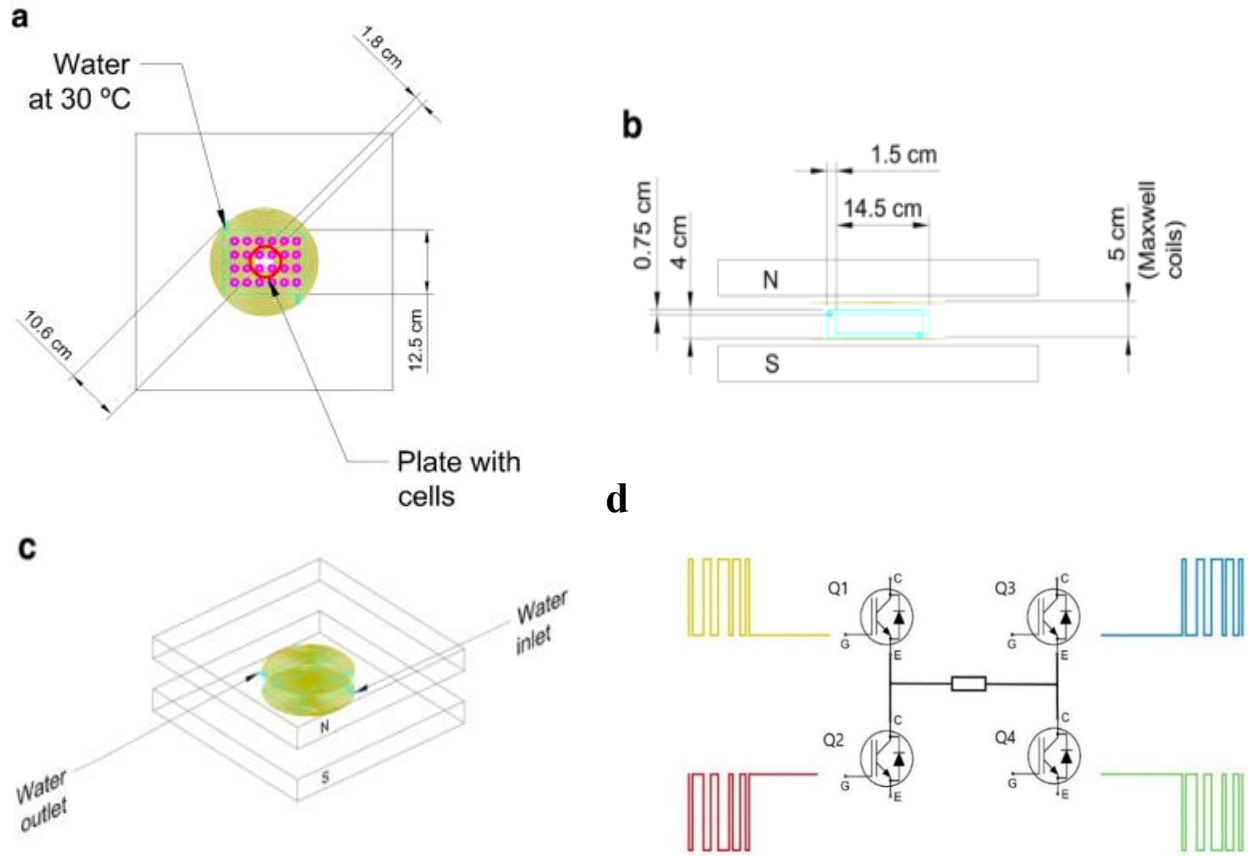

Figure 40: Maxwell coils and permanent magnet (100 mT). The cell culture plate was maintained under stable conditions by a flow of water at 37 °C. Top view, where the wells (purple color) are inside the water jacket (cyan color) (a). Only wells inside the red circle are used in this work. Front view of the equipment with its dimensions (b). Isometric view, where the arrows indicate the water inlet and outlet in the water jacket (c). Low frequency IGBTs on time (d).

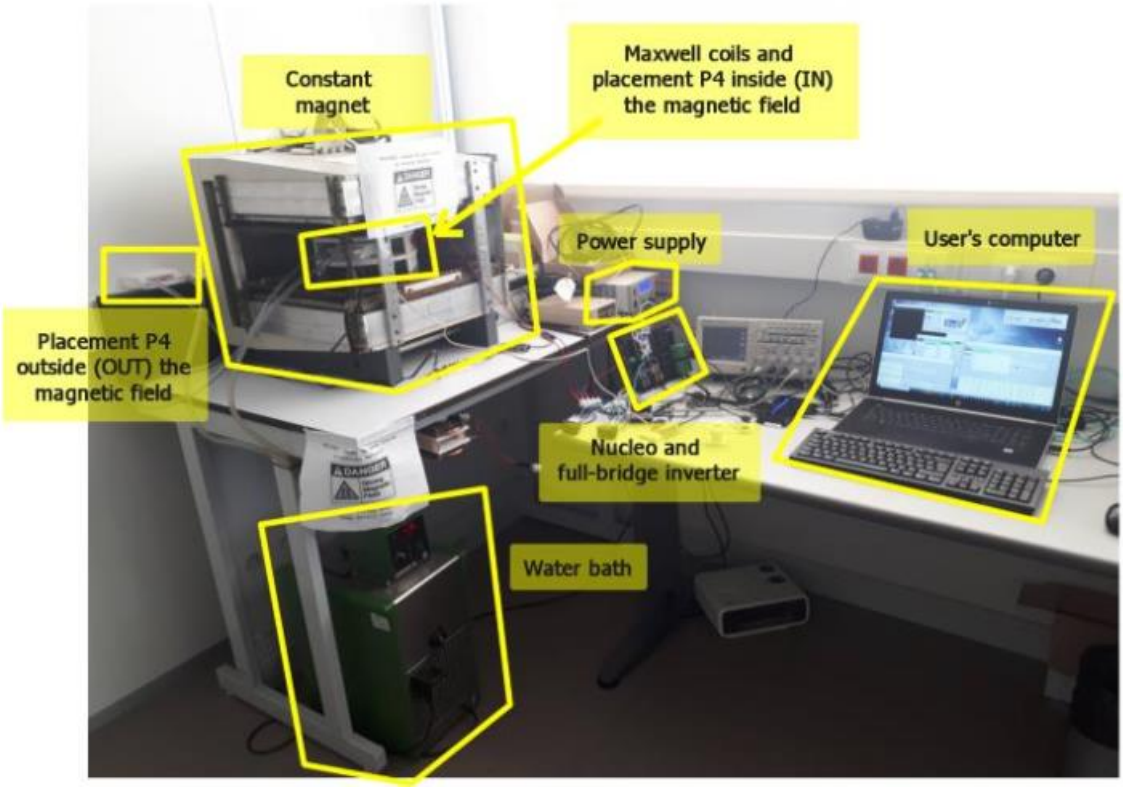

Figure 41: Nanorobotic device for magneto-mechanical cells destruction.

7.2.2. In vitro treatment protocol

For nanorobotic experiments, we used B16F10 cancer cells. Thus, we utilized the results previously obtained as by (Amaya-Jaramillo et al., 2017) as a starting point, where they tested different parameters that might influence the antitumoral therapy performance. First of all, the incubation time with the particles was tested at 3, 6, 12 and 24 hours, showing that 24 hours had a better performance due to higher particle internalization. Then, the exposure time to the magnetic field was studied. Experiments performed at 30 min and 60 min of exposure time showed better results for the larger time. Moreover, two current waveforms that generate the magnetic field were tested; square and sinusoidal. Square waveform has a better performance. The sharper slopes on the square signal may produce faster and more abrupt movements of the particles, inducing more damage to the cellular membranes. The frequency will affect to the particle movement too, meaning that this parameter will have an effect on the cellular viability. Frequencies of 1 and 10 Hz were tested, showing a better performance for the lowest frequency. This may be since at 10 Hz, the particles move up and down so fast that they don't have time to be in touch with the top and bottom of the lysosome, only performing their movement inside of this organelle and therefore not damaging the membrane. Furthermore, particles of different

sizes (2 µm, 500 nm, and 300 nm) at different concentrations ranging from 0.025 to 0.1 mg/ml were tested. The biggest particles at the highest concentrations achieved the lowest cellular viabilities.

The B16F10 cancer cells were cultivated in plates of 4 wells or P4 at a density of 5 x 10^4 cells/cm^2. Two groups have been prepared, the first group to be placed inside the coil for 1 h of exposure and the second group to be kept outside the coil and maintained at 37°C. Each group includes two conditions: the control (untreated), and the treated group with three different MMPs ceoncentration each well. 24h later, when cells reach 85-95% of confluence, the cells were incubated with SiMAG-MP-DNA and SiMAG-K-DNA MMPs at three different concentrations 25µg/ml-50 µg/ml-100 µg/ml for other 24 h. Next, the first group was placed inside the coil for irradiation during 1 h at 1 Hz of frequency with square signal. Cell viability was analyzed 24 h post-treatment using Calcein/PI fluorescent staining and cells death were observed under fluorescent microscope.

8. Statistical analysis

Cell viability for both assays was calculated according to the following formula:

$$Cell\ viability = \frac{Average\ absorbance\ of\ treated\ cells}{Average\ absorbance\ of\ control\ cells}\ x\ 100$$

The obtained data were statistically analyzed using the software package GraphPad Prism Version 8.0.1 for Windows. Data were tested by Shapiro–Wilk test for normality and presented as mean ± SEM (n = 3). The differences between data groups were calculated using the ANOVA test, considered statistically significant at $p < 0.05$.

IV Chapter 4: Results and Discussion

1. Safety of the pulsed electromagnetic fields device

In MHT treatments, all samples must be thermally isolated, especially from the solenoid coil that experiences significant heating during the EMF exposure. In order to demonstrate that the cell killing effects during MHT treatment are only produced by MHT treatment, and not by the coil heating, thus a PLA sample holder connected to the water pump was designed to keep the temperature of the samples (cells or mice) stable at 37°C during AMF exposure.

For in vitro assays, the cells were cultured in petri dishes of 35 mm and placed inside the holder. The temperature of the culture dishes was measured throughout AMF exposure using an optical temperature probe immersed in the medium. A second optical probe was placed within a beaker of water at room temperature. Figure 43 represents the temperature variation during the AMF exposure using TP signal (2.78 mT/300 kHz), TS signal (2.14 mT/300 kHz), and TR signal (3.42 mT/300 kHz) for 30 min. In all cases, no increase in temperature was observed during the exposure to any type of AMF waveform. The temperature of the sample remains stable at around 37°C during the AMF exposure, as shown in Figure 42.A, proving to be adequate thermal isolation. In Figure 42, a thermal image of the coil and sample holder was taken during AMF exposure demonstrating also shows a stable temperature of the sample at 37°C while the coil reached a temperature of 86°C. Hence, the sample is isolated from the superficial thermal interferences. The use of low amplitude values will not significantly affect the generation of heat since it has been demonstrated that signals with high slopes could induce higher power losses without the need to use very high magnetic field amplitudes (Rosales et al., 2016).

A **B**

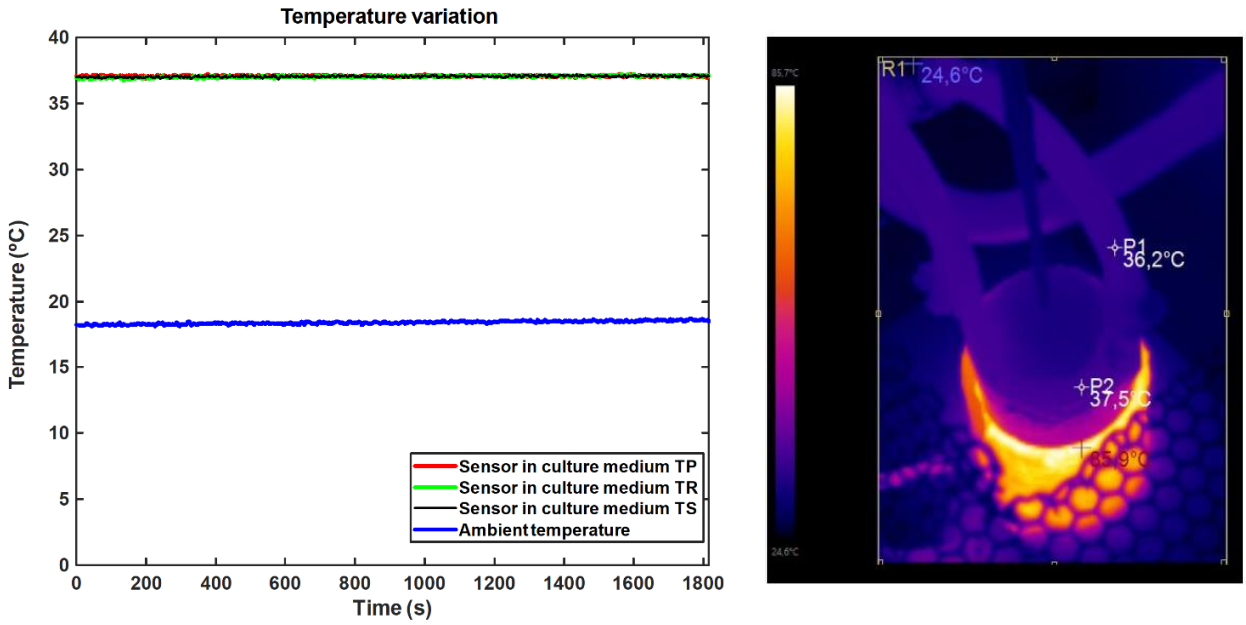

C

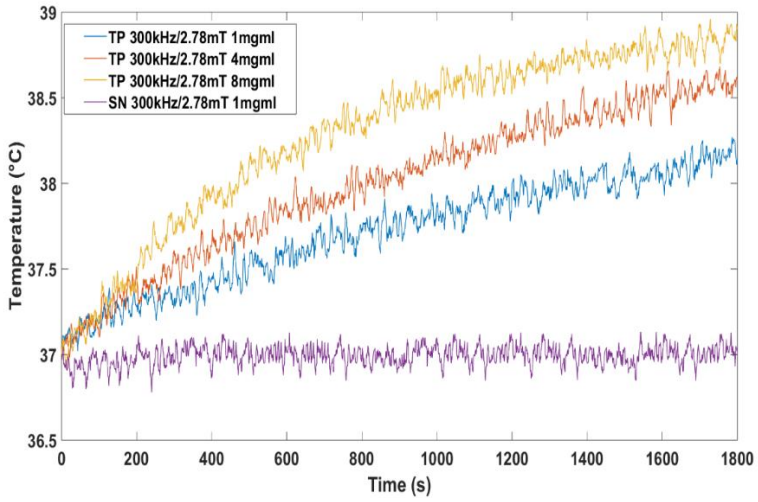

Figure 42: Data of temperature measurement during hyperthermia treatment without APS-MNPs .The red, black, and green curves represent the cell culture medium temperature for different non-harmonic signals. The blue curve represents the room temperature (A). Thermal image of the coil and sample holder holding cell culture dishes during AMF exposure showing a stable temperature around 37°C for the sample holder, while the coil reached approximately 86°C(B). Temperature curves of APS-SPION measured with TP signal at different concentrations of 1mg/ml, 4mg/ml and 8mg/ml and with SN at 1mg/ml, both for 300 kHz and 2.78 mT for 30 min of exposure (C).

In order to define the optimum AMF parameters to initiate MHT treatment with cancer cells, we launched certain temperature measurements in the presence of MNPs. Figure 42.C

represents temperature curves of MNPs at certain AMF parameters, which are TP at 300 kHz / 2.78 mT for 1mg/ml, 4mg/ml and 8mg/ml and SN at 300 kHz / 2.78 mT for 1mg/ml. The results showed that the MNPs concentration increase did not significantly impact the temperature generation inside cell culture medium or DMEM of 1ml. The final temperature in cell culture medium measured by the optic fiber sensor, did not reach the hyperthermic interval [39-43°C]. The TP waveform gave an increase of 1°C, 1.5°C and 1.9°C at 1mg/ml, 4mg/ml and 8 mg/ml respectively. Comparing the final temperature of TP at 1mg/ml to SN for the same concentration, the TP waveform is more effective than the SN. However, the temperature data measured might be not accurate using an optic fiber sensor and more precise instruments are needed, especially, since some research have proven that local temperature measured in cell culture medium is not equal to the temperature at the surface of MNPs, and the further we get from MNPs surface, the lower temperature becomes (Gu et al., 2023).

For the purpose to determine any damage effects on cancer cells caused by the exposure to the non-sinusoidal signals (TS/TP/TR) and their safety of application, the viability of the cancer cells (B16F10 and CT2A) exposed to AMF in the absence of MNPs was assessed using a Calcein-AM/PI staining assay and compared to their corresponding controls (cells without AMF exposure). The results from the Calcein-AM/PI assay (Figure 43) show that the exposure to AMF did not affect cell viability in any of the AMF waveforms analyzed.

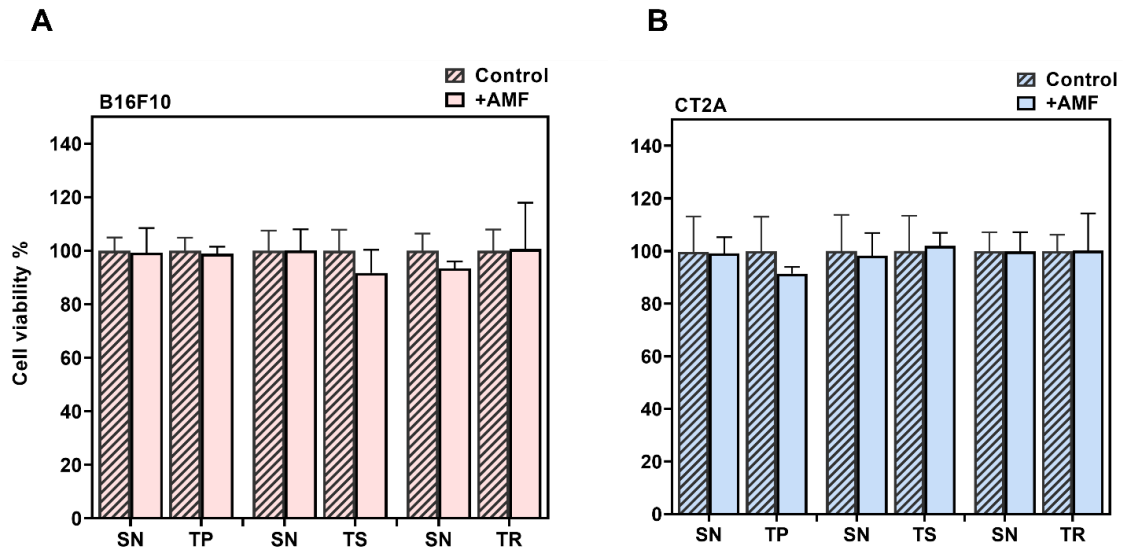

Figure 43: Determination of the safety of the MHT applicator using different signals. (A) B16F10 and (B) CT2A cell viability evaluated with Calcein/PI 24 h after different waveform AMF application for 30 min (+AMF) compared to cells not exposed to AMF (control). AMF waveforms SN: sinusoidal, TP: trapezoidal, TS: almost square, TR: triangular.

2. Viability of cells incubated with APS-MNPs

To determine the optimal concentration of APS-MNPs that would not affect cell viability, cells were incubated with several concentrations of MNPs, and the resulting cell viability was analyzed after various incubation times.

The cell viability results of B16F10 and CT2A cells incubated with APS-MNPs of 10.6 nm at 1 and 5 mg/mL are depicted in Figure 44. Both cell lines exhibited similar responses to the presence of MNPs, although CT2A cells showed lower cell viability when incubated with MNPs at 5 mg/mL for 24 h and 48 h compared to B16F10 cells. XTT results showed a non significant decrease in cell viability when both cell lines were incubated with MNPs at 1 mg/mL during all time periods tested. However, when cells were incubated with the APS-MNPs at 5 mg/mL, a significant reduction in cell viability was observed after 24 h and 48 h of incubation in both cell lines, whilst cell viability remained over 90% within 6 h. This could be explained by the fact that at 6 h, most MNPs remain trapped within endosomes, limiting direct contact with critical organelles like mitochondria or nuclei, preventing immediate toxicity (Feng et al., 2018) (Wei et al., 2021).

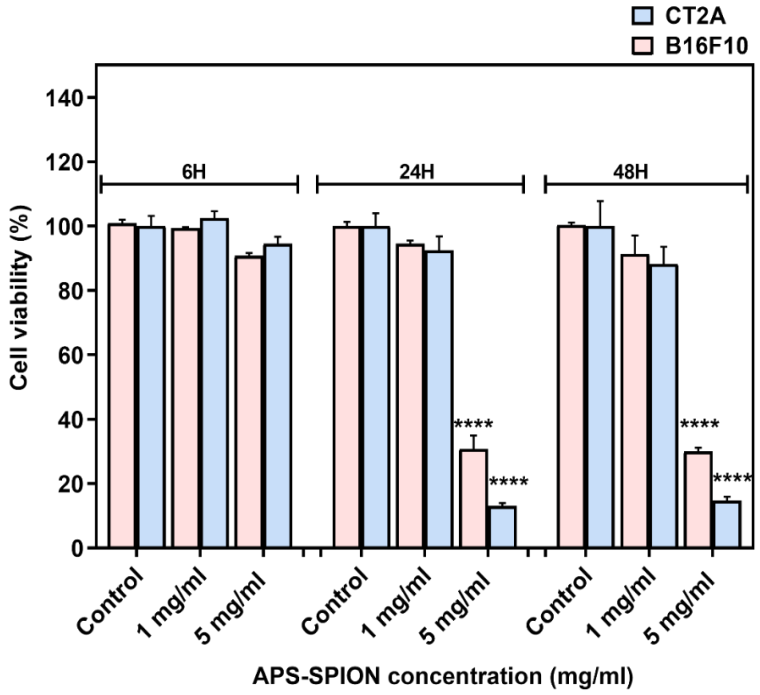

*Figure 44: B16F10 and CT2A cell viability evaluated by XTT assay after incubation with APS-SPION (10.6 nm) at 1 and 5 mg/mL for 6 h, 24 h, and 48 h. Data represent the mean ± SEM of three independent experiments (n = 3). ANOVA, post hoc Fisher's LSD test; **** $p < 0.0001$.*

During the study, two different sizes have been used, APS-MNPs of 10.6 nm were used during the study MHT effect using non-sinusoidal signals as the only treatment. And APS-MNPs of 8.3 nm were utilized for the combination treatment between MHT using the non-sinusoidal signal and chemotherapy. Hence, the cell viability results of CT2A cells incubated with APS-MNPs of 8.3 nm at 1 mg/m are depicted in Figure 45.

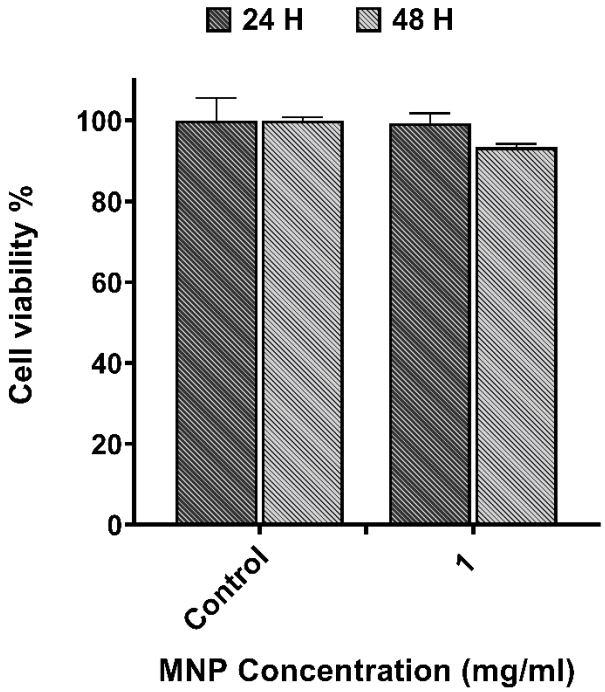

Figure 45: Cell viability of CT2A cancer cells incubated with APS-MNPs (8 nm) at 1 mg/ml for 24h and 48h revealed by XTT assay. Data represent the mean ± SEM of three independent experiments (n = 3). ANOVA, post hoc Fisher's LSD test.

3. 5-FU and DMSO toxicity

To define the toxicity of the therpeutic agent 5-FU within cells, the CT2A cells were incubated with 5-FU and its solvant DMSO, at different concentrations . The cytotoxicity results obtained from the XTT assay for 5-FU and DMSO within CT2A cells are represented in Figure 46. The DMSO toxicity was evaluated in parallel because it serves as a solvent for the preparation of the chemotherapeutic drug. The results showed non-significant cytotoxicity on CT2A cells 48h after incubation with 5-FU and DMSO at different concentrations of 0.1 µg/ml, 0.125 µg/ml and 0.2 µg/ml.

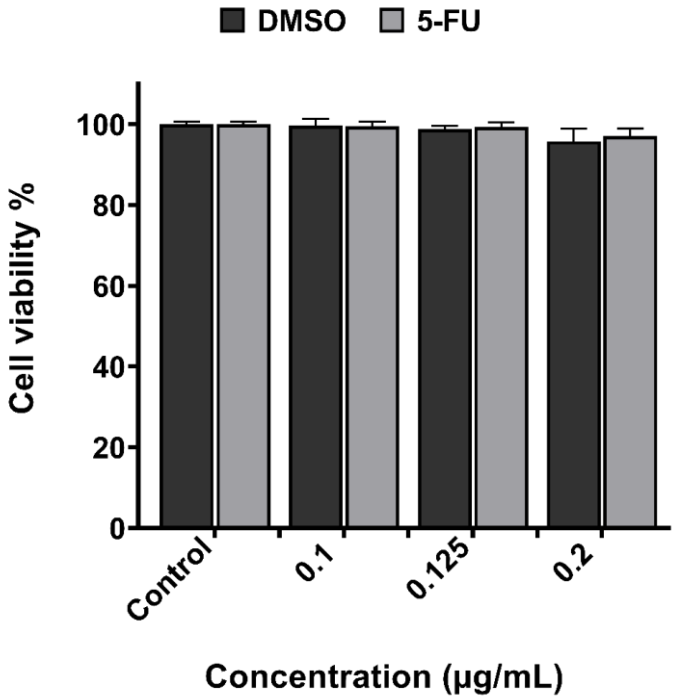

Figure 46: Quantification of cytotoxicity performed by the XTT assay of 5-FU and its solvent (DMSO) in CT2A cells 48h after incubation with different concentrations. Data represent the mean ± SEM of three independent experiments (n = 3). ANOVA, post hoc Fisher's LSD test.

4. Cell internalization of APS-SPION

The internalization of APS-SPION into cancer cells has been described previously across different cellular types (Fortes Brollo et al., 2018) (Sanz-Ortega et al., 2019), indicating that macropinocytosis is the primary mechanism by which the nanoparticles are internalized inside cells and that the APS coating does not induce any endosome/lysosome damage (Portilla, Mulens-Arias, et al., 2022). To assess the internalization of the nanoparticles by B16F10 and CT2A cells in our study, the cells were preincubated with 10.6 nm APS-SPION for 24 h and evaluated by microscopy. APS-SPION accumulations were detected under bright field microscopy (Figure 47). Nanoparticles were observed outside and also inside the cells as black cytoplasmic spots of distinct sizes (arrows in Figure 47 A,D). Figure 48 shows the intracellular distribution of APS-SPION visualized in cells with strong labeling for lysosomes (Figure 47 B,E), as determined by immunostaining with the anti- CD63 green fluorescent antibody that specifically stains the lysosomes. The resulting image confirmed the presence of APS-SPION within the cancer cells. Our results from the internalization of MNPs in Figure 47 further support the previous research on cellular uptake of these nanoparticles directly inside cells

under a visible light microscope (Luengo et al., 2013) or by confocal microscopy, ICP-OES, TEM, and Prussian blue staining (Fortes Brollo et al., 2018) (Sanz-Ortega et al., 2019).An evident intracellular uptake of MNPs was observed by the images extracted from Calcein/PI staining consistent with other studies carried out in different cell lines (Luengo et al., 2013).

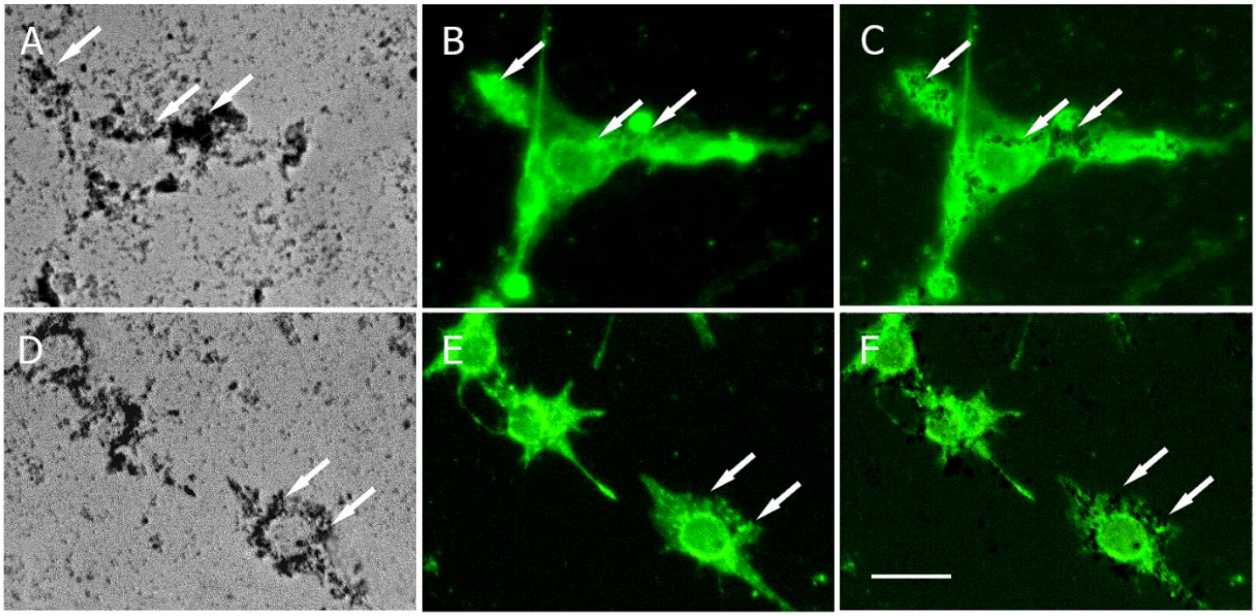

Figure 47: Cellular localization of MNPs in B16F10 (A–C) and CT2A (D–F) cells. Cells were incubated with MNPs for 24 h and then stained with an anti-CD63 to mark lysosomes. Photomicrographs show MNPs in bright field microscopy as black dots (A,D) and lysosomes by fluorescence microscopy, marked in green (B,E). Note that cells with strong lysosome labeling show large accumulations of MNPs (arrows). Panels (C,F) show the merged images from panels (A,B) and (D,E), respectively. Scale bar: 20 µm.

5. Evaluation of the in vitro magnetic hyperthermia treatment using pulsed alternating magnetic fields

In the interest of enhancing MHT treatment efficacy and raising the therapeutic effects against cancer cells, CT2A and B16F10 have been treated by MHT generated by non-sinusoidal signals (TS, TP,TR) for 30 min, in comparison to SN signal under the same treatment conditions. Cell viability results 24 h after MHT treatment of B16F10 and CT2A cells preincubated with MNPs at 1 mg/mL and exposed to the AMF for 30 min are depicted in Figure 48 A, C, respectively. The graphs show the cell viability with all the predefined experimental conditions (−AMF−MNP, −AMF+MNP, +AMF−MNP, +AMF+MNP). The cytotoxicity of APS-SPION on both cell lines evaluated by Calcein/PI was slightly different from those obtained with the

XTT results assay (Figure 44), but, still, MNPs were found to be not cytotoxic, with cell viability rates of more than 80% in B16F10 cells (Figure 48 A) and more than 90% in CT2A cells (Figure 48 C). This slight difference may be due to the different tests used. The cell viability of cells exposed to AMF alone remains, as well, higher than 80% with B16F10 and 90% with CT2A (Figures 48 A and 5C, respectively). These observations prove that the cell viability reduction observed after MHT treatments is produced by the effect of the combination of AMF and SPION. Cell viability after MHT treatment was clearly different between the treatment using non-sinusoidal signal (TP, TS, and TR) and sinusoidal signal (SN). The treatments using TP, TR, and TS exert a more efficient effect in damaging the cancer cells (Figure 48).

The application of AMF using non-sinusoidal waveforms (TP, TS, and TR) produced in both cell lines a greater decrease in cell viability compared to the application of SN waveform (Figure 48). The TP-AMF exposure of B16F10 loaded with 1 mg/mL APS-SPION produced a significant decrease in cell viability (53 ± 5%) compared to the application of SN-AMF that reduced cell viability to 89 ± 9% at 300 kHz/2.78 mT. TP was the most effective waveform in B16F10 cells (Figure 48 A). Cell viability was non-significantly reduced with the application of a TS-AMF (65 ± 14%) and SN-AMF (90 ± 0.8) at 200 kHz/2.14 mT, whereas the reduction in cell numbers was nearly equal by the application of TR-AMF and SN-AMF waveforms (over 80 ± 14%) at 300 kHz/3.42 mT. In CT2A cells, the AMF application to cells loaded with 1 mg/mL APS-SPION produced a minimal decrease in cell viability by both TP-AMF (83 ± 2%) over SN-AMF (95 ± 8%) at 300 kHz/2.78 mT and by TS-AMF (67 ± 7%) over SN-AMF (82 ± 4%) at 200 kHz/2.14 mT. The TR-AMF waveform was more effective on CT2A at 1 mg/mL and led to a significant cell viability reduction of 52 ± 6% over the SN-AMF (80 ± 11%) at 300 kHz/3.42 mT (Figure 48 C).

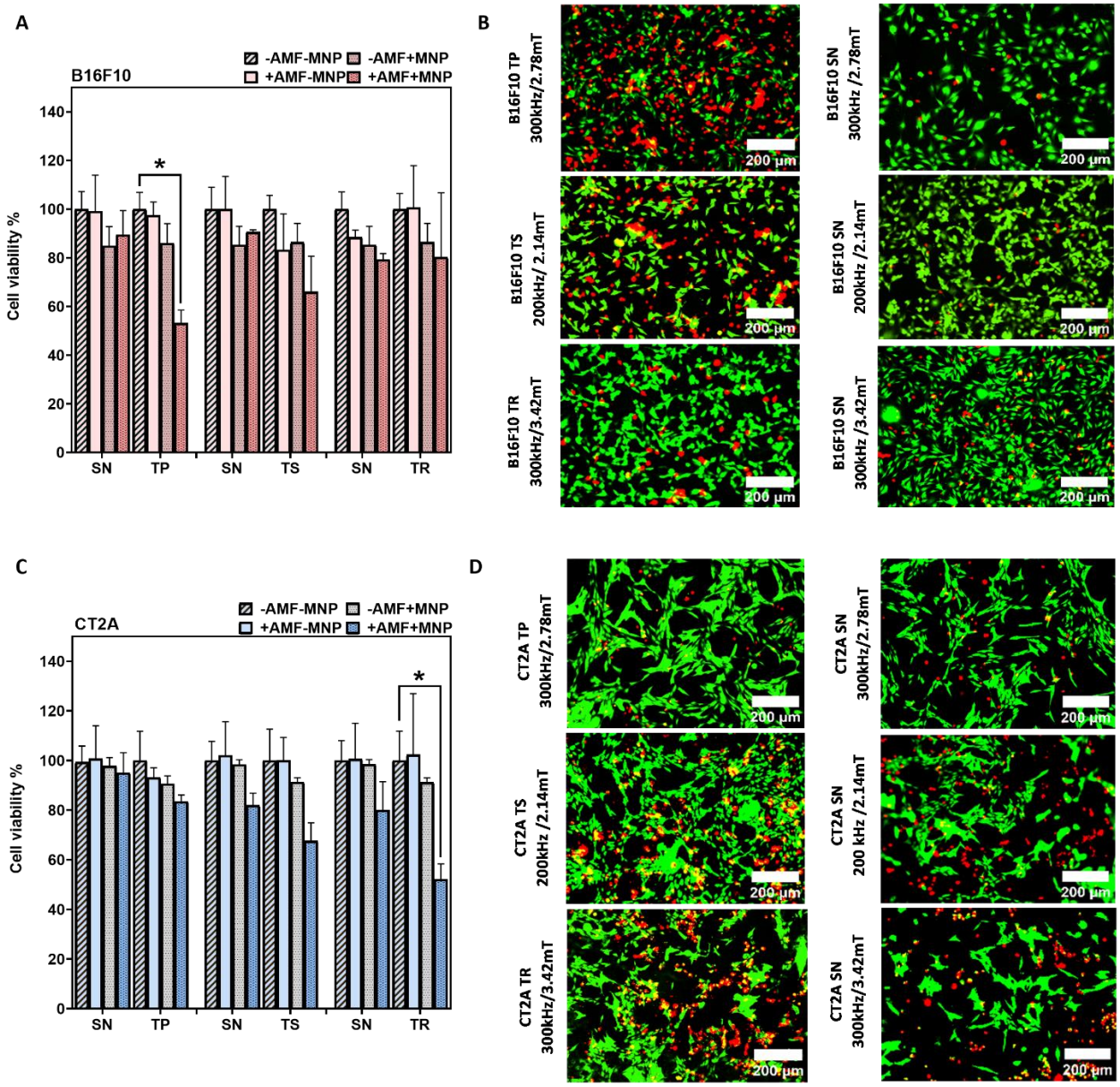

*Figure 48: Cell viability evaluation in B16F10 and CT2A cell lines after MHT treatments. Cell viability counting results obtained using fluorescence microscopy in B16F10 (A) and CT2A (C) cells preincubated with 1 mg/mL of APS-SPION and exposed for 30 min to different AMF signals (SN/TP: 300 kHz and 2.78 mT, SN/TR: 300 kHz and 3.42 mT, SN/TS: 200 kHz and 2.14 mT). Cells were stained with Calcein-AM and PI 24 h after MHT treatments. Live and dead cells were quantified by Image J software version 1.8.0 for each experimental condition. Representative images obtained by fluorescence microscopy of the treated group (+AMF+MNP) cells stained with Calcein (green) and PI (red) (B,D). Scale bar: 200 µm. ANOVA, post hoc Fisher's LSD test; * $p < 0.05$.*

The images of the treated groups +AMF + MNP in both cancer cell lines obtained by fluorescent microscope are presented in Figure 48 B,D to further corroborate the damage effects of the hyperthermic treatment in B16F10 and CT2A cells by the non-sinusoidal signals. In these images, live cells are shown in green and dead cells in red after Calcein-AM and PI staining, respectively.

To further evaluate the effects of MHT treatment with the non-sinusoidal signals on the cell damage, the same experiment was carried out in B16F10 and CT2A with higher concentrations of MNPs, and the cell viability was directly evaluated after the hyperthermic treatment (0 h). The concentration of MNPs was increased to 4 mg/mL, and the incubation time was reduced to 2 h to prevent any cytotoxic effect, according to previous cytotoxicity results obtained with APS-SPION (Figure 49). This hyperthermia treatment strategy was adopted in order to maximize the treatment quality in vitro and to achieve an effective and rapid cellular uptake of the MNPs. The results of Figure 49 show that the cell viability reduction generated by the application of non-sinusoidal signals was obviously superior with all waveforms (TP, TS, and TR) compared to the SN waveform. In contrast to Figure 49 A in B16F10 cells, the TR signal denoted the same mortality as the SN signal. The cumulative heat effect generated in cells by applying the MHT treatment planning at 4 mg/mL for 30 min of exposure to AMF was more efficient than by applying it at 1 mg/mL in most of the experimental cases.

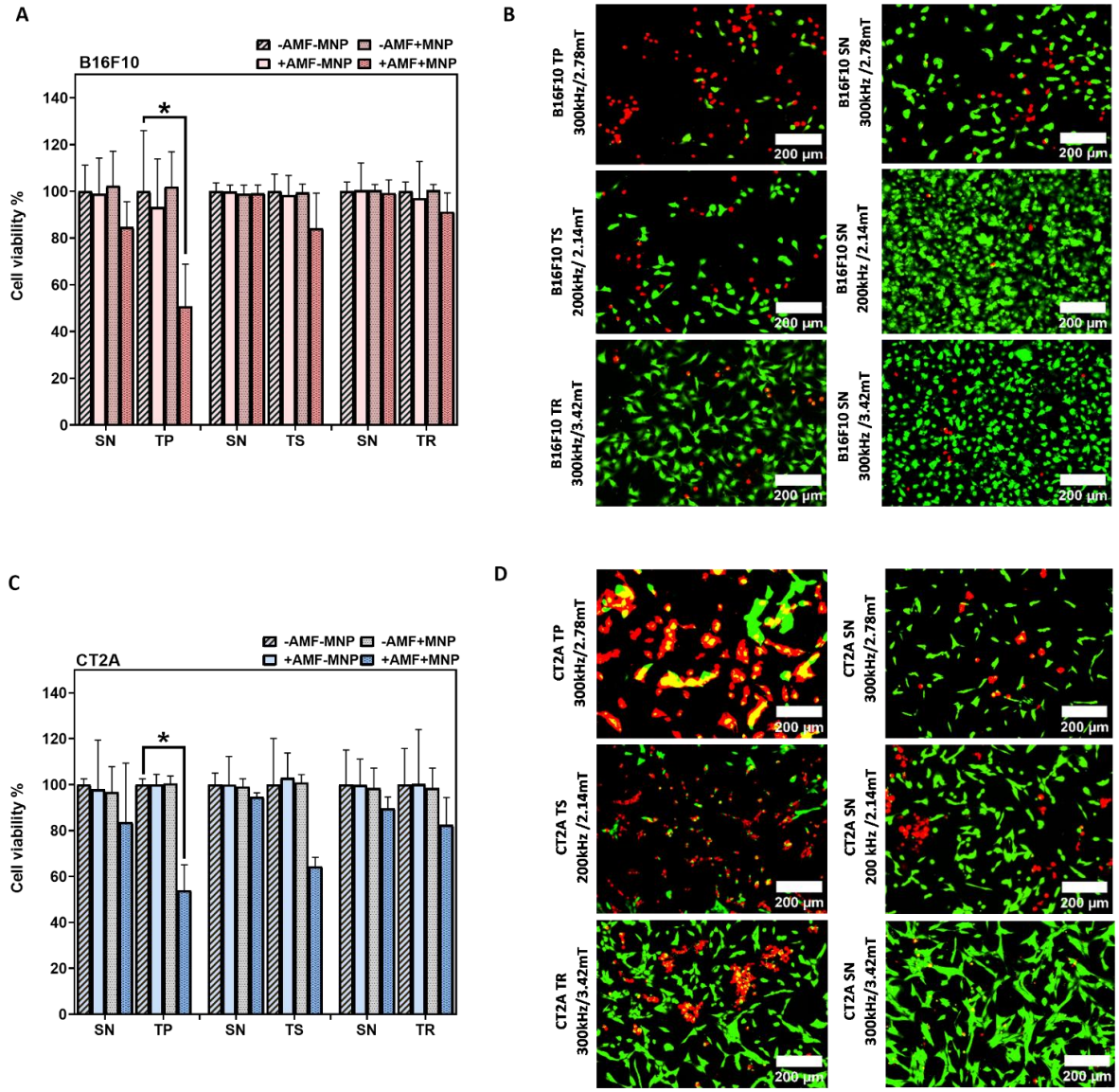

*Figure 49: After magnetic hyperthermia cell viability evaluation in B16F10 and CT2A cell lines. Cell viability counting results obtained using fluorescence microscopy with B16F10 (A) and CT2A (C) preincubated with 4 mg/mL of APS-SPION and exposed for 30 min to different AMF signals (SN/TP: 300 kHz and 2.78 mT, SN/TR: 300 kHz and 3.42 mT, SN/TS: 200 kHz and 2.14 mT). Cells were stained with Calcein-AM and PI directly after MHT treatments. Live and dead cells were quantified using Image J software version 1.8.0 for each experimental condition. Representative images obtained using fluorescence microscopy, of the treated group (+AMF+MNP) cells stained with Calcein (green) and PI (red) (B,D). Scale bar: 200 µm. ANOVA, post hoc Fisher's LSD test; * $p < 0.05$.*

Cell viability results after MHT treatment applied on B16F10 and CT2A cells preincubated with 4 mg/mL MNPs and exposed for 30 min to AMFs using different waveforms are shown in Figure 49. The graphs show the cell viability with all the predefined experimental conditions (−AMF−MNP, −AMF+MNP, +AMF−MNP, +AMF+MNP). No cytotoxicity was exerted by APS-SPION at 4 mg/mL, and cell viability was kept at around 96–100% for both cell lines. The exposure of cells to only AMF was shown to be safe as well, and the viability remained around 93–100%. Hence, a decrease in cellular viability greater than 7% is the result of the coaction between APS-SPION and AMF signals during MHT treatment. In Figure 49 A,C, the TP-AMF exposition of 4 mg/mL MNP-loaded B16F10 cells and CT2A cells induced a significant decrease in cell viability by 50 ± 18% and 53 ± 11% at 300 kHz/2.78 mT, respectively. Cell viability was non-significantly reduced by TS-AMF and TR-AMF over SN-AMF at 200 kHz/2.14 mT and at 300 kHz/3.42 mT, respectively, in both cancer cell lines. Again, the images of the treated group +AMF+MNP with B16F10 and CT2A cell lines obtained by fluorescent microscope are presented in Figure 49 B,D to further indicate the damage effects of the anticancer hyperthermic treatment by the non-sinusoidal signals, where live cells show as green and dead cells as red with Calcein-AM and PI staining.

To recapitulate, Figure 50 represents the mortality produced by the coaction of SPION and different AMF signals, which are non-sinusoidal (TP, TS, TR) and sinusoidal (SN) applied at the same frequency and amplitude on B16F10 and CT2A preincubated with MNPs 1 mg/mL and 4 mg/mL. Cell mortality was evaluated 24 h after MHT treatment when cells were incubated with MNPs at 1 mg/mL (Figure 50 A) and directly after treatment when MNPs were incubated at 4 mg/mL (Figure 50 B). The cell death achieved by TP, TS, and TR AMF application had a superior impact among all the cases tested compared with the cell death produced by the corresponding SN waveform. TP and TS waveforms significantly reduced cell viability in B16F10 cells preincubated with MNPs at 1 mg/mL (Figure 50 A), except for TR-AMF MHT treatment 24 h later on B16F10 at 1 mg/mL, which gave nearly equal rate of mortality with SN-AMF at 300 kHz/3.42 mT. Comparatively, the cell mortality decrease observed directly after TP-AMF and TS-AMF exposure on CT2A preincubated at 4 mg/mL was highly significant over SN-AMF as opposed to cell viability decrease 24 h after MHT treatment in the same cells preincubated with MNPs at 1 mg/mL. In summary, promising results were achieved by the applicability of the non-sinusoidal signals (TP, TS, and TR) at the best conditions (4 mg/mL over 2 h of incubation with cells), where cell mortality was directly evaluated after exposure to AMF. These outcomes seem to be due to the following reasons. Firstly, the cells have recovered

and proliferated 24 h after the treatment since the rate of proliferation is unlimited in the presence of nutrients as they are tumoral cells. In addition, the decrease in pH due to cell proliferation, serum in culture media, and incubation time were considered as factors causing MNP aggregation (Ozturk et al., 2020). The MNP aggregation decreases nanoparticle-induced MHT (Mejías et al., 2019). During hyperthermia, the heat shock proteins are also activated in response to MHT, which plays a role in fighting the effects of increased temperature by preventing protein denaturation, promoting cellular survival, and overcoming cell death (Moros et al., 2015) (Carter et al., 2021). Finally, it seems that the signals of lower slopes (TR) at low MNP concentration require superior frequencies to increase the efficiency of treatment, which confirms the assumption by (Rosales et al., 2016). In fact, certain requirements must be met when using the magnetic field generator; a suitable power supply circuit is required to produce non-sinusoidal waveforms at high amplitude and frequency, preventing interferences. However, the non-sinusoidal signals have revealed their strong effect and superiority over the sinusoidal signal for the same frequency and amplitude. The direct evaluation of MHT outcome against cancer during in vitro tests seems to be more accurate and makes it possible to prevent interferences that may appear in the long term of the experiment. Furthermore, there are some differences between MHT effects on B16F10 and CT2A, which is expected since it has been described previously that the cancer cells exert different responses to thermal stress (Ludwig et al., 2017) and that the cell death pathway may depend on the location of magnetic nanoparticles and the intracellular concentration inside cells (Beola et al., 2018).

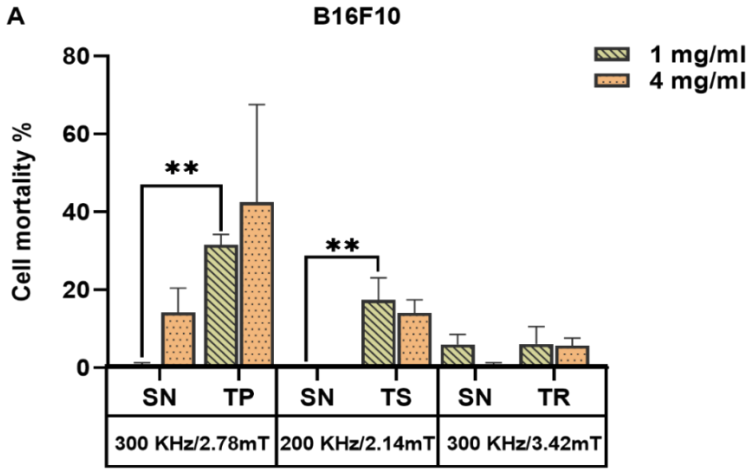

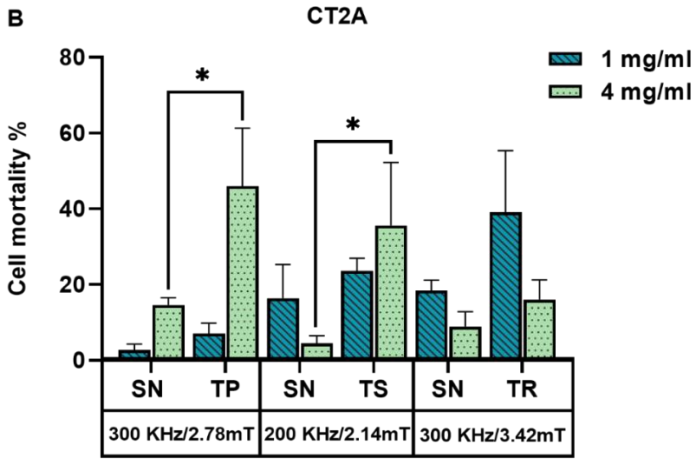

*Figure 50: Cell death rates of B16F10 (A) and CT2A (B) cells preincubated with MNPs at 1 mg/mL and 4 mg/mL and exposed for 30 min to AMFs using different waveforms (TP/SN, TS/SN, TR/SN) at the indicated parameters. To evaluate cell mortality, cells were stained with Calcein-AM/PI, and fluorescence microscopy images were quantified using Image J software. Data represent the mean ± SEM of three independent experiments (n = 3). ANOVA, post hoc Fisher's LSD test; * $p < 0.05$, ** $p < 0.01$.*

6. Effects of MNP-mediated MHT in combination with chemotherapy

In this section, we aimed to exploit the synergistic effects of combining MHT produced by TP-AMFs with 5-FU and to optimize the therapeutic outcomes in comparison to TP-AMFs magnetic hyperthermia alone. For that purpose, CT2A cells were incubated with APS-MNPs at 1mg/ml and exposed to two cycles of MHT employing a TS signal at 200 kHz and 2 mT for 30 minutes each cycle (separated by a 45 min break) both as a single treatment and in combination with 0.1 µg/ml 5-FU. The results obtained on CT2A cells after MHT treatments generated by TS signal combined with the chemotherapeutic drug 5-FU are illustrated in Figure 51. In previous section (Figure 46) we defined the toxicity effects of both 5-FU and DMSO alone on cells. In this section we examined the in vitro therapeutic potential of different treatments and to determine the cell death type (apoptosis or necrosis) we prepared different predefined experimental groups of CT2A cell cultures: Control, AMF, 5-FU, MNP, MHT only (two cycles), MHT+5-FU (two cycles). Annexin V and PI analysis was performed 24 h after treatment of CT2A cells preincubated with APS-MNP (1 mg/ml) and 5-FU (0.1 µg/ml) for 24 h followed by exposure to two MHT cycles (30 min each cycle, 45 min time of rest between cycles) using TS waveform at 200 kHz of frequency and 2 mT of amplitude. The APS-MNPs

were chosen for this study due to their small size and positively charged coating, which enables their rapid internalization by cells, since cells have a net negative charge on their outer surface. Regarding the numerical data of the quantified cell viability using fluorescence microscopy, as shown in Figure 51, the treatment with MHT alone resulted in a significant decrease in cell viability of 31.4±3% in CT2A cells. In contrast, chemo-magnetic hyperthermia treatment led to a further significant decrease of 58.9±2% in CT2A cell viability compared to the untreated control group. Treatment with chemotherapy alone did not produce a significant reduction in viability, with or without AMF. The 5-FU dose was chosen at low dose in order to mimic physiological conditions. During in vivo tests (in the body), chemotherapeutic drugs are distributed throughout the bloodstream and tissues, resulting in relatively low local concentrations at the target site (tumor). Thus, low doses in vitro help replicate these physiological conditions, providing more relevant results.

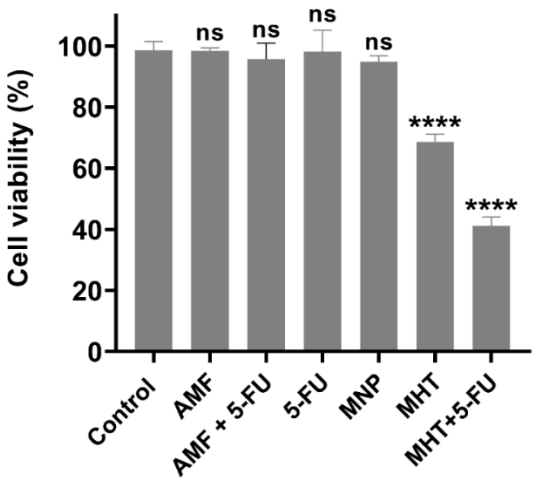

*Figure 51: Cell viability assessment with Calcein/PI by fluorescence microscopy 24h after MHT treatment induced by TP-AMFs at 200 kHz /2 mT and 1 mg/ml of APS-MNP in combination with 1µg/ml of 5-FU to provoke cell death in CT2A cells groups (Control, AMF, AMF+5-FU, MNP, MHT, MHT+5-FU). Data represent the mean ± SEM of three independent experiments (n = 3). ANOVA, post hoc Fisher's LSD test. **** $p < 0.0001$ versus control.*

The analysis of CT2A cancer cell death in Figure 52, using Annexin/PI staining, showed that cell death, by necrosis and apoptosis, was significantly higher in the group treated with MHT and chemotherapy (47.3 ± 2%) compared to the group treated with MHT alone (30.8 ± 3%). The other tested groups did not show significant cell death. Additionally, the combination of MHT and chemotherapy resulted in a significant increase in the number of apoptotic cells (11.6

±2%) compared to the MHT-treated group, where apoptotic cells were barely observed. The fluorescence microscopy images in Figure 53, represents CT2A cells untreated (control group), exposed to chemotherapy (5-FU) alone, MHT alone (MHT) and MHT+chemotherapy (MHT+5-FU), to further illustrate the effective therapeutic impact of the combined treatment in eliminating CT2A cells.

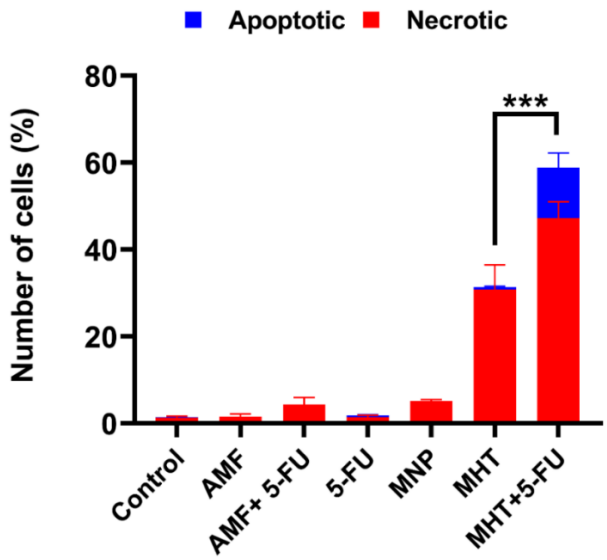

*Figure 52: Analysis of cell death pathway using Annexin V/PI in CT2A treated and untreated groups to determine apoptosis and necrosis relative percentage. Data are represented as mean ± SEM (n=3); *** $p < 0.001$ versus control.*

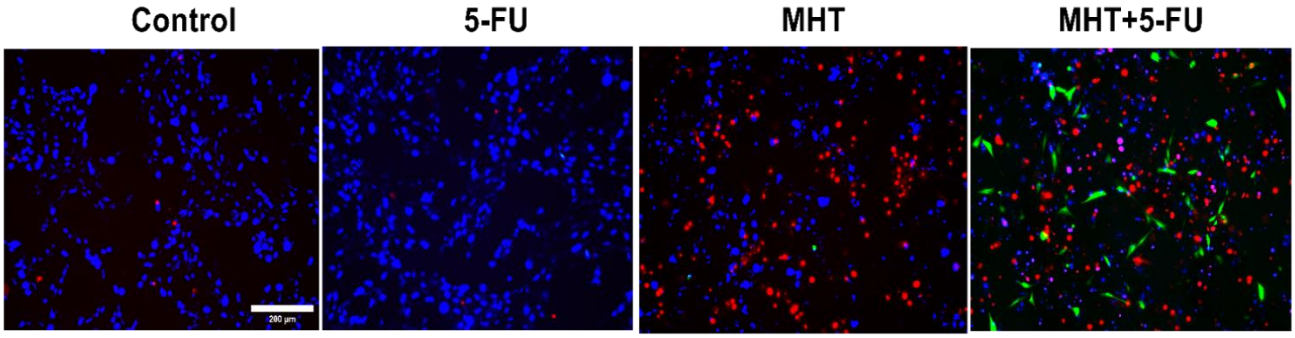

Figure 53: Fluorescence microscopy images of CT2A cells obtained after Annexin/PI staining show the group treated with chemotherapy alone (5-FU), the group treated with two consecutive cycles of MHT using a TS waveform at 200 kHz and 2mT (MHT), and the group treated with two consecutive cycles of MHT combined with 5-FU at 1µg/ml (MHT+5-FU), compared to the control group. In the images, apoptotic cells are observed in green (Annexin V), necrotic cells in red (PI), and the nuclei of living cells in blue (Hoechst). Scale bar:200µm.

7. CRT Immunocytofluorescence analysis

A cell death type, known as immunogenic cell death (ICD), can be identified through the activation of certain damage-associated molecular patterns (DAMPs) in dying cancer cells following MHT and 5-FU treatments. This ICD contributes to the recognition of dying cells by APCs. DAMPs include the overexpression and translocation of calreticulin (CRT), heat shock proteins (HSP70 and HSP90), extracellular release of adenosine triphosphate (ATP), high-mobility group box-1 (HMGB1), type I IFNs, and members of the IL-1 cytokine family (A. Ahmed & Tait, 2020) (Troitskaya et al., 2022). Hence, to analyze whether a specific treatment enhanced ICD in CT2A cells, we evaluated the number of CRT-positive cells after the different treatments. CRT serves as a danger signal that triggers ICD, activating systemic antitumor immunity. Differences among the experimental groups were determined based on the rate of CRT-positive cells quantified from fluorescence microscopy images obtained after an immunostaining assay using an anti-CRT antibody (Figure 54 and 55).

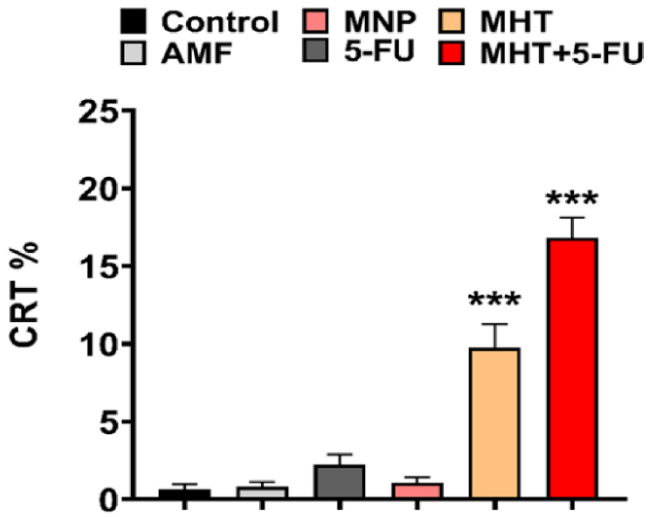

*Figure 54: Quantification data of CRT positive cells in CT2A cell line 24h after treatment by quantifying the number of cells positive for the CRT marker. Data are represented as mean ±SEM (n=3), *** $p < 0.001$ versus control. Scale bar: 200µm.*

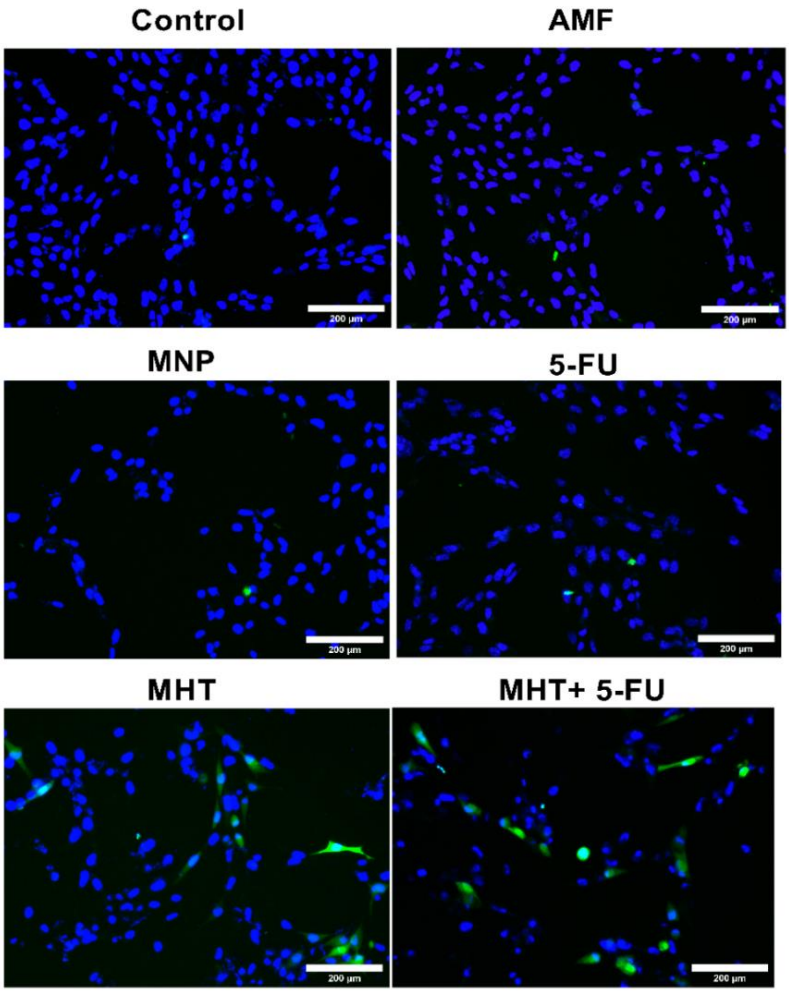

Figure 55: Immunocytofluorescent images of the ICD-associated marker (CRT) in CT2A cells 24h after MHT treatments. The representatives images correspond to the groups exposed to the following treatments: AMF, MNP, 5-FU, MHT, MHT+5-FU compared to the untreated group. Scale bar: 200µm.

The data in Figure 54 show that CRT expression in CT2A cells significantly increased in the group with MHT treatment (2 cycles MHT) to 10 ±1% and in the group receiving the combined treatment (2 cycles MHT+5-FU) to 17±1%, compared to the control group. The other experimental groups exposed to AMF, 5-FU and MNP did not show significant CRT expression. Therefore, this data suggests that the combination of MHT and 5-FU treatments increases the production of CRT-positive cells, resulting in a more effective method for eliminating cancer cells, as this type of cell death can enhance the immune response of the organism to eradicate cancer cells.

8. MNP-mediated MHT: In vivo preliminary results

To demonstrate the enhancement of MHT therapeutic efficacy using the non-sinusoidal signals compared to the sinusoidal one, six groups of C57BL/6 mice were used: the untreated group (control group), the group intratumorally injected with APS-MNPs without AMF (MNPs), the group exposed to SN signal (SN-AMF), the group exposed to TS signal (TS-AMF), the group treated with MHT produced by SN-AMF (MHT (SN)) and the group treated with MHT produced by TS-AMF (MHT (TS)).

In vivo MHT post-treatment preliminary results are depicted in Figure 56. After several cycles of MHT, the tumor size of all the groups was measured before and after each treatment session, from day 0 to 14, the difference in tumor volume among the mice groups is shown in the graphical representation (Figure 56). In the last treatment day (day 14), we identified a slight decrease of the tumor size in the group treated by MHT (TS), MHT (SN) and the control group, whereas the group exposed to TS-AMF alone noted an important decrease of the tumor size. The MHT(TS) group and those exposed to only TS-AMF had the lowest tumor size. The observation of the tumor growth from day 6 to day 14 for the MHT(TS) group shows clearly (as preliminary results) a slower tumor growth compared to MHT(SN) and the rest of groups, indicating an improvement of the treatment efficacy due to the application of the TS waveform. Moreover, a slight decrease was noted in the tumor volume from day 12 to 14. The group exposed to TS-AMF only noted the highest tumor volume in day 12 among all the groups, later an important reduction was shown in day 14. While the group treated by MNPs alone noted a significant increase of the tumor volume on day 14. It is important to consider the variability in immune system strength among the mice due to genetic, environmental, and immunological factors, which impact the evolution and progression of the tumor inside the mouse body (Sellers et al., 2012) (Niemi et al., 2020). This is a reason that in some mice groups the evolution and progress of the tumor after treatment sessions is different between groups and days, and also a reason for the mice death one week after the last treatment in the groups exposed to AMF (SN and TS). Moreover, the small number of mice used in this preliminary study is another reason for the difference in the tumor evolution between the animal groups.

The tumor weight is the most accurate parameter for evaluating tumor growth, for the fact the caliper measurements do not account for the depth of the tumor within the muscle and do not captures the entire 3D mass. Therefore, one week after the last treatment (day 14), the tumor's final weight has been measured after sacrificing the mice and extracting the tumors from the surviving groups: the control group, the group treated with only MNPs (MNPs), the group

treated with MHT using SN-AMF and the group treated with MHT using TS-AMF. The tumor weight results are illustrated in Figure 57. A significant reduction in tumor weight was observed in the MHT (TS) group (0.095 g) compared to the control group (0.15 g) and was due to heat generated by MNPs exposed to the TS signal. A decrease in tumor weight, compared to the control, was also seen in the MHT (SN) group (0.125 g) and the MNPs group (0.135 g). These preliminary results revealed that the treatment by MHT using TS-AMF improves MHT outcomes against the tumor, demonstrated by slow tumor growth (Figure 56) and reduction of tumor weight after treatment (Figure 57). The non-sinusoidal signal TS has demonstrated its efficacy again compared to the SN signal in enhancing the therapeutic efficiency of MHT.

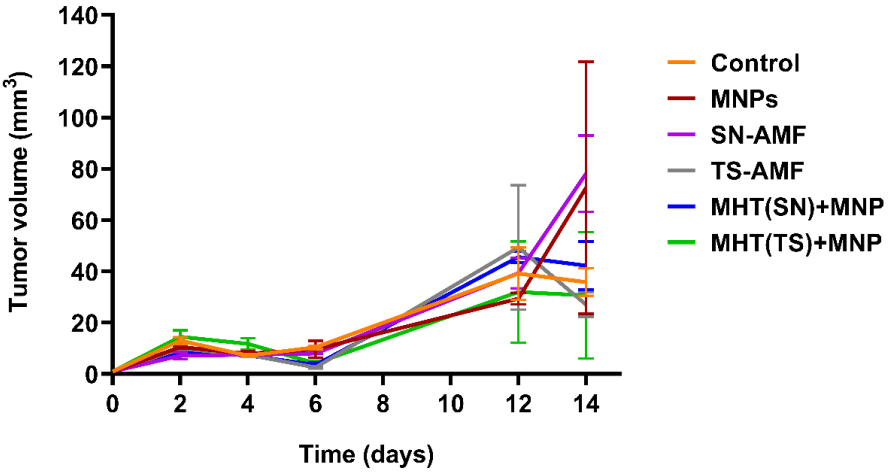

Figure 56: Tumor volume of C57BL/6 mice after magnetic hyperthermia treatment using pulsed-AMF compared to the control groups.

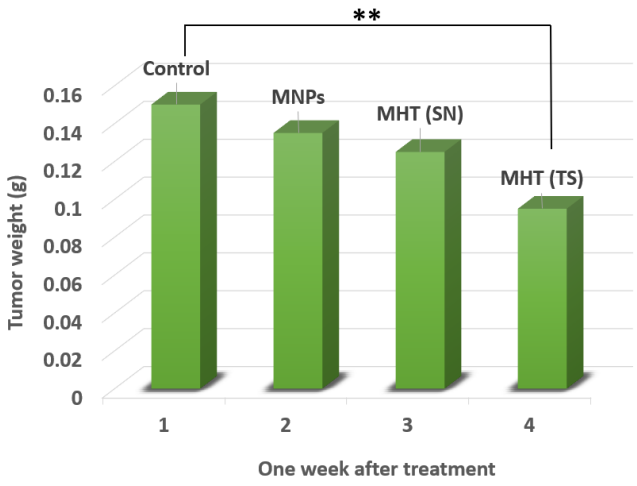

Figure 57: Tumor weight in different groups (control, MNPs, MHT (SN), MHT (TS)) of mice one week after treatment.

The in vivo results demonstrated again that the non-sinusoidal signal do not have killing effects against the mice that survived after several exposures of 30 min of duration to TS signal at 200 kHz and 2mT. Hence the non-sinusoidal signals are confirmed to be safe for application for low frequency and amplitude values. An application of these non-sinusoidal signal at high frequency and amplitude may lead to tissues damage and lead to mice death, therefore a safety limit needs to be assessed for future use.

9. Nanorobotics antitumor treatments

9.1. Results of the first set-up

The outcomes obtained using the magneto-mechanical destruction approach of cancer cells are represented in the following section.

We demonstrated the formation of microfilaments, an important effect that was observed in cell culture samples (in DMEM) after the magnetic field exposure: alignment of MMPs under AMF. These microfilaments are expected to induce morphological changes and damage to cells. Thus, they are expected to have an important effect on the cell viability of B16F10. The ferromagnetic properties of SiMAG-MP-DNA induce this phenomenon when exposed to the AMF (Figure 58). However, the magnetic microfilaments seen were formed outside the cells, MMPs that have not been internalized. The alignment formed inside of the cells is probably too small to be observed under this microscope or the amount of MMPs internalized is not enough for their occurrence under AMF. It is important to have these magnetic microfilaments inside the cells for a significant cell destruction.

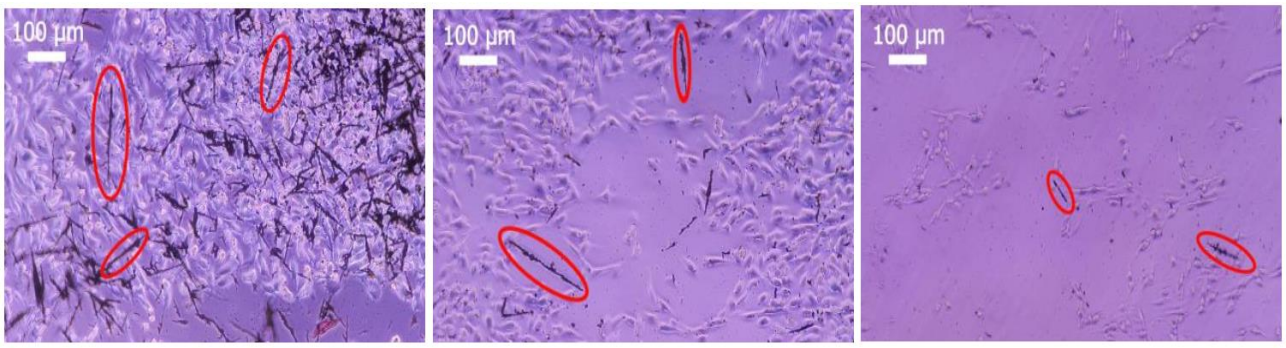

Figure 58: Images taken under the light microscope of the well with a concentration of MMPs of 12.5 µg/mL (left), 6.25 (middle) and 2.5 µg/mL (right) after magnetic field exposure for 1 hour using square waveform and 1Hz. Some linear aggregations are indicated under a red circle.

The post-treatment outcomes are illustrated in Figure 59, they showed that for the concentration of 50 µg/mL there was a difference between the wells placed inside the magnetic field and the wells placed outside the magnetic field. A decrease in cell viability was observed after treatment in the wells exposed to the magnetic field, pointing out promising results. SiMAG-K-DNA of 1 µm had a similar performance to SiMAG-MP-DNA of 2-10µm, showing significant cell viability decrease for the concentration of 50 µg/mL between the wells placed inside and outside the magnetic field.

SiMAG-MP-DNA (2-10 µm) and SiMAG-K-DNA (1 µm) were both good candidates as they showed good results for melanoma for the concentration of 50 µg/mL. SiMAG-K-DNA (1 µm) showed the best results. Nevertheless, the ferromagnetic properties and the bigger size of SiMAG-MPDNA (2-10 µm) make this kind of MMPs hypothetically better for achieving significant cellular death

A) **B)**

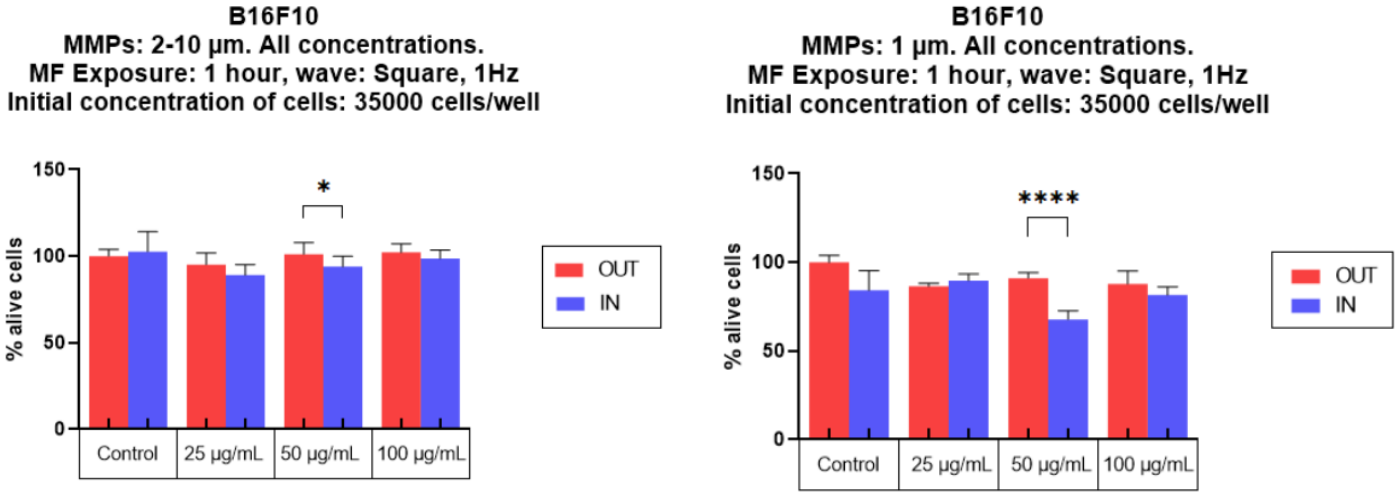

Figure 59: Cell viability of B16F10 preincubated 24 hours with MMPs of 2-10 µm (A) and 1 µm (B) at different concentrations (25, 50 and 100 µg/mL) exposed to a magnetic field of 1 Hz (IN). Reference wells placed outside the magnetic field were incubated in all experiments with the same type and concentration of MMPs (OUT). Moreover, on each plate, one well was left as a control not containing MMPs. Data represent the mean ± S.D.

V Discussion

Our study demonstrates an enhancement of the efficiency of MHT for killing cancer cells with nonharmonic signals. TP, TS, and TR are more effective and capable of enhancing the efficiency of MHT against tumoral cells; these results support the previously published studies by (Barrera et al., 2020) (Zeinoun, Domingo-Diez, et al., 2021) (Allia et al., 2019). This is consistent with another experimental study that has revealed the capability of the non-sinusoidal waveforms to enhance the energy dissipated by MNPs excited by a non-sinusoidal signal as compared to the energy dissipated by MNPs excited by a conventional signal (Zeinoun, Domingo-Diez, et al., 2021). The application of these new waveforms was found to increase heat production efficiency to above 71% by the TS and 45% by the TP over the SN signal, while the TR signal trailed behind in increasing the heat efficiency and was less powerful than SN. The adequate mathematical model that describes heat generation by MNPs when subjected to non-sinusoidal waveforms and its relationship with inducing higher cell mortality is still unknown. But we assume that by increasing the slope of the waveform, the rates of magnetic field energy absorption and conversion to heat by MNPs increase considerably due to a faster reorientation and alignment of nanoparticles' magnetic moments with the direction of the magnetic field, compared to the sinusoidal, which leads to an increase in cell death. The outcomes of our study of the SN waveform have shown mild or no cell damage due to the use of lower AMF intensity. In addition, the temperature of the cell samples in the presence of MNP remained stable at around 37°C while we obtained more temperature degrees with the non-sinusoidal waveforms of 1°C and 1.5°C (Figure 42.C). Therefore, the treatment with the SN waveform did not induce considerable cell damage. The intensity was not an obstacle for us since we aimed to improve the treatment efficacy by applying non-sinusoidal waveforms of a high slope, which is an alternative to increasing the heating efficiency and, hence, the efficacy of the treatment. For the in vitro tests, non-sinusoidal waveforms' applicability in MHT was found to increase cell death significantly on the B16F10 cell line to 31 ± 2% by TP-AMF and to 17 ± 5% by TS-AMF at 1 mg/mL and 30 min of exposition to AMF. In addition, the cell death was significantly increased to 46 ± 15% in CT2A by TP-AMF for 30 min of exposition at 4 mg/mL. The TP and TS both have a strong effect on CT2A at 4 mg/mL and 30 min of exposure to AMF. The applicability of the conventional signals during MHT treatment is often not effective. SK-Hep1 hepatocellular carcinoma cells were treated with MHT at 5 mg/mL for 24 h using an SN-AMF signal at 43.5 kHz/14.35 mT for 30 min exposure time, and nonsignificant mortality was seen after treatment (20% of cell death) (B. W. Chen et al., 2021).

Neither an increase in temperature of the culture medium nor a significant reduction in cell viability was observed following the exposure of murine pancreatic adenocarcinoma Pan02 loaded with APS-MNP (0.25 mg/mL) to the AMF at 250 kHz/31.41 mT (Mejías et al., 2019). In our results, cell death produced with SN-AMF was not significant, while MHT treatments using TP, TS, and TR signals reached a highly superior mortality. Among the explored cases, MHT using non-sinusoidal waveforms is particularly promising for anticancer therapy owing to the enhancement of antitumor killing effects. In addition, the TP or TS could be more efficient waveforms due to the increased slope. Hyperthermia may affect cell viability by even tiny changes in temperature. Less than a half-degree increase in temperature can negatively impact cell viability (Villanueva et al., 2010). The application of an AC field with a strength of 30.5 kA/m and 233 kHz has reduced cell viability without any perceptible rise in temperature (Creixell et al., 2011). Since MNPs are internalized in closed lysosomes distributed in the cytoplasm at different sizes, as depicted in Figure 47 C,F, and no cytotoxicity was observed with MNP or AMF separately, the cell death found in our study and produced by TP, TS, and TR signals is generated by the synergistic combination of APS-MNPs and AMF. It has been previously described that very local intracellular heat release by MNPs induces protein denaturation, DNA damage, and depolymerization of cytoskeletal components (Egea-Benavente et al., 2021). During the treatment by MHT, local temperature increments on the surface of MNPs at thermosensitive intracellular sites will obviously lead to cell death. The nucleolar and ribosomal DNA is one of the possible highly thermosensitive sites (Matos-Perdomo & Machín, 2019). A maximum temperature of 8°C was measured at 100 kHz/30 mT for an exposition time of 12 min on the surface of the nano-heaters inside cells without any appreciable extracellular temperature. The maximum determined intracellular heat generation in the vicinity of MNPs was lower (5.9°C) than what was measured on the surface of MNPs (8.0°C) using a nanothermometer and required double time to reach it (Gu et al., 2023). This local heat generation is sufficient to produce a significant cell death using effective non-sinusoidal signals (TP, TS) over the conventional signal, which is considerably improved when the frequency and amplitude are raised to the highest levels tolerated for human use. However, temperature assessment around the surface of MNPs or a single MNP in the intracellular and extracellular media remains a challenge, and accurate measurement tools are needed. Our data obtained further support the concept that local MHT therapy with temperature hot-spot generation at the surface of the nanoparticles is responsible for the induction of cellular mortality without any temperature change in the media (Gu et al., 2023) (Ovejero et al., 2021).

In vitro studies have demonstrated that heat is not the only agent responsible for provoking cell death following MHT treatment and that some contributing mechanisms are related to an increase in lysosomal membrane permeability by targeted MNPs under an AMF, which matches up with an augmentation of reactive oxygen species (ROS) production and an increase in the cytosolic activity of the lysosomal protease cathepsin D and causes cell death (Domenech et al., 2013) (Connord et al., 2015). Lysosomes contain hydrolytic enzymes, and any perturbation of the lysosomal membrane leads to the release of the lysosomal enzymes into the cytoplasm of the cell, which includes proteolytic enzymes of the cathepsin family. This, in turn, activates several intracellular cascades that promote the lysosome-dependent cell death (LDCD) (Serrano-Puebla & Boya, 2018). It has been found that in parallel to the decrease in cell viability, there is an altered expression of procaspases, production of reactive oxygen species, and altered mRNA expression of Ki-67, TOP2A, and TPX2 after MHT exposure (Ludwig et al., 2017). Therefore, the MHT mechanism of action is thought to be due to the fact that the external electromagnetic energy is converted to not only heat but to mechanical effects that cause the vibration of MNP inside cells and organelles membrane, which provoke the membranes to lose their integrity, as demonstrated in (D. H. Kim et al., 2010). Moreover, it has been discussed that AMF exposure enhances the MNPs' internalization inside cells; thus, the non-sinusoidal (TP, TS, TR) signals may contribute to better improving this internalization compared to the conventional signals. It is a new challenge to study the effects of the new signals (TP, TS, TR) on cells and how they may better cross cell membranes, which could have a role in increasing the sensitivity of cancer cells to hyperthermic treatment (Beola et al., 2018). All the mentioned mechanisms contribute by the end to decrease in one way or another the cell viability.

The in vivo magnetic hyperthermia preliminary results from intratumorally injected APS-MNPs in C57BL/6 mice have reported a slower tumor growth and a significant reduction in tumor weight after treatment by MHT produced by TS signal (0.095 g) compared to the control group (0.15 g) and was lower than the weight of the tumor from the group treated by MHT produced by SN signal (0.125 g) and MNPs group without AMF exposure (0.135 g). These preliminary results revealed that the treatment by MHT using TS-AMF had an effect against the tumor demonstrated by slow growth of tumor and a reduction in the tumor weight after the treatment days (Figure 58).

Hence, the in vitro results plus the in vivo preliminary results have demonstrated the capability of the nonharmonic signals to reach greater efficiency of the therapeutic mechanism by producing larger cellular stress effects.

The combination of hyperthermia with chemotherapy represents a new approach that has demonstrated numerous advantages in several studies. In (Beola et al., 2023) an in vivo study was conducted to eliminate GBM cells using drug-loaded lipid MNPs for combined hyperthermia and chemotherapy, proving to be an effective local treatment. Similarly, (Shirvalilou et al., 2023) and (T. J. Li et al., 2013) observed a substantial tumor remission in a mouse model after treatment with hyperthermia and 5-FU, compared to hyperthermia or chemotherapy alone. The novelty of our work lies in the combination of MHT generated by a non-sinusoidal signal with 5-FU at low concentration, to achieve a substantial optimization in cancer treatment and promoting an immune response against tumor cells. Various studies have demonstrated the potential that offer the pulsed alternating magnetic fields to enhance MHT over the sinusoidal fields. In our previous report (Souiade et al., 2023) we demonstrated the efficacy of the non-sinusoidal waveforms in improving MHT treatment efficiency against two cancer cell lines, glioblastoma and melanoma, compared to traditional treatment. Furthermore, a developed pulsed magnetic field (PMF) generator has shown fourfold higher efficiency compared to sinusoidal waves.

The treatment strategy employed in this study was designed to optimize the therapeutic potential of MHT in a GBM cell line and inducing ICD pathway (Figure 53 and Figure 54). The induction of ICD leads to increased expression of DAMPs, such as CRT, by dying cells, which in turn evoke an adaptive immune response (Z. Li et al., 2022) (Huaqi et al., 2023). The CRT proteins serve as an "eat me" signal for immune cells, and their release is critical for ICD induction, causing dying cells to become immunostimulatory entities. Once CRT binds to APCs via specific receptors, leading to their stimulation, it then promotes APC to further activate the adaptive immune response, including the activation of Naive T cells, along with CD4 and CD8 cells, which trigger and destroy cancer cells (Persano et al., 2021). Eventually, the quantification of cell death by annexin/PI staining assay among the experimental groups was consistent with the immunocytofluorescent analysis of CRT positive cells. The TP-AMFs magnetic hyperthermia treatment combined with 5-FU led to a considerable cell death (Figure 52) and to an intense ICD evidenced by a higher CRT staining compared to MHT or chemotherapy alone (Figure 53). This suggests the translocation of CRT to the membrane surface of damaged cells (Persano et al., 2021). MHT treatment alone, using 2 cycles of exposure to AMF for 30 min

each cycle separated by a 45 min break, resulted in a cell mortality rate of 31±3%, compared to the cell death rate of 24±3% obtained with one cycle (Souiade et al., 2023). In (Persano et al., 2021) three consecutive cycles of MHT by conventional sinusoidal waveform have been applied at 182 kHz and 16mT, with 30 min of exposition to SN-AMF each cycle separated by 5 min break, have shown to cause a reduction in cell viability of 30% in human GBM cells, 24h post-treatment. Furthermore, the combination of TP-AMFs magnetic hyperthermia and chemotherapy resulted in a significantly higher cell mortality rate of 58.9 ±2%, driven by 47.3 ±2% through necrosis and 11.6 ±2% through apoptosis. This demonstrates the ability of low intensity TP-AMFs magnetic hyperthermia in improving cancer treatment when combined with traditional. Interestingly, our findings revealed that necrotic cell death induced by chemo-magnetic hyperthermia was significantly higher than that observed in the group of cells treated with MHT alone. Moreover, apoptotic cells were only present in the group treated with chemo-magnetic hyperthermia. These results may be attributed to the ability of MHT treatments to enhance the effectiveness of chemotherapy by sensitizing cancer cells to chemotherapeutic drugs and facilitating their uptake into cells by increasing the cell membrane fluidity (Ribeiro et al., 2022), ultimately leading to greater damage to cancer cells. The results obtained further support the approach of combining different cancer treatments to induce various types of cell death, such as ICD and apoptosis. These mechanisms are particularly relevant in cancer therapy because, unlike necrosis, they do not cause inflammation or damage to nearby healthy tissues (Meng et al., 2021).

VI Chapter 5: In-*silico* study of MHT induced by Trapezoidal pulsed alternating magnetic field

In this section we aimed, firstly, to evaluate the effects of eddy currents induced by the TPAMFs in biological materials, to assess a safe exposure limit in order to prevent eddy current heating as much as possible during preclinical tests. Second, we simulated the heat generating by MNPs using the TPAMFs based on Rosensweig mathematical model. Therefore, this study was carried out in the Sim4Life multiphysics platform (ZMT, Switzerland), after modelling our home-made solenoid coil on two high-resolution digital phantoms of a cell culture medium and a mouse model (35.5 g) under different AMFs exposure parameters.

1. Introduction

Magnetic hyperthermia is a cancer thermal therapy modality with an excellent potential that is used as alternative or adjuvant treatment to chemotherapy and radiotherapy. MHT offers a great deal of potential for cancer therapy because of its ability to induce a localized temperature increase into tumors. The principle behind this hyperthermia treatment modality is that MNPs can be designed in different shape, size and composition, to absorb energy from an external magnetic field and convert it into heat. Recently, researchers have considered the use of MHT because, unlike microwave, ultrasounds and laser hyperthermia, this modality is minimally invasive treatment and prevents overheating of healthy tissues. The clinical procedure involves injecting a magnetic nanofluid into the tumoral tissue of the patient and applying the external magnetic field to induce heat through nanoparticles and raise the temperature of the tumor to 39-45°C (Thiesen & Jordan, 2008) (Peiravi et al., 2022). Electromagnetic wave energy is the preferred source of heat over other traditional heating methods owing to their penetration capability to reach the tumor where MNPs are delivered. Electromagnetic systems operating in the radiofrequency (RF) and microwave (MW) spectra gained great scientific and clinical interest for hyperthermia and magnetic hyperthermia applications for cancer treatment. Exposure to an AMF during MHT can cause eddy currents in adjacent healthy tissues, resulting in unwanted and harmful heating. These eddy currents are caused by the applied external AMF due to the electrical resistance of the tissues and have been demonstrated to limit treatment efficacy in clinical trials. The eddy currents can have an adverse effect on the normal functioning of biological organs. Their magnitude depends, in part, on the AMF's frequency (f) and intensity (H_a), as well as the size and the electrical properties of the tissue exposed to the field, thus, it is important to impose security restrictions of the energy applied to ensure the

safety and effectiveness of MHT treatment (Stigliano et al., 2016). Researchers have explored various methods to reduce the effects of eddy currents during MHT, including dynamic movement of the coil during treatment (Balousis et al., 2021) and the adjustment of AMF parameters with a carful balancing to maintain sufficient therapeutic heating of the tumor (Caizer, 2021), where the product ($H_a \times f$) should remain below a safe threshold to avoid unwanted effects on healthy tissues. Usually, the accepted limit is $H_a \times f < 5 \times 10^9\ A{\cdot}m^{-1}{\cdot}s^{-1}$ (Hergt & Dutz, 2007).The application of non-sinusoidal alternating magnetic fields has emerged as a new approach in recent years to enhance the efficiency of MHT treatment by increasing the heating of MNPs compared to the use of sinusoidal signals. It became possible to increase the heat produced by MNPs by using waveforms with higher slope instead of increasing the frequency and/or the amplitude of the signal, which increase significantly the rate of heat production and the damages against cancerous cells (Zeinoun, Serrano, et al., 2021) (Souiade et al., 2023). Thus, our study aims to explore the eddy current effects of non-sinusoidal AMFs generated by our MHT device within biological materials for the purpose of understanding the potential risks associated with their application and determining a threshold limit of safe exposure. For instance, our designed MHT device is not able to produce high magnetic field intensity, hence a computational study using an appropriate software for modeling the system is capable of analyzing and understanding the interplay between the non-sinusoidal electromagnetic fields and thermal behavior associated.

- **Magnetic hyperthermia modeling methods**

With the increased number of systems designed for cancer thermotherapy, an accurate evaluation of electromagnetic fields spatial distribution and behaviour is critical to understand the way the system operates, and its clinical application. In silico studies have become increasingly popular in recent years and are suitable for modeling complex systems and scenarios where physical experimentation is challenging in order to predict behaviors and interactions between electromagnetic power and biological materials. The importance of modeling hyperthermia applicators, analyzing electromagnetic behaviour, and simulating MNPs heating stems from the difficulties encountered in measuring the temperatures inside the treated region when the tumors are located at depth, also from the eddy currents produced and from the degree of variability and complexity of the treatments between each patient, which varies according to the size, shape and location of the tumor. Computational electromagnetics (CEM) involves using computational methods or numerical methods to model and evaluate

electromagnetic fields distribution and associated eddy currents, besides, the thermal behavior of ferrofluids (Vicentini et al., 2022) (Rahpeima & Id, 2022) (Pefanis et al., 2022). As a result, optimum therapeutic conditions can be achieved.

Common Computational Electromagnetic Techniques (Lwin & Yokota, 2019) (Goyal & Bhargava, 2018)

- Finite Element Method (FEM): FEM divides the problem domain into smaller elements, allowing for the numerical solution of Maxwell's equations. It's versatile and suitable for complex geometries and material properties .
- Finite Difference Time Domain (FDTD): FDTD discretizes space and time into a grid, enabling the direct numerical solution of Maxwell's equations. It's widely used in time-domain simulations of electromagnetic wave propagation.
- Method of Moments (MoM): MoM discretizes surfaces and currents, representing them as a set of basis functions. It's commonly used for analyzing scattering and radiation problems.
- Finite Integration Technique (FIT): FIT discretizes space using a meshless approach, making it suitable for problems with irregular geometries. It's particularly useful for analyzing open-region electromagnetic problems.

For instance, a numerical analysis of SAR and temperature distribution in two-dimensional human head model based on Finite Difference Time Domain (FDTD) parameters, and the polarization of electromagnetic wave (Lwin & Yokota, 2019). (Goyal & Bhargava, 2018)used the FEM to generate temperature profiles for blood and tissue at different electromagnetic wave power and electromagnetic wave frequencies. Among the different simulation platforms that use such numerical methods for biological materials heating by electromagnetic simulation are COMSOL Multiphysics and Sim4Life, both utilize FEM and FDTD methods, respectively.

The presented study aims to simulate and analyze the eddy currents effects produced by non-sinusoidal electromagnetic fields within a cell culture medium 3D model and a virtual mouse model, and also to simulate MNPs heating using the computational platform Sim4Life that directly correlates the AMF parameters to the thermal response of the in-vitro or in vivo virtual model for the comprehension and description of the phenomena that take place in the MHT experimental system built in our laboratory at the CTB. For that purpose, the temperature distribution of the system is estimated in space and time. The simulation is based on the FEM to study the effects EM radiation, the temperature distributions and to discuss the heat behavior

in the biological medium in the absence and presence of nanoparticles. This study provides reference numerical solutions for heat transport through biological media, thus helping to understand the thermos-physiological response of the nanofluid to the imposed electromagnetic radiation. Maxwell's equations and the bio-heat equation are used to estimate the electric field and the heat distribution.

The first part of the internship is to simulate and study a real MHT instrumentation that applies the electromagnetic radiation generated by a solenoid coil within a biological medium DMEM, used for cell culture during in vitro studies, without nanoparticles and with nanoparticles, in order to obtain simulations and calculations as real and precise as possible, such as the spatial distribution of the electromagnetic field and the spatio-temporal distribution of the temperature and the SAR. Therefore, two simulation environments are created; in the first, we simulate thermal distribution into cell culture medium contained in a Petri dish without nanoparticles, in the second, we simulate it in the presence of nanoparticles. Later, we evaluate the eddy currents effects produced by sinusoidal and non-sinusoidal electromagnetic fields at different frequencies and intensities.

The second part was an experimental study to calculate the specific absorption rate of our APS-MNPS sample under electromagnetic radiation produced by two different commercial applicators of hyperthermia.

2. Materials and Methods:

2.1. Sim4life platform:

Sim4life (ZMT, Zurich, Switzerland) is an advanced computational simulation platform developed by ZMT Zurich MedTech AG in collaboration with the IT'IS Foundation. It integrates computer-aided design (CAD) tools with multiphysics solvers, high-resolution anatomical models, and physiological simulations for testing the effectiveness and safety of devices and medical treatments, based on the Virtual Population ViP 3.0 models of the IT'IS foundation in Zurich (https://sim4life.swiss/). Sim4Life has a wide range of applications, such as for the development of medical devices, the assessment of electromagnetic safety in the workplace and in the environment and the evaluation of exposure limits for electromagnetic fields. Sim4Life include the following multiphysics solvers:

Electromagnetics Full Wave Solvers (P-EM-FDTD) the most frequently applied of their kind in near-field dosimetry, enable accelerated full wave, large-scale EM modeling (> billion voxels) with Yee discretization on geometrically adaptive, inhomogeneous, rectilinear meshes with conformal sub-cell correction and thin-layer models, with support for dispersive materials.
Quasi-Static Electromagnetic Solvers (P-EM-QS) enable the efficient modeling of static and quasi-static EM regimes by applying the finite element method on graded voxel meshes. The solvers address the most challenging low frequency problems at the cutting edge of medical and EM compliance applications. Each solver is optimized for a different approximation of Maxwell's equations, offering improved speed, convergence, and accuracy for a wide range of scenarios. User-defined fields or current distributions can be used as sources.
Thermodynamics Solvers (P-THERMAL) enable the modeling of heat transfer in living tissue with advanced perfusion and thermoregulation models. The two solvers adapted from SEMCAD X are based on 1) the finite-difference time-domain solver with conformal surface correction and 2) a steady-state finite volume solver to support adaptive rectilinear meshes and arbitrary active domain shapes.
Fluid Dynamics Solvers (P-FLOW) facilitate the modeling of realistic physiological and pathological biofluidic scenarios in the presence or absence of vascular implants. Stationary and transient Navier-Stokes and Stokes equations are efficiently solved with either a finite element method with Schur complement preconditioning, adaptive time-stepping, and tunable stabilization or a finite volume method based on a smooth pressure correction algorithm. Both solver types rely on platform-independent fast parallel processing, runtime solver monitoring, and advanced convergence criteria.
Acoustics Solver (P-ACOUSTICS) based on the linear pressure wave equation (LAPWE), extended and optimized for heterogeneous materials for the modeling of the propagation of pressure waves through highly inhomogeneous media like tissue and bone. All relevant phenomena like scattering, reflection, refraction, diffraction, interference, and absorption are captured by this method. The dissipated acoustics energy can be translated into a heat source for Sim4Life's thermal solver (P-THERMAL) to capture the coupling of acoustic and thermal phenomena.
In the next section, we introduce the equations that govern the phenomenon of the MHT process and need to be solved in our simulation study which consists of three parts, magnetic field generation by a current-conducting coil, heat transfer in the biological media and heat generation by MNP.

a. Electromagnetic field generation and propagation

Maxwell's equations describe the physics of electromagnetic field propagation, introduced in the time domain (Akimov, 2022). The equations can be transformed into the frequency domain, where E, D, B, H, and J are the electric field (E), displacement current (D), magnetic flux density (B), magnetic field strength (H), and the current density field (J), ρ the free electric charge density, t the time variable (s), $\nabla\times$ is the curl operator, and $\nabla.$ the divergence operator. For the magnetic field B, respectively, given as follows:

$$\nabla.\vec{D} = \rho \tag{28}$$

$$\nabla.\vec{B} = 0 \tag{29}$$

$$\nabla \times \vec{H} = \vec{J} + \frac{\partial \vec{D}}{\partial t} \tag{30}$$

$$\nabla \times \vec{E} = -\frac{\partial \vec{B}}{\partial t} \tag{31}$$

ε is the electric permittivity, and μ is the magnetic permeability which corresponds, in vacuum, to $\varepsilon_0 = 8.854 \times 10^{-12}\ F/m$ and to $\mu_0 = 4\pi \times 10^{-7}\ H/m$, respectively.

$$\vec{D} = \varepsilon \vec{E} \tag{32}$$

$$\vec{B} = \mu \vec{H} \tag{33}$$

b. Heat transfer in biological media

Next, Pennes' bioheat transfer equation has been utilized to predict temperature profiles during hyperthermia. PBHTE can still be applied to almost all cases of thermal modeling used to estimate power absorption and temperature distribution in the target region. Accurate temperature assessment is one of the main challenges of MNP hyperthermia. Therefore, numerical studies play a crucial role in evaluating the thermal behavior of ferrofluids. In MHT treatment, the thermal energy converted from the magnetic field is regarded as the input of

Pennes bio-heat transfer equation (PBHTE) equation. The temperature of the tumor region T can be predicted by solving a modified version of the PBHT equation (Paulides et al., 2013).

$$\rho c \frac{\partial T}{\partial t} = \nabla.(k\nabla T) + \rho Q + \rho S - \rho_b c_b \rho \omega(T - T_b) \quad (34)$$

where ρ is the volume density of mass, c is the specific heat capacity, t is the time, k is the thermal conductivity of the tissue, S is the specific absorption rate, ω is the blood perfusion rate, Tb is the blood temperature, T is the temperature of tissue, Q is the metabolic heat generation per unit of volume.

c. Heat generation by MNPs

The principle of MHT is to use the heat energy from MNPs to damage cancer cells when an external AMF is applied. During magnetic therapy and depending on the particle sizes, one of the mechanisms of heat generation will be dominant in a magnetic fluid. The thermogenesis mechanism of MNPs has been described by Rosenzweig's theory, in which the heat energy absorbed by MNPs is related to the frequency and amplitude of the AMF, and the properties of the MNPs. According to factors related to the particle and field characteristics, different proportions of Neel and Brownian relaxation processes can be observed in MNPs. The amount of power losses dissipated by MNPs in an AMF correspond to the equation (21).

2.2. Magnetic hyperthermia simulation in Sim4Life

2.2.1. Construction of the model

The main purpose in our numerical investigation is to simulate a magnetic hyperthermia applicator made by a 14-turn solenoid coil and a wire's radius of r = 30.5 mm (Figure 60), operating at a frequency range from 100 to 500 kHz and 1000 kHz, and for magnetic field intensity of 5 mT, 15 mT and 35 mT, irradiating within a simulated 3D model of biological material "DMEM" contained in a petri dish ,and within a 35.5g mouse model V1.0 includes 52 tissues and a length witout tail of 95 mm (Figure 61) download from the IT'IS foundation database (Zurich, Switzerland).

As we can see in Figure 60, the physical model simulated is composed of three different domains, namely, the solenoid coil, the petri dish and the cell culture medium. Each piece represents a fundamental part in the model to be examined. The most important part is the

solenoid coil for local hyperthermia which is represented by 14 layers (parallel circles in yellow) with 1mm of space between the layers and an average radius r = 30.5mm. The configuration of solenoid was modeled using coil from templates tools in the ribbon and was placed at a distance of 10 mm from the petri dish surface (in white) containing DMEM (in red).

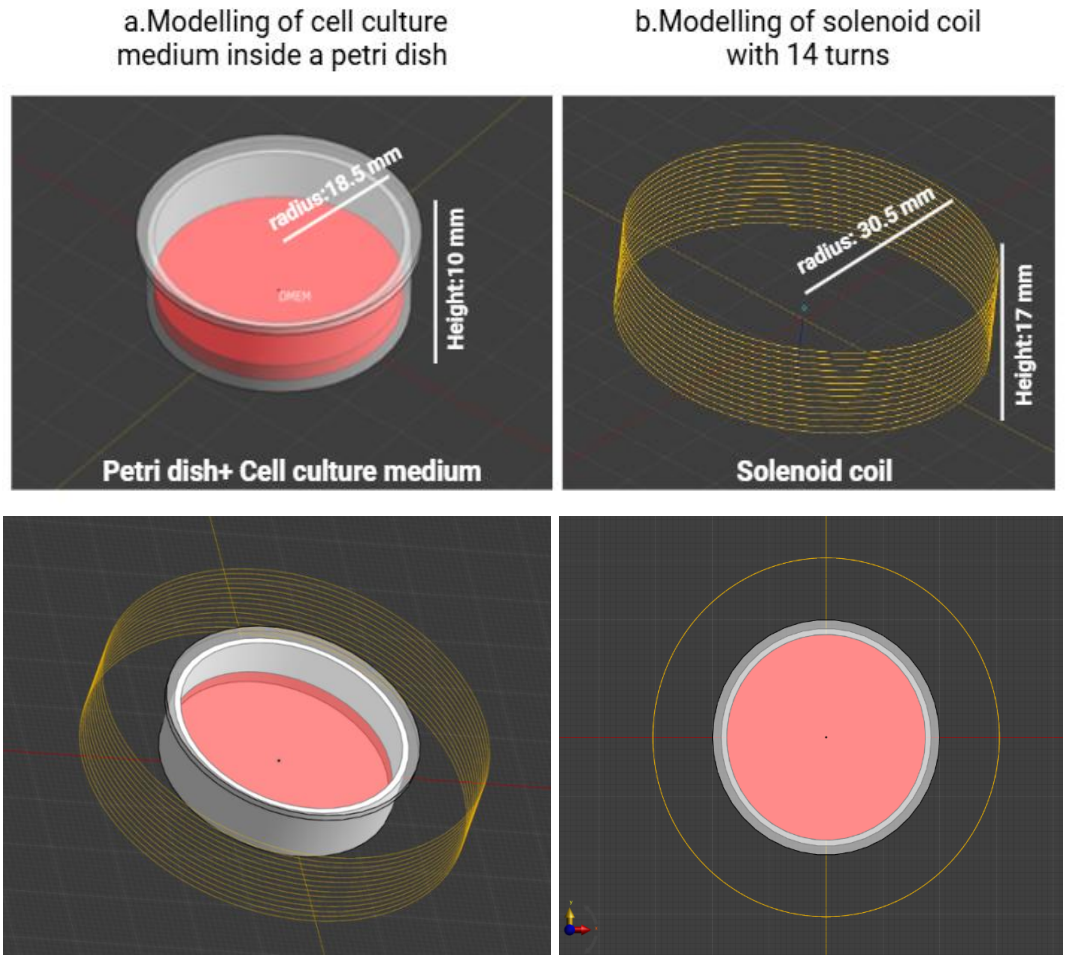

Figure 60: Geometrical 3D model of DMEM contained inside petri dish and MHT coil's device.

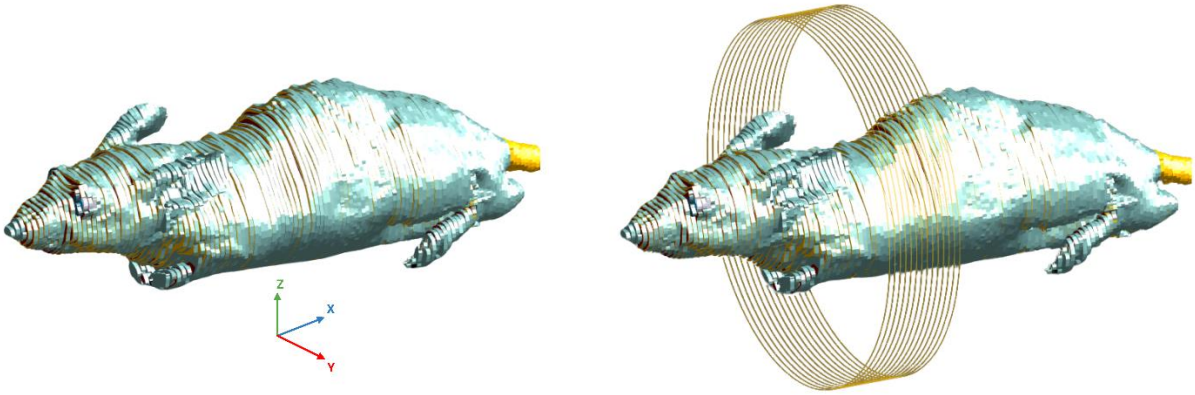

Figure 61: Schematic illustration of the anatomical OF1 male mouse model of 54 tissues from IT'IS foundation database positioned inside the coil.

2.2.2. Simulation process

2.2.2.1. Low-Frequency Magneto Quasi Static simulation

The part of the simulation includes the most important part of the practice. From the same model two different simulations were created, which allow us to calculate and compare different configurations; the first one is performed to obtain the temperature increase results without nanoparticles and the second one, with nanoparticles. The first step is to create from the simulation tab a new simulation called 'Electromagnetic low frequency Magneto-Quasi-Static simulation, based on the finite element method. Inside the simulation folder created, several properties need to be assessed depending on what we are going to simulate. The frequency chosen by the solver is defined in the Setup folder. First, we tested the simulation 3D model considering a frequency f = 200 kHz and magnetic field intensity H= 2 mT, that has been experimentally utilized on cells and mice for the validation of the coil and evaluation of eddy currents effects that may cause damage to biological media. Later, for the full study a range of frequency from 100Hz to 500H and 1000 kHz are used. The dielectric properties used in our study for the petri dish made by polystyrene were assigned from Simf4life material database, whereas for the biological media DMEM we defined the dielectric properties manually in the materials settings of the simulation tab as indicated in Table 2 (Y. Huang et al., 1997) (Lang et al., 2015) (Alwani et al., 2016) (Talone et al., 2021). Regarding the OF1 mouse model, the model includes 54 tissues and the physical properties involved are: the density, electric conductivity, permittivity, thermal conductivity, heat capacity, heat generation rate, heat

transfer rate, and tissue blood perfusion rate, which were assigned manually from the database of IT'IS foundation (Database Summary » IT'IS Foundation), for some tissues, the dielectric properties are relative to the frequency selected. Once the material properties and the source frequency have been assessed, we passed to create a new current source to simulate sinusoidal electromagnetic field where we assigned the solenoid coil as a wire current source for the excitation of the geometrical model. For this study, the excitation current in each wire was set for 10-25-50 A. The Overall Field of the Sensors folder is in essence a field sensor which encloses the entire computational domain and records the electric **E** and/or the magnetic **H** fields.

Model part	***Mass density (kg/m^3)***	***Electric Conductivity (S/m)***	***Relative permittivity***	***Specific heat capacity (J/kg/K)***	***Thermal conductivity (W/m/K)***
Air	1.205	0	1	-	-
Petri dish	1000	0.00047	2.54	1131	0.15
DMEM	1000	1.6	80	4181.3	0.6

Table 2: Dielectric and Thermal properties of the different in vitro model parts (Lang et al., 2015) (Talone et al., 2021).

To solve partial differential equations numerically, the field must be discretized into a collection of elements (cells). The differential equations are approximated by a group of algebraic equations, which are then solved to create a set of discrete values that approximates the partial differential system solution over the field. Therefore, Sim4life platform creates automatically a grid that comprises our model. However, some grid discretization settings needed to be modified. The model was discretized with an equidistant mesh of 0.5 mm resolution and 0.5 mm maximum step. In order to minimize the effects of the boundary conditions free space was added around the petri dish and/or mouse model. For the petri dish and DMEM model, the spatial dimensions of the computational domain amount to 162 x 162 x 66 cm resulting in 1.732 million grid cells. Once grid cells have been created the generation of voxels is primordial.

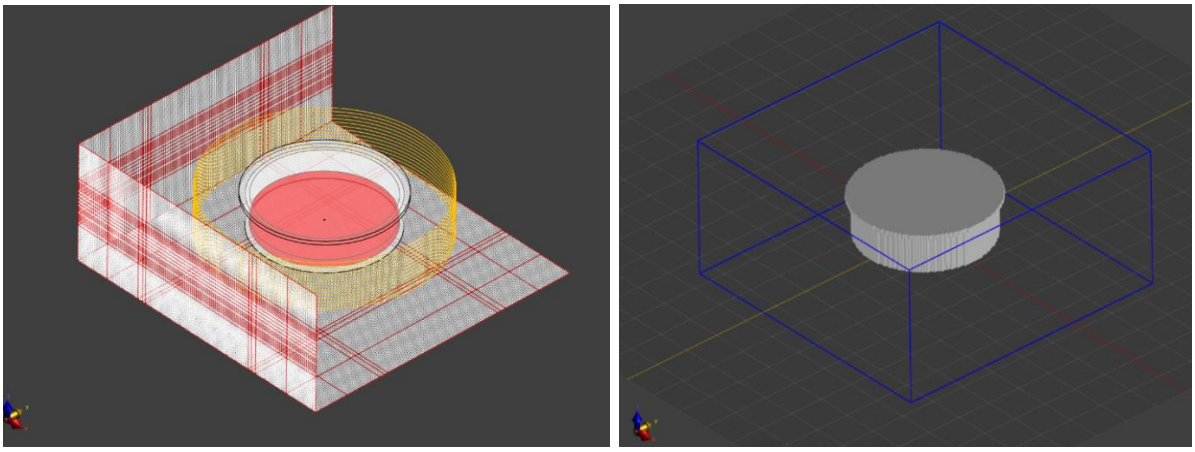

Figure 62: 3D view of grid creation (left) and the voxelled 3D model of petri dish and DMEM.

For the mouse model, the resolution and maximum step in the EM-LF-MQS simulation were assessed at 0.5 mm while for thermal simulation at 0.7 mm and the spatial dimensions of the computational domain amount, respectively, to 288 x 202 x 202 cm resulting in 11.752 million grid cells and 180 x 90 x 91 cm resulting in 1.474 million grid cells.

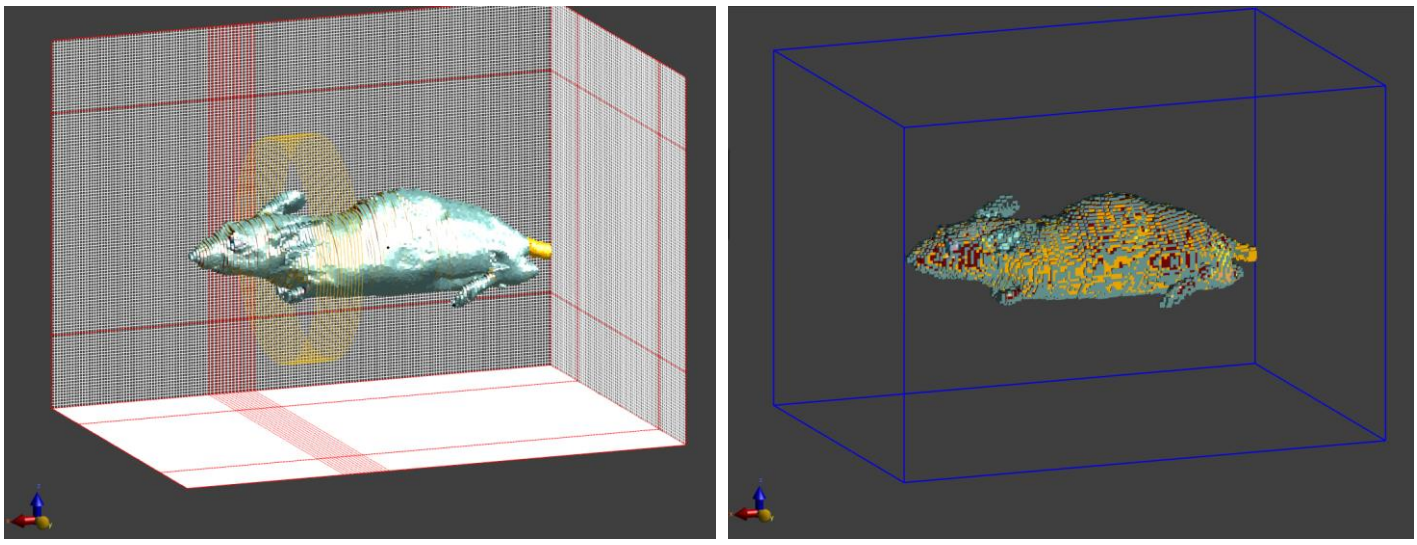

Figure 63: 3D view of the grid creation and the voxelled OF1 mouse model.

2.2.2.2. Thermal simulation:

The purpose of this simulation is to define the heat transfer and thermal behaviour inside the biological materials using sinusoidal and non-sinusoidal AMF, and the heat generation

distribution by MNPs. Therefore, for thermal simulation we used the transient solver within the sim4life platform which is governed by the Pennes Bioheat Equation to simulate the temperature changes and transfer over time inside the biological models (Petri dish + DMEM, mouse). Firstly, without nanoparticles to evaluate the eddy currents effects and the safety threshold of the system for the fact that the radiation emitted by the solenoid coil could be absorbed by the biological material and lead to the heating of the medium. Thus, to demonstrate that heat is generated only by the exposition of nanoparticles to electromagnetic field it is primordial to test first the system in the absence of nanoparticles. Secondly, we simulate the presence of nanoparticles within DMEM. The thermal properties of the biological medium DMEM were defined from, while the polystyrene of the petri dish from the materials database of Sim4life (Table 2). Regarding the OF1 mouse tissues thermal properties they were defined from were assigned manually from the database of IT'IS foundation (Database Summary » IT'IS Foundation). Later, a homogeneous initial temperature was defined at the physiological body temperature 37°C and refers to the temperature of each domain at the beginning of the analysis.

- **Thermal simulation using sinusoidal EMFs**

For thermal simulation using sinusoidal fields, simply, the transient heat source was defined by the output overall field from the MQS simulation.

- **Thermal simulation using non-sinusoidal EMFs**

For thermal simulation of the non-sinusoidal electromagnetic field, we computed the sinusoidal field in Sim4Life, we extracted the electric field and then modelled the electric field of the non-sinusoidal AMFs in MATLAB by Fourier series (**Annex 1**) using the following equation:

$$E(t) = E_0 \sum_{n=1}^{\infty} C_n \, e^{jn\omega t} \tag{35}$$

where $\omega = 2\pi f$ and C_n are Fourier coefficients calculated by the equation 36 using a_n and b_n coefficients in Table 3 :

$$C_n = \sqrt{a_n^2 + b_n^2} \tag{36}$$

The a_n and b_n coefficients were calculated from the Equation 37 using MATLB(**Annex 1).**

$$f(t) = \frac{a_0}{2} + \sum_{n=1}^{\infty} (a_n \cos(n\omega t) + b_n \sin(n\omega t)) \tag{37}$$

	COEFFICIENTS (n)	1	3	5	7	9	11
TP	bn	0,573159	0,063684	-0,022926	-0,011697	0,007076	0,004737
TS	an	0,248602	0,146500	0,052740	0,005074	0,003069	0,010897
	bn	0,534949	0,059439	-0,021398	-0,010917	0,006604	0,004421
TT	an	0,455647	0,012417	0,004470	0,009299	0,005625	0,000924
	bn	0,171948	0,019105	-0,006878	-0,003509	0,002123	0,001421
TR	bn	0,405285	0,045032	0,016211	-0,008271	0,005004	0,003349

Table 3: Fourier Coefficients of the asymmetric non-sinusoidal signals; TS, TP, TT, TR calculated for 1 A (peak).

The detailed calculations for modelling the electric field of the non-sinusoidal AMFs can be found in **Annex 1.**

Finally, we calculated the power loss density (W/m^3) (Annex) from the electric field of the non-sinusoidal AMFs employing the equation (38) and imported the resulting heat source to Sim4Life for simulating the temperature distribution in the model in order to evaluate the eddy currents effects of the non-sinusoidal AMFs.

$$P_{loss\ density} = \sigma \frac{\left|\overrightarrow{E(r)}\right|^2}{2} \tag{38}$$

- **Thermal simulation of MNPs**

To simulate MNPs heat generation, we used Rosensweig's model in equation.21 (Rosensweig, 2002) and we multiplied the result by the volume fraction of MNPs to mimic the real scenario.

$$P = \pi\, \mu_0\, \chi_0 H_0^2 f\ \frac{2\pi f\tau}{1+(2\pi f\tau)^2}$$

The dissipation power from MNPs was calculated in MATLAB (Annex 1) and imported as heat source. The parameters in the Rosensweig equation correspond to: $\tau = 1\times10^{-5}$, $\mu_0 = 4\times10^{-7}\times\pi$ and $\chi_0 = 10.47$, the relaxation time (τ) and the magnetic susceptibility (χ_0) has been calculated from experimental measurments using similar MNPs and sinusoidal AMF. The volume fraction of MNPs corresponds to the concentration divided on the density of 5265 kg/m^3.

The H_0 has been extracted from the MQS simulations of the sinusoidal fields to simulate the MNPs heating using sinusoidal waveform, while to simulate the heating of MNPs using non-

sinusoidal waveforms we modelled the magnetic field H_0 of the non-sinusoidal AMFs in MATLAB by Fourier series (**Annex 1**) using the following equation:

$$H(t) = H_0 \sum_{n=1}^{\infty} C_n \, e^{in\omega t} \quad (39)$$

For the boundary conditions, which specify the thermal conditions at the boundaries of the 3D model, there are three types usually applied for thermal analysis (Mfolozi et al., 2018) which are:

- Dirichlet: the surrounding air or outside temperature is fixed.
- Neumann: a fixed heat flux present at the interface of the model, either passing in or out the model
- Mixed: both Dirichlet and Neumann types coexist.

For our simulation study we defined the thermal simulation boundary conditions as a mixed type considering a heat transfer coefficient of 25 $W/m^2/K$ to mimic the experimental condition of a forced convection at the interface between the skin and the outside environment. Later, the model grid creation was defined at a maximum step of 0.5 mm for the cell culture model and of 0.7 mm for the OF1 mouse model, respectively. Finally, the voxels were created simulation processed

3. Results and Discussion

In general, exposure to an electromagnetic field causes distribution of energy within the biological tissues, which may lead to hot spots due to the occurrence of eddy current, hence, the biological tissues will be damaged. In this section we elucidate the safety of our magnetic field generator for preclinical tests using the sinusoidal and non-sinusoidal waveforms. Then we present the simulated heat generation by MNPs in the biological media DMEM. Moreover, we present a comparison within the models using a wide range of parameters of the magnetic field, to be able to see a more appreciable difference and define an appropriate threshold for consideration before any preclinical treatment.

3.1. In vitro eddy currents evaluation: Petri dish+DMEM

3.1.1. Magnetic field distribution

In order to assess the optimal grid step for an accurate simulation and system problem's solution, a wide range of grid step of LF EM-MQS simulation was tested from 0.3 mm to 2 mm. The grid step is a critical parameter that affects the accuracy, stability and computational efficiency. The smaller the step of the grid the better is the accuracy of the simulation by capturing finer details of the system's behaviour. A large step grid can reduce the accuracy and lead to instability and divergence of the solution. The optimal grid step should be small enough to resolve the system's problem.

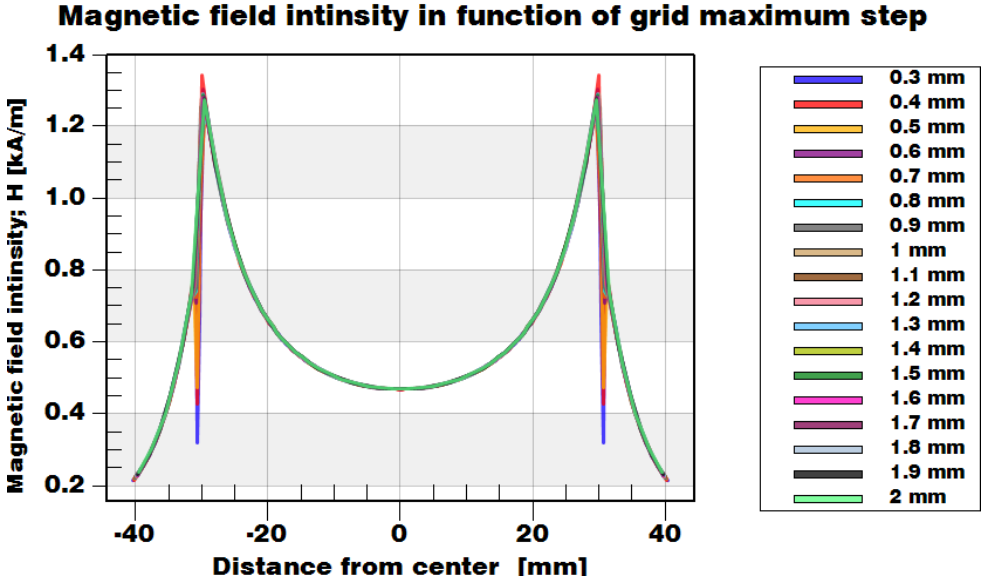

Figure 64: Spatial distribution of magnetic field intensity H in function of the grid maximum step inside cell culture medium model using the sinusoidal signal at 200 kHz and 2 mT for 30 min.

The data in Figure 64, showed that the magnetic field spatial distribution by SN using grid steps from 0.5 mm to 2 mm reached a similar magnetic field intensity at the extremities of the coil (-30 mm and 30 mm), while for 0.3 and 0.4 grid step magnetic field intensity was slightly higher. The magnetic field distribution between the distance -20 mm and 20 mm, where the model is located, had the same magnetic field intensity among all the grid steps used. Hence the 0.5 mm grid maximum step was used to perform all simulations.

The magnetic field spatial distribution within cell culture medium model (petri dish + DMEM) by SN at a frequency of 200 kHz and magnetic field intensity 2 mT using 0.5 mm grid step is depicted in Figure 65. The results revealed that the magnetic field is more intense around the solenoid coil's wires and decreases the further away we go from wires. Inside the DMEM the magnetic field strength (H) reached a maximum value of 580±112 A/m.

A) **B)**

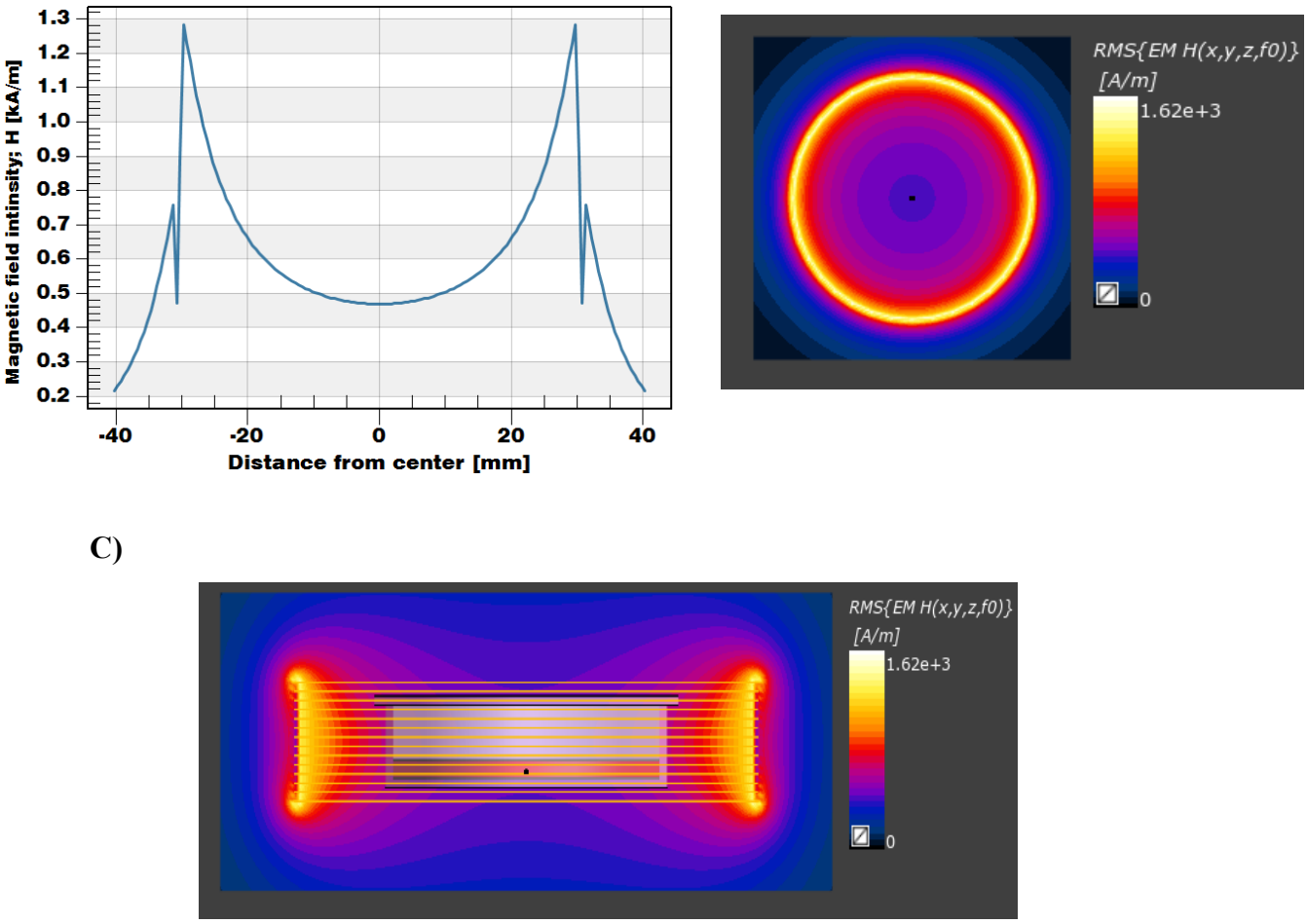

Figure 65: Magnetic field strength inside cell culture medium model for the sinusoidal signal (SN) at 200 kHz and 2 mT represented on plan XY (A, B). and on plan YZ (C).

3.1.2. Electric field and SAR distribution

In parallel, the propagation of the electric field strength and SAR, for SN signal at 200 kHz and 2 mT and for 30 min of irradiation, inside the cell culture medium DEME are depicted in Figure 66 and 67. Electric field and SAR distribution inside DMEM can be seen clearly via the color map (Figure 66 and 67). The yellow color represented the highest rate of electric field and SAR

which is found at the extremities of DMEM and reached its peak for 11.2 V/m and 0.129 W/kg, respectively, while low power is located at the center of cell culture medium by blue color.

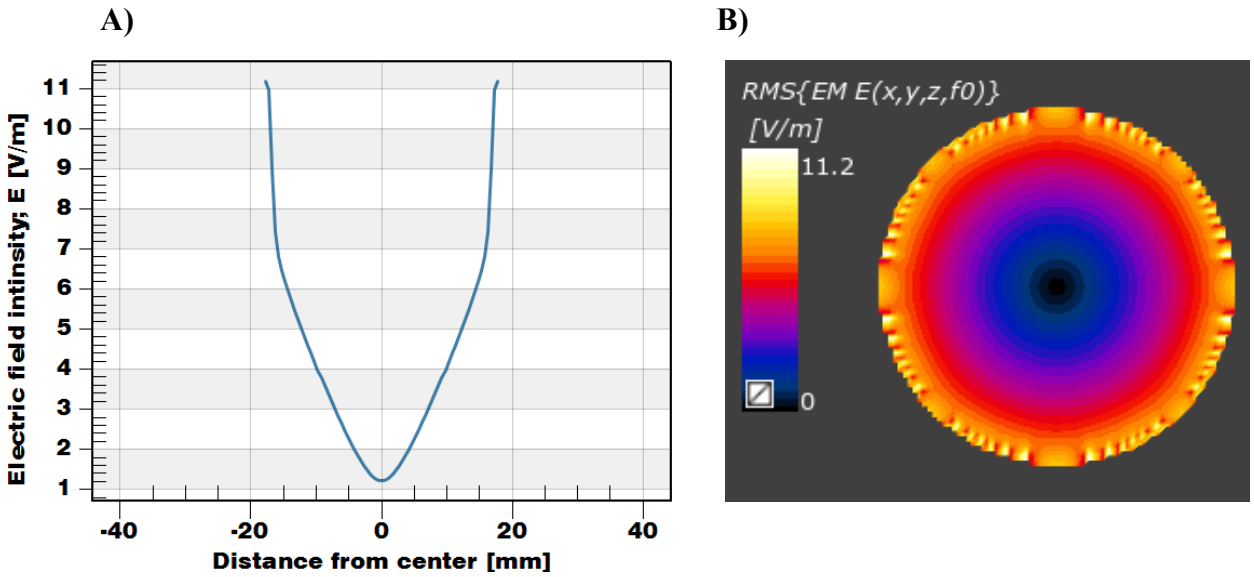

Figure 66: Distribution of electric field strength inside the cell culture medium model for sinusoidal signal (SN) at 200 kHz and 2 mT represented on plan XY (A, B).

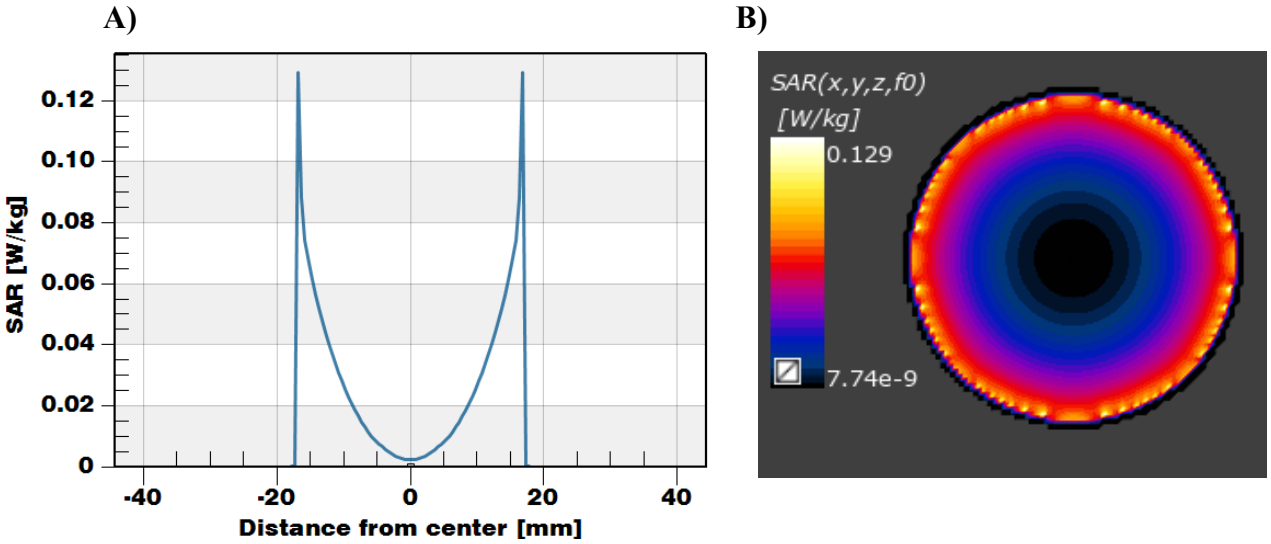

Figure 67: Distribution of SAR inside the cell culture medium model for sinusoidal signal (SN) at 200 kHz and 2 mT represented on plan XY (A, B).

As we can see in all the images of DMEM (Figure. 65.B; Figure 66.B; Figure 67.B), the shape of the representation and the scale of the legend changes, reflecting that in the center the penetration decreases slightly due to the reduction in field strength.

3.1.3. Heat distribution

To evaluate the eddy current effects inside biological media using sinusoidal and non-sinusoidal signals, a cell culture medium contained in a petri dish 3D model has been irradiated by a mimic coil model of 14 turns for 200 kHz and 2 mT. The eddy current effects were first tested at 200 kHz and 2 mT, seeking comparison to the experimental data, than simulations were carried out using a range of frequency from 100 kHz to 500 kHz and 1000 kHz. and magnetic field intensities of 5-15-35 A, considering a heat transfer coefficient of 25 W/ m^2/K for the forced convection condition. The thermal spatial distribution in the biological media DMEM 30 min after irradiation to SN and TS at 200 kHz and 2 mT .are illustrated in Figure 68. The thermal profiles of DMEM irradiated by SN and TS signal deduced from the expression of power loss density in equation (36), showed a stable temperature around 37°C.

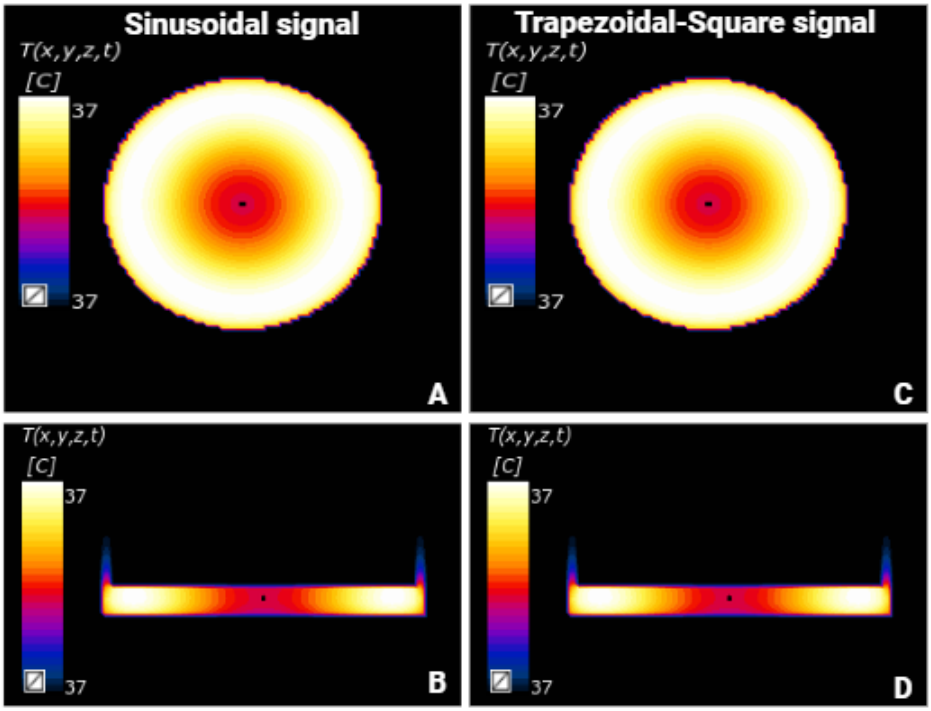

Figure 68: Resulting cross-sectional temperature spatial distribution inside biological medium for 200 kHz and 2 mT at t_{max}=1800s for Sinusoidal signal (A, B) and for Trapezoidal-Square signal (C, D) on plan XY (A, C) and plan YZ (B, D).

The spatial temperature distribution over time (30 min) for all the signals generated by MHT system; SN, TS, TP, TT, TR, at 200 kHz and 2 mT is depicted in Figure 69. No significant temperature increase has been reported after irradiation with TS, TP, TT, TR compared to SN, revealing the absence of eddy current effects by the application of non-sinusoidal signals at

200 kHz and 2 mT. The comparison of these results to the experimental results reported in Figure 42.A and Figure 43 validate the simulated solenoid coil for the in-silico study and safety of the signals for low frequency and amplitude.

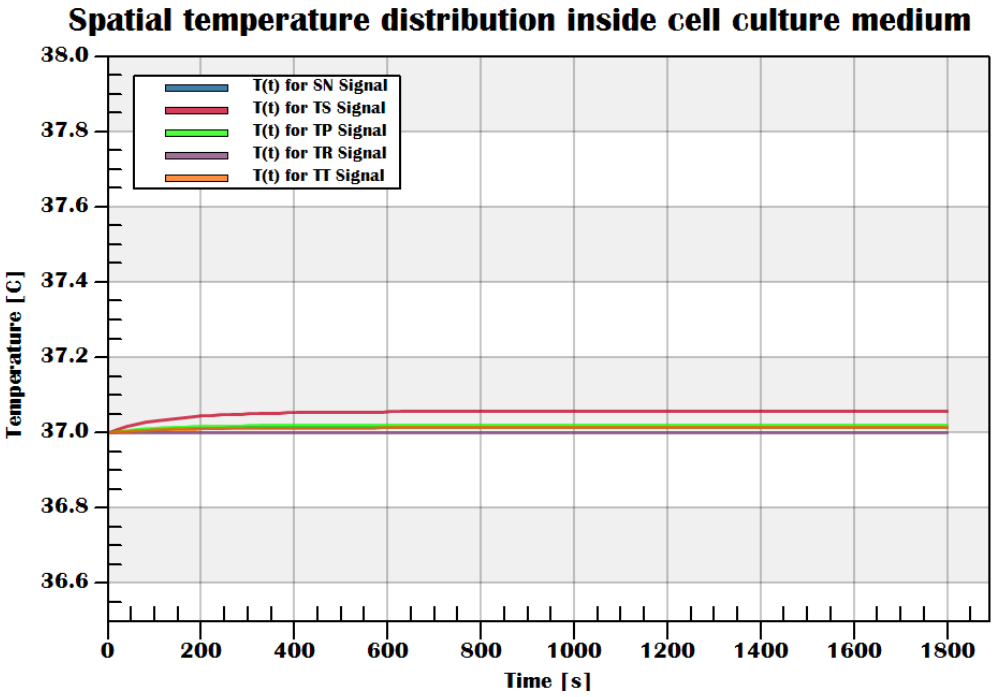

Figure 69: Temperature spatial variation in function of time(s) for different TP-AMFs signals: Sinusoidal (SN), Trapezoidal-Square (TS), Trapezoidal (TP), Trapezoidal-Triangular (TT), Triangular (TR) showing an increase of temperature around 37°C inside cell culture medium at 200 kHz and 2 mT.

A selection of higher AC magnetic field parameters (frequency, magnetic field intensity) may lead to non-negligeable eddy current heating, thus impacting harmfully on the biological materials. In order to evaluate the safety of the AMF applicator for preclinical tests in terms of EM dosimetry and to define a threshold limit of non-sinusoidal signals application, we investigated the influence of the pulsed alternating magnetic fields using a wide range of frequency *f* and the magnetic field intensity, on inducing eddy currents inside biological media. Temperature spatial variation data using a range of values for the AC magnetic field parameter, frequency from 100 kHz to 1000 kHz and magnetic field intensities of 5-15-35mT, with the non-sinusoidal waveforms TR, TT, TP, TS are illustrated in Figure 70 compared to the sinusoidal one in Figure 71. The results reported in Figure 71 demonstrate that the non-sinusoidal AMFs TS and TP have more important eddy current effects compared to the SN one.

In contrast, we observed with the TT and TR signals lower eddy currents effects compared to SN revealed by lower temperature increment. We can also observe that the temperature increments have an asymptotic behaviour versus the amplitude and or the frequency, since for high values the eddy current effects are increased highly. This is well illustrated by Figure 70 which shows negligeable eddy current effects at 5 mT for all non-sinusoidal AMFs (TS, TP, TT, TR, SN) used and among all the range of frequency used, revealed by a stable temperature around 37°C. At a higher magnetic field intensity 15 mT and with TS and TP signals we observed a temperature increase of 1°C and 0.5 °C, respectively, for 400 kHz. Whereas for TT and SN temperature increase up to 0.5°C was observed for 500 kHz. Than the temperature increases exponentially with the frequency where it reached a maximum temperature increment for 1000 kHz, estimated by 45.9°C for TS, 40.2°C for TP, 39.5°C for SN, 39°C for TT, 37.2°C for TR. The TR signal did not show a temperature increment at 15 mT (similar to 5 mT) for all frequencies, but at *35 mT*, a temperature increments up to 0.5°C was observed for 700 kHz. For TS, TP, TT and SN at 35 mT, temperature increased up to 0.5°C for 200 kHz and reached a maximum temperature increment for 1000 kHz, estimated by 72.6°C for TS, 50.1°C for TP, 47°C for SN, 45.09°C for TT, 38°C for TR.

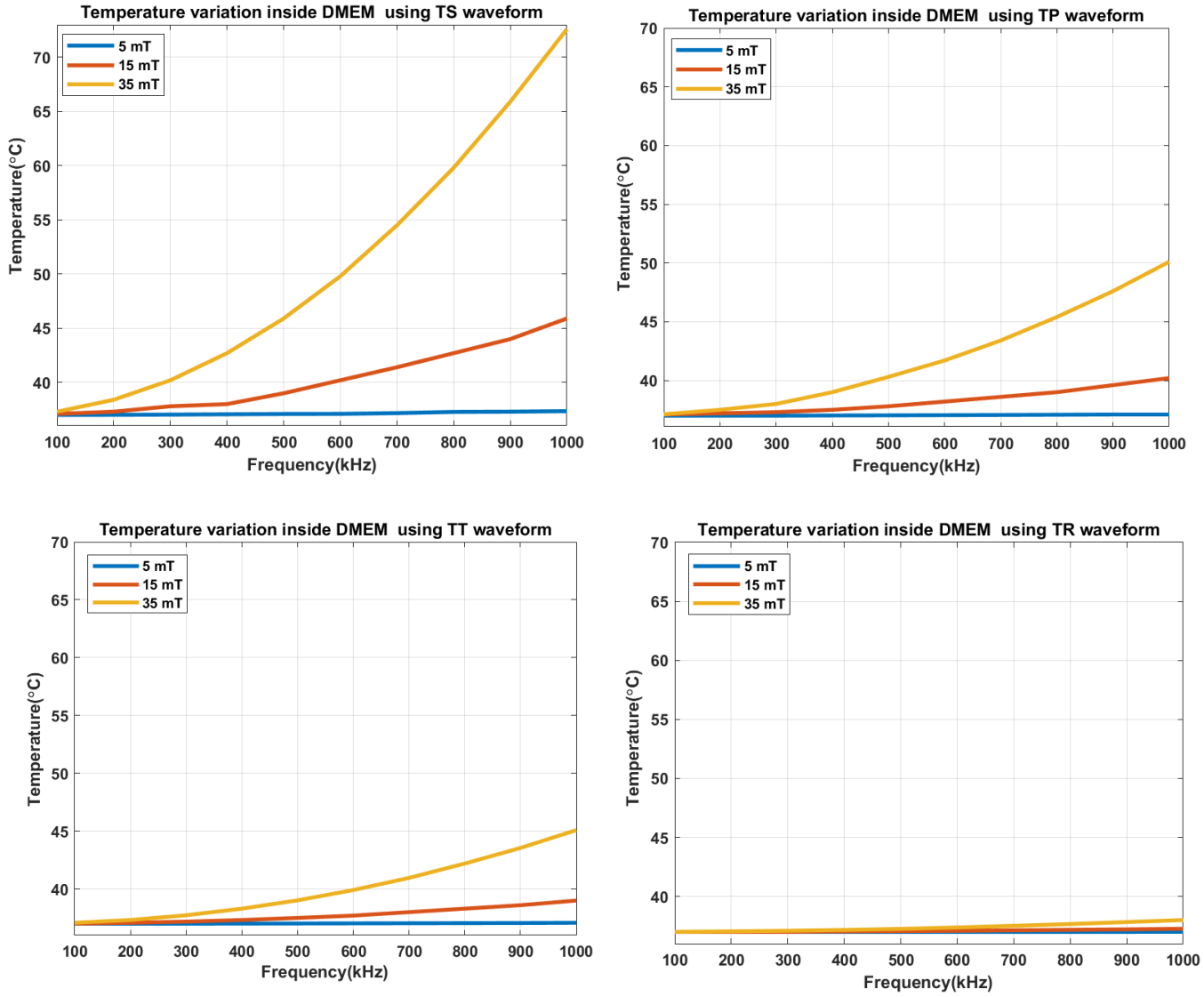

Figure 70: Influence of the non-sinusoidal AMFs TS (A), TP, TT, TR, on the maximum temperature increase in a cell culture model, versus the AC magnetic field parameters of frequency from 100 kHz to 1000 kHz and magnetic field intensities of 5-15-35mT and for an exposure duration of 30 min.

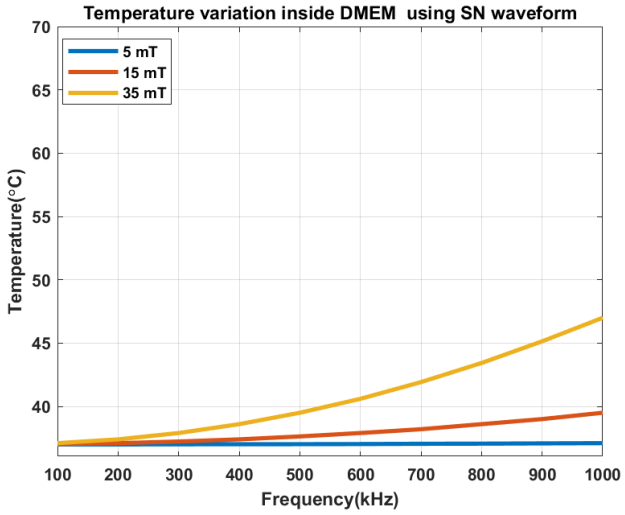

Figure 71: Influence of the sinusoidal AMF on the maximum temperature increase in a cell culture model versus the AC magnetic field parameters of frequency from 100 kHz to 1000 kHz and magnetic field intensities of 5-15-35mT and for an exposure duration of 30 min.

3.2. In vivo eddy currents evaluation

3.2.1. Magnetic field distribution

The results in Figure 72 revealed the magnetic field distribution using 0.6 mm grid step. The magnetic field is more intense around the solenoid coil's wires and decreases the further away we go from wires. Inside the Mouse body the magnetic field strength (H) has a maximum value of 564.3± 91 A/m.

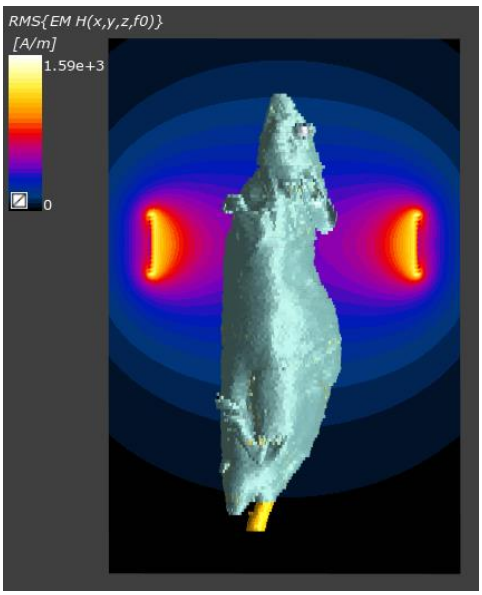

Figure 72: Magnetic field strength inside the OF1 mouse body model for the sinusoidal signal (SN) at 200 kHz and 2 mT represented on plan XZ (C).

3.2.2. Electric field or SAR distribution

In parallel, Figure 73 (A and B) shows the distribution of the electric field strength and SAR inside the mouse body model for 200 kHz and 2 mT, during 30 min of irradiation. The maximum electric field strength covers the body at the dorsal and ventral part of the mouse model and reached a maximum of 29.2 V/m and a maximum SAR of 0.029 W/kg, while lower electric field strength and SAR values are located inside of the body. As we can see in all the figures (Figure 73), the shape of the representation and the scale of the legend changes, reflecting that the electric field strength and SAR decreases slightly with the penetration depth increase.

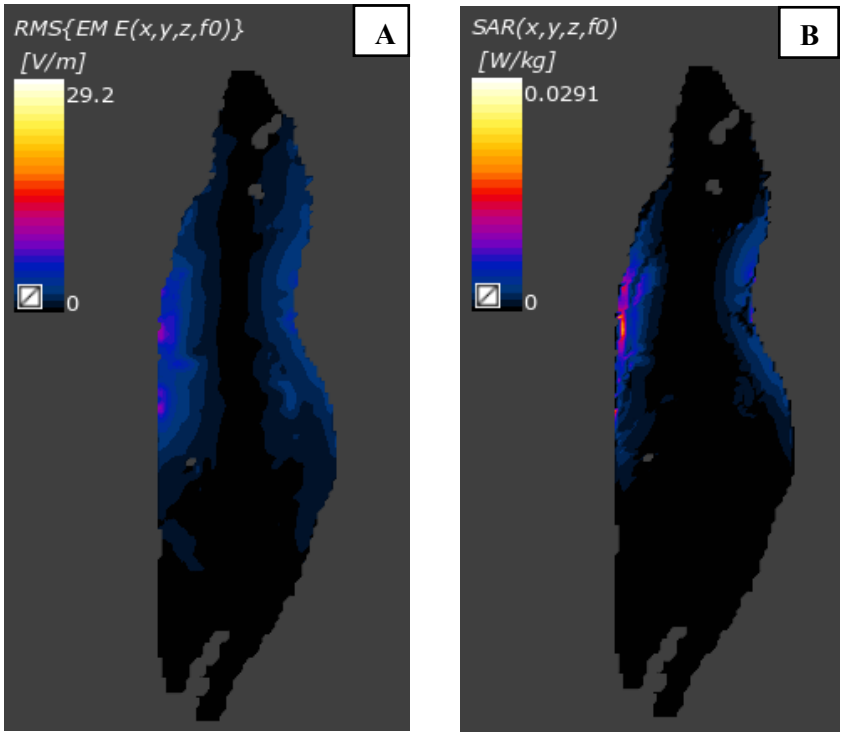

Figure 73: Distribution of the electric field strength (A) and the SAR (B) inside the OF1 mouse body model for the sinusoidal signal (SN) at 200 kHz and 2 mT represented on plan XZ.

3.2.3. Heat distribution

To predict the eddy current effects and evaluate the risk associated with the application of non-sinusoidal signals, in silico models (mouse and human) represent essential tools for the understanding of EMF behaviour within the biological tissues. The OF1 mouse model of g was used for our in-silico study containing 54 tissues defined in the IT'S Foundation database. After extracting the electric field distributed in the mouse body by the sinusoidal signal in Sim4life,

the electric field for the non-sinusoidal signals was modeled in MATLAB for each signal and then imported the heat source to Sim4life for simulating the eddy currents and generating the thermal profile of temperature distribution in the mouse body on plan XZ. The thermal maps in Figure 74 correspond to the SN signal (A) and to the TS signal (B) at 200 kHz and *2* mT, is reported in Figure 74.

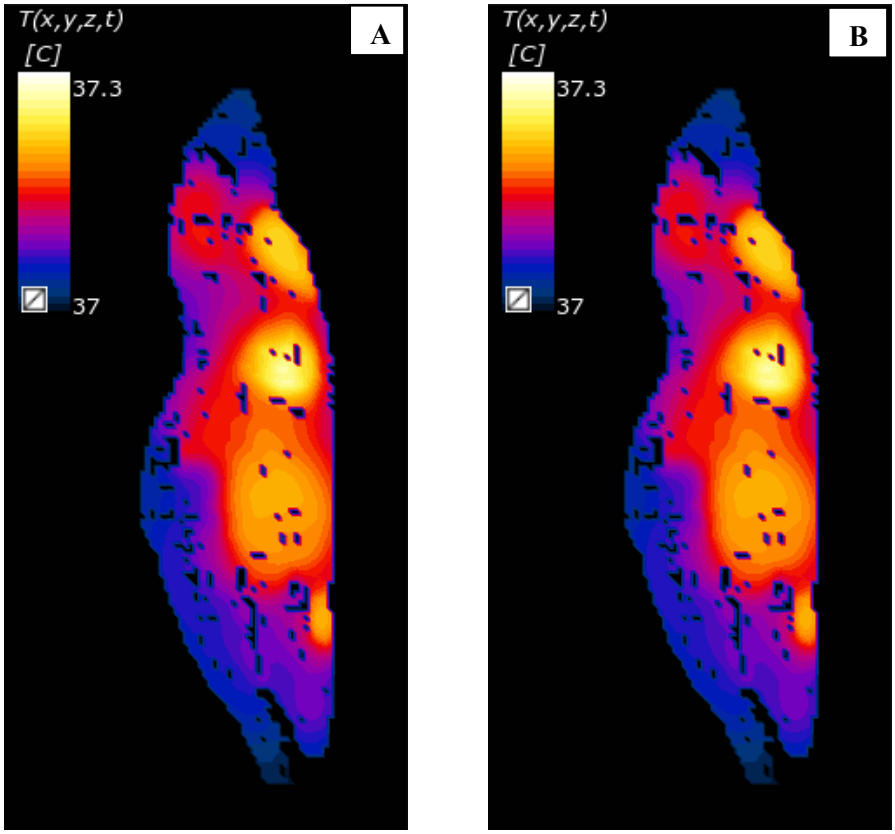

Figure 74: Resulting cross-sectional temperature spatial distribution in a 35.5 g mouse model at t $_{max}$=1800s for Sinusoidal signal (A) and for Trapezoidal-Square signal (B) at f = 200 kHz and 2 mT for 30 min of exposure, represented on plan XZ.

The mouse body model was first tested at 200 kHz and 2 mT for 30 min of exposure using a heat transfer coefficient, between the holder and the external air, fixed at 25 W/m2/K. In Figure 74, we observed no significant eddy current effects with the TS waveform and the temperature increase was estimated by 0.3°C in the heart, liver and glands tissues, similarly to the SN waveform. For the fact that the biological tissues are different in their dielectric properties, the EMF energy absorption was grater by the heart, liver and glands tissues. These results suggested the absence of eddy current effects that could lead to hot spots inside the mouse body and which could be lethal. The in vivo experimental results in Figure 56 were TS and SN were used to

irradiate the mice, demonstrated that there is no lethal effects by the application of these signals for MHT treatment and the mice survived after several exposures of 30 min. Hence, the simulation results on mice are further demonstrating the absence of eddy current effects, were the temperature is stable around a safe level of 37.3°C

Similarly to the in vitro simulation study, the purpose of the in vivo simulation study is to evaluate the safety of the AMF applicator for preclinical tests in terms of EMF dosimetry and to define a threshold limit of the non-sinusoidal AMF signals. Therefore, we investigated the influence of the pulsed alternating magnetic fields (TS, TP, TT, TR) using a wide range of frequency *f* and magnetic field intensity *H,* on inducing eddy currents in the mouse body. Figure 75 reported the temperature variation using a range of AC magnetic field parameters, frequency from 100 kHz to 1000 kHz and magnetic field intensities of 5-15-35mT, using non-sinusoidal waveforms TR, TT, TP, TS compared to the sinusoidal one in Figure 76. The results showed that the non-sinusoidal signals TS and TP have more important eddy current effects compared to the SN one. In contrast, the TT and TR signals showed different outcomes, the TT showed similar eddy currents effects demonstrated by similar temperature increment and the TR showed lower eddy currents effects compared to SN revealed by lower temperature increment. Moreover, negligeable eddy currents have been observed at 5 mT current amplitude for all the frequency range used and among all signals (TS, TP, TT, TR, SN), revealed by a stable temperature around 37°C. At higher magnetic field intensity 15 mT, TS and TP signals gave a temperature increase of 1°C and 0.5 °C, respectively, for 400 kHz. Whereas for TT and SN, a temperature increases up to 0.5°C was observed for 500 kHz. For all the waveforms, the temperature increases exponentially with the frequency at 15 mT where it reached a maximum temperature increment for 1000 kHz, estimated by 43.6°C for TS, 39.5°C for TP, 38.6°C for TT and SN. The TR signal did not show a temperature increment at 15 mT (similar to 5mT) for all frequencies, while at 35 mT a temperature increments up to 0.5°C were observed for 700 kHz. For TT and SN, the temperature increased up to 0.6°C for 300 kHz and 35 mT of amplitude. Also, TS and TP showed a temperature increase up to 2°C and to 0.6°C with TS and

TP, respectively, for 200 kHz and 35 mT. Then, the temperature reached a maximum increment for 1000 kHz, estimated by 63.2°C for TS, 46.7°C for TP, 43°C for TT and SN, 37.9°C for TR.

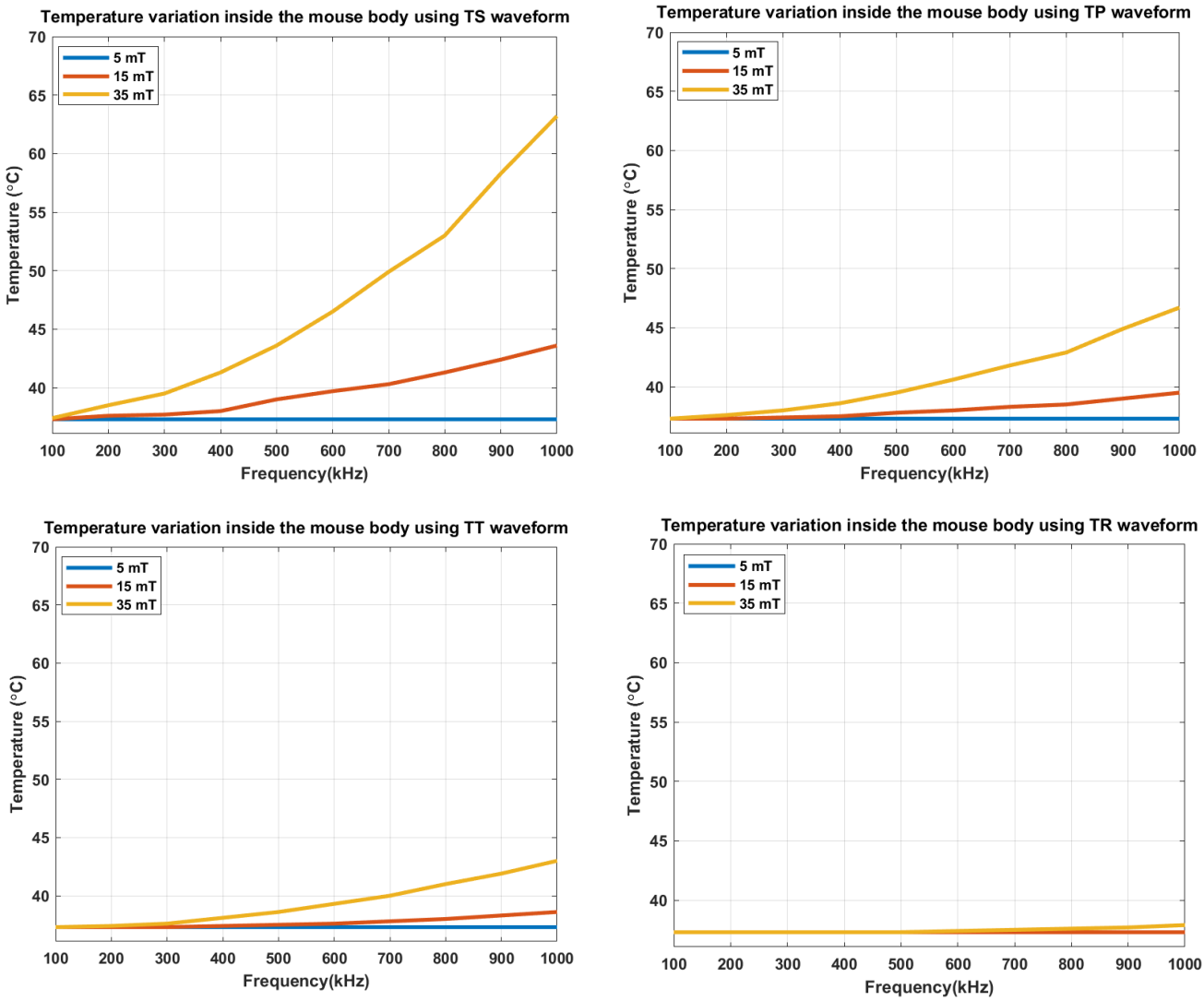

Figure 75: Influence of the non-sinusoidal AMFs TS (A), TP, TT, TR, on the maximum temperature increase in 35.5 g mouse body model, versus the AC magnetic field parameters of frequency from 100 kHz to 1000 kHz and magnetic field intensities of 5-15-35mT and for an exposure duration of 30 min.

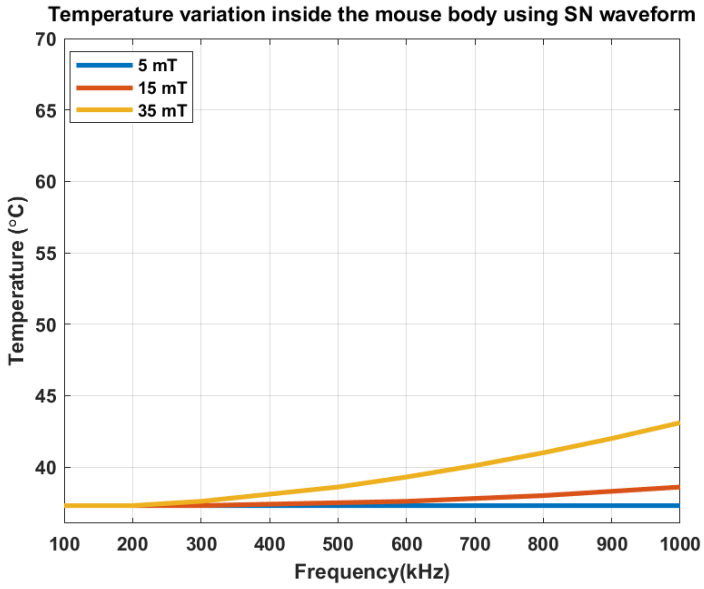

Figure 76: Influence of the sinusoidal AMFs on the maximum temperature increase in a 35.5 g mouse body model versus the AC magnetic field of frequency from 100 kHz to 1000 kHz and magnetic field intensities of 5-15-35mT and for an exposure duration of 30 min.

To recapitulate, Figure 77 and 78, represents the temperature increment versus the product $H \times f$ for all the AMF waveforms: SN, TS, TP, TT, TR, calculated for a cell culture medium and a 35.5 g mouse, respectively. For the sinusoidal AMF, significant heating can be seen with the waveform of high slopes such as TS and TP AMF waveforms. Below the Hergt-Dutz limit (5×10^9 A/(m.s)), negligible temperature increases was observed with all the applied AMF waveforms for both cell culture medium model and mouse model, except or the TS waveform for the cell culture medium model, where non-negligeable temperature changes occurred and temperature raised by 1°C when $H \times f = 4.7 \times 10^9$ A/m.s. Temperature increments lower than 1°C were found only when the product $H \times f < 4.7 \times 10^9$ A/m.s for both models. According to the Atkinson- Brezovitch limit (Atkinson et al., 1984) where the safety limit was assessed at 4.85 $\times$ 10^8 A/(m.s), the temperature changes are considered to be non-negligeable for $H \times f > 3.9 \times 10^8$. The product $H \times f$ for the sinusoidal signals is under the Herget-Dutz limit (Hergt & Dutz, 2007), while it exceeds the Atkinson-Brezovitch limit. Anyway, the proposed biophysical constraint by Atkinson-Brezovitch or the Hergt and Dutz limit don't satisfy our condition for the non-sinusoidal waveform since it take into consideration only the frequency and magnetic field intensity, hence, the product $H \times f$ will be the same among all the waveform of the AMF. Therefore, a new physical constraint should be calculated by considering a specific factor to

each waveform (TS, TP, TT, TR). As seen in both figures (78 and 79), the thermal changes are more important when the applied AMF signal is TS or TP and are quite similar to SN when the applied AMF signal is TP, while they are less important with the TR AMF signal.

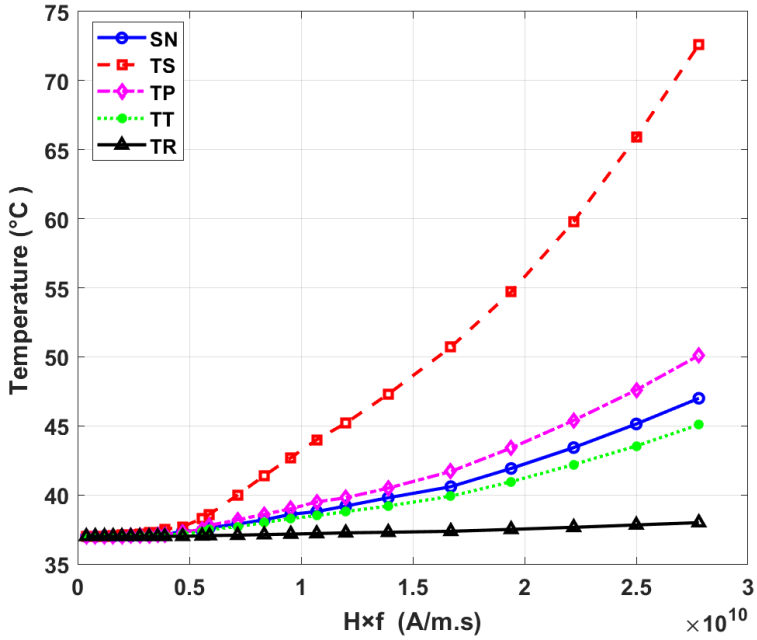

Figure 77: Temperature increases in function of the product H×f A/(m.s) calculated for a cell culture medium-DMEM for 30 min o exposure to AMF.

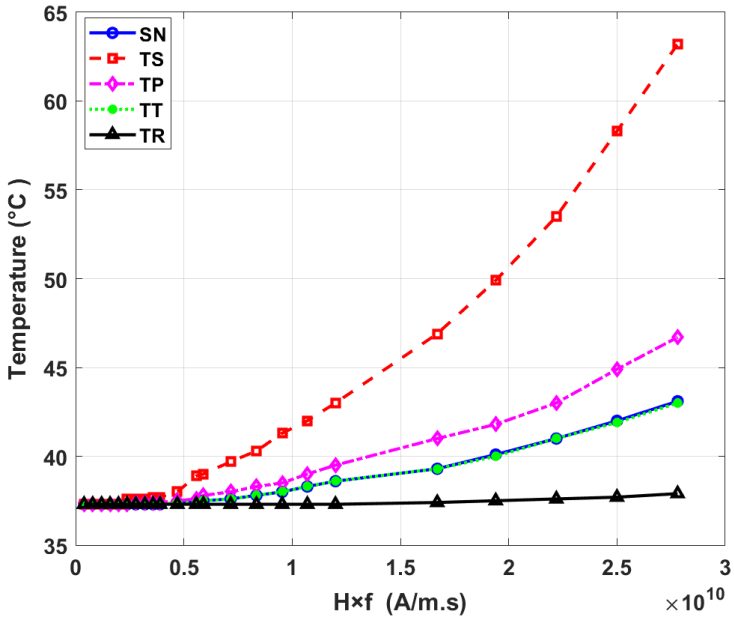

Figure 78: Temperature increases in function of the product H×f A/(m.s) calculated for a 35.5 g mouse model for 30 min o exposure to AMF.

Waveform	*Amplitude [mT]*	*Frequency [kHz]*	*H × f [A/(m.s)]*	*Maximum temperature in the cell culture medium DMEM*	*Maximum temperature in the mouse body tissues*
TS	5	100	3.9e+8	37	37.3
		200	7.9e+8	37.01	37.3
		300	1.2e+9	37.03	37.3
		400	1.59e+9	37.06	37.3
		500	1.98e+9	37.09	37.3
		600	2.38e+9	37.1	37.6
		700	2.78e+9	37.17	37.6
		800	3.20e+9	37.28	37.6
		900	3.58e+9	37.3	37.7
		1000	3.9e+9	37.5	37.7
TS	15	100	1.2e+9	37.03	37.3
		200	2.38e+9	37.1	37.6
		300	3.58e+9	37.3	37.7
		400	4.7e+9	38	38
		500	5.9e+9	38.6	39
		600	7.2e+9	40	39.7
		700	8.35e+9	41.4	40.3
		800	9.54e+9	42.7	41.3
		900	1e+10	44	42
		1000	1.2e+10	45.9	43.6
TS	35	100	2.78e+9	37.17	37.3
		200	5.57e+9	38.3	38.9
		300	8.35e+9	41.4	40.3
		400	1e+10	44	42
		500	1.39e+10	47.3	43.6
		600	1.67e+10	50.7	46.9
		700	1.94e+10	54.7	49.9
		800	2.22e+10	59.8	53.5
		900	2.5e+10	65.9	58.3
		1000	2.78e+10	72.6	63.2
		100	3.9e+8	37	37.3

TP	5	200	7.9e+8	37	37.3
		300	1.2e+9	37	37.3
		400	1.59e+9	37.02	37.3
		500	1.98e+9	37.03	37.3
		600	2.38e+9	37.04	37.3
		700	2.78e+9	37.06	37.4
		800	3.20e+9	37.08	37.4
		900	3.58e+9	37.1	37.4
		1000	3.9e+9	37.1	37.4
TP	15	100	1.2e+9	37	37.3
		200	2.38e+9	37.04	37.3
		300	3.58e+9	37.1	37.4
		400	4.7e+9	37.5	37.5
		500	5.9e+9	37.8	37.8
		600	7.2e+9	38.2	38
		700	8.35e+9	38.6	38.3
		800	9.54e+9	39	38.5
		900	1e+10	39.5	39
		1000	1.2e+10	40.2	39.5
TP	35	100	2.78e+9	37.06	37.4
		200	5.57e+9	37.6	37.6
		300	8.35e+9	38.6	38.3
		400	1e+10	39.5	39
		500	1.39e+10	40.5	39.5
		600	1.67e+10	41.7	41
		700	1.94e+10	43.4	41.8
		800	2.22e+10	45.4	43
		900	2.5e+10	47.6	44.9
		1000	2.78e+10	50.1	46.7
TT	5	100	3.9e+8	37	37.3
		200	7.9e+8	37	37.3
		300	1.2e+9	37	37.3
		400	1.59e+9	37.01	37.3
		500	1.98e+9	37.02	37.3
		600	2.38e+9	37.03	37.3

		700	2.78e+9	37.04	37.3
		800	3.20e+9	37.05	37.3
		900	3.58e+9	37.06	37.3
		1000	3.9e+9	37.08	37.3
TT	15	100	1.2e+9	37	37.3
		200	2.38e+9	37.03	37.3
		300	3.58e+9	37.06	37.3
		400	4.7e+9	37.18	37.4
		500	5.9e+9	37.6	37.5
		600	7.2e+9	37.7	37.6
		700	8.35e+9	38	37.8
		800	9.54e+9	38.3	38
		900	1e+10	38.5	38.3
		1000	1.2e+10	39	38.6
TT	35	100	2.78e+9	37.04	37.3
		200	5.57e+9	37.5	37.4
		300	8.35e+9	38	37.8
		400	1e+10	38.5	38.3
		500	1.39e+10	39.2	38.8
		600	1.67e+10	39.91	39.3
		700	1.94e+10	40.96	40
		800	2.22e+10	42.2	41
		900	2.5e+10	43.55	41.9
		1000	2.78e+10	45.09	43
TR	5	100	3.9e+8	37	37.3
		200	7.9e+8	37	37.3
		300	1.2e+9	37	37.3
		400	1.59e+9	37	37.3
		500	1.98e+9	37	37.3
		600	2.38e+9	37	37.3
		700	2.78e+9	37	37.3
		800	3.20e+9	37	37.3
		900	3.58e+9	37	37.3
		1000	3.9e+9	37	37.3
		100	1.2e+9	37	37.3

TR	15	200	2.38e+9	37	37.3
		300	3.58e+9	37	37.3
		400	4.7e+9	37.01	37.3
		500	5.9e+9	37.06	37.3
		600	7.2e+9	37.09	37.3
		700	8.35e+9	37.13	37.3
		800	9.54e+9	37.17	37.3
		900	1e+10	37.21	37.3
		1000	1.2e+10	37.2	37.3
TR	35	100	2.78e+9	37	37.3
		200	5.57e+9	37.04	37.3
		300	8.35e+9	37.13	37.3
		400	1e+10	37.21	37.3
		500	1.39e+10	37.3	37.3
		600	1.67e+10	37.37	37.4
		700	1.94e+10	37.5	37.5
		800	2.22e+10	37.66	37.6
		900	2.5e+10	37.83	37.7
		1000	2.78e+10	38	37.9
SN	5	100	3.9e+8	37	37.3
		200	7.9e+8	37	37.3
		300	1.2e+9	37.01	37.3
		400	1.59e+9	37.016	37.3
		500	1.98e+9	37.02	37.3
		600	2.38e+9	37.03	37.3
		700	2.78e+9	37.05	37.3
		800	3.20e+9	37.06	37.3
		900	3.58e+9	37.08	37.3
		1000	3.9e+9	37.1	37.3
SN	15	100	1.2e+9	37.01	37.3
		200	2.38e+9	37.03	37.3
		300	3.58e+9	37.08	37.3
		400	4.7e+9	37.4	37.4
		500	5.9e+9	37.6	37.5
		600	7.2e+9	37.9	37.6

		700	8.35e+9	38.2	37.8
		800	9.54e+9	38.6	38
		900	1e+10	38.8	38.3
		1000	1.2e+10	39.5	38.6
SN	35	100	2.78e+9	37.05	37.3
		200	5.57e+9	37.5	37.4
		300	8.35e+9	38.2	37.8
		400	1e+10	38.8	38.3
		500	1.39e+10	39.8	38.8
		600	1.67e+10	40.6	39.3
		700	1.94e+10	41.92	40.1
		800	2.22e+10	43.43	41
		900	2.5e+10	45.14	42
		1000	2.78e+10	47	43.1

Table 4: The AMF's parameters used of waveform, frequency, amplitude, the product H×f and their corresponding maximum temperature increment in the cell culture medium_DMEM and the mouse body tissues for an exposure of 30 min.

3.3. Simulation of the heat generation by MNPs

To simulate MNPs heat generation inside the biological media (DMEM) using sinusoidal and non-sinusoidal waveforms, the Rosensweig's MNPs heat generation model was used as a heat source in sim4life. In this section we aimed to mimic the experimental scenario and to compare the simulation results to the experimental results obtained in Figure 42.C. Therefore, we investigated the temperature generation by MNPs in DMEM at different concentrations of 1mg/ml, 4mg/ml and 8mg/ml for 30 min exposure to the AMF. After computing the sinusoidal AMF in sim4life, we extracted the corresponding H field and we modelled the H Field of the non-sinusoidal ones using Fourier coefficients, then we created the heat source from Rosensweig model (Equation 21) using 300 kHz and 2.78 mT.

The temperature distribution by MNPs in the petri dish exposed to TP AMF at 300 kHz and 2 mT reported in Figure 79, have shown a linear response to the concentration of MNPs. The comparison between these results and the experimental results obtained in Figure 42.C, where MNPs have been exposed to TP at similar concentrations for 30 min, have revealed a difference in the maximum temperature reached for each concentration. The experimental results obtained

for TP (300 kHz and 2.78 mT) at 1 mg/ml, 4mg/ml and 8 mg/ml had higher temperature values of 38.15°C, 38.61°C and 38.9°C, respectively. Whereas the simulation results obtained, for same AMF conditions, were lower. We obtained an increase to 37.2°C for 1mg/ml, 37.9°C for 4 mg/ml and 38.7°C for 8 mg/ml. The Rosensweig model in (Rosensweig, 2002) does not match experimental data or the real behaviour of MNPs, because this model assumes a linear response between the applied magnetic field and the magnetization of MNPs, which can be non-linear.

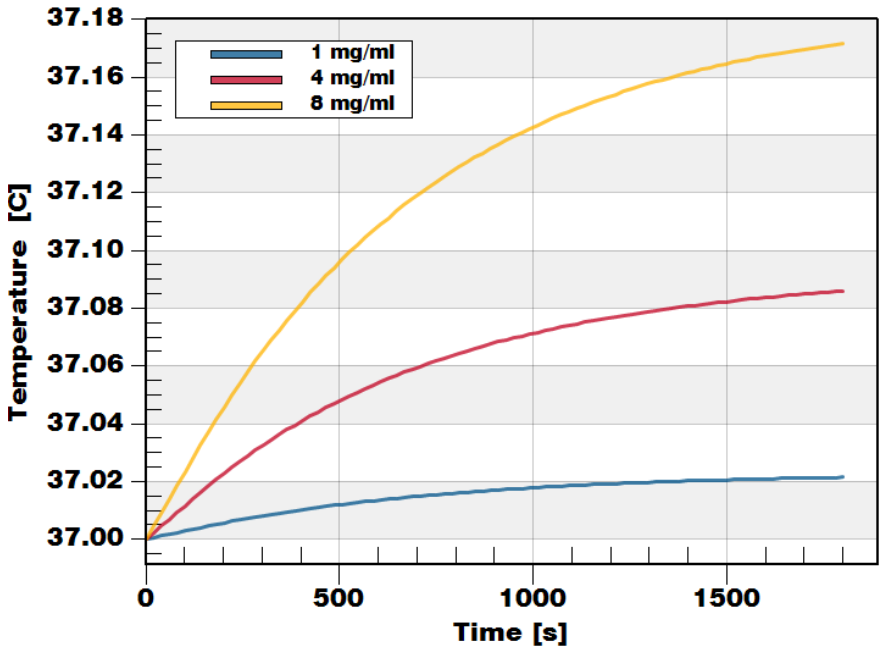

Figure 79: Temperature spatial variation in function of time (s) by TP-AMF signal inside the cell culture medium for different concentrations: 1 mg/ml, 4 mg/ml and 8 mg/ml at 300 kHz and 2.78 mT.

Table 5 shown the maximum temperature increments by MNPs at t=1800s reached for each AMF waveform at 300 kHz and 2.78 mT. The TS waveform had the highest temperature increase among all the modelled waveforms for the same conditions, thus, the TS confirmed to be the most efficient waveform in producing more heat than SN, but also, TP, TT and TR.

In contrast, when we evaluated the eddy current effects, we observed that both TS and TP had higher temperature increase then the SN and TT gave similar effects as the SN, due to the fact that the energy absorbed by the biological media using TS and/or TP was more important than that of the SN. This energy absorbed was modelled using the summation of the extracted electric fields from sim4life and which changes with the frequency computed in sim4life. While, when we modelled MNPs heating we used the summation of the extracted H field which does not change with frequency and have a fixed value. Hence by multiplying the H field into

Fourier coefficients of the TP waveform, the H field become lower than the H field of SN and led to lower heat power generation.

	Waveform				
Concentration	**TS**	**TP**	**TT**	**TR**	**SN**
1 mg/ml	37°C	37°C	37°C	37°C	37°C
4 mg/ml	37.2°C	37.1°C	37.1°C	37°C	37.2°C
8 mg/ml	37.4°C	37.2°C	37.2°C	37.51°C	37.4°C

Table 5: Maximum temperature generated by MNPs in the cell culture medium model at t_{max}=1800 s by the non-sinusoidal signals TS, TP, TT, TR and the SN for different concentrations :1mg/ml, 4mg/ml and 8 mg/ml at 300 kHz 2.78 mT.

3.4. Magnetic hyperthermia experimental study: dosimetry

The experimental part was carried out in the MAGNACHARTA laboratory of the BLKAN CENTER. During my work, I used two different hyperthermia systems to measure the Specific Absorption Rate-SAR of my sample of APS-SPION nanoparticles of 12 nm. The presentation of the heating curve and the examination of the SAR was made by the program Origin Pro.

SAR is the rate at which energy is absorbed by the magnetic nanoparticles when exposed to electromagnetic radiation. Calorimetric methods can be used to measure SAR, which involve measuring the temperature increase of a sample exposed to electromagnetic radiation. Calorimetric methods are often used in research settings to study the effects of electromagnetic radiation on biological tissues and materials.

To measure the increase in temperature two different heating systems have been used. The first hyperthermia system consists of a common coil (1.2 kW Ambrell Easyheat 0112, New York, United States), with an inner diameter of the coil of 2.5 cm and 8 turns, it induces an alternating magnetic field of frequency 375 kHz and amplitude 20–70mT, according to the applied AC current figure 80, and the second system SPG-10 Ultrahigh Frequency Induction Heating Machine provided by Shuangping Corporation with 2.5cm of the inner diameter of the coil and 2 turns, works at a frequency of 765 kHz presented in the figure 81.

Figure 80: Ambrell Easyheat Heating System.

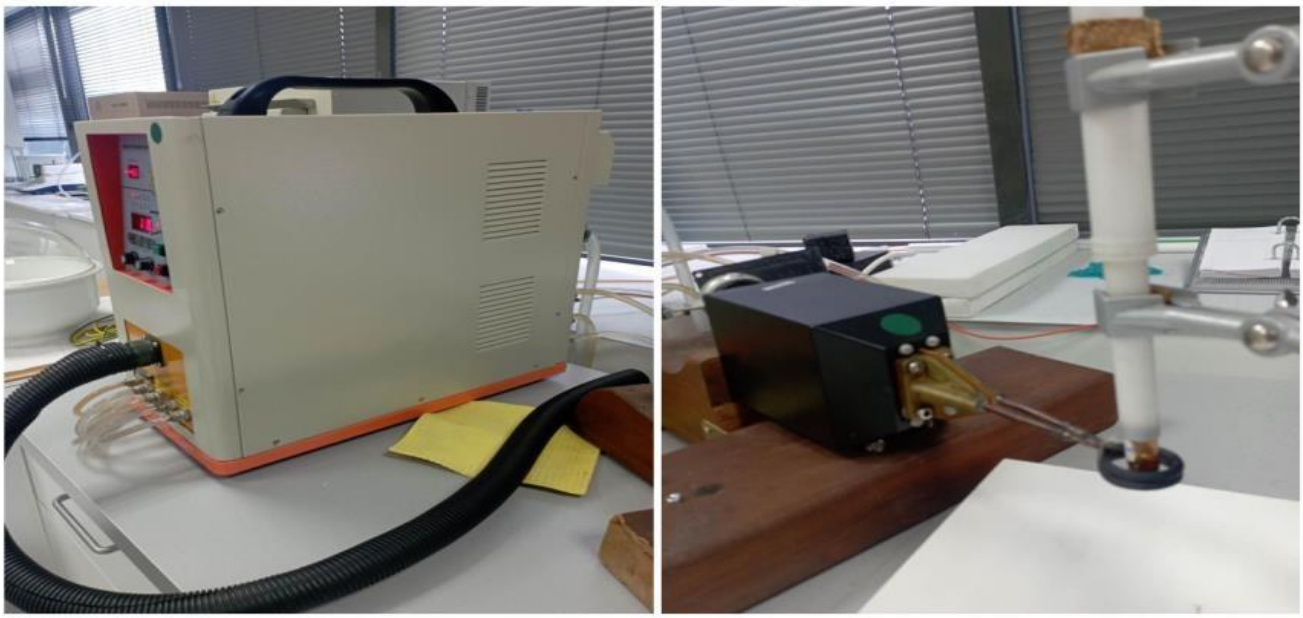

Figure 81: SPG-10 Ultrahigh Frequency Induction Heating Machine.

Fitting of heating curves refers to the process of analyzing experimental data to determine the thermal properties of a sample, typically by fitting a mathematical model to the heating curve data. The goal is to obtain accurate estimates of the specific absorption rate SAR. Origin Pro (version 2023) was used to construct the curve fit. Using a defined mathematical model.

Here are the steps involved in fitting the heating curves:

- Collect heating curve data: Experimental data is collected in a file by heating the APS-MNP sample at a constant rate and recording its temperature as a function of time.
- Select a mathematical model: the mathematical model for fitting follows the mathematical model ExpDec1 in Origin (One-phase exponential decay function with time constant parameter):

$$y = y0 + A\ .e\ (-\ x\ t) \tag{38}$$

- Evaluate the goodness of fit: The quality of the fit is evaluated by calculating statistical metrics such as the sum of squared errors, the root means square error, or the R-squared value. A good fit is one that has low error and high R-squared value.
- Finally, the fitted parameters are used to calculate the SAR. The mathematical model used to calculate it is depicted in the Equation 38.

Overall, fitting heating curves is a powerful technique for analyzing the thermal properties of materials and can provide valuable insights into their behavior. The following curves (Figure 82) correspond to the increase of temperature with the nanoparticles sample measured with the SPG-10 Ultrahigh Frequency Induction Heating System at 765kHz/20mT (**A**) and the Ambrell Easyheat Heating System at 375kHz/20mT (**B**).

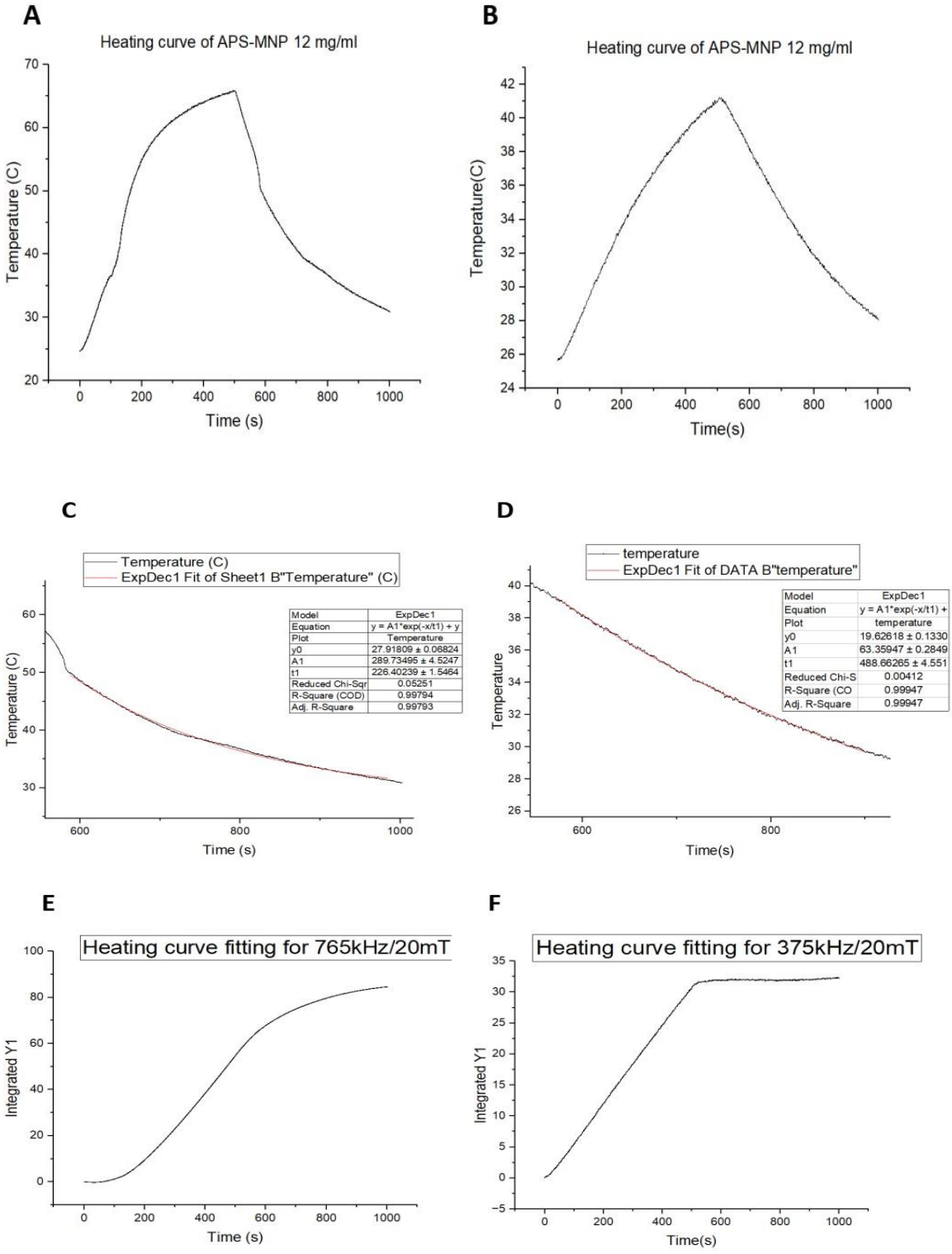

Figure 82: Heating curves of APS-MNP 12 nm A (765kHz/20mT) and B (375kHz/20mT). Fitting heat curves E and F by Origin program C and D represent the decay period from cooling curves.

The decay period (cooling period) was used to estimate the SAR. The purpose from using the cooling period is to extract the actual temperature rise caused by the magnetic field of the nanoparticles alone to increase the accuracy of the SAR estimate later by excluding additional heating contributions. By exponentially adjusting the cooling step of the experimental curve, we can estimate the cooling constant and hence the actual temperature increase after removing the heat exchange between the samples and the environment. By applying this correction, we transformed a non-adiabatic heating curve into an adiabatic curve.

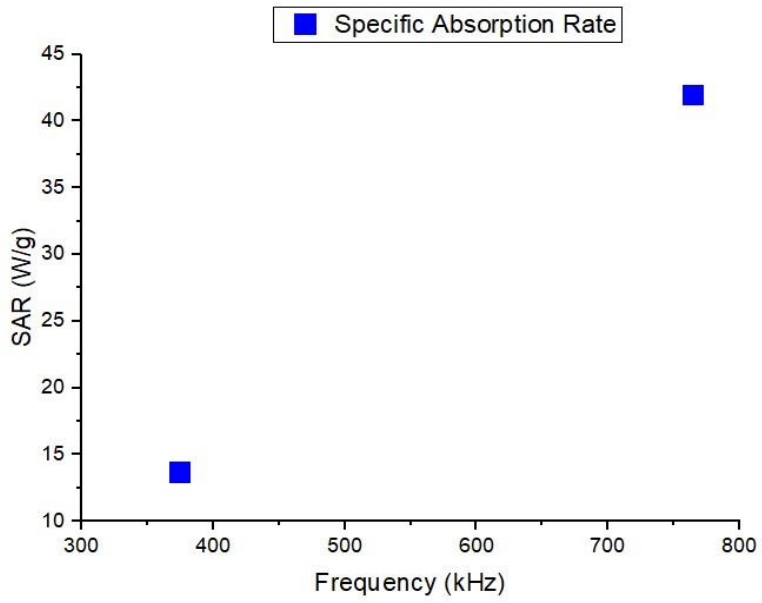

Figure 83: The graph represents the Specific Absorption Rate of 12.3 mg/ml of APS-MNP with two different frequencies 375kHz and 765kHz at 20mT.

The Specific Absorption Rate (SAR) has been estimated using Origin Pro software by analyzing the temperature increase of APS-MNP sample exposed to a defined electromagnetic field. When the SPG-10 Ultrahigh Frequency Induction Heating System was used at 765kHz/20mT the estimated SAR value reached 41.9 W/g much higher than with the estimated SAR value measured using the Ambrell Easyheat Heating System at 375kHz/20mT of 13.63 W/g (Figure 83). The heating rate of magnetic nanoparticles increased with large values of the AMF parameters. This is because a stronger magnetic field induces more rapid and efficient rotation of the nanoparticles, resulting in greater energy dissipation as heat. At low frequencies, the

magnetic moment of the nanoparticles can align with the field direction, leading to efficient heating. At higher frequencies, however, the magnetic moment may not be able to follow the rapidly changing field direction, leading to less efficient heating. The optimal frequency for heating nanoparticles will depend on their size, shape, and magnetic properties. In general, the heating rate of magnetic nanoparticles can be optimized by selecting an AMF with an appropriate intensity and frequency for a given set of nanoparticles. However, it is important to note that excessive heating can damage surrounding tissues, and the temperature must be carefully monitored to ensure the safety and efficacy of the treatment. Therefore, careful optimization of the magnetic field parameters is necessary to achieve the desired therapeutic effect while minimizing potential side effects.

4. Discussion

In cancer treatment using EMFs, a precise control is necessary to achieve therapeutic effects without causing damage to surrounding tissues. The selection of AC magnetic field parameters of frequency and amplitude must align with the safety restrictions to ensure optimal performance, efficiency, safety, and compliance with application-specific requirements. Mismatched parameters can lead to poor energy transfer, ineffective results, or damage to the targeted biosystem and even to the applicator. Thus, understanding the interaction between the applicator, the EM field, and the target medium is critical for successful implementation. Besides, inductive coils in EMFs applicators are used in low-frequency applications such as in MHT. Low-frequency fields generally penetrate deeper and may induce electrical currents in the body, while high-frequency EM fields (e.g., microwaves) are absorbed more superficially and can cause tissue heating (Foster & Schwan, 1989) (Ziegelberger et al., 2020). MHT applicators, as described previously, generate the magnetic fields to heat the nanoparticles in a targeted area. When the nanoparticles are exposed to electromagnetic radiation, they absorb the energy of the radiation and convert it into heat. The rate at which this conversion occurs depends on a number of factors, including the size and shape of the nanoparticles, and the properties of the material from which the nanoparticles are manufactured. Besides, the magnetic field intensity and the frequency of the radiation and the waveform of the AMF.

Therefore, simulations models are essential tools for a comprehensive understanding of the MNPs behaviour and to support the experimental studies. The evaluation of the safety of a MHT

applicator before preclinical studies (in vitro, in vivo) is important in order to predict and prevent the level at which the radiation intensity may lead to damage effects and to optimize the treatment procedure using an optimum frequency, amplitude and signal's waveform. Therefore, the evaluation of eddy current effects by non-sinusoidal signals using Sim4life computational platform was the main objective of my internship at the Aristotle University, seeking to define the threshold limit of these signals application in biological media.

As shown in our study, the thermal simulations obtained with Sim4Life demonstrate negligeable eddy current effects in biological media or biological tissues at low magnetic field intensities and/or frequencies among all the applied signals (TS, TP, TT, TR, SN). In contrast, the eddy current effects became no more negligeable for larger magnetic field intensities and/or frequencies, and that are more important with waveforms of higher slopes such as TS and TP, while TT and SN had similar effects, and TR was the less efficient waveform and induced the weakest eddy currents. Anyway, the selection of the frequency and magnetic field intensity should be done in accordance to the waveform shape of the EMFs. Furthermore, a reduction or an increase in the time duration of the EM applied field will leads to a reduction or an increment in the eddy current effects (Vicentini et al., 2022).

Finally, the heating simulations by MNPs using the Rosensweig models demonstrate a linearity between the heat generated and the concentration of MNPs. The heating rate by MNPs was higher with the TS signal compared to the SN and the rest of signals. The adequate mathematical model that describes the heat generation by MNPs when subjected to non-sinusoidal AMF is still unknown but we assume that the dependency of the heating rate of nanoparticles on the waveform's slope can be explained by the fact that when increasing the slope of the waveform, the rates of magnetic field energy absorption and conversion to heat by MNPs increase considerably due to faster reorientation and alignment of MNPs magnetic moments with the direction of the magnetic field, compared to the sinusoidal, or the MNPs magnetic moments reach a larger alignment with the direction of the magnetic field when using a higher slope AMF. Overall, the simulation data did not match with the experimental data and a more suitable model able to simulate the real behaviour of MNPs needs to be developed or the Rosensweig model needs to be enhanced.

5. Conclusion

Our findings from the in-*silico* simulations through the Sim4life allow us to predict the thermal behavior inside biological materials under the exposure to pulsed AMFs within a wide range of frequencies, amplitudes, and waveforms, providing beneficial pieces of information on the eddy currents heating during preclinical experiments. Besides, it helped us to study the heat generation by MNPs in biological media during MHT treatment. This FEM-based numerical analysis helped us to define the safety aspects earlier in the treatment process and is valuable for preclinical treatment planning to avoid any situations where hot spots may be induced. The numerical data achieved by our study are beneficial to optimize MHT treatment and to define the optimum AMFs parameters to be applied in experimental investigation, thereby addressing ethical concerns related to animal testing. The obtained thermal results inside the DMEM have shown negligible eddy current heating by applying the non-sinusoidal AMFs at 200 kHz and 2 mT, demonstrated by a stable spatial temperature distribution over 37°C, which matches the experimental results, where no increase in temperature has been shown in cell culture medium during in vitro tests at the same AMF conditions (Souiade et al., 2023) (Souiade et al., 2025) . Moreover, the thermal simulation results inside the mouse tissues revealed negligible eddy current heating at lower magnetic field intensities of 2 mT and 5 mT while important and non-negligeable ones occurs in both phantoms (DMEM and mouse) at 15mT and 35mT, specifically for high frequencies, demonstrated by a temperature increase inside the biological tissues. The temperature increment becomes more important with AMFs waveforms of high slope, mainly the TS and TP waveforms, which will lead to significant damage in tissues during the hyperthermic treatment. The Hergt-Dutz seems to be a guarantee of safety compared to the Atkinson-Brezovitch-Chakraborty criterion, and was our guideline in this research to ensure safe application of the pulsed AMFs for preclinical testing, since its adoption in animal studies is helpful to mitigate risks of tissue damage from eddy currents, and enabling researchers to maximize MHT efficacy.

VII Chapter 6: Scientific publication and original contributions

VII.1 Magnetic hyperthermia

VII.1.1 Conferences:

- *35th Annual Meeting of the European Society for Hyperthermic Oncology-ESHO Cologne, Germany, 2023.* ***"Improving the efficacy of magnetic nanoparticle-mediated hyperthermia using trapezoidal pulsed electromagnetic fields as an in vitro anticancer treatment in uveal melanoma and glioblastoma multiforme cell lines".***
- *Congreso Annual de la Sociedad Española de Inginieria Biomédica (CASEIB) XXXVII, Cartagena, Spain, 2023: "****Improving the efficacy of Magnetic nanoparticle-mediated hyperthermia using trapezoidal pulsed electromagnetic fields as an in vitro anticancer treatment in uveal melanoma and glioblastoma multiforme cell lines".***
- *36th Annual Meeting of the European Society for Hyperthermic Oncology-ESHO Malaga, Spain, 2024.* ***"Pulsed Alternating Fields Magnetic Hyperthermia in Combination with Chemotherapy as a Cancer Treatment for Glioblastoma Multiforme: An In Vitro and In Silico Study".***

VII.1.2 Scientific Publications:

- *MDPI International Journal of Molecular Sciences: Souiade, L., Domingo-Diez, J., Alcaide, C., Gámez, B., Gámez, L., Ramos, M., & Serrano Olmedo, J. J. (2023): "****Improving the Efficacy of Magnetic Nanoparticle-Mediated Hyperthermia Using Trapezoidal Pulsed Electromagnetic Fields as an In Vitro Anticancer Treatment in Melanoma and Glioblastoma Multiforme Cell Lines****".*
- *MDPI Nanomaterials: Souiade, L., Rodriguez-Garcia, M.-R., Serrano-Olmedo, J.-J., & Ramos-Gómez, M. (2025): "****Pulsed Alternating Fields Magnetic Hyperthermia in Combination with Chemotherapy (5-Fluorouracil) as a Cancer Treatment for Glioblastoma Multiform: An In Vitro Study****".*

VII.2 Optical hyperthermia

VII.2.1 Conferences

- *35th Annual Meeting of the European Society for Hyperthermic Oncology-ESHO Cologne, Germany, 2023.* ***"Effectiveness of Gold Nanorods of Different Sizes in Photothermal Therapy to Eliminate Melanoma and Glioblastoma Cells".***
- *Congreso Annual de la Sociedad Española de Inginieria Biomédica (CASEIB) XXXVII, Cartagena, Spain, 2023: "****Effectiveness of Gold Nanorods of Different Sizes in Photothermal Therapy to Eliminate Melanoma and Glioblastoma Cells".***

VII.2.2 Scientific Publications

- *MDPI International Journal of Molecular Sciences: Domingo-Diez, J., Souiade, L., Manzaneda-González, V., Sánchez-Díez, M., Megias, D., Guerrero-Martínez, A., Ramírez-Castillejo, C., Serrano-Olmedo, J., & Ramos-Gómez, M. (2023): "****Effectiveness of Gold Nanorods of Different Sizes in Photothermal Therapy to Eliminate Melanoma and Glioblastoma Cells"****.*

VIII Chapter 7: Conclusion

Our study investigated the role of non-sinusoidal AMFs in increasing the therapeutic effects and enhancing MHT treatment against cancer for preclinical tests. A newly designed MHT applicator able to generate different AMFs waveforms and a frequency rage from 100 kHz to 500 kHz and 1MHz, have been tested in vitro on two different cancer cell lines (glioblastoma and melanoma) and in vivo on a melanoma tumor model in C57BL/6 mice. On another hand, the eddy current effects of the non-sinusoidal AMFs have been evaluated using the software Sim4life and MNPs heat generation have been modelled, in order to define the safety limit for the new waveforms and to study the behaviour of MNPs under sinusoidal and non-sinusoidal waveforms.

We succeed in demonstrating an increase in the cell death rate in both glioblastoma and melanoma cell lines using the TS and TP waveforms. These waveforms were more efficient against cancer and had considerable capability to provoke significant damage in cells compared to the conventional waveform SN. The in vitro results showed to increase cell death significantly on the B16F10 cell line to 31 ± 2% by TP and to 17 ± 5% by TS at 1 mg/mL, and to 46 ± 15% in CT2A by TP-AMF at 4 mg/m. We also demonstrated the efficacy of the synergistic effect between MHT produced by TS waveform and the chemotherapeutic drug (5-FU) in increasing the cell death rate to 58.9±2%, compared to MHT alone to 31.4±3%. Cell death was primarily driven by the necrosis pathway (47.3±2%) and apoptosis (11.6±2). This combination of treatments has improved the therapeutic effects more, enhanced better the in vitro treatment outcomes and produced an enhanced immunogenic cell death compared to the application of MHT produced by TS waveform as a single treatment. We observed an increase in the CRT positive cells to 17±1% using the combined treatment, whereas only 10±1% was produced by MHT treatment alone, this suggests that the combination can promote immune system activation to target and destroy the remaining cancer cells via APC stimulation by CRT exposure on cancer cells surface.

The in vivo preliminary results were also positive and demonstrated a slow tumor growth and a reduction of tumor weight in the C57BL/6 mice group treated by several sessions of MHT produced by TS-AMF, compared to the mice group treated by MHT produced by SN-AMF. The tumor weight reduction was significant compared to the control group. The mice survived after several exposures to non-sinusoidal AMFs which demonstrated again the application safety of these new signals.

The thermal data and temperature profiles obtained from the in-*silico* study within the high resolution digital phantoms used provided beneficial informations for fututе application f these TPAMFs for preclinical assays. The results have shown negligeable eddy current effects by using the non-sinusoidal signals at the magnetic field parameters f =200 kHz and H = 2 mT, demonstrated by a stable temperature around 37°C. These simulation results match with the experimental results, where no increase in temperature has been shown in cell culture medium during in vitro tests. The simulations revealed non-negligeable eddy currents at higher magnetic field intensities of 35 mT and 15 mT for high frequencies, this is indicated by a temperature increase obtained in the biological media and/or biological tissues. The temperature increment becomes more important with signals of high slope, such as, the TS and TP waveforms, these led to more significant eddy current effects.

The outcomes achived by this study hold meaningful benefits for MHT treatment and future studies as the non-sinusoidal signals demonstrated their potential enhanement to the traditional signlas. The approach was explored through in vitro, in vivo, and in-*silico* tests, to show the great contribution of the new signals in enhancing the treatment against the most dangerous form of cancer, beside, their safe application in biological tissues. The application of TPAMFs will allow for lower drug doses making it more safe and adequate treatment . Moreover, the combination with cancer treatment traditional methods, such as chemotherapy and radiotherapy, will be a better alternative for cancer treatment then MHT as single treatment for both preclinical and clinical assays. For future clinical application, in-silico simulations on human phantoms will be needed before the application of the TPAMFs in MHT clinical assays, in order, to evaluate the hot spots occurrence in tissues, since the human body is larger in size which will increase the eddy current effects.

References

Abbas, Z., & Rehman, S. (2018). An Overview of Cancer Treatment Modalities. In *Neoplasm*. InTech. https://doi.org/10.5772/intechopen.76558

Ahmed, A., & Tait, S. W. G. (2020). Targeting immunogenic cell death in cancer. *Molecular Oncology*, *14*(12), 2994–3006. https://doi.org/10.1002/1878-0261.12851

Ahmed, S., Rajak, B. L., Gogoi, M., & Sarma, H. D. (2020). Magnetic nanoparticles mediated cancer hyperthermia. In *Smart Healthcare for Disease Diagnosis and Prevention*. INC. https://doi.org/10.1016/B978-0-12-817913-0.00016-X

Ajinkya, N., Yu, X., Kaithal, P., Luo, H., Somani, P., & Ramakrishna, S. (2020). Magnetic iron oxide nanoparticle (Ionp) synthesis to applications: Present and future. *Materials*, *13*(20), 1–35. https://doi.org/10.3390/ma13204644

Akimov, Y. (2022). Theory of electromagnetic fields. *Emergent Micro and Nanomaterials for Optical, Infrared, and Terahertz Applications*, *5*, 23–60. https://doi.org/10.1201/9781003202608-2

Aklan, B., Zilles, B., Paprottka, P., Manz, K., Pfirrmann, M., Santl, M., Abdel-Rahman, S., & Lindner, L. H. (2019). Regional deep hyperthermia: quantitative evaluation of predicted and direct measured temperature distributions in patients with high-risk extremity soft-tissue sarcoma. *International Journal of Hyperthermia*, *36*(1), 170–185. https://doi.org/10.1080/02656736.2018.1545098

Allia, P., Barrera, G., & Tiberto, P. (2019). Nonharmonic Driving Fields for Enhancement of Nanoparticle Heating Efficiency in Magnetic Hyperthermia. *Physical Review Applied*, *12*(3). https://doi.org/10.1103/PhysRevApplied.12.034041

Alrushaid, N., Khan, F. A., Al-Suhaimi, E. A., & Elaissari, A. (2023). Nanotechnology in Cancer Diagnosis and Treatment. *Pharmaceutics*, *15*(3). https://doi.org/10.3390/pharmaceutics15031025

Alwani, S., Kaur, R., Michel, D., Chitanda, J. M., Verrall, R. E., Karunakaran, C., & Badea, I. (2016). Lysine-functionalized nanodiamonds as gene carriers: Development of stable colloidal dispersion for in vitro cellular uptake studies and siRNA delivery application. *International Journal of Nanomedicine*, *11*, 687–702. https://doi.org/10.2147/IJN.S92218

Amaya-Jaramillo, C. D., Pérez-Portilla, A. P., Serrano-Olmedo, J. J., & Ramos-Gómez, M. (2017). Induction of cell death by magnetic particles in response to a gradient magnetic field inside a uniform magnetic field. *Journal of Nanoparticle Research*, *19*(10). https://doi.org/10.1007/s11051-017-4018-0

Arndt-Jovin, D. J., & Jovin, T. M. (1989). Fluorescence Labeling and Microscopy of DNA. *Methods in Cell Biology*, *30*(C), 417–448. https://doi.org/10.1016/S0091-679X(08)60989-9

Atkinson, W. J., Brezovich, I. A., & Chakraborty, D. P. (1984). Usable Frequencies in Hyperthermia with Thermal Seeds. *IEEE Transactions on Biomedical Engineering*, *BME-31*(1), 70–75. https://doi.org/10.1109/TBME.1984.325372

Balivada, S., Rachakatla, R. S., Wang, H., Samarakoon, T. N., Dani, R. K., Pyle, M., Kroh, F. O., Walker, B., Leaym, X., Koper, O. B., Tamura, M., Chikan, V., Bossmann, S. H., & Troyer, D. L. (2010). A/C magnetic hyperthermia of melanoma mediated by iron(0)/iron oxide core/shell magnetic nanoparticles: A mouse study. *BMC Cancer*, *10*. https://doi.org/10.1186/1471-2407-10-119

Balousis, A., Maniotis, N., & Samaras, T. (2021). Improvement of magnetic particle hyperthermia: Healthy tissues sparing by reduction in eddy currents. *Nanomaterials*, *11*(2), 1–11. https://doi.org/10.3390/nano11020556

Barrera, G., Allia, P., & Tiberto, P. (2020). Fine tuning and optimization of magnetic hyperthermia treatments using versatile trapezoidal driving-field waveforms. *Nanoscale Advances*, *2*(10), 4652–4664. https://doi.org/10.1039/d0na00358a

Bayda, S., Adeel, M., Tuccinardi, T., Cordani, M., & Rizzolio, F. (2020). The history of nanoscience and nanotechnology: From chemical-physical applications to nanomedicine. *Molecules*, *25*(1), 1–15. https://doi.org/10.3390/molecules25010112

Behrouzkia, Z., Joveini, Z., Keshavarzi, B., Eyvazzadeh, N., & Aghdam, R. Z. (2016). Hyperthermia: How can it be used? *Oman Medical Journal*, *31*(2), 89–97. https://doi.org/10.5001/omj.2016.19

Beola, L., Asín, L., Fratila, R. M., Herrero, V., De La Fuente, J. M., Grazú, V., & Gutiérrez, L. (2018). Dual Role of Magnetic Nanoparticles as Intracellular Hotspots and Extracellular Matrix Disruptors Triggered by Magnetic Hyperthermia in 3D Cell Culture Models. *ACS Applied Materials and Interfaces*, *10*(51), 44301–44313. https://doi.org/10.1021/acsami.8b18270

Beola, L., Iturrioz-Rodríguez, N., Pucci, C., Bertorelli, R., & Ciofani, G. (2023). Drug-Loaded Lipid Magnetic Nanoparticles for Combined Local Hyperthermia and Chemotherapy against Glioblastoma Multiforme. *ACS Nano*, *17*(18), 18441–18455. https://doi.org/10.1021/acsnano.3c06085

Berridge, M. V., Herst, P. M., & Tan, A. S. (2005). Tetrazolium dyes as tools in cell biology: New insights into their cellular reduction. *Biotechnology Annual Review*, *11*(SUPPL.), 127–152. https://doi.org/10.1016/S1387-2656(05)11004-7

Bettaieb, A., & Averill-Bates, D. A. (2015). Thermotolerance induced at a mild temperature of 40°C alleviates heat shock-induced ER stress and apoptosis in HeLa cells. *Biochimica et Biophysica Acta - Molecular Cell Research*, *1853*(1), 52–62. https://doi.org/10.1016/j.bbamcr.2014.09.016

Brusentsov, N. A., Gogosov, V. V., Brusentsova, T. N., Sergeev, A. V., Jurchenko, N. Y., Kuznetsov, A. A., Kuznetsov, O. A., & Shumakov, L. I. (2001). Evaluation of ferromagnetic fluids and suspensions for the site-specific radiofrequency-induced hyperthermia of MX11 sarcoma cells in vitro. *Journal of Magnetism and Magnetic Materials*, *225*(1–2), 113–117. https://doi.org/10.1016/S0304-8853(00)01238-5

Cai, K., Wang, A. Z., Yin, L., & Cheng, J. (2017). Bio-nano interface: The impact of biological environment on nanomaterials and their delivery properties. *Journal of Controlled Release*, *263*, 211–222. https://doi.org/10.1016/j.jconrel.2016.11.034

Caizer, C. (2021). Optimization study on specific loss power in superparamagnetic hyperthermia with magnetite nanoparticles for high efficiency in alternative cancer therapy. *Nanomaterials*, *11*(1), 1–22. https://doi.org/10.3390/nano11010040

Carter, T. J., Agliardi, G., Lin, F. Y., Ellis, M., Jones, C., Robson, M., Richard-Londt, A., Southern, P., Lythgoe, M., Zaw Thin, M., Ryzhov, V., de Rosales, R. T. M., Gruettner, C., Abdollah, M. R. A., Pedley, R. B., Pankhurst, Q. A., Kalber, T. L., Brandner, S., Quezada, S., … Chester, K. (2021). Potential of Magnetic Hyperthermia to Stimulate Localized Immune Activation. *Small*, *17*(14). https://doi.org/10.1002/smll.202005241

Chang, D., Lim, M., Goos, J. A. C. M., Qiao, R., Ng, Y. Y., Mansfeld, F. M., Jackson, M., Davis, T. P., & Kavallaris, M. (2018). Biologically targeted magnetic hyperthermia: Potential and limitations. *Frontiers in Pharmacology*, *9*(AUG). https://doi.org/10.3389/fphar.2018.00831

Chaturvedi, V. K., Singh, A., Singh, V. K., & Singh, M. P. (2018). Cancer Nanotechnology: A New Revolution for Cancer Diagnosis and Therapy. *Current Drug Metabolism*, *20*(6), 416–429. https://doi.org/10.2174/1389200219666180918111528

Chen, B. W., Chiu, G. W., He, Y. C., Huang, C. Y., Huang, H. T., Sung, S. Y., Hsieh, C. L., Chang, W. C., Hsu, M. S., Wei, Z. H., & Yao, D. J. (2021). Extracellular and intracellular intermittent magnetic-fluid hyperthermia treatment of SK-Hep1 hepatocellular carcinoma cells based on magnetic nanoparticles coated with polystyrene sulfonic acid. *PLoS ONE*, *16*(2 February), 1–19. https://doi.org/10.1371/journal.pone.0245286

Chen, M., Wu, J., Ning, P., Wang, J., Ma, Z., Huang, L., Plaza, G. R., Shen, Y., Xu, C., Han, Y., Lesniak, M. S., Liu, Z., & Cheng, Y. (2020). Remote Control of Mechanical Forces via Mitochondrial-Targeted Magnetic Nanospinners for Efficient Cancer Treatment. *Small*, *16*(3), 1–14. https://doi.org/10.1002/smll.201905424

Cheng, Y., Weng, S., Yu, L., Zhu, N., Yang, M., & Yuan, Y. (2019). The Role of Hyperthermia in the Multidisciplinary Treatment of Malignant Tumors. *Integrative Cancer Therapies*, *18*. https://doi.org/10.1177/1534735419876345

Chicheł, A., Skowronek, J., Kubaszewska, M., & Kanikowski, M. (2007). Hyperthermia - Description of a method and a review of clinical applications. *Reports of Practical Oncology and Radiotherapy*, *12*(5), 267–275. https://doi.org/10.1016/S1507-1367(10)60065-X

Chubarov, A. S. (2022). Serum Albumin for Magnetic Nanoparticles Coating. *Magnetochemistry*, *8*(2). https://doi.org/10.3390/magnetochemistry8020013

Connord, V., Clerc, P., Hallali, N., El Hajj Diab, D., Fourmy, D., Gigoux, V., & Carrey, J. (2015). Real-time analysis of magnetic hyperthermia experiments on living cells under a confocal microscope. *Small*, *11*(20), 2437–2445. https://doi.org/10.1002/smll.201402669

Crăciunescu, I., Palade, P., Iacob, N., Ispas, G. M., Stanciu, A. E., Kuncser, V., & Turcu, R. P. (2021). High-Performance Functionalized Magnetic Nanoparticles with Tailored Sizes and Shapes for Localized Hyperthermia Applications. *Journal of Physical Chemistry C*, *125*(20), 11132–11146. https://doi.org/10.1021/acs.jpcc.1c01053

Creixell, M., Torres-lugo, M., Rinaldi, C., & Boh, A. C. (2011). EGFR-Targeted Magnetic Nanoparticle Heaters Kill Cancer Cells without a. *ACS Nano*, *5*(9), 7124–7129.

Czarnywojtek, A., Borowska, M., Dyrka, K., Van Gool, S., Sawicka-Gutaj, N., Moskal, J., Kościński, J., Graczyk, P., Hałas, T., Lewandowska, A. M., Czepczyński, R., & Ruchała, M. (2023). Glioblastoma Multiforme: The Latest Diagnostics and Treatment Techniques. *Pharmacology*, *108*(5), 423–431. https://doi.org/10.1159/000531319

Danewalia, S. S., & Singh, K. (2021). Bioactive glasses and glass–ceramics for hyperthermia treatment of cancer: state-of-art, challenges, and future perspectives. *Materials Today Bio*, *10*(February), 100100. https://doi.org/10.1016/j.mtbio.2021.100100

Datta, N. R., Ordóñez, S. G., Gaipl, U. S., Paulides, M. M., Crezee, H., Gellermann, J., Marder, D., Puric, E., & Bodis, S. (2015). Local hyperthermia combined with radiotherapy and-/or chemotherapy: Recent advances and promises for the future. *Cancer Treatment Reviews*, *41*(9), 742–753. https://doi.org/10.1016/j.ctrv.2015.05.009

de Andrade Mello, P., Bian, S., Savio, L. E. B., Zhang, H., Zhang, J., Junger, W., Wink, M. R., Lenz, G., Buffon, A., Wu, Y., & Robson, S. C. (2017). Hyperthermia and associated changes in membrane fluidity potentiate P2X7 activation to promote tumor cell death. *Oncotarget*, *8*(40), 67254–67268. https://doi.org/10.18632/oncotarget.18595

De La Presa, P., Luengo, Y., Multigner, M., Costo, R., Morales, M. P., Rivero, G., & Hernando, A. (2012). Study of heating efficiency as a function of concentration, size, and applied field in γ-Fe2O3 nanoparticles. *Journal of Physical Chemistry C*, *116*(48), 25602–25610. https://doi.org/10.1021/jp310771p

Domenech, M., Marrero-Berrios, I., Torres-Lugo, M., & Rinaldi, C. (2013). Lysosomal membrane permeabilization by targeted magnetic nanoparticles in alternating magnetic fields. *ACS Nano*, *7*(6), 5091–5101. https://doi.org/10.1021/nn4007048

Egea-Benavente, D., Ovejero, J. G., Morales, M. D. P., & Barber, D. F. (2021). Understanding mnps behaviour in response to amf in biological milieus and the effects at the cellular level: Implications for a rational design that drives magnetic hyperthermia therapy toward clinical implementation. In *Cancers* (Vol. 13, Issue 18). MDPI. https://doi.org/10.3390/cancers13184583

Etemadi, H., & Plieger, P. G. (2020). Magnetic fluid hyperthermia based on magnetic nanoparticles: Physical characteristics, historical perspective, clinical trials, technological challenges, and recent advances. *Advanced Therapeutics*, *3*(11). https://doi.org/10.1002/adtp.202000061

Etheridge, M. L., Hurley, K. R., Zhang, J., Jeon, S., Ring, H. L., Hogan, C., Haynes, C. L., Garwood, M., & Bischof, J. C. (2014). Accounting for biological aggregation in heating and imaging of magnetic nanoparticles. *Technology*, *02*(03), 214–228. https://doi.org/10.1142/s2339547814500198

Farzin, A., Etesami, S. A., Quint, J., Memic, A., & Tamayol, A. (2020). Magnetic Nanoparticles in Cancer Therapy and Diagnosis. *Advanced Healthcare Materials*, *9*(9), 1–29. https://doi.org/10.1002/adhm.201901058

Feng, Q., Liu, Y., Huang, J., Chen, K., Huang, J., & Xiao, K. (2018). Uptake, distribution, clearance, and toxicity of iron oxide nanoparticles with different sizes and coatings. *Scientific Reports*, *8*(1), 1–13. https://doi.org/10.1038/s41598-018-19628-z

Ferretti, A. M., Usseglio, S., Mondini, S., Drago, C., La Mattina, R., Chini, B., Verderio, C., Leonzino, M., Cagnoli, C., Joshi, P., Boraschi, D., Italiani, P., Li, Y., Swartzwelter, B. J., Sironi, L., Gelosa, P., Castiglioni, L., Guerrini, U., & Ponti, A. (2021). Towards bio-compatible magnetic nanoparticles: Immune-related effects, in-vitro internalization, and in-vivo bio-distribution of zwitterionic ferrite nanoparticles with unexpected renal clearance. *Journal of Colloid and Interface Science*, *582*, 678–700. https://doi.org/10.1016/j.jcis.2020.08.026

Fortes Brollo, M. E., Hernández Flores, P., Gutiérrez, L., Johansson, C., Barber, D. F., & Morales, M. D. P. (2018). Magnetic properties of nanoparticles as a function of their spatial distribution on liposomes and cells. *Physical Chemistry Chemical Physics*, *20*(26), 17829–17838. https://doi.org/10.1039/c8cp03016b

Foster, K. R., & Schwan, H. P. (1989). Dielectric properties of tissues and biological materials: a critical review. *Critical Reviews in Biomedical Engineering*, *17*(1), 25–104.

Frank, Matthew G. annis, Watkins, M. (2019). 乳鼠心肌提取 HHS Public Access. *Physiology & Behavior*, *2014*(80), 678–687. https://doi.org/10.1101/pdb.top071795.Fluorescence

Frtús, A., Smolková, B., Uzhytchak, M., Lunova, M., Jirsa, M., Kubinová, Š., Dejneka, A., & Lunov, O. (2020). Analyzing the mechanisms of iron oxide nanoparticles interactions with cells: A road from failure to success in clinical applications. In *Journal of Controlled Release* (Vol. 328, pp. 59–77). Elsevier B.V. https://doi.org/10.1016/j.jconrel.2020.08.036

Fu, Q., Wang, J., & Huang, T. (2018). The effect of hyperthermia on the DNA damage response induced by γ-rays, as determined through in situ cell tracking. *Journal of Radiation Research*, *59*(5), 577–582. https://doi.org/10.1093/jrr/rry057

Gao, S., Zheng, M., Ren, X., Tang, Y., & Liang, X. (2016). *Local hyperthermia in head and neck cancer : mechanism , application and advance*.

Garaio, E., Collantes, J. M., Plazaola, F., Garcia, J. A., & Castellanos-Rubio, I. (2014). A multifrequency eletromagnetic applicator with an integrated AC magnetometer for magnetic hyperthermia experiments. *Measurement Science and Technology*, *25*(11). https://doi.org/10.1088/0957-0233/25/11/115702

Gas, P. (2011). Essential facts on the history of hyperthermia and their connections with electromedicine. *Przeglad Elektrotechniczny*, *87*(12 B), 37–40.

GILCHRIST, R. K., MEDAL, R., SHOREY, W. D., HANSELMAN, R. C., PARROTT, J. C., & TAYLOR, C. B. (1957). Selective inductive heating of lymph nodes. *Annals of Surgery*, *146*(4), 596–606. https://doi.org/10.1097/00000658-195710000-00007

Glazer, E. S., & Curley, S. A. (2011). The ongoing history of thermal therapy for cancer. *Surgical Oncology Clinics of North America*, *20*(2), 229–235. https://doi.org/10.1016/j.soc.2010.11.001

Goyal, R., & Bhargava, R. (2018). FEM simulation of EM field effect on body tissues with bio-nanofluid (blood with nanoparticles) for nanoparticle mediated hyperthermia. *Mathematical Biosciences*, *300*, 76–86. https://doi.org/10.1016/j.mbs.2018.03.016

Gu, Y., Piñol, R., Moreno-Loshuertos, R., Brites, C. D. S., Zeler, J., Martínez, A., Maurin-Pasturel, G., Fernández-Silva, P., Marco-Brualla, J., Téllez, P., Cases, R., Belsué, R. N., Bonvin, D., Carlos, L. D., & Millán, A. (2023). Local Temperature Increments and Induced Cell Death in Intracellular Magnetic Hyperthermia. *ACS Nano*. https://doi.org/10.1021/ACSNANO.3C00388

Gudoshnikov, S. A., Liubimov, B. Y., & Usov, N. A. (2012). Hysteresis losses in a dense superparamagnetic nanoparticle assembly. *AIP Advances*, *2*(1). https://doi.org/10.1063/1.3688084

Hager, E. D. (2008). Locoregional Hyperthermia. *Hyperthermia in Cancer Treatment: A Primer*, 167–182. https://doi.org/10.1007/978-0-387-33441-7_12

Hergt, R., Andrä, W., D'Ambly, C. G., Hilger, I., Kaiser, W. A., Richter, U., & Schmidt, H. G. (1998). Physical limits of hyperthermia using magnetite fine particles. *IEEE Transactions on Magnetics*, *34*(5 PART 2), 37453754.

Hergt, R., & Dutz, S. (2007). Magnetic particle hyperthermia-biophysical limitations of a visionary tumour therapy. *Journal of Magnetism and Magnetic Materials*, *311*(1 SPEC. ISS.), 187–192. https://doi.org/10.1016/j.jmmm.2006.10.1156

Hossain, S., & Hossain, S. (2022). Hyperthermia Using Magnetic Cobalt Ferrite Magnetoelectric Nanoparticles. *IEEE Transactions on Magnetics*, *58*(12). https://doi.org/10.1109/TMAG.2022.3212789

Huang, R. X., & Zhou, P. K. (2020). DNA damage response signaling pathways and targets for radiotherapy sensitization in cancer. *Signal Transduction and Targeted Therapy*, *5*(1). https://doi.org/10.1038/s41392-020-0150-x

Huang, Y., Wang, X. B., Becker, F. F., & Gascoyne, P. R. C. (1997). Introducing dielectrophoresis as a new force field for field-flow fractionation. *Biophysical Journal*, *73*(2), 1118–1129. https://doi.org/10.1016/S0006-3495(97)78144-X

Huaqi, Y., Bingqi, D., Yanhui, Z., Yongkang, M., Shiming, Z., Zhenghui, S., Zheng, D., Jiangshan, P., & Tiejun, Y. (2023). Hyperthermia inhibits cellular function and induces immunogenic cell death in renal cell carcinoma. *BMC Cancer*, *23*(1), 1–7. https://doi.org/10.1186/s12885-023-11106-8

Hulla, J. E., Sahu, S. C., & Hayes, A. W. (2015). Nanotechnology: History and future. *Human and Experimental Toxicology*, *34*(12), 1318–1321. https://doi.org/10.1177/0960327115603588

J. L. Duval, Faucheux, N., Warocquier-Clérout, R., & Nagel, M. D. (1999). Part of the Biomedical Engineering and Bioengineering Commons Recommended Citation

Recommended Citation Duval. *Cells and Materials*, *9*(1), 3. https://digitalcommons.usu.edu/cellsandmaterials/vol9/iss1/3

Johannsen, M., Gneveckow, U., Eckelt, L., Feussner, A., Waldöfner, N., Scholz, R., Deger, S., Wust, P., Loening, S. A., & Jordan, A. (2005). Clinical hyperthermia of prostate cancer using magnetic nanoparticles: Presentation of a new interstitial technique. *International Journal of Hyperthermia*, *21*(7), 637–647. https://doi.org/10.1080/02656730500158360

Johannsen, M., Gneveckow, U., Thiesen, B., Taymoorian, K., Cho, C. H., Waldöfner, N., Scholz, R., Jordan, A., Loening, S. A., & Wust, P. (2007). Thermotherapy of Prostate Cancer Using Magnetic Nanoparticles: Feasibility, Imaging, and Three-Dimensional Temperature Distribution. *European Urology*, *52*(6), 1653–1662. https://doi.org/10.1016/j.eururo.2006.11.023

Johnson, S., Nguyen, V., & Coder, D. (2013). Assessment of cell viability. *Current Protocols in Cytometry*, *SUPPL.64*, 1–26. https://doi.org/10.1002/0471142956.cy0902s64

Jordan, A., Scholz, R., Wust, P., Fähling, H., & Felix, R. (1999). Magnetic fluid hyperthermia (MFH): Cancer treatment with AC magnetic field induced excitation of biocompatible superparamagnetic nanoparticles. *Journal of Magnetism and Magnetic Materials*, *201*(1–3), 413–419. https://doi.org/10.1016/S0304-8853(99)00088-8

Khandhar, A. P., Ferguson, R. M., Simon, J. A., & Krishnan, K. M. (2012). Enhancing cancer therapeutics using size-optimized magnetic fluid hyperthermia. *Journal of Applied Physics*, *111*(7), 109–112. https://doi.org/10.1063/1.3671427

Kim, D. H., Rozhkova, E. A., Ulasov, I. V., Bader, S. D., Rajh, T., Lesniak, M. S., & Novosad, V. (2010). Biofunctionalized magnetic-vortex microdiscs for targeted cancer-cell destruction. *Nature Materials*, *9*(2), 165–171. https://doi.org/10.1038/nmat2591

Kim, H. C., Kim, E., Jeong, S. W., Ha, T. L., Park, S. I., Lee, S. G., Lee, S. J., & Lee, S. W. (2015). Magnetic nanoparticle-conjugated polymeric micelles for combined hyperthermia and chemotherapy. *Nanoscale*, *7*(39), 16470–16480. https://doi.org/10.1039/c5nr04130a

Kim, S., Yu, J., Kang, J., Kim, Y., & Ko, T. Y. (2024). *Current understanding of modulated electro-hyperthermia in cancer treatment*. *39*(3), 160–168.

Kok, H. P., Ceelen, W., Brace, C. L., Ivkov, R., Haar, G., Crezee, J., Radiation, M., Radiology, I., & Kingdom, U. (2021). *HHS Public Access*. *37*(1), 711–741. https://doi.org/10.1080/02656736.2020.1779357.Heating

Kok, H. P., & Crezee, J. (2020). *Hyperthermia Treatment Planning : Clinical Application and Ongoing Developments Hyperthermia Treatment Planning : Clinical Application and Ongoing Developments*. https://doi.org/10.1109/JERM.2020.3032838

Kritika, N., & Roy, I. (2022). Therapeutic applications of magnetic nanoparticles: recent advances. *Materials Advances*, *3*(20), 7425–7444. https://doi.org/10.1039/d2ma00444e

Kumar, C. S. S. R., & Mohammad, F. (2011). Magnetic nanomaterials for hyperthermia-based therapy and controlled drug delivery. *Advanced Drug Delivery Reviews*, *63*(9), 789–808. https://doi.org/10.1016/j.addr.2011.03.008

Lang, Q., Wu, Y., Ren, Y., Tao, Y., Lei, L., & Jiang, H. (2015). AC Electrothermal Circulatory Pumping Chip for Cell Culture. *ACS Applied Materials and Interfaces*, *7*(48), 26792–26801. https://doi.org/10.1021/acsami.5b08863

Langlands, A. (1990). Hyperthermia in the treatment of cancer. In *Medical Journal of Australia* (Vol. 152, Issue 6). https://doi.org/10.5694/j.1326-5377.1990.tb120944.x

Lassche, G., Crezee, J., & Van Herpen, C. M. L. (2019). Whole-body hyperthermia in combination with systemic therapy in advanced solid malignancies. *Critical Reviews in*

Oncology/Hematology, *139*(December 2018), 67–74. https://doi.org/10.1016/j.critrevonc.2019.04.023

Laurent, S., Dutz, S., Häfeli, U. O., & Mahmoudi, M. (2011). Magnetic fluid hyperthermia: Focus on superparamagnetic iron oxide nanoparticles. *Advances in Colloid and Interface Science*, *166*(1–2), 8–23. https://doi.org/10.1016/j.cis.2011.04.003

Lee, S., Son, B., Park, G., Kim, H., Kang, H., Jeon, J., Youn, H., & Youn, B. (2018). Immunogenic effect of hyperthermia on enhancing radiotherapeutic efficacy. *International Journal of Molecular Sciences*, *19*(9), 1–21. https://doi.org/10.3390/ijms19092795

Li, T. J., Huang, C. C., Ruan, P. W., Chuang, K. Y., Huang, K. J., Shieh, D. Bin, & Yeh, C. S. (2013). In vivo anti-cancer efficacy of magnetite nanocrystal - based system using locoregional hyperthermia combined with 5-fluorouracil chemotherapy. *Biomaterials*, *34*(32), 7873–7883. https://doi.org/10.1016/j.biomaterials.2013.07.012

Li, Z., Lai, X., Fu, S., Ren, L., Cai, H., Zhang, H., Gu, Z., Ma, X., & Luo, K. (2022). Immunogenic Cell Death Activates the Tumor Immune Microenvironment to Boost the Immunotherapy Efficiency. *Advanced Science*, *9*(22), 1–37. https://doi.org/10.1002/advs.202201734

Liu, J., Li, N., Li, L., Li, D., Liu, K., Zhao, L., Tang, J., & Li, L. (2013). Local hyperthermia for esophageal cancer in a rabbit tumor model: Magnetic stent hyperthermia versus magnetic fluid hyperthermia. *Oncology Letters*, *6*(6), 1550–1558. https://doi.org/10.3892/ol.2013.1618

Liu, X., Li, K., Wang, L., Zhang, M., & Wang, X. (2021). Variations of human heat shock proteins in multiple cancers. *Clinical and Translational Medicine*, *11*(2), 1–10. https://doi.org/10.1002/ctm2.320

Liu, X., Zhang, Y., Wang, Y., Zhu, W., Li, G., Ma, X., Zhang, Y., Chen, S., Tiwari, S., Shi, K., Zhang, S., Fan, H. M., Zhao, Y. X., & Liang, X. J. (2020). Comprehensive understanding of magnetic hyperthermia for improving antitumor therapeutic efficacy. *Theranostics*, *10*(8), 3793–3815. https://doi.org/10.7150/thno.40805

Lu, B., Wang, J., Hendriks, A. J., & Nolte, T. M. (2023). Clearance of nanoparticles from blood: effects of hydrodynamic size and surface coatings. *Environmental Science: Nano*, *11*(1), 406–417. https://doi.org/10.1039/d3en00812f

Ludwig, R., Teran, F. J., Teichgraeber, U., & Hilger, I. (2017). Nanoparticle-based hyperthermia distinctly impacts production of ROS, expression of Ki-67, TOP2A, and TPX2, and induction of apoptosis in pancreatic cancer. *International Journal of Nanomedicine*, *12*, 1009–1018. https://doi.org/10.2147/IJN.S108577

Luengo, Y., Nardecchia, S., Morales, M. P., & Serrano, M. C. (2013). Different cell responses induced by exposure to maghemite nanoparticles. *Nanoscale*, *5*(23), 11428–11437. https://doi.org/10.1039/c3nr02148c

Lwin, Z. M., & Yokota, M. (2019). Numerical analysis of SAR and temperature distribution in two dimensional human head model based on FDTD parameters and the polarization of electromagnetic wave. *AEU - International Journal of Electronics and Communications*, *104*, 91–98. https://doi.org/10.1016/j.aeue.2019.03.010

Maier-Hauff, K., Rothe, R., Scholz, R., Gneveckow, U., Wust, P., Thiesen, B., Feussner, A., Deimling, A., Waldoefner, N., Felix, R., & Jordan, A. (2007). Intracranial thermotherapy using magnetic nanoparticles combined with external beam radiotherapy: Results of a feasibility study on patients with glioblastoma multiforme. *Journal of Neuro-Oncology*, *81*(1), 53–60. https://doi.org/10.1007/s11060-006-9195-0

Manh, D. H., Phong, P. T., Nam, P. H., Tung, D. K., Phuc, N. X., & Lee, I. J. (2014). Structural and magnetic study of La0.7Sr0.3MnO 3 nanoparticles and AC magnetic

heating characteristics for hyperthermia applications. *Physica B: Condensed Matter*, *444*, 94–102. https://doi.org/10.1016/j.physb.2014.03.025

Martins, P. M., Lima, A. C., Ribeiro, S., Lanceros-Mendez, S., & Martins, P. (2021). Magnetic Nanoparticles for Biomedical Applications: From the Soul of the Earth to the Deep History of Ourselves. *ACS Applied Bio Materials*, *4*(8), 5839–5870. https://doi.org/10.1021/acsabm.1c00440

Massart, R. (1981). Preparation of Aqueous Magnetic Liquids in Alkaline and Acidic Media. *IEEE Transactions on Magnetics*, *17*(2), 1247–1248. https://doi.org/10.1109/TMAG.1981.1061188

Master, A. M., Williams, P. N., Pothayee, N., Pothayee, N., Zhang, R., Vishwasrao, H. M., Golovin, Y. I., Riffle, J. S., Sokolsky, M., & Kabanov, A. V. (2016). Remote actuation of magnetic nanoparticles for cancer cell selective treatment through cytoskeletal disruption. *Scientific Reports*, *6*(April), 1–13. https://doi.org/10.1038/srep33560

Matos-Perdomo, E., & Machín, F. (2019). Nucleolar and ribosomal DNA structure under stress: Yeast lessons for aging and cancer. *Cells*, *8*(8), 1–22. https://doi.org/10.3390/cells8080779

Mejías, R., Hernández Flores, P., Talelli, M., Tajada-Herráiz, J. L., Brollo, M. E. F., Portilla, Y., Morales, M. P., & Barber, D. F. (2019). Cell-Promoted Nanoparticle Aggregation Decreases Nanoparticle-Induced Hyperthermia under an Alternating Magnetic Field Independently of Nanoparticle Coating, Core Size, and Subcellular Localization. *ACS Applied Materials and Interfaces*, *11*(1), 340–355. https://doi.org/10.1021/acsami.8b18451

Meng, X., Dang, T., & Chai, J. (2021). From Apoptosis to Necroptosis: The Death Wishes to Cancer. *Cancer Control*, *28*, 1–12. https://doi.org/10.1177/10732748211066311

Mfolozi, S., Malan, A., Bello-Ochende, T., & Martin, L. J. (2018). Numeric analysis of temperature distribution in man using a 3D human model. *BioRxiv*. https://doi.org/10.1101/330357

Michelle Longmire, Peter L. Choyke, M.D., and Hisataka Kobayashi, M.D., Ph. D. (2012). *Clearance Properties of Nano-sized Particles and Molecules as Imagin Agents: Consideration and Caveats*. *3*(5), 703–717. https://doi.org/10.2217/17435889.3.5.703.Clearance

Mier, Y. H., Hernandez, A. V., & Salas, L. L. (2002). Magnetic induction heating system for local hyperthermia research. *Annual International Conference of the IEEE Engineering in Medicine and Biology - Proceedings*, *2*, 1744–1745. https://doi.org/10.1109/IEMBS.2002.1106631

Mohseni, M., & Rajaei, A. (2018). Design of alternating magnetic field generator for magnetic fluid hyperthermia research application. *Scientia Iranica*, *25*(6D), 3507–3516. https://doi.org/10.24200/sci.2017.4380

Moros, M., Ambrosone, A., Stepien, G., Fabozzi, F., Marchesano, V., Castaldi, A., Tino, A., De La Fuente, J. M., & Tortiglione, C. (2015). Deciphering intracellular events triggered by mild magnetic hyperthermia in vitro and in vivo. *Nanomedicine*, *10*(14), 2167–2183. https://doi.org/10.2217/nnm.15.70

Nakamura, K., Yoshikawa, N., Yamaguchi, Y., Kagota, S., Shinozuka, K., & Kunitomo, M. (2002). Characterization of mouse melanoma cell lines by their mortal malignancy using an experimental metastatic model. *Life Sciences*, *70*(7), 791–798. https://doi.org/10.1016/S0024-3205(01)01454-0

Narayanaswamy, V., Sambasivam, S., Saj, A., Alaabed, S., Issa, B., Al-Omari, I. A., & Obaidat, I. M. (2021a). Role of magnetite nanoparticles size and concentration on

hyperthermia under various field frequencies and strengths. *Molecules*, *26*(4), 1–14. https://doi.org/10.3390/molecules26040796

Narayanaswamy, V., Sambasivam, S., Saj, A., Alaabed, S., Issa, B., Al-Omari, I. A., & Obaidat, I. M. (2021b). Role of magnetite nanoparticles size and concentration on hyperthermia under various field frequencies and strengths. *Molecules*, *26*(4), 1–14. https://doi.org/10.3390/molecules26040796

Niemi, V., Gaskarth, D., & Kemp, R. A. (2020). Extensive variability in the composition of immune infiltrate in different mouse models of cancer. *Laboratory Animal Research*, *36*(1), 1–10. https://doi.org/10.1186/s42826-020-00075-9

Nowak-Jary, J., & Machnicka, B. (2023). In vivo Biodistribution and Clearance of Magnetic Iron Oxide Nanoparticles for Medical Applications. *International Journal of Nanomedicine*, *18*, 4067–4100. https://doi.org/10.2147/IJN.S415063

Obaidat, I. M., Narayanaswamy, V., Alaabed, S., Sambasivam, S., & Muralee Gopi, C. V. V. (2019). Principles of magnetic hyperthermia: A focus on using multifunctional hybrid magnetic nanoparticles. *Magnetochemistry*, *5*(4). https://doi.org/10.3390/magnetochemistry5040067

Olsson, M., & Zhivotovsky, B. (2011). Caspases and cancer. *Cell Death and Differentiation*, *18*(9), 1441–1449. https://doi.org/10.1038/cdd.2011.30

Osaci, M., & Cacciola, M. (2020). Influence of the magnetic nanoparticle coating on the magnetic relaxation time. *Beilstein Journal of Nanotechnology*, *11*(December 2019), 1207–1216. https://doi.org/10.3762/bjnano.11.105

Ovejero, J. G., Serantes, D., Veintemillas-verdaguer, S., Zeballos, N., Fuente, M. De, Morales, P., Fernando, L., Gru, C., & Grazu, V. (2021). *Selective Magnetic Nanoheating: Combining Iron Oxide Nanoparticles for Multi-Hot-Spot Induction and Sequential Regulation*. https://doi.org/10.1021/acs.nanolett.1c02178

Ozturk, K., Arslan, F. B., Tavukcuoglu, E., Esendagli, G., & Calis, S. (2020). Aggregation of chitosan nanoparticles in cell culture: Reasons and resolutions. *International Journal of Pharmaceutics*, *578*(February), 119119. https://doi.org/10.1016/j.ijpharm.2020.119119

Paulides, M. M., Stauffer, P. R., Neufeld, E., Maccarini, P. F., Kyriakou, A., Canters, R. A. M., Diederich, C. J., Jurriaan, F., Rhoon, G. C. Van, Paulides, M. M., Stauffer, P. R., Neufeld, E., Maccarini, P. F., Kyriakou, A., Canters, R. A. M., Diederich, C. J., Bakker, J. F., & Van, G. C. (2013). *Simulation techniques in hyperthermia treatment planning*. *6736*(May). https://doi.org/10.3109/02656736.2013.790092

Pefanis, G., Maniotis, N., Tsiapla, A., Makridis, A., Samaras, T., & Angelakeris, M. (2022). *Numerical Simulation of Temperature Variations during the Application of Safety Protocols in Magnetic Particle Hyperthermia*.

Peiravi, M., Eslami, H., Ansari, M., & Zare-Zardini, H. (2022). Magnetic hyperthermia: Potentials and limitations. In *Journal of the Indian Chemical Society* (Vol. 99, Issue 1). Elsevier B.V. https://doi.org/10.1016/j.jics.2021.100269

Penny, C., Muxworthy, A. R., & Fabian, K. (2019). Mean-field modelling of magnetic nanoparticles: The effect of particle size and shape on the Curie temperature. *Physical Review B*, *99*(17), 174414. https://doi.org/10.1103/PhysRevB.99.174414

Périgo, E. A., Hemery, G., Sandre, O., Ortega, D., Garaio, E., Plazaola, F., & Teran, F. J. (2015). Fundamentals and advances in magnetic hyperthermia. *Applied Physics Reviews*, *2*(4). https://doi.org/10.1063/1.4935688

Persano, S., Vicini, F., Poggi, A., Fernandez, J. L. C., Rizzo, G. M. R., Gavilán, H., Silvestri, N., & Pellegrino, T. (2021). Elucidating the innate immunological effects of mild magnetic hyperthermia on U87 human glioblastoma cells: An in vitro study. *Pharmaceutics*, *13*(10), 1–22. https://doi.org/10.3390/pharmaceutics13101668

Pirollo, K. F., & Chang, E. H. (2008). Does a targeting ligand influence nanoparticle tumor localization or uptake? *Trends in Biotechnology*, *26*(10), 552–558. https://doi.org/10.1016/j.tibtech.2008.06.007

Portilla, Y., Fernández-Afonso, Y., Pérez-Yagüe, S., Mulens-Arias, V., Morales, M. P., Gutiérrez, L., & Barber, D. F. (2022). Different coatings on magnetic nanoparticles dictate their degradation kinetics in vivo for 15 months after intravenous administration in mice. *Journal of Nanobiotechnology*, *20*(1), 1–23. https://doi.org/10.1186/s12951-022-01747-5

Portilla, Y., Mulens-Arias, V., Paradela, A., Ramos-Fernández, A., Pérez-Yagüe, S., Morales, M. P., & Barber, D. F. (2022a). The surface coating of iron oxide nanoparticles drives their intracellular trafficking and degradation in endolysosomes differently depending on the cell type. *Biomaterials*, *281*. https://doi.org/10.1016/j.biomaterials.2022.121365

Portilla, Y., Mulens-Arias, V., Paradela, A., Ramos-Fernández, A., Pérez-Yagüe, S., Morales, M. P., & Barber, D. F. (2022b). The surface coating of iron oxide nanoparticles drives their intracellular trafficking and degradation in endolysosomes differently depending on the cell type. *Biomaterials*, *281*, 121365. https://doi.org/10.1016/j.biomaterials.2022.121365

Rahpeima, R., & Id, C. L. (2022). *Numerical study of magnetic hyperthermia ablation of breast tumor on an anatomically realistic breast phantom*. 1–30. https://doi.org/10.1371/journal.pone.0274801

Rashidi, N., Davidson, M., Apostolopoulos, V., & Nurgali, K. (2024). Nanoparticles in cancer diagnosis and treatment: Progress, challenges, and opportunities. *Journal of Drug Delivery Science and Technology*, *95*(March), 105599. https://doi.org/10.1016/j.jddst.2024.105599

Ressel, A., Schmitt, O., Weiss, C., & Feyerabend, T. (2002). Therapeutic outcome and side-effects after radiotherapy, chemotherapy and/or hyperthermia treatment of head and neck tumour xenografts. *European Journal of Cancer*, *38*(4), 594–601. https://doi.org/10.1016/S0959-8049(01)00411-7

Ribeiro, T. P., Moreira, J. A., Monterio, F. J., & Laranjeira, M. S. (2022). Nanomaterials in cancer: Reviewing the combination of hyperthermia and triggered chemotherapy. *Journal of Controlled Release*, *347*(May), 89–103. https://doi.org/10.1016/j.jconrel.2022.04.045

Rosales, A. M., Aznar, E., Coll, C., García Mendoza, R. A., Lorena Urbano Bojorge, A., González, N. F., Martínez-Máñez, R., del Pozo Guerrero, F., & Olmedo, J. J. S. (2016). Study of the dependency of the specific power absorption rate on several characteristics of the excitation magnetic signal when irradiating a SPION-containing ferrofluid. *Journal of Magnetics*, *21*(3), 460–467. https://doi.org/10.4283/JMAG.2016.21.3.460

Rosensweig, R. E. (2002). Heating magnetic fluid with alternating magnetic field. *Journal of Magnetism and Magnetic Materials*, *252*(1-3 SPEC. ISS.), 370–374. https://doi.org/10.1016/S0304-8853(02)00706-0

Roti, J. L. (2008). Cellular responses to hyperthermia (40-46°C): Cell killing and molecular events. *International Journal of Hyperthermia*, *24*(1), 3–15. https://doi.org/10.1080/02656730701769841

Rubia-Rodríguez, I., Santana-Otero, A., Spassov, S., Tombácz, E., Johansson, C., De La Presa, P., Teran, F. J., Morales, M. D. P., Veintemillas-Verdaguer, S., Thanh, N. T. K., Besenhard, M. O., Wilhelm, C., Gazeau, F., Harmer, Q., Mayes, E., Manshian, B. B., Soenen, S. J., Gu, Y., Millán, Á., … Ortega, D. (2021). Whither magnetic hyperthermia? A tentative roadmap. *Materials*, *14*(4), 1–37. https://doi.org/10.3390/ma14040706

Salas, G., Veintemillas-Verdaguer, S., & Morales, M. D. P. (2013). Relationship between physico-chemical properties of magnetic fluids and their heating capacity. *International Journal of Hyperthermia*, *29*(8), 768–776. https://doi.org/10.3109/02656736.2013.826824

Salmanian, G., Hassanzadeh-Tabrizi, S. A., & Koupaei, N. (2021). Magnetic chitosan nanocomposites for simultaneous hyperthermia and drug delivery applications: A review. In *International Journal of Biological Macromolecules* (Vol. 184, pp. 618–635). Elsevier B.V. https://doi.org/10.1016/j.ijbiomac.2021.06.108

Sanz, B., Calatayud, M. P., De Biasi, E., Lima, E., Mansilla, M. V., Zysler, R. D., Ibarra, M. R., & Goya, G. F. (2016). In silico before in vivo: How to predict the heating efficiency of magnetic nanoparticles within the intracellular space. *Scientific Reports*, *6*(September), 1–10. https://doi.org/10.1038/srep38733

Sanz-Ortega, L., Portilla, Y., Pérez-Yagüe, S., & Barber, D. F. (2019). Magnetic targeting of adoptively transferred tumour-specific nanoparticle-loaded CD8+ T cells does not improve their tumour infiltration in a mouse model of cancer but promotes the retention of these cells in tumour-draining lymph nodes. *Journal of Nanobiotechnology*, *17*(1), 1–25. https://doi.org/10.1186/s12951-019-0520-0

Sellers, R. S., Clifford, C. B., Treuting, P. M., & Brayton, C. (2012). Immunological variation between inbred laboratory mouse strains: Points to consider in phenotyping genetically immunomodified mice. *Veterinary Pathology*, *49*(1), 32–43. https://doi.org/10.1177/0300985811429314

Serrano-Puebla, A., & Boya, P. (2018). Lysosomal membrane permeabilization as a cell death mechanism in cancer cells. *Biochemical Society Transactions*, *46*(2), 207–215. https://doi.org/10.1042/BST20170130

Sharma, S. K., Shrivastava, N., Rossi, F., Tung, L. D., & Thanh, N. T. K. (2019). Nanoparticles-based magnetic and photo induced hyperthermia for cancer treatment. *Nano Today*, *29*(xxxx), 100795. https://doi.org/10.1016/j.nantod.2019.100795

Shirvalilou, S., Khoee, S., Khoei, S., Karimi, M. R., Sadri, E., & Shirvaliloo, M. (2023). Targeted magnetochemotherapy modified by 5-Fu-loaded thermally on/off switching nanoheaters for the eradication of CT26 murine colon cancer by inducing apoptotic and autophagic cell death. *Cancer Nanotechnology*, *14*(1), 1–17. https://doi.org/10.1186/s12645-023-00164-z

Shirvalilou, S., Khoei, S., Esfahani, A. J., Kamali, M., Shirvaliloo, M., Sheervalilou, R., & Mirzaghavami, P. (2021). Magnetic Hyperthermia as an adjuvant cancer therapy in combination with radiotherapy versus radiotherapy alone for recurrent/progressive glioblastoma: a systematic review. *Journal of Neuro-Oncology*, *152*(3), 419–428. https://doi.org/10.1007/s11060-021-03729-3

Singh, I. S., & Hasday, J. D. (2013). Fever, hyperthermia and the heat shock response. *International Journal of Hyperthermia*, *29*(5), 423–435. https://doi.org/10.3109/02656736.2013.808766

Slimani, Y., Hannachi, E., Tombuloglu, H., Güner, S., Almessiere, M. A., Baykal, A., Aljafary, M. A., Al-Suhaimi, E. A., Nawaz, M., & Ercan, I. (2019). Magnetic nanoparticles based nanocontainers for biomedical application. *Smart Nanocontainers: Micro and Nano Technologies*, 229–250. https://doi.org/10.1016/B978-0-12-816770-0.00014-9

Somu, P., Mohanty, S., Basavegowda, N., Yadav, A. K., Paul, S., & Baek, K. H. (2024). The Interplay between Heat Shock Proteins and Cancer Pathogenesis: A Novel Strategy for Cancer Therapeutics. *Cancers*, *16*(3), 1–31. https://doi.org/10.3390/cancers16030638

Souiade, L., Domingo-Diez, J., Alcaide, C., Gámez, B., Gámez, L., Ramos, M., & Serrano Olmedo, J. J. (2023). Improving the Efficacy of Magnetic Nanoparticle-Mediated Hyperthermia Using Trapezoidal Pulsed Electromagnetic Fields as an In Vitro Anticancer Treatment in Melanoma and Glioblastoma Multiforme Cell Lines. *International Journal of Molecular Sciences*, *24*(21), 1–18. https://doi.org/10.3390/ijms242115933

Stigliano, R. V., Shubitidze, F., Petryk, J. D., Shoshiashvili, L., Petryk, A. A., & Hoopes, P. J. (2016). Mitigation of eddy current heating during magnetic nanoparticle hyperthermia therapy. *International Journal of Hyperthermia*, *32*(7), 735–748. https://doi.org/10.1080/02656736.2016.1195018

Sulyok, I., Fleischmann, E., Stift, A., Roth, G., Lebherz-Eichinger, D., Kasper, D., Spittler, A., & Kimberger, O. (2012). Effect of preoperative fever-range whole-body hyperthermia on immunological markers in patients undergoing colorectal cancer surgery. *British Journal of Anaesthesia*, *109*(5), 754–761. https://doi.org/10.1093/bja/aes248

Sung, H., Ferlay, J., Siegel, R. L., Laversanne, M., Soerjomataram, I., Jemal, A., & Bray, F. (2021). Global Cancer Statistics 2020: GLOBOCAN Estimates of Incidence and Mortality Worldwide for 36 Cancers in 185 Countries. *CA: A Cancer Journal for Clinicians*, *71*(3), 209–249. https://doi.org/10.3322/caac.21660

Suto, M., Hirota, Y., Mamiya, H., Fujita, A., Kasuya, R., Tohji, K., & Jeyadevan, B. (2009). Heat dissipation mechanism of magnetite nanoparticles in magnetic fluid hyperthermia. *Journal of Magnetism and Magnetic Materials*, *321*(10), 1493–1496. https://doi.org/10.1016/j.jmmm.2009.02.070

Szwed, M., & Marczak, A. (2024). Application of Nanoparticles for Magnetic Hyperthermia for Cancer Treatment—The Current State of Knowledge. *Cancers*, *16*(6). https://doi.org/10.3390/cancers16061156

Talone, B., Bazzarelli, M., Schirato, A., Dello Vicario, F., Viola, D., Jacchetti, E., Bregonzio, M., Raimondi, M. T., Cerullo, G., & Polli, D. (2021). Phototoxicity induced in living HeLa cells by focused femtosecond laser pulses: a data-driven approach. *Biomedical Optics Express*, *12*(12), 7886. https://doi.org/10.1364/boe.441225

Tekade, R. K., Maheshwari, R., Soni, N., Tekade, M., & Chougule, M. B. (2017). Nanotechnology for the Development of Nanomedicine. In *Nanotechnology-Based Approaches for Targeting and Delivery of Drugs and Genes*. Elsevier Inc. https://doi.org/10.1016/B978-0-12-809717-5.00001-4

Thiesen, B., & Jordan, A. (2008). Clinical applications of magnetic nanoparticles for hyperthermia. *International Journal of Hyperthermia*, *24*(6), 467–474. https://doi.org/10.1080/02656730802104757

Treatments, H. A. (2021). *Hyperthermia-Based Anti-Cancer Treatments*. 7–10.

Troitskaya, O. S., Novak, D. D., Richter, V. A., & Koval, O. A. (2022). Immunogenic Cell Death in Cancer Therapy. *Acta Naturae*, *14*(1), 40–53. https://doi.org/10.32607/actanaturae.11523

van der Zee, J., & van Rhoon, G. C. (2006). Cervical cancer: Radiotherapy and hyperthermia. *International Journal of Hyperthermia*, *22*(3), 229–234. https://doi.org/10.1080/02656730600722578

Vicentini, M., Ferrero, R., & Manzin, A. (2024). Influence of coil geometry, supply conditions and nanoparticle heating properties on magnetic hyperthermia in mouse models. *International Journal of Thermal Sciences*, *203*(June), 109151. https://doi.org/10.1016/j.ijthermalsci.2024.109151

Vicentini, M., Vassallo, M., Ferrero, R., Androulakis, I., & Manzin, A. (2022). In silico evaluation of adverse eddy current effects in preclinical tests of magnetic hyperthermia. *Computer Methods and Programs in Biomedicine*, *223*. https://doi.org/10.1016/j.cmpb.2022.106975

Villanueva, A., Cãete, M., Roca, A. G., Calero, M., Veintemillas-Verdaguer, S., Serna, C. J., Del Puerto Morales, M., & Miranda, R. (2009). The influence of surface functionalization on the enhanced internalization of magnetic nanoparticles in cancer cells. *Nanotechnology*, *20*(11). https://doi.org/10.1088/0957-4484/20/11/115103

Villanueva, A., De La Presa, P., Alonso, J. M., Rueda, T., Martínez, A., Crespo, P., Morales, M. P., Gonzalez-Fernandez, M. A., Valdés, J., & Rivero, G. (2010). Hyperthermia hela cell treatment with silica-coated manganese oxide nanoparticles. *Journal of Physical Chemistry C*, *114*(5), 1976–1981. https://doi.org/10.1021/jp907046f

Wei, H., Hu, Y., Wang, J., Gao, X., Qian, X., & Tang, M. (2021). Superparamagnetic iron oxide nanoparticles: Cytotoxicity, metabolism, and cellular behavior in biomedicine applications. *International Journal of Nanomedicine*, *16*(August), 6097–6113. https://doi.org/10.2147/IJN.S321984

Wydra, R. J., Rychahou, P. G., Evers, B. M., Anderson, K. W., Dziubla, T. D., & Hilt, J. Z. (2015). The role of ROS generation from magnetic nanoparticles in an alternating magnetic field on cytotoxicity. *Acta Biomaterialia*, *25*, 284–290. https://doi.org/10.1016/j.actbio.2015.06.037

Yang, C. T., Li, K. Y., Meng, F. Q., Lin, J. F., Young, I. C., Ivkov, R., & Lin, F. H. (2018). ROS-induced HepG2 cell death from hyperthermia using magnetic hydroxyapatite nanoparticles. *Nanotechnology*, *29*(37). https://doi.org/10.1088/1361-6528/aacda1

Yang, W., Hao, X., Yan, R., & Yang, Q. (2012). Study on hyperthermia with magnetic fluids. *2012 6th International Conference on Electromagnetic Field Problems and Applications, ICEF'2012*, *2*. https://doi.org/10.1109/ICEF.2012.6310428

Zaidi, A. K., Bagewadikar, R. S., Subramanian, M., Kaklij, G. S., & Patil, M. S. (2004). Effect of whole body hyperthermia (39°C, 1 h) on radiation-induced apoptosis in Swiss mice. *Journal of Thermal Biology*, *29*(1), 3–8. https://doi.org/10.1016/j.jtherbio.2003.08.007

Zeinoun, M., Domingo-Diez, J., Rodriguez-Garcia, M., Garcia, O., Vasic, M., Ramos, M., & Olmedo, J. J. S. (2021). Enhancing magnetic hyperthermia nanoparticle heating efficiency with non-sinusoidal alternating magnetic field waveforms. *Nanomaterials*, *11*(12). https://doi.org/10.3390/nano11123240

Zeinoun, M., Serrano, D., Medina, P. T., Garcia, O., Vasic, M., & Serrano-Olmedo, J. J. (2021). Configurable High-Frequency Alternating Magnetic Field Generator for Nanomedical Magnetic Hyperthermia Applications. *IEEE Access*, *9*, 105805–105816. https://doi.org/10.1109/ACCESS.2021.3099428

Zhang, E., Kircher, M. F., Koch, M., Eliasson, L., Goldberg, S. N., & Renström, E. (2014). Dynamic magnetic fields remote-control apoptosis via nanoparticle rotation. *ACS Nano*, *8*(4), 3192–3201. https://doi.org/10.1021/nn406302j

Zhang, Y., Li, Z., Huang, Y., Zou, B., & Xu, Y. (2023). Amplifying cancer treatment: advances in tumor immunotherapy and nanoparticle-based hyperthermia. *Frontiers in Immunology*, *14*(October), 1–18. https://doi.org/10.3389/fimmu.2023.1258786

Zheng, N., Xu, A., Lin, X., Mo, Z., Xie, X., Huang, Z., Liang, Y., Cai, Z., Tan, J., & Shao, X. (2021). Whole-body hyperthermia combined with chemotherapy and intensity-modulated radiotherapy for treatment of advanced nasopharyngeal carcinoma: a retrospective study with propensity score matching. *International Journal of Hyperthermia*, *38*(1), 1304–1312. https://doi.org/10.1080/02656736.2021.1971778

Zhu, M., Yang, M., Zhang, J., Yin, Y., Fan, X., Zhang, Y., Qin, S., Zhang, H., & Yu, F. (2021). Immunogenic Cell Death Induction by Ionizing Radiation. *Frontiers in Immunology*, *12*(August), 1–9. https://doi.org/10.3389/fimmu.2021.705361

Ziegelberger, G., Croft, R., Feychting, M., Green, A. C., Hirata, A., d'Inzeo, G., Jokela, K., Loughran, S., Marino, C., Miller, S., Oftedal, G., Okuno, T., van Rongen, E., Röösli, M., Sienkiewicz, Z., Tattersall, J., & Watanabe, S. (2020). Guidelines for limiting exposure to electromagnetic fields (100 kHz to 300 GHz). In *Health Physics* (Vol. 118, Issue 5). https://doi.org/10.1097/HP.0000000000001210

Zimmerman, H. M. (1961). Experimental brain tumors. *Neurologia Medico-Chirurgica*, *3*(2), 29–47. https://doi.org/10.2176/nmc.3.29

Zubarev, A. Y., Iskakova, L., & Abu-Bakr, A. F. (2015). Effect of interparticle interaction on magnetic hyperthermia in ferrofluids. *Physica A: Statistical Mechanics and Its Applications*, *438*, 487–492. https://doi.org/10.1016/j.physa.2015.07.014

ANNEX 1

Electric field calculations of the non-sinusoidal AMFs

The electric field of the non-sinusoidal AMFs can be obtained from the summation of the electric fields of sinusoidal AMFs.

The electric field has the following form:

$$E\,(t) = E_0\, e^{\,jn\omega t}$$

And Fourier series trigonometric form as:

$$f(t) = \frac{a_0}{2} + \sum_{n=1}^{\infty}(a_n \cos(\mathrm{n}\omega\mathrm{t}) + b_n \sin(n\omega t))$$

where the angular frequency $\omega = 2\pi f$.

Hence, for $a_n = C_n \cos \phi_n$; $bn = -C_n \sin \phi_n$; $a_0 = 0$, the Fourier series become:

$$f(t) = \sum_{n=1}^{\infty}(C_n \cos\phi_n \cos(\mathrm{n}\omega\mathrm{t}) - C_n \sin\phi_n \sin(n\omega t))$$

$$f(t) = \sum_{n=1}^{\infty}(C_n \cos(\mathrm{n}\omega\mathrm{t} + \phi_n) - C_n \sin(n\omega t + \phi_n))$$

$$f(t) = \sum_{n=1}^{\infty}(C_n \cos(\mathrm{n}\omega\mathrm{t} + \phi_n) - C_n \sin(n\omega t + \phi_n))$$

Where $\phi = \mathrm{arctg}\,(-\frac{b_n}{a_n})$.

Using Euler's identity, the Fourier series can be expressed as follows:

$$f(t) = \sum_{n=1}^{\infty} Cn\; e^{\,jn\omega t}\; e^{\,j\phi}$$

Thus the electric field is obtained as :

$$E\,(t) = \sum_{n=1}^{\infty} E_0\; Cn\; e^{\,jn\omega t}\; e^{\,j\phi}$$

$$E(t) = \sum_{n=1}^{\infty} E_0\,(C_n \cos(\mathrm{n}\omega\mathrm{t} + \phi_n) - C_n \sin(n\omega t + \phi_n))$$

Where n= 1,3,5,7

The Fourier coefficients a_n and b_n where calculated using the formula:

Coefficients b_n:

$$b_n = \frac{2}{T}\int_0^T f(t)\sin(n\omega_0 t)\ dt$$

Coefficients a_n:

$$a_n = \frac{2}{T}\int_0^T f(t)\cos(n\omega_0 t)\ dt$$

Thus the Cn coefficients are calculated using:

$$C_n = \sqrt{a_n^2 + b_n^2}$$

MATLAB code for Fourier coefficients of the non-sinusoidal AMFs

```
function [an,bn]= trapsquare(freq,App,n)

T = 1/(freq*1000);

for i = 1:n
 bn(i)=App/2*(224/(30*(i)^2*(pi)^2)*(sin(3/4*pi*(i))+sin(1/4*pi*(i))));

 an(i)=App/2*(-
232*cos(pi*i)/(30*(i)^2*(pi)^2)+224*cos(3*pi*i/4)/(30*(i)^2*(pi)^2)+232/(30*(i)^2*(pi)^2)-
224*cos(pi*i/4)/(30*(i)^2*(pi)^2));

end
x=0:0.0000005:(1-0.0000005);
for i = 1:length(bn)
   for j=1:length(x)
     funciones(i,j)= an(i)*cos(2*i*pi*x(j)/T)+bn(i)*sin(2*i*pi*x(j)/T);
   end
end
   suma=sum(funciones);
   figure
plot(x,suma)
grid on
end
---------------------------------------------------------------------------------
function [bn] = trapezoidal(freq,App,n)
T = 1/(freq*1000);
for i = 1:n
bn(i)= 8*App/((2*i-1)^2*(pi)^2)*sin(pi*(2*i-1)/4);

end
```

```
x=0:0.0000005:(1-0.0000005);
for i = 1:length(bn)
   for j=1:length(x)
      funciones(i,j)= bn(i)*sin(2*(2*i-1)*pi*x(j)/T);

   end
end
   suma=sum(funciones);
   figure
plot(x,suma)
grid on
end
```

```
function [an,bn] = traptriang(freq,App,n)

T = 1/(freq*1000);

for i = 1:n
   bn(i)=App/2*(12/(5*(i)^2*(pi)^2)*(sin(3/4*pi*(i))+sin(1/4*pi*(i))));
   an(i)=App/2*(-56*cos(pi*i)/(20*(i)^2*(pi)^2)-
48*cos(3*pi*i/4)/(20*(i)^2*(pi)^2)+56/(20*(i)^2*(pi)^2)+48*cos(pi*i/4)/(20*(i)^2*(pi)^2));
end
x=0:0.0000005:(1-0.0000005);
for i = 1:length(bn)
   for j=1:length(x)
     funciones(i,j)= an(i)*cos(2*i*pi*x(j)/T)+bn(i)*sin(2*i*pi*x(j)/T);
   end
end
   suma=sum(funciones);
   figure
plot(x,suma)
grid on
end
```

```
function [bn] = triangular(freq,App,n)
T = 1/(freq*1000);
for i = 1:n
   bn(i)= 4*App/((2*i-1)^2*(pi)^2)*sin(pi*(2*i-1)/2);
end
x=0:0.0000005:(1-0.0000005);
for i = 1:length(bn)
   for j=1:length(x)
      funciones(i,j)= bn(i)*sin(2*(2*i-1)*pi*x(j)/T);

   end
end
   suma=sum(funciones);
   figure
```

```
plot(x,suma)
grid on
end
--------------------------------------------------------------------------------

freq= 0.001;
%bn= trapezoidal(freq,1,10);
%[an,bn]= traptriang(freq,1,30);
%[an,bn]= trapsquare(freq,1,30);
%bn= triangular(freq,1,20);
T = 1/(freq*1000);
%%
x=0:0.0000005:(1-0.0000005);
%% faf
for i = 1:length(bn)
   for j=1:length(x)
      funciones(i,j)= bn(i)*sin(2*(2*i-1)*pi*x(j)/T);
      %funciones(i,j)= an(i)*cos(2*i*pi*x(j)/T)+bn(i)*sin(2*i*pi*x(j)/T);
   end
end
%%
suma=sum(funciones);
%%
figure
plot(x,suma)
grid on
```

MATLAB code for Power loss density generation for non-sinusoidal AMFs

```
EFieldData1 = load('EFieldExportedData1A500kHz.mat');

EField1 = EFieldData1.Snapshot0; % Extracting the elements of the E-field matrix in
snapshot0 structure(x+yi)

E_SN1 = EField1;

EFieldData3 = load('EFieldExportedData1A1500kHz.mat');

EField3 = EFieldData3.Snapshot0;

E_SN3 = EField3;

EFieldData5 = load('EFieldExportedData1A2500kHz.mat');

EField5 = EFieldData5.Snapshot0;

E_SN5 = EField5;

EFieldData7 = load('EFieldExportedData1A3500kHz.mat');

EField7 = EFieldData7.Snapshot0;

E_SN7 = EField7;
```

```
EFieldData9 = load('EFieldExportedData1A4500kHz.mat');
EField9 = EFieldData9.Snapshot0;
E_SN9 = EField9;
EFieldData11 = load('EFieldExportedData1A5500kHz.mat');
EField11 = EFieldData11.Snapshot0;
E_SN11 = EField11;
%% TS SIGNAL
sigma = 0.4; % electric conductivity
A = 50; % amplitude (A)
f = 200e3 ; % Hz
C1_ts = 0.5898 ;
C3_ts = 0.1580;
C5_ts = 0.0569;
C7_ts = 0.0118;
C9_ts = 0.0073;
C11_ts = 0.0117;
for t = 0:0.1:(1-0.1)
   E_Ts1 = E_SN1*C1_ts*(cos(-1.135+ pi/2 + 2*pi*f*t))+E_SN1*C1_ts*(sin(-1.135+ pi/2 +
2*pi*f*t));
   E_Ts3 = E_SN3*C3_ts*(cos(-0.3848+ pi/2 + 6*pi*f*t))+E_SN3*C3_ts*(sin(-0.3848+
pi/2 + 6*pi*f*t));
   E_Ts5 = E_SN5*C5_ts*(cos(0.3839+ pi/2 + 10*pi*f*t))+E_SN5*C5_ts*(sin(0.3839+ pi/2
+ 10*pi*f*t));
   E_Ts7 = E_SN7*C7_ts*(cos(1.14 + pi/2 + 14*pi*f*t))+E_SN7*C7_ts*(sin(1.14 + pi/2 +
14*pi*f*t));
   E_Ts9 = E_SN9*C9_ts*(cos(-1.135+ pi/2 + 18*pi*f*t))+E_SN9*C9_ts*(sin(-1.135+ pi/2
+ 18*pi*f*t));
   E_Ts11 = E_SN11*C11_ts*(cos(-0.385+pi/2 + 22*pi*f*t))+E_SN11*C11_ts*(sin(-
0.385+pi/2 + 22*pi*f*t));
   TS_signal= A*(E_Ts1+E_Ts3+E_Ts5+E_Ts7+E_Ts9+E_Ts11);
end
E_TS = sqrt(sum(TS_signal.^2,2));
Efield_TS = abs(E_TS);
PLD_TS = ((Efield_TS).^2)*sigma/2;
```

```
hwrite("TS10mT500kHz.cache","/datacache/_Object/0/_Object/_Field_",PLD_TS')
%% TP SIGNAL
C1_tp = 0.5732 ;
C3_tp = 0.0637;
C5_tp = 0.0229;
C7_tp = 0.0117;
C9_tp = 0.0071;
C11_tp= 0.0047;
for t = 0:0.1:(1-0.1)
   E_Tp1 = E_SN1*C1_tp*(cos(pi + 2*pi*f*t))+E_SN1*C1_tp*(sin(pi+ 2*pi*f*t));
   E_Tp3 = E_SN3*C3_tp*(cos(pi + 6*pi*f*t))+E_SN3*C3_tp*(sin(pi + 6*pi*f*t));
   E_Tp5 = E_SN5*C5_tp*(cos(pi + 10*pi*f*t))+E_SN5*C5_tp*(sin(pi + 10*pi*f*t));
   E_Tp7 = E_SN7*C7_tp*(cos(pi + 14*pi*f*t))+E_SN7*C7_tp*(sin(pi + 14*pi*f*t));
   E_Tp9 = E_SN9*C9_tp*(cos(pi + 18*pi*f*t))+E_SN9*C9_tp*(sin(pi + 18*pi*f*t));
   E_Tp11= E_SN11*C11_tp*(cos(pi + 22*pi*f*t))+E_SN11*C11_tp*(sin(pi + 22*pi*f*t));
   TP_signal= A*(E_Tp1+E_Tp3+E_Tp5+E_Tp7+E_Tp9+E_Tp11);
end
E_TP = sqrt(sum(TP_signal.^2,2));
Efield_TP = abs(E_TP);
PLD_TP = ((Efield_TP).^2)*sigma/2;
hwrite("TP10mT500kHz.cache","/datacache/_Object/0/_Object/_Field_",PLD_TP')
%% TT SIGNAL
C1_tt = 0.487 ;
C3_tt = 0.0228;
C5_tt = 0.0082;
C7_tt = 0.00954;
C9_tt = 0.00601;
C11_tt = 0.00169;
for t =  0:0.1:(1-0.1)
   E_TT100 = E_SN1*C1_tt*(cos(-0.36+ pi/2 + 2*pi*f*t))+E_SN1*C1_tt*(sin(-0.36+ pi/2 +
2*pi*f*t));
```

```
    E_TT300 = E_SN3*C3_tt*(cos(-0.99+ pi/2 + 6*pi*f*t))+E_SN3*C3_tt*(sin(-0.99+ pi/2 +
6*pi*f*t));

    E_TT500 = E_SN5*C5_tt*(cos(0.99+ pi/2 + 10*pi*f*t))+E_SN5*C5_tt*(sin(0.99+ pi/2 +
10*pi*f*t));

    E_TT700 = E_SN7*C7_tt*(cos(0.36 + pi/2 + 14*pi*f*t))+E_SN7*C7_tt*(sin(0.36 + pi/2
+ 14*pi*f*t));

    E_TT900 = E_SN9*C9_tt*(cos(-0.36+ pi/2 + 18*pi*f*t))+E_SN9*C9_tt*(sin(-0.36+ pi/2
+ 18*pi*f*t));

    E_TT1100= E_SN11*C11_tt*(cos(-0.99+pi/2 + 22*pi*f*t))+E_SN11*C11_tt*(sin(-
0.99+pi/2 + 22*pi*f*t));

    TT_signal= A*(E_TT100+E_TT300+E_TT500+E_TT700+E_TT900+E_TT1100);

end

E_TT = sqrt(sum(TT_signal.^2,2));

Efield_TT = abs(E_TT);

PLD_TT = ((Efield_TT).^2)*sigma/2;

hwrite("TT10mT500kHz.cache","/datacache/_Object/0/_Object/_Field_",PLD_TT')

%% TR SIGNAL

C1_tr = 0.4052 ;

C3_tr = -0.0450;

C5_tr = 0.0162;

C7_tr = -0.0082;

C9_tr = 0.005;

C11_tr= -0.00335;

for t = 0:0.1:(1-0.1)

    E_Tr1 = E_SN1*C1_tr*(cos(pi + 2*pi*f*t))+E_SN1*C1_tr*(sin(pi + 2*pi*f*t));

    E_Tr3 = E_SN3*C3_tr*(cos(pi + 6*pi*f*t))+E_SN3*C3_tr*(sin(pi + 6*pi*f*t));

    E_Tr5 = E_SN5*C5_tr*(cos(pi + 10*pi*f*t))+E_SN5*C5_tr*(sin(pi + 10*pi*f*t));

    E_Tr7 = E_SN7*C7_tr*(cos(pi + 14*pi*f*t))+E_SN7*C7_tr*(sin(pi + 14*pi*f*t));

    E_Tr9 = E_SN9*C9_tr*(cos(pi + 14*pi*f*t))+E_SN9*C9_tr*(sin(pi + 14*pi*f*t));

    E_Tr11 = E_SN11*C11_tr*(cos(pi + 14*pi*f*t))+E_SN11*C11_tr*(sin(pi + 14*pi*f*t));

    TR_signal= A*(E_Tr1+E_Tr3+E_Tr5+E_Tr7+E_Tr9+E_Tr11);

end

E_TR = sqrt(sum(TR_signal.^2, 2));
```

```
Efield_TR= abs(E_TR);
PLD_TR = ((Efield_TR).^2)*sigma/2;
hwrite("TR10mT500kHz.cache","/datacache/_Object/0/_Object/_Field_",PLD_TR')
clc;
clear;
close all;
excelFile = 'TemperatureData2.xlsx';
data = readtable(excelFile);
x = data{:, 1};
y1 = data{:, 2};
y2 = data{:, 3};
y3 = data{:, 4};
y4 = data{:, 5};
y5 = data{:, 6};

% Create figure and plot the curves
figure;
plot(x, y1, 'b-o',  'LineWidth', 2,'MarkerSize',6, 'DisplayName', 'Curve 1'); % Blue solid
hold on;
plot(x, y2, 'LineWidth', 2, 'DisplayName', 'Curve 2');
plot(x, y3,  'LineWidth', 2, 'DisplayName', 'Curve 3');
plot(x, y4, 'LineWidth', 2, 'DisplayName', 'Curve 4');
plot(x, y5,  'LineWidth', 2, 'DisplayName', 'Curve 5');
hold off;

xlabel('H.f (A/m.s)');
ylabel('Temperature');
grid on;
legend('Location', 'best');
```

MATLAB code for MNPs power heat generation

```
% H-FIELD IMPORTATION
HFieldData = load('HFieldExportedData1A1kHz.mat');
HField = HFieldData.Snapshot0;
H = HField;
%%
HFieldData_sn = load('HFieldExportedData10A1kHz.mat');
HField_sn = HFieldData_sn.Snapshot0;
Hsn = sqrt(sum(HField_sn.^2,2));
%%
% TS WAVEFORM
A = 10; % amplitude (Ap)
f = 200e3; % kHz
C1_ts = 0.5898 ;
C3_ts = 0.1580;
C5_ts = 0.0569;
C7_ts = 0.0118;
C9_ts = 0.0073;
C11_ts = 0.0117;
for t =  0:0.1:(1-0.1)
   H_TS100 = H*C1_ts*(cos(-1.135+ pi/2 + 2*pi*f*t))+H*C1_ts*(sin(-1.135+ pi/2 +
2*pi*f*t));
   H_TS300 = H*C3_ts*(cos(-0.3848+ pi/2 + 6*pi*f*t))+H*C3_ts*(sin(-0.3848+ pi/2 +
6*pi*f*t));
   H_TS500 = H*C5_ts*(cos(0.3839+ pi/2 + 10*pi*f*t))+H*C5_ts*(sin(0.3839+ pi/2 +
10*pi*f*t));
   H_TS700 = H*C7_ts*(cos(1.14 + pi/2 + 14*pi*f*t))+H*C7_ts*(sin(1.14 + pi/2 +
14*pi*f*t));
   H_TS900 = H*C9_ts*(cos(-1.135+ pi/2 + 18*pi*f*t))+H*C9_ts*(sin(-1.135+ pi/2 +
18*pi*f*t));
   H_TS1100= H*C11_ts*(cos(-0.385+pi/2 + 22*pi*f*t))+H*C11_ts*(sin(-0.385+pi/2 +
22*pi*f*t));
   H_TS_signal= A*(H_TS100+H_TS300+H_TS500+H_TS700+H_TS900+H_TS1100);
end
```

```
Hts = sqrt(sum(H_TS_signal.^2,2));
%%
% TP WAVEFORM
C1_tp = 0.5732 ;
C3_tp = 0.0637;
C5_tp = 0.0229;
C7_tp = 0.0117;
C9_tp = 0.0071;
C11_tp= 0.0047;
for t = 0:0.1:(1-0.1)
   H_TP100 = H*C1_tp*(cos(pi + 2*pi*f*t))+H*C1_tp*(sin(pi + 2*pi*f*t));
   H_TP300 = H*C3_tp*(cos(pi + 6*pi*f*t))+H*C3_tp*(sin(pi + 6*pi*f*t));
   H_TP500 = H*C5_tp*(cos(pi + 10*pi*f*t))+H*C5_tp*(sin(pi + 10*pi*f*t));
   H_TP700 = H*C7_tp*(cos(pi + 14*pi*f*t))+H*C7_tp*(sin(pi + 14*pi*f*t));
   H_TP900 = H*C9_tp*(cos(pi + 18*pi*f*t))+H*C9_tp*(sin(pi + 18*pi*f*t));
   H_TP1100= H*C11_tp*(cos(pi + 22*pi*f*t))+H*C11_tp*(sin(pi + 22*pi*f*t));
   H_TP_signal= A*(H_TP100+H_TP300+H_TP500+H_TP700+H_TP900+H_TP1100);
end
Htp = sqrt(sum(H_TP_signal.^2,2));
%%
% TT WAVEFORM
C1_tt = 0.487 ;
C3_tt = 0.0228;
C5_tt = 0.0082;
C7_tt = 0.00954;
C9_tt = 0.00601;
C11_tt = 0.00169;
for t =  0:0.1:(1-0.1)
   H_TT100 = H*C1_tt*(cos(-0.36+ pi/2 + 2*pi*f*t))+H*C1_tt*(sin(-0.36+ pi/2 +
2*pi*f*t));
   H_TT300 = H*C3_tt*(cos(-0.99+ pi/2 + 6*pi*f*t))+H*C3_tt*(sin(-0.99+ pi/2 +
6*pi*f*t));
```

```
   H_TT500 = H*C5_tt*(cos(0.99+ pi/2 + 10*pi*f*t))+H*C5_tt*(sin(0.99+ pi/2 +
10*pi*f*t));
   H_TT700 = H*C7_tt*(cos(0.36 + pi/2 + 14*pi*f*t))+H*C7_tt*(sin(0.36 + pi/2 +
14*pi*f*t));
   H_TT900 = H*C9_tt*(cos(-0.36+ pi/2 + 18*pi*f*t))+H*C9_tt*(sin(-0.36+ pi/2 +
18*pi*f*t));
   H_TT1100= H*C11_tt*(cos(-0.99+pi/2 + 22*pi*f*t))+H*C11_tt*(sin(-0.99+pi/2 +
22*pi*f*t));
   H_TT_signal= A*(H_TT100+H_TT300+H_TT500+H_TT700+H_TT900+H_TT1100);
end
Htt = sqrt(sum(H_TT_signal.^2,2));
%%
% TR WAVEFORM
C1_tr = 0.4053 ;
C3_tr = -0.045;
C5_tr = 0.01621;
C7_tr = -0.00827;
C9_tr = 0.005;
C11_tr= -0.00335;
for t =  0:0.1:(1-0.1)
   H_TR100 = H*C1_tr*(cos(pi + 2*pi*f*t))+H*C1_tr*(sin(pi+ 2*pi*f*t));
   H_TR300 = H*C3_tr*(cos(pi + 6*pi*f*t))+H*C3_tr*(sin(pi + 6*pi*f*t));
   H_TR500 = H*C5_tr*(cos(pi + 10*pi*f*t))+H*C5_tr*(sin(pi + 10*pi*f*t));
   H_TR700 = H*C7_tr*(cos(pi + 14*pi*f*t))+H*C7_tr*(sin(pi + 14*pi*f*t));
   H_TR900 = H*C9_tr*(cos(pi + 18*pi*f*t))+H*C9_tr*(sin(pi + 18*pi*f*t));
   H_TR1100 = H*C11_tr*(cos(pi + 22*pi*f*t))+H*C11_tr*(sin(pi + 22*pi*f*t));
   H_TR_signal= A*(H_TR100+H_TR300+H_TR500+H_TR700+H_TR900+H_TR1100);
end
Htr = sqrt(sum(H_TR_signal.^2,2));
%%
% MNP thermal heating
f1 =200e3; % kHz
tau = 1e-5; %s (relaxation time)
```

```
a = 2*pi*f*tau;
c = 1 ; %mg/ml (kg/m^3)
rho = 5265; %kg/m^3
phi = c/rho; % volume fraction
mue0 = 4e-7*pi; % H/m (vaccum permeability)
chi0 = 10.47; % (equilibrium magnetic susceptibility)

PDiss_sn = phi*pi*mue0*chi0*Hsn.^2*f1*(a/(1+a^2));
PDiss_ts = phi*pi*mue0*chi0*Hts.^2*f1*(a/(1+a^2));
PDiss_tp = phi*pi*mue0*chi0*Htp.^2*f1*(a/(1+a^2));
PDiss_tt = phi*pi*mue0*chi0*Htt.^2*f1*(a/(1+a^2));
PDiss_tr = phi*pi*mue0*chi0*Htr.^2*f1*(a/(1+a^2));

hwrite("PDissMNPsSN75mgml.cache","/datacache/_Object/0/_Object/_Field_",PDiss_sn')
hwrite("PDissMNPsTS75mgml.cache","/datacache/_Object/0/_Object/_Field_",PDiss_ts')
hwrite("PDissMNPsTP75mgml.cache","/datacache/_Object/0/_Object/_Field_",PDiss_tp')
hwrite("PDissMNPsTT75mgml.cache","/datacache/_Object/0/_Object/_Field_",PDiss_tt')
hwrite("PDissMNPsTR75mgml.cache","/datacache/_Object/0/_Object/_Field_",PDiss_tr')
```

MATLAB codes used for MHT data processing

MATLAB code for Temperature data processing

Experimental data

```
clear all
clc
excel = readtable('TP300KHZ20App');
Sensor_culture_temperatureTS_aux = table2array(excel(:,2));
Sensor_culture_temperatureTP_aux = table2array (excel(:,4));
Sensor_culture_temperatureTR_aux = table2array(excel(:,6));
Sensor_ambient_temperature_aux = table2array(excel(:,8));
timee = table2array(excel(:,1));
```

```
ti = datestr(timee,'HH:MM:SS.FFF');
tim = zeros(length(ti),2); %I will save in the first column the actual value of the time and in the second column the time with respect to the first value
for j = (1:1:length(ti))
   hour = str2num(ti(j,1:2));
   minute = str2num(ti(j,4:5));
   second = str2num(ti(j,7:end));
   time_seconds = (hour*3600) + (minute*60) + second;
   tim(j,1) = time_seconds;
   if (j ~= 1)
      absolute_time = time_seconds - tim(1,1);
      tim(j,2) = absolute_time;
   end
end
time_aux = {};
Sensor_culture_temperatureTS_c = {};
Sensor_culture_temperatureTP_c = {};
Sensor_culture_temperatureTR_c = {};
Sensor_ambient_temperature_c = {};
n_invalid_values = 0;
for i = (1:1:height(excel))
   if (Sensor_culture_temperatureTS_aux(i,1)==0)||(Sensor_culture_temperatureTP_aux(i,1)==0)||(Sensor_culture_temperatureTR_aux(i,1)==0)||(Sensor_ambient_temperature_aux(i,1)==0)
      n_invalid_values = n_invalid_values + 1;
   else
      time_aux{end + 1} = tim(i,2);
      Sensor_culture_temperatureTS_c{end + 1} = Sensor_culture_temperatureTS_aux(i,1);
      Sensor_culture_temperatureTP_c{end + 1} = Sensor_culture_temperatureTP_aux(i,1);
      Sensor_culture_temperatureTR_c{end + 1} = Sensor_culture_temperatureTR_aux(i,1);
      Sensor_ambient_temperature_c{end + 1}   = Sensor_ambient_temperature_aux(i,1);
   end
end
```

```
t = cell2mat(time_aux);
Sensor_culture_temperatureTS = cell2mat(Sensor_culture_temperatureTS_c);
Sensor_culture_temperatureTP = cell2mat(Sensor_culture_temperatureTP_c);
Sensor_culture_temperatureTR = cell2mat(Sensor_culture_temperatureTR_c);
Sensor_ambient_temperature = cell2mat(Sensor_ambient_temperature_c);
total_time = t(1,end)/60;
fprintf('The experiment was runned for %.2f minutes',total_time)


clear excel i time_aux Sensor_culture_temperatureTS_c Sensor_ambient_temperature_c
Sensor_culture_temperatureTP_c
%% Plot data
figure
p1 = plot(t, Sensor_culture_temperatureTP);
p1.LineWidth = 3;
p1.Color = [1 0 0];
hold on
p2 = plot(t, Sensor_culture_temperatureTR);
p2.LineWidth = 3;
p2.Color = [0 1 0];
hold on
p3 = plot(t, Sensor_culture_temperatureTS);
p3.LineWidth = 2;
p3.Color = [0 0 0];
hold on
p4 = plot(t, Sensor_ambient_temperature);
p4.LineWidth = 3;
p4.Color = [0 0 1];
hold on
hold off
grid on
axis tight
ylim([0 40])
```

```
title('Temperature variation')
xlabel('Time (s)')
ylabel('Temperature (ºC)')
l = legend('Sensor in culture medium TP','Sensor in culture medium TR','Sensor in culture medium TS','Ambient temperature', 'Location', 'southeast');
clear l p1 p2 p3 p4
```

Simulation data

```
frequency = 100:100:1000;
% Define temperature data
temperature1=readmatrix("SN_2D_1mT.xlsx");
temperature2=readmatrix("SN_2D_5mT.xlsx");
temperature3=readmatrix("SN_2D_10mT.xlsx");
%plot the curves
figure
plot(frequency,temperature1,'LineWidth', 2.5)
hold on  %retain the current curve
plot(frequency,temperature2,'LineWidth', 2.5)
plot(frequency,temperature3,'LineWidth', 2.5)
xlabel('Frequency(kHz)');
ylabel('Temperature(\circC)');
title('Temperature distribution inside cell culture medium at different amplitudes');
grid on
hold off
```